Nuclear Magnetic Resonance Studies of Aqueous Electrolyte Ion Adsorption in Microporous Carbon Electrodes

Ryan John Bragg

Lancaster University

Department of Chemistry

This thesis is submitted for the degree of

Doctor of Philosophy

September 2024

Declaration

I hereby declare that this thesis is the product of my own work, and its content does not include contributions from collaborations unless explicitly stated. The content of this thesis has not been submitted, in whole or in part, for the award of any other degree, diploma, or qualification at Lancaster University or any other institution, except as noted in the preface and specified in the text.

Ryan John Bragg

September 2024

Abstract

To improve processes that rely on guest-surface interactions within microporous carbonaceous materials (*e.g.,* electrocatalysis, gas sorption, and energy storage) it is critical to understand the behaviour of adsorbed species within these materials. A particular application of interest is electric double-layer capacitors (or supercapacitors), where charge is stored through the non-faradaic electrosorption of ions at the electrolyte-surface interface. However, despite extensive research, the adsorption mechanisms in these complex nanoscale structures remain unclear. This is especially true for aqueous electrolytes, where limited prior study and the challenges of pH effects further complicate our understanding.

In this thesis, solid-state nuclear magnetic resonance (NMR) spectroscopy is used to observe and quantify aqueous adsorbate partitioning behaviour driven by spontaneous physisorption within the micropores. The solvation properties of the electrolyte ions are shown to influence the ionophilicity/ionophobicity of the adsorbate-carbon system, with ionophilic and ionophobic systems exhibiting distinct behaviour concerning the electrolyte loading volume. Additionally, the diameter of micropores is shown to influence spontaneous electrolyte partitioning behaviour and disrupt ion solvation. *In situ* NMR spectroscopy experiments conducted on a working supercapacitor with microporous carbon electrodes and aqueous sodium sulphate or aqueous sodium bis(trifluoromethane)sulphonimide electrolytes reveals that spontaneous electrolyte partitioning behaviour affects the charge-balancing mechanism. The findings suggest that spontaneously ionophilic systems favour charge-balancing by counter-ion adsorption under an applied voltage, and spontaneously ionophobic systems favour a co-ion ejection mechanism under an applied potential. Finally, planewave-based electronic density functional theory (DFT) simulations were conducted on periodic graphene systems, with magnetic shielding parameters calculated using the gauge-including projector augmented wave (GIPAW) method. The complexities arising from the unique electronic structure of graphene are discussed, and the associated convergence challenges in determining magnetic shielding values are identified. Converged nucleus-independent chemical shift (NICS) values and ^{13}C chemical shifts are presented for both a pristine periodic graphene system and a Stone-Wales defected system.

The work outlined in this thesis provides molecular-level insight into the role of electrolyte properties on spontaneous physisorption behaviour and charged electrosorption behaviour within microporous carbon electrodes.

Acknowledgements

First and foremost, I would like to express my sincere gratitude to my supervisor, Prof. John Griffin, for giving me the opportunity to work on this project, and for his unwavering support and guidance throughout. It has been a privilege to work with such an outstanding researcher, and I am grateful for the rigorous scientific training that he has provided. I would also like to thank Dr Kieran Griffiths and Chris Cook for fostering a welcoming and humorous work environment, offering exceptional moral support, and always being willing to discuss ideas and assist with experiments. Additionally, I extend my thanks to Dr Abby Haworth and Dr Valerie Seymour for the solid-state NMR spectroscopy training they provided at the outset of my studies.

Beyond the Griffin group, I would like to thank my collaborators: Prof. Rob Dryfe, Prof. Volker Presser, Prof. Jonathan Yates, and Prof. Chris Pickard, for their invaluable insights. I am also thankful to Dr Imgon Hwang and Mantas Lekatas for making my initial collaborative work thoroughly enjoyable. I also extend my thanks Dr Kacper Polus and Dr Sara Baldock for performing XPS and SEM measurements, respectively, and to the EPSRC for financial support.

I would like to thank my partner, Sia, for being a steadfast beacon of positivity and affection, and for believing in me through every challenge. Finally, I extend my heartfelt thanks to my family for their unwavering support and love. I would not be where I am today without the encouragement and care you have all generously provided.

List of publications

The following publications include contributions from the author that are relevant to the content of this thesis:

1. **R.J. Bragg**, K. Griffiths, I. Hwang, M. Leketas, K. Polus, V. Presser, R.A.W. Dryfe and J.M. Griffin, "Solvation effects on aqueous ion adsorption and electrosorption in carbon micropores", *Carbon*, 2024, **229**, 119531.

2. **R.J. Bragg**, J.R Yates, C.J. Pickard, and J.M. Griffin, "Determining magnetic shielding parameters of periodic aromatic materials using DFT", *Manuscript in preparation*.

and the following works feature contributions from the author that are not included in this thesis:

3. I. Hwang, M. Leketas, K. Griffiths, **R. Bragg**, J.M. Griffin and R.A.W. Dryfe, "Effect of Salt Concentration in Water-In-Salt Electrolyte on Supercapacitor Applications", *ChemElectroChem*, 2024, **11**, 1–8.

4. K. Griffiths, H. Brough, **R.J. Bragg**, N.R. Halcovitch, and J.M. Griffin, "Molecular insights into solid-state photochromism in bulk and confined *N*-salicylidenes", *J. Mater. Chem. C.*, 2024, **12**, 19453-19462.

5. I. Hwang, M. Leketas, S. Kaewmorakot, **R.J. Bragg**, J.M. Griffin and R.A.W. Dryfe, "Concentration-dependent behavior on alkali metal trifluoroacetates and their role in water-in-salt electrolyte supercapacitors", *Manuscript in preparation*.

6. K. Griffiths, C. Cook, **R.J. Bragg**, and J.M. Griffin, "An investigation into the structure of organic anode materials with NMR crystallography", *Manuscript in preparation*.

Table of contents

Chapter 1

Introduction

Porous carbonaceous materials (PCMs) are an important class of materials used in a wide range of industrial and scientific applications, such as catalysis, filtration, and energy storage.[1–6] Most applications aim to exploit the adsorptive properties of the carbon, wherein guest species are physically adsorbed to the internal surface which are accessed via the porous network. PCMs typically exhibit high internal surface areas (from 1000 $m^2 g^{-1}$ to upwards of 2000 $m^2 g^{-1}$), and pore sizes can be selectively controlled, ranging from the microporous (< 2 nm diameter) to the mesoporous (2-50 nm) regime, with PCMs exhibiting varying pore size distributions and pore hierarchies being attainable.[7–11] The physical structure of the carbon is typically tailored by carefully adjusting the synthetic conditions or by selecting specific precursor materials. A further physical property of interest is electrical conductivity, where PCMs typically exhibit good electrical conductivity due to extensive conjugation of aromatic carbon rings throughout their structures.[12,13] These properties make PCMs particularly desirable for electrochemical devices and processes involving adsorption and/or electro-sorption of specific molecules and ions, such as capacitive deionisation (CDI) and supercapacitors.[2,8,14–17] To optimise the use of PCMs for specific applications, an understanding as to how adsorbate species behave within microporous networks must be attained. However, PCMs typically exhibit complex amorphous structures that lack long-range order, presenting significant difficulties for characterisation by conventional spectroscopic techniques. Characterisation of adsorbate behaviour also provides challenges, as any technique must be able to distinguish the adsorbed species from non-adsorbed species in addition to isolating the adsorbate from the carbon structure. A further complication regarding adsorbate behaviour is the fact that they are often highly dynamic, thus characterisation techniques are required to operate within a sufficiently short timescale to accurately capture the behaviour of the adsorbates.

The complexity of the system has led to significant ambiguity regarding the precise behaviour and properties of adsorbed species within PCMs, motivating numerous studies attempting to

elucidate adsorbate behaviour. Theoretical modelling has provided insight into the behaviour of guest species within microporous networks, with studies highlighting the importance of specific ion properties, relative pore and ion dimensions, and the solvation properties of solvents and solutes.[6,10,18–22] The behaviour of spontaneously adsorbed species has been shown to have significant implications for the charging mechanisms in electrochemical devices.[10,16,23–26] The ionophobicity or ionophilicity of PCMs, a property termed by Kondrat *et al*. denoting the proclivity for adsorbate species to enter the pores before charging, has also been shown to influence the charge storage mechanism and charging kinetics of electrochemical devices.[25–27]

Recently, nuclear magnetic resonance (NMR) spectroscopy has re-emerged as a highly sensitive probe of the behaviour of adsorbates within PCMs.[7,13,28,29] NMR spectroscopy does not require long-range structural order, can observe both solids and liquids, is element-specific and quantitative, and can probe the dynamic behaviour of adsorbate species. Importantly, the phenomenon of the nucleus-independent chemical shift (NICS), an effect arising from ring current shielding induced by the circulation of π-electrons within the conjugated aromatic rings throughout the PCM, allows for the distinction between adsorbed and non-adsorbed species to be made.[30,31] The magnitude of the NICS can be influenced by pore size, with the effect of proximity to the pore wall being extensively studied both theoretically and experimentally.[18,22,32–34] The domain size and homogeneity of the graphene-like fragments making up the PCM structure have also been shown to influence the NICS.[22,32,34–36] The magnitude of the measured frequency difference between free and adsorbed species (termed $\Delta\delta$, derived from the difference between the chemical shift of the in-pore environment, $\delta_{\text{in-pore}}$, and the chemical shift of the bulk solution, δ_{bulk}, with $\Delta\delta = \delta_{\text{in-pore}} - \delta_{\text{bulk}}$) has been shown to be multifaceted, with the magnitude being determined by the NICS as well as other factors such as ion dynamics, electrolyte concentration, and specific ion effects.[7,10,33] As well as investigating spontaneous adsorption behaviour, the separation of adsorbed species from those in the bulk electrolyte has enabled *in situ* NMR measurements to provide quantitative insight into charging mechanisms for supercapacitors.[16,29,31,37]

The study of ion behaviour within PCMs using NMR spectroscopy has thus far largely focused on organic systems due to the extensive use of organic electrolytes in electrochemical devices.[13,16,24] However, there is an increasing interest in aqueous systems owing to their relevancy in capacitive deionisation, as well as developments in electrical storage devices continuing to push towards the use of greener reagents.[38,39] Prior NMR studies have

investigated the confinement of aqueous alkali-metal salts within myriad PCMs and the relevance of ion-water interactions for select electrolytes.[10,24,40]

The work presented in this thesis details a systematic NMR study investigating spontaneous ion adsorption behaviour and electrosorption behaviour across a series of aqueous alkali metal salt solutions within a set of model PCMs.

Chapter 2 presents the background theory of electric double-layer capacitors, and how these devices can be electrochemically characterised. Theory regarding microporous carbon electrode structure and electrolyte composition are also detailed alongside relevant theoretical models.

Chapter 3 introduces the fundamental concepts and experimental practices of NMR spectroscopy, the primary experimental technique of this thesis. An overview of the application of electronic density functional theory in determining magnetic shielding parameters for periodic systems is also provided.

Chapter 4 presents the application of NMR spectroscopy to study spontaneous ion adsorption behaviour within aqueous supercapacitors. Specific ionic properties are shown to influence spontaneous ion and solvent partitioning within microporous carbons. Solvation strength is identified as a key factor that influences the ionophilicity of the carbon-electrolyte system and the local solvation environment of ions within confined environments.

Chapter 5 discusses the challenges of performing *in situ* NMR experiments on aqueous supercapacitors. The effects of different electrolyte properties on the observed charging mechanism are quantitatively investigated, and the response of the NMR spectra to applied potentials are discussed.

Chapter 6 details the challenges of determining magnetic shielding parameters for periodic graphene structures and presents approaches to obtain convergence. ^{13}C chemical shifts, NICS values, and ring current maps are shown for periodic slit-pores of both graphene and simplified Stone-Wales defected graphene systems.

Chapter 7 presents the main conclusions of this work and proposes directions for future studies.

Chapter 2

Activated carbon electrodes and supercapacitance

2.1 Energy storage fundamentals

In principle, a supercapacitor can be constructed by placing two conducting electrodes into an electrolyte. When a potential difference is applied between the electrodes, the electrolyte ions will be attracted to the electrode surface of opposing charge, with cations moving towards the negative electrode and anions moving towards the positive electrode (**Figure 2.1**). In the simplest scenario, in which two parallel and perfectly flat electrode surfaces are considered, the attracted counterions will form an electrical double-layer (EDL) along the surface of each electrode, balancing the electrode charge.[41]

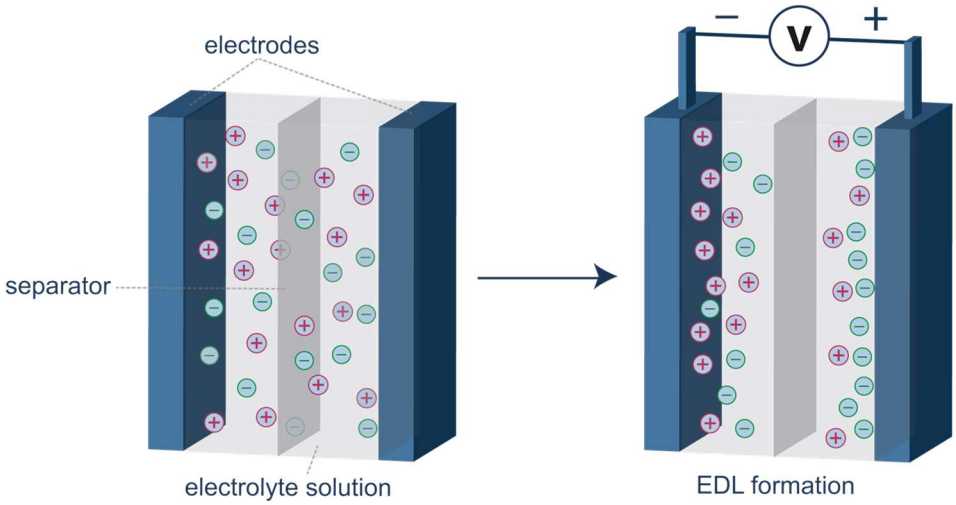

Figure 2.1. Schematic depicting the formation of the electrical double-layer at the electrode interface as a voltage is applied across the electrodes.

The idea that excess ionic charge in an electrolyte solution balances the charge across the electrode via the formation of an EDL was first introduced by Helmholtz in 1853.[42]

Importantly, removing the applied potential does not break the formation of the EDL, with the electrolyte counterions remaining electrosorbed to the electrode surface, maintaining a stored charge within the electrodes. The stored electrical charge is then released by connecting the opposing electrodes across an external circuit, enabling the desorption of electrolyte ions from the electrode surface, and the simultaneous travel of electrons across the external circuit. Practically, EDLs are formed at the electrode-electrolyte interface for both the anode and cathode. As such, the system can be considered as two capacitors in series, with the total capacitance across the cell, C_{T}, being given by:

$$\frac{1}{C_{\mathrm{T}}} = \frac{1}{C_1} + \frac{1}{C_2} \tag{2.1}$$

where C_1 and C_2 are the capacitances of the two electrodes. Conventionally, capacitance is reported in Farads (F) and is often normalised by the mass of the electrode or the electrolyte volume.[43] In symmetrical cells with identical electrodes, the individual electrode capacitances, C_{e}, are often assumed to be equivalent as a first approximation. In reality, however, C_1 and C_2 may differ due to variations in adsorption mechanisms at each electrode and differences in potential limits, which arise from the stability of the electrode-electrolyte interphase when cations are adsorbed instead of anions.[44–46] Nevertheless, in the absence of a reference electrode, the approximation $C_1 \cong C_2$ is often sufficient, with C_{e} being defined as:[47]

$$C_e = 2C_{\mathrm{T}} \tag{2.2}$$

Recently, Gittens *et al*. have drawn attention to inconsistencies in capacitance determination within the field.[43] The recommendation of the authors for a symmetrical cell, and the methodology used herein, is to report C_e normalised by the mass of a single electrode, m_e. This effectively provides the capacitance of the working electrode. Conventionally, supercapacitor devices fall into one of two categories: EDL capacitors (EDLCs), where capacitance is solely determined by non-faradaic adsorptive charge storage, and pseudo-capacitors, where charge storage is augmented by faradaic contributions arising from rapid reversible redox reactions between the electrolyte and the electrode surface.[12] Supercapacitor devices considered herein are exclusively EDLCs. For model parallel-plate electrodes, the electric field, E, between two charged plates is given by:

$$E = \frac{q}{\varepsilon_0 \varepsilon_r A} \tag{2.3}$$

where q is the charge stored in an electrode, ε_0 and ε_r are the dielectric constants of free space and the electrolyte, respectively, and A is the electrode surface area. Thus, E can be defined as:

$$E = \frac{V}{d} \tag{2.4}$$

where V is the applied potential across the cell and d is the distance separating the electrode and electrosorbed electrolyte during charge separation. The relationship between C_{T}, V, and q is given by:

$$C_{\mathrm{T}} = \frac{q}{V} \tag{2.5}$$

Thus, the capacitance of an electrode in a parallel-plate system can be derived from Equations 2.3-2.5, giving:[12,48,49]

$$C_{\mathrm{T}} = \frac{\varepsilon_0 \varepsilon_r A}{d} \tag{2.6}$$

Strictly, Equation 2.6 is only accurate for model systems comprising equivalent electrodes that are parallel to each other. As such, when considering complex electrode materials that deviate from this model, calculating the true capacitance of the system becomes difficult. With that being said, the terms of Equation 2.3 still maintain relevancy within even the most complex electrode structures. By far, one of the most widespread categories of complex electrode materials is that of microporous activated carbons. The extensive use of this material family is due to their facile synthesis, abundancy of precursors, structural tunability, and good electrochemical performance.[9,13,50] It is for these reasons that this material family is the system of interest within this thesis. The desirable electrochemical performance of microporous carbon electrode materials can be fundamentally linked to key structural factors such as large internal surface areas > 2000 $m^2\ g^{-1}$ and atomic-scale electrode-ion separation within the carbon pores (several Å).[51] Exploiting these fundamental contributions towards capacitance has resulted in the electrochemical performance of supercapacitors far exceeding that of conventional dielectric capacitor devices (often by several orders of magnitude).[52] In recent years, substantial

efforts have been made attempting to isolate further contributions towards capacitance across a range of increasingly complex supercapacitor devices that utilise microporous carbon electrodes.[23,37]

The following sections detail the determination of capacitance via electrochemical analysis and offers an overview of key concepts relating to electrolyte composition and microporous carbon structure in supercapacitor devices. Additionally, possible contributions to capacitance beyond those predicted by a model parallel-electrode system, including findings from experimental studies and extensive modelling, are detailed.

2.2 Electrochemical characterisation of supercapacitors

2.2.1 Cyclic voltammetry

For the study of supercapacitor performance, cyclic voltammetry (CV) is a common method applied in electrochemical analysis. A cell potential, V, is applied across the cell that increases linearly with time at a set scan rate, $\mathrm{d}V/\mathrm{d}t$, to a set maximum voltage, $V_{\max}$ (**Figure 2.2a**). Once $V_{\max}$ is reached, a negative scan rate is then applied, and the potential is swept in the reverse direction to a minimum voltage, $V_{\min}$. As the potential is swept, the current response of the cell, I, is recorded (**Figure 2.2b**). The values of $V_{\max}$ and $V_{\min}$ are typically determined as to avoid electrochemical decomposition of supercapacitor components (typically the electrolyte). Differentiating Equation 2.5 with respect to time gives:

$$I = C_{\mathrm{T}} \frac{\mathrm{d}V}{\mathrm{d}t} \tag{2.7}$$

Equation 2.7 shows that, for a CV experiment, the sign of the current will match that of the scan rate. For an ideal EDLC, in which there is no electrical resistance, the cyclic voltammogram should exhibit a rectangular shape, as predicted by Equation 2.7 (**Figure 2.2c**). However, in practice, EDLC devices are non-ideal, exhibiting several sources of resistance, including ionic resistance within the electrolyte and electronic resistance across the electrode, current collector, and circuitry. A non-ideal supercapacitor is therefore typically modelled as a series circuit comprising a resistor and a capacitor (an RC circuit). The voltage across the RC circuit, V_{T}, is derived using Kirchhoff's loop rule:

$$V_{\mathrm{T}} - V_{\mathrm{R}} - V_{\mathrm{C}} = 0 \tag{2.8}$$

where V_{R} is the voltage across the resistor, and V_{C} is the voltage across the capacitor. V_{T} is given by:

$$V_{\mathrm{T}} = \frac{\mathrm{d}V}{\mathrm{d}t}t \tag{2.9}$$

where t is the time elapsed since the start of the sweep. V_{R} is derived using Ohm's law:

$$V_{\mathrm{R}} = IR = \frac{\mathrm{d}q}{\mathrm{d}t}R \tag{2.10}$$

where R is the equivalent series resistance across the RC circuit. The voltage applied across a capacitor is given by Equation 2.5, allowing Equation 2.8 to be rewritten as:[49]

$$V_{\mathrm{T}} = \frac{\mathrm{d}q}{\mathrm{d}t}R + \frac{q}{C_{\mathrm{T}}} \tag{2.11}$$

Multiplying Equation 2.11 by C_{T} and rearranging gives the following differential equation:

$$\frac{\mathrm{d}t}{RC_{\mathrm{T}}} = \frac{\mathrm{d}q}{V_{\mathrm{T}}C_{\mathrm{T}} - q} \tag{2.12}$$

which, assuming $q = 0$ at $t = 0$, can be integrated and rearranged to isolate the charge accumulated across the capacitor in an RC series circuit:

$$\int_{t=0}^{t} \frac{1}{RC_{\mathrm{T}}}\mathrm{d}t = \int_{q=0}^{q} \frac{1}{V_{\mathrm{T}}C_{\mathrm{T}} - q}\mathrm{d}q\,, \tag{2.13}$$

$$\frac{t}{RC_{\mathrm{T}}} = -\ln\left(\frac{V_{\mathrm{T}}C_{\mathrm{T}} - q}{V_{\mathrm{T}}C_{\mathrm{T}}}\right), \tag{2.14}$$

$$\exp\left(\frac{-t}{RC_{\mathrm{T}}}\right) = \frac{V_{\mathrm{T}}C_{\mathrm{T}} - q}{V_{\mathrm{T}}C_{\mathrm{T}}}, \tag{2.15}$$

$$q = V_{\mathrm{T}}C_{\mathrm{T}}\left[1 - \exp\left(\frac{-t}{RC_{\mathrm{T}}}\right)\right]. \tag{2.16}$$

Assuming that $q = 0$ at $t = 0$, the current response of the RC circuit can be expressed as:[49]

$$I = \frac{\mathrm{d}V}{\mathrm{d}t} C_{\mathrm{T}} \left[1 - \exp\left(\frac{-t}{RC_{\mathrm{T}}}\right)\right] \tag{2.17}$$

As such, the additional resistances across the cell result in a current response that differs from an ideal capacitor. In practice, EDLC devices with internal resistances typically exhibit 'leaf-shaped' cyclic voltammograms (**Figure 2.2d**), with the current decaying towards the product of C_{T} and the scan rate, as determined by Equation 2.17. C_{T} can also be quickly estimated from the measured current at plateaued regions of the cyclic voltammogram, at which the current response is close to ideal, and Equation 2.7 can be applied (**Figure 2.2d**). However, a better estimation of C_{T} from a cyclic voltammogram is given by:

$$C_{\mathrm{T}} = \frac{\int_{V_{\mathrm{min}}}^{V_{\mathrm{max}}} I \, \mathrm{d}V}{\frac{\mathrm{d}V}{\mathrm{d}t} \cdot |V_{\mathrm{max}} - V_{\mathrm{min}}|} \tag{2.18}$$

where V_{max} and V_{min} are the bounds of the discharge voltage window in which capacitive behaviour is observed, $|V_{\mathrm{max}} - V_{\mathrm{min}}|$.[43,49]

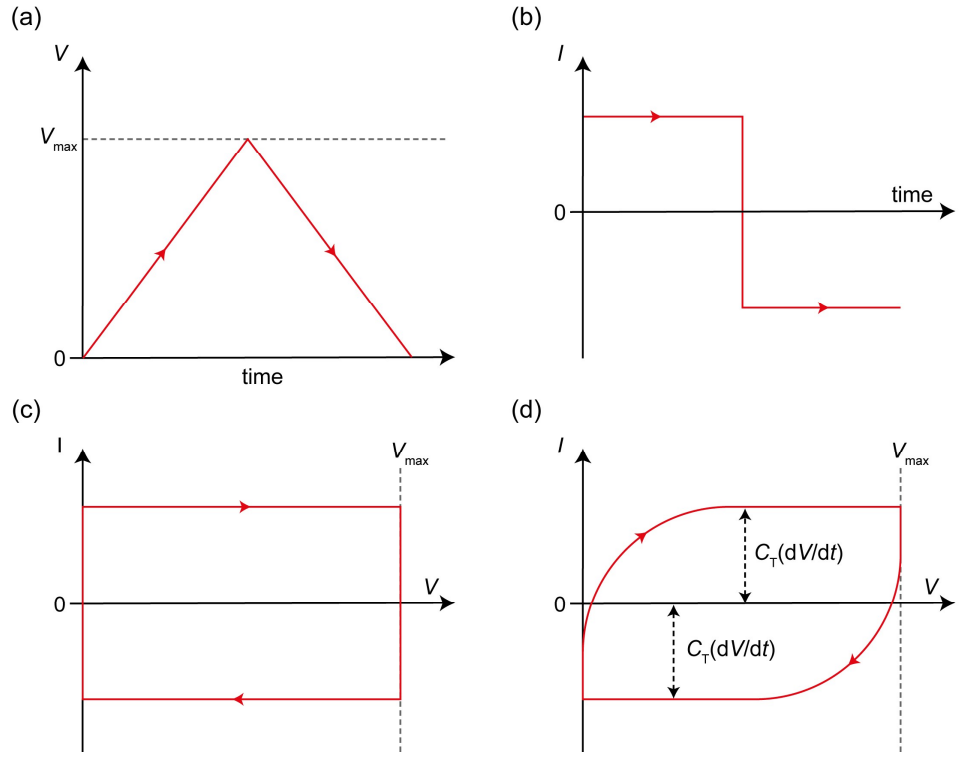

Figure 2.2. Plots corresponding to cyclic voltammetry experiment showing (a) applied voltage against time, (b) the measured current response, and (c) the cyclic voltammogram for an ideal capacitor (*i.e.*, no resistance). (d) A cyclic voltammogram for a non-ideal capacitor that exhibits resistance.

For symmetrical two-electrode EDLC devices, the general approach is to integrate over the full area of the CV curve and to then apply an additional factor of a half to C_T to estimate the discharge capacitance.[43] It is generally recommended that several cycles are performed prior to capacitance measurement in order to isolate irreversible faradaic interactions from reversible capacitive behaviour. Cyclic voltammetry experiments provide a method to readily observe capacitive behaviour, with faradaic processes being easily identified as peaks in I due to faradaic current contributions.

2.2.2 Galvanostatic charge-discharge experiments

Another electrochemical method that allows the determination of C_T is the galvanostatic charge-discharge (GCD) experiment. The GCD experiment is best suited for determining C_T as its conditions correlate more closely to how a load is applied to a supercapacitor in the majority of applications.[47] In a GCD experiment, a constant I is applied across the capacitor and the response of V is measured (**Figure 2.3a**). A positive I gives a positive increase in V over time, as shown by Equation 2.7. V_{max} and V_{min} are then defined to bound the potential window of the experiment, with the positive current reversing once $V_T = V_{max}$, and the negative current reversing when $V_T = V_{min}$ (**Figure 2.3b**). For a constant I, and at $t = 0$ where $V = 0$, Equation 2.8 can be rewritten as:

$$V_T = I \cdot \left(R + \frac{t}{C_T}\right) \tag{2.19}$$

which can be differentiated with respect to time, giving:

$$\frac{dV}{dt} = \frac{I}{C_T} \tag{2.20}$$

Therefore, the GCD experiment can readily provide C_T by simply measuring the change in the voltage with respect to time. The resistance, R, across the device can also be obtained by measuring the voltage drop, ΔV, as the applied current is changed, ΔI, as described by Ohm's law, where $R = \Delta V/\Delta I$. If no dwell time is implemented and I is reversed upon reaching the bounds of the potential window, $\Delta I \cong 2I$ and the resistance is determined by $R = \Delta V/2I$.[43,53–55] As with CV experiments, several charge-discharge cycles are recommended prior to the analysis of the discharge gradient.

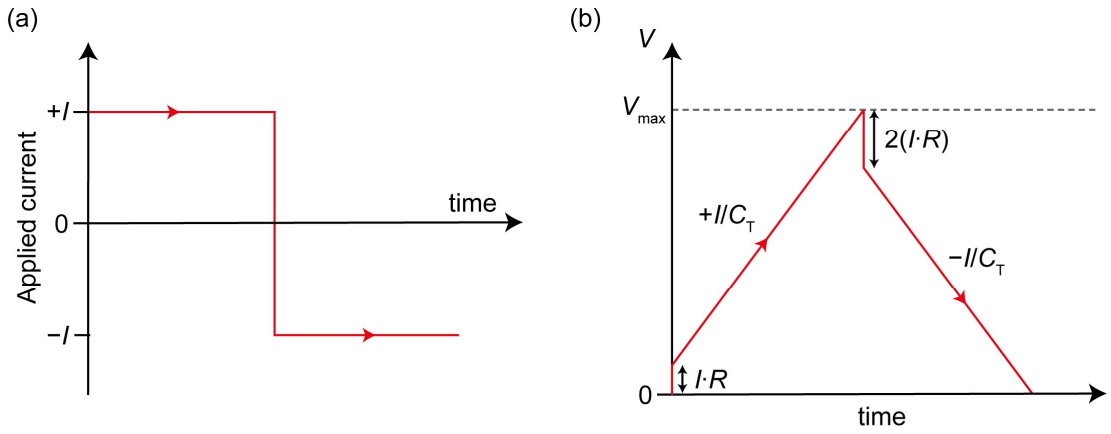

Figure 2.3. Plots depicting the galvanostatic charge-discharge experiment, showing the (a) applied current and (b) measured voltage response.

2.2.3 Chronoamperometry

In chronoamperometry (CA) experiments, a constant V_T is applied and the response of I is measured (**Figure 2.4a**).

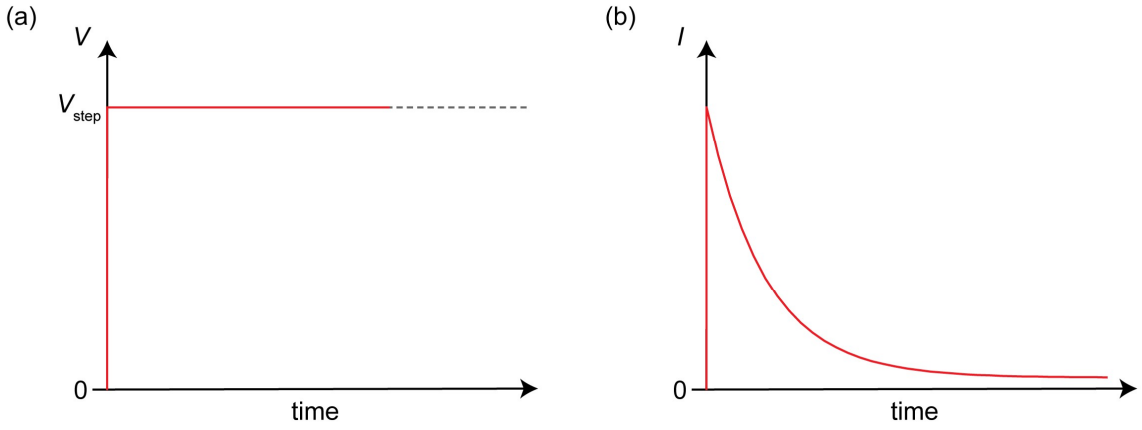

Figure 2.4. Plots of the chronoamperometry experiment showing (a) applied voltage against time and (b) the measured current response.

This method provides useful information regarding the equilibrium state of the supercapacitor at a given V_T, a particularly useful tool when paired with spectroscopic techniques. The current response for a fixed voltage is given by the time-derivative of Equation 2.16:[49]

$$I = \frac{V_T}{R}\exp\left(\frac{-t}{RC_T}\right) \tag{2.21}$$

As such, I is observed to decay towards zero as time elapses in the CA experiment (**Figure 2.4b**). Practically, a minimum current, $|I_{min}|$, is defined instead of waiting for $I = 0$. When

$|I_T| < |I_{min}|$, the cell is considered equilibrated, and spectroscopic measurements can be performed on the cell at a given state.

2.3 Electrolytes

The suitability of an electrolyte for application in a supercapacitor is governed by two key parameters: the maximum operating voltage before electrolyte decomposition, V_{max}, and the ionic conductivity, κ. The relevancy of V_{max} is intrinsically related to the energy stored across the system. The work required, $\mathrm{d}U$, to move an infinitesimal charge from the negative plate to the positive plate is given by:

$$\mathrm{d}U = V\mathrm{d}q \tag{2.22}$$

where V is the voltage on the capacitor and $\mathrm{d}q$ is the charge element. Substituting in Equation 2.5, and then integrating with respect to the charge stored across the whole capacitor, Q, gives the energy stored across the device, U:

$$U = \int_0^Q \frac{q}{C_T}\mathrm{d}q = \frac{1}{2}\frac{Q^2}{C_T} \tag{2.23}$$

This energy expression can then be expressed in three equivalent forms using various permutations of Equation 2.5:

$$U = \frac{1}{2}\frac{Q^2}{C_T} = \frac{1}{2}QV = \frac{1}{2}C_T V^2 \tag{2.24}$$

Importantly, V_{max} determines the theoretical maximum energy stored across the capacitor, U_{max}. The electrochemical performance of supercapacitors is therefore dependent upon V_{max}, a parameter largely limited by electrolyte stability. Desirable supercapacitor electrolytes exhibit wide electrochemical stability windows to maximise V_{max}, and exhibit high ionic conductivities, κ, facilitating the easy transport of ions towards the electrode surface.[56,57]

2.3.1 Organic electrolytes

Currently, most commercial supercapacitor devices use organic electrolytes as they tend to exhibit wide and stable operational potential windows (approximately 2.5 V).[48,50,58] An organic

electrolyte of particular interest is 1 M tetraethylammonium tetrafluoroborate (NEt_4BF_4) in acetonitrile (ACN) as it exhibits a V_{max} of 2.7 V and a relatively high κ of ~60 mS cm^{-1}.[13,50,58,59] However, it is worth noting the ionic conductivity of organic electrolytes is relatively poor compared to other electrolytes, exhibiting specific resistances that are at least 20-50 times greater than concentrated aqueous electrolytes.[48] Additionally, there are substantial concerns regarding safety and the widespread applicability of high-performance organic electrolytes (particularly those comprising acetonitrile). This is largely due to issues related to toxicity, flammability, complex cell-assembly, and sustainability.[58,60] Substantial work has been performed attempting to develop low resistivity, non-toxic organic electrolytes to replace acetonitrile, but these efforts have led to minimal returns. Propylene carbonate is currently the best commercial alternative as it offers a suitable balance between power and energy stored.[58,61]

2.3.2 Room temperature ionic liquids

An alternative class of electrolyte is that of room temperature ionic liquids. These are solvent-free electrolytes exhibiting high operating voltages (V_{max} > 4 V), good thermal stability, and low toxicity.[27,40,50,62,63] Room temperature ionic liquids are typically defined as compounds completely composed of ions with a melting point below 100 °C. Many ionic liquids comprise either imidazolium, pyrrolidinium, pyridinium, piperidinium, or tetra-alkylammonium cations, paired with chloride, tetrafluoroborate, bis(fluorosulfuonyl)imide, or bis(trifluoro-methanesulfonyl)imide anions.[50,63,64] As ionic liquids are solvent-free electrolytes, V_{max} is not limited by the breakdown of the solvent, and is entirely determined by the electrochemical stability of the ions. This gives rise to the high V_{max} values often observed for ionic liquids. Furthermore, ionic liquids typically perform well across a broad temperature range due to their negligible volatility. This was shown by Lai *et al.*, who demonstrated a 1-ethyl-3-methylimidazolium tetrafluoroborate-based supercapacitor that demonstrated over > 90% capacity retention over 5000 cycles across temperatures ranging from −20 to 60 °C.[65,66] The complexity and size of many ionic liquid species also provides scope for chemical modification, potentially facilitating the tailoring of electrochemical properties. However, ionic liquids suffer from high-costs due to their often-complex molecular structures, and low κ (< 10 mS cm^{-1}) due to their high viscosities.[67–70] The issue of poor ionic conductivity can be alleviated by creating blends of ionic liquid and acetonitrile. However, these combinations demonstrate the aforementioned issues of toxicity and flammability that are often associated with organic electrolytes.[58,68,69]

2.3.3 Aqueous electrolytes

Supercapacitors using aqueous electrolytes (*e.g.,* lithium bis(trifluoromethane)sulphonimide (LiTFSI), KOH, and H_2SO_4) have been shown to exhibit high specific capacitance and exceptional rate performance due to their small ion diameters, high solubilities, and excellent ionic conductivity (at least an order of magnitude greater than nonaqueous electrolytes, with $\kappa = 0.8$ S cm^{-1} for 1 M H_2SO_4 at 25 °C).[4,50,70,71] Aqueous electrolytes also benefit from less stringent drying, purification, and assembly processes, as well as being relatively cheap and more environmentally-friendly than their nonaqueous counterparts. The use of aqueous electrolytes extends beyond conventional energy storage devices, with fundamental adsorption behaviours demonstrating significance in analogous applications such as capacitive deionisation (CDI).[2,15,38] Unfortunately, aqueous electrolytes face a significant barrier due to hydrogen and oxygen evolution reactions, which occur at approximately 0 V (for hydrogen evolution) and +1.23 V for oxygen evolution, both referenced to the standard hydrogen electrode (SHE) at 25 °C. These reactions subsequently limit the operational potential window.[48,50,72]

There has been substantial research effort focussing on expanding the potential window of aqueous supercapacitors, as the total energy stored scales with the square of $V_{\max}$ (Equation 2.24). Asymmetric electrode devices, where a pseudocapacitive or battery-like cathode is paired with an EDLC-driven anode (*e.g.,* activated carbon), have been shown to expand the potential window of aqueous electrolytes by exploiting high overpotentials for H_2 and O_2 evolution at the anode and cathode, respectively.[73,74] Long *et al*. demonstrated that the potential window of 0.5 M K_2SO_4 can be increased from 0.9 V to ~2.0 V by changing from a symmetric device (MnO_2 | MnO_2) to an asymmetric device (MnO_2 | activated carbon).[74] Careful tailoring of the individual electrode potential ranges and electrode masses to balance the charge across the two electrodes has also been shown to increase the stable potential window of aqueous electrolytes.[46,75–78] The addition of various organic additives such as ethylene glycol,[79] poly(ethylene glycol),[80] and dimethyl sulfoxide,[81] have also demonstrated enhanced electrochemical stability through the formation of strong hydrogen bonds with water molecules, limiting the electrochemical activity of water.

2.3.4 Water-in-salt electrolytes

A recent development in aqueous electrolytes is that of highly concentrated, water-in-salt electrolytes (WiSE). Here, the electrolyte salt outnumbers the water by both weight and volume.[70,82] Suo *et al*. demonstrated that a WiSE electrolyte can expand the stable potential window of aqueous systems, with 21 molal LiTFSI exhibiting a stable potential window of 3 V.[83] The broad potential window can be attributed to a greater number of contact ion pairs and aggregates between cations and anions due to the reduced water population. The coordination between cations and anions causes the reduction potential of the electrolyte to be dominated by ion decomposition instead of water electrolysis.[82–84] Upon electrolyte degradation, the anion is preferentially decomposed, forming an electronically-insulating, but ionically-conductive solid electrolyte interphase (SEI) on the surface of the anode which increases the chemical stability of the cations.[85,86] Simultaneously, most water molecules are coordinated to the cation through a donation of the oxygen lone pair, increasing the oxidation potential of water and improving anodic stability.[87]

2.4 Porous carbonaceous electrodes

2.4.1 Synthesis of porous carbons

Pores are categorised according to their diameters into three types following IUPAC classification: micropores (< 2 nm), mesopores (2-50 nm), and macropores (> 50 nm).[88] Intuitively, narrower pores give rise to a larger internal surface area, facilitating the adsorption of a greater number of charged ions at the electrode-electrolyte interface, ultimately resulting in a larger capacitance (as described by Equation 2.6). Activated carbons are the most commonly used supercapacitor electrode material due to their large surface area, high electrical conductivities, and moderate costs.[51] Activated carbons are typically prepared through a thermal and/or chemical activation process of carbonaceous precursors (*e.g.,* wood, coal, coconut shells, fruit pits, and synthetic polymers).[6,13] Conventionally, synthesis begins with carbonisation (heat treatment in an inert atmosphere at 700-1000 °C), a process in which the precursor is converted to graphitic sheets and fragments comprising various sizes and degrees of perfection (*e.g.,* defect density, curvature, and ‘dangling’ carbons). Once carbonised, the material is subjected to either physical (or thermal) activation, where the sample is heated at high temperatures (700-1200 °C) in the presence of oxidising gases (*e.g.,* steam, CO_2, and air), or chemical activation, typically carried out at a lower temperature (400-700 °C) in the presence

of activating agents (*e.g.,* H_3PO_4, KOH, NaOH, K_2CO_3, and $ZnCl_2$).[6] The activation step introduces porosity through the removal of carbon, with careful selection of synthesis conditions determining the structural properties of the activated material (*e.g.,* graphitic domain size, total pore volume, pore-width distribution, and surface functionalisation).[9,89,90] A wide range of activated carbons with surface areas exceeding 2000 $m^2\ g^{-1}$ have been synthesised and their electrochemical properties studied.[90–94]

Most activated carbons are synthesised from organic carbon-rich precursors due to their relative affordability and large accessible surface areas once activated. However, the pore-width distribution of these materials is often poor due to the disordered nature of the precursors. This limits their usage in devices requiring specific pore widths, and causes difficulties for analysis using spectroscopic techniques that are sensitive to variations in micropore struture.[13] Thus, for the study of electrolyte-electrode behaviour, alternative classes of activated carbons exhibiting well-defined physical properties are desirable.[10] An example of such a material is polyether ether ketone (PEEK)-derived activated carbons (PDCs).[10,13,24,95,96] PDCs have a simple two-step synthesis procedure, whereby PEEK is carbonised (typically at ~900 °C) and then physically activated (conventionally in the presence of steam or CO_2).[10,97] PDCs are favoured for electrode-electrolyte behaviour studies as they exhibit high-surface area microporous structures where the pore diameters can be readily controlled through activation conditions.

Porous carbons can also be synthesised using inorganic precursors, or materials that predominantly comprise carbon-carbon bonds with no excessive hydrogen content.[89] An important category of activated carbons derived from inorganic precursors is that of carbide-derived-carbons (CDCs). CDCs are synthesised by the high-temperature chlorination of carbides (*e.g.,* TiC and SiC), in which metals and metalloids are removed as chlorides, leaving behind a porous carbon.[8,9,23] CDCs encompass a large group of carbons, ranging from extremely disordered to highly ordered structures, as determined by the synthesis method (*e.g.,* halogenation, hydrothermal treatment, and vacuum deposition), applied temperature, pressure, and choice of host carbide.[8] The resulting CDCs exhibit narrow pore-size distributions, with a mean value that is tuneable to within 0.05 nm, and surface areas ranging between 1000 $m^2\ g^{-1}$ and 3000 $m^2\ g^{-1}$.[13,23] CDCs are also largely amorphous, similar to activated carbons, but their narrow pore size distribution and limited number of functional groups makes them useful model materials for the investigation of electrode-adsorbate behaviour.[9]

2.4.2 Local carbon structure

Activated carbons synthesised by the methodologies outlined above, particularly commercial materials, are often amorphous. As such, the characterisation of the local structures of these materials presents substantial challenges, resulting in ambiguity surrounding structure-property and structure-performance relationships.[13] Characterisation of graphitic carbon materials has been a topic of interest for over half a century, with X-ray diffraction (XRD) studies by Franklin in 1951 distinguishing graphitising and non-graphitising carbons.[98] Generally, conventional analysis of Bragg reflections of activated carbons provides limited information due to the substantial broadening from long-range disorder. However, the determination of pair distribution functions (PDF) from X-ray and neutron diffraction experiments can provide insight into the local structure of amorphous carbons.[36,99,100] PDF studies show that porous carbons exhibit a high degree of local ordering, generally in the form of six-membered hexagonal rings in which the carbons are sp^2-hybridised.[99,101] PDF correlations are typically defined up to a distance of approximately 20 Å, indicating that local order extends to at least this length scale. It is important to note here that PDF patterns (a weighted histogram of interatomic distances) must be interpreted and deconvoluted with the utmost care as a large variety of local structures can correlate to similar interatomic distances.[102]

Aberration-corrected high-resolution transmission electron microscopy (HRTEM) is another characterisation technique that has been used to investigate the local structure of activated carbons. HRTEM images by Harris corroborate the general structure detailed by PDF, showing predominantly sp^2-hybridised domains arranged in disordered and fragmented fullerene-like structures.[103–105] Furthermore, HRTEM images have shown the existence of 5-membered rings and extensive curvature of the graphitic carbon layers, developing upon broad predictions made by PDF measurements. Adsorptive properties of models constructed from fullerene-like carbon structures, as proposed by Harris, have been shown to be largely consistent with experimental observations.[13,103]

^{13}C magic angle spinning (MAS) NMR spectroscopy, a nucleus-specific characterisation technique that is sensitive to the local environment of the nuclei, can also provide insights into the local structure of microporous carbons.[22] Forse *et al*. showed that, for a titanium carbide-derived CDC (or TiC-CDC), a broad resonance centred about 125 ppm is observed, a region close to that of the sp^2-hybridised carbons of graphene (~120 ppm) (**Figure 2.5**).[106] These observations were found to be consistent across a range of synthesised TiC-CDCs, indicating

a predominantly sp^2-hybridised and highly disordered carbon structure, corroborating the fullerene-like model detailed by Harris.[103] Notably, the ^{13}C NMR spectra of the TiC-CDC series exhibited minimal observable differences, with each spectrum displaying a relatively broad resonance. This significant resonance broadening was attributed to the highly anisotropic magnetic susceptibility of these materials, which arises from the extended aromatic structure of the carbon surfaces.[107] Consequently, this broadening hindered the analysis of system-specific variations in the local carbon structure.[108]

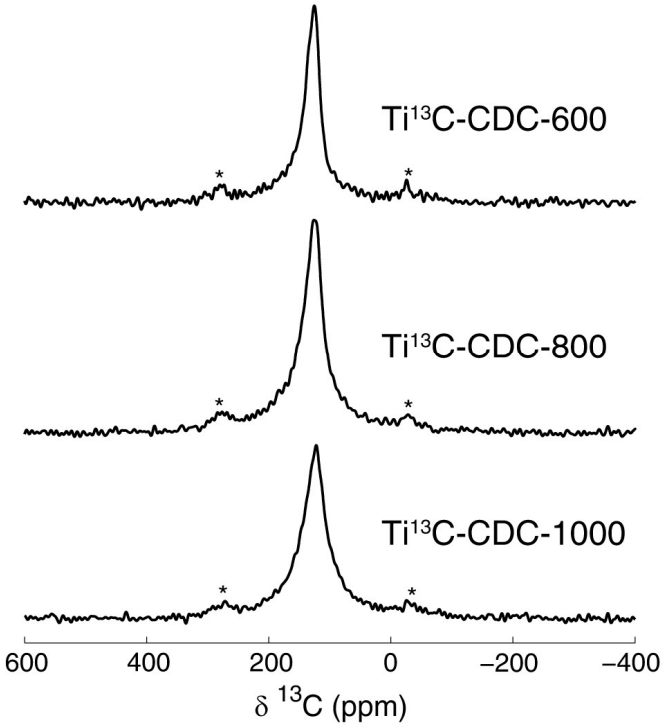

Figure 2.5. ^{13}C magic angle spinning (MAS) NMR spectra of a range of TiC-CDCs. Figure adapted from the supporting information of Ref. [22].

Raman spectroscopy can also provide insight into the local carbon structure of microporous carbons through the analysis of two main bands, the D-band (~1350 cm^{-1}) and the G-band (~1580 cm^{-1}).[6,109] The D-band represents the ring-breathing mode from sp^2-hybridised carbon rings, requiring adjacent defects to be Raman active. As such the D-band is associated with disordered and defected regions.[110,111] The full-width at half-maximum (FWHM) of the D-band peak provides a means of estimating the extent of carbon defects that deviate from graphitic, sp^2-hybridised carbon-carbon bonding.[112] The G-band represents the in-plane stretching vibrations of the sp^2-hybridised carbon atoms and is associated with graphitic regions.

Another important field of research that has assisted in the elucidation of the local structure of microporous carbons has been computational modelling, from which two distinct approaches have been developed: reconstructive and mimetic simulations.[113] Reconstructive calculations,

such as Hybrid Reverse Monte Carlo (HRMC), aim to produce realistic models by generating atomic configurations of carbon atoms that coincide with experimental data. This is typically achieved by varying atomic coordinates as to minimise the energy of the system (calculated using a classical force field) while maintaining good agreement between simulated and experimental PDF data.[113,114] This approach has been used to model the local carbon structures of TiC-CDCs,[102,115] saccharose-derived activated carbons,[116,117] and activated phenol-aldehyde-derived carbon fibres.[118] However, experimental PDF data can be inaccurate, either through systematic errors or simply through length-scale limitations in which the technique can accurately describe an amorphous activated carbon. As such, reconstruction techniques often struggle to discriminate between structural features from PDF data alone, and are inherently limited to materials that have been previously experimentally characterised.[113]

The mimetic approach aims to simulate the synthesis conditions of a select microporous carbon, resulting in a predicted carbon structure that can be tailored by altering the conditions inside the model system.[119] This approach does not require prior experimental data, and typically generates the structure by modelling a fluid-like monoatomic carbon at a high temperature that is subsequently quenched (*i.e.*, rapidly cooled) in a molecular dynamics (MD) simulation. The bonding structure and pore morphology can be changed by varying the initial and final temperature, and the cooling rate. Mimetic simulations by Palmer *et al*. have qualitatively reproduced chlorination temperature-dependent trends in porosity and specific surface area for a series of TiC-CDCs by varying the quench-rates in the simulation.[113] Similar work has been performed for SiC-CDCs, wherein slower quench rates and a post-quench compression of the system improves the match with the experimental target.[120]

2.4.3 Pore structure

Alongside the inherent variations in local structure and chemical environments, microporous carbons can display a wide range of pore structures. The pore size distribution and the specific surface area that is accessible to electrolytes are important characteristics that determine the electrochemical performance of the carbon as a supercapacitor electrode material. As such, the accurate determination of these parameters is essential to gain a better understanding of electrolyte-electrode interactions. However, as with local structure determination, the characterisation of these parameters proves to be challenging.

2.4.3.1 Gas sorption experiments

Pore size distributions are typically extracted from gas adsorption isotherms of small molecules (*e.g.,* N_2, CO_2, and Ar). Porous samples are first degassed by a heating step under vacuum and then cooled to temperatures near the gas condensation point (77 K for N_2 and 87 K for Ar) prior to adsorption measurements. The system is cooled so that the probe gas condensates within the sample and diffuses throughout the porous network, physically adsorbing onto the sample surface.[88,121–123] Smaller micropores are preferentially occupied over larger mesopores due to their larger adsorption potentials. The adsorption isotherm is constructed from sequential measurements where a known quantity of guest molecules is introduced into the system, typically plotted as the volume adsorbed ($cm^3\ g^{-1}$), and the relative pressure p/p_0 (where p_0 is the relative internal atmospheric pressure of the sample at a given temperature) of the system is measured following equilibration.[88,124]

Pore size distribution data is extracted from the gas adsorption isotherm via a decomposition of the isotherm into a kernel of partial isotherms. There are many different approaches to this decomposition step, with various models employing a range of assumptions (often pore shape and pore connectivity) to best model adsorption mechanisms within porous materials. In recent years, classical density functional theory (cDFT) models of inhomogeneous fluids within porous materials have greatly aided in qualitatively classifying the specifics of adsorption and capillary condensation within microporous and mesoporous solids.[123,125,126] The predicted isotherms are typically obtained by calculating the density profile of the adsorbed species within the pores across a range of applied pressures via minimisation of the potential energy function. Following the construction of the modelled isotherm, experimental and calculated isotherms are compared to gain insight into experimental adsorption mechanisms. A relatively simplistic model for modelling porosity within porous carbons is the Barrett-Joyner-Halenda (BJH) model, in which pores are assumed to be cylindrical and isolated from one another, and that the sample volume is entirely occupied by the guest.[127] The non-local DFT (NLDFT) approach by Lastoskie *et al*., which treats porosity as a series of non-interconnected slit-pores and employs a smoothed density approximation, was shown to give a quantitative improvement in the accuracy of calculated pore size distributions for activated carbons.[125] The popular quenched solid DFT (QSDFT) model by Neimark *et al*. also assumes that the carbon comprises disconnected pores, but instead models slit-pores with a roughened surface.[124] The roughened surface removes sharp gaps in the pore size distribution arising from step-like transitions in the number of adsorbate monolayers as the pore width is increased, as typically seen in models that

treat the pore walls as homogenous, graphite-like plane surfaces (*e.g.*, the NLDFT model).[128–130] Using the selected model, the isotherm is converted to a pore size distribution using the following equation:

$$\Gamma(P) = \int_{H_{\min}}^{H_{\max}} \Gamma(P, H) f(H)\, \mathrm{d}H \tag{2.25}$$

where $\Gamma(P)$ is the adsorption isotherm at bulk gas pressure, $\Gamma(P, H)$ is the adsorption isotherm at pressure P in a model pore of width H. The integration limits, $H_{\min}$ and $H_{\max}$, correspond to the smallest and largest pore widths present in the material, respectively. $f(H)$ is the pore size distribution function, with the value given at H representing the total volume of all pores between H and $H + \mathrm{d}H$.[130] It is critical to consider the underlying assumptions that the selected model is making when interpreting pore size distributions, with different models potentially giving significantly different values. Further considerations must also be made regarding the choice of gas adsorbate, with different species sometimes resulting in significantly different adsorption isotherms within the same material due to variance in adsorbent-adsorbate reactivity and adsorbate-pore accessibility.[123,130] Additionally, the lack of model microporous carbons that exhibit well-defined pore sizes ultimately makes the validation of many of these theoretical models a challenging task. As such, it is often best practice to report structural parameters determined from fits from several models that make different assumptions.

2.4.3.2 Determining pore structure by NMR spectroscopy

Recently, NMR spectroscopy has emerged as a means of determining porosity in activated carbons. This approach is enabled by the distinct magnetic environment within the pores caused by ring current-induced diamagnetic fields as a result of the inherent aromaticity throughout the carbon structure (a topic discussed in detail in Chapter 3 and Chapter 4).[16,31,40,64] As illustrated by **Figure 2.6**, two distinct resonances are typically observed, with the more negative chemical shift correlating with adsorbed species. As such, species adsorbed within the pores can be distinguished from those in the bulk. Generally, a known volume of adsorbate (typically an electrolyte or solvent) is added to the porous material and an NMR spectrum is recorded. Assuming the loading volume is less than that of the total pore volume, the NMR spectrum of the guest species shows a single resonance correlated to species adsorbed within the pores (or an in-pore resonance).[16] This process is repeated, gradually increasing the loading volume until the intensity of the in-pore resonance ceases to grow as a function of loading volume. Assuming

appropriate calibration, an integration of the equilibrated in-pore resonance allows an estimation of the number of adsorbed molecules, which can be converted to pore volume provided the adsorbate density is known.[7,10,13,131] Importantly, the choice of guest species (*e.g.*, water, acetonitrile, cyclohexane, ionic-liquids, or ionic salt electrolytes) influences the total accessible pore volume due to differences in ionic radii and adsorbate-adsorbent interactions, leading to variance when comparing measurements performed with different adsorbates.

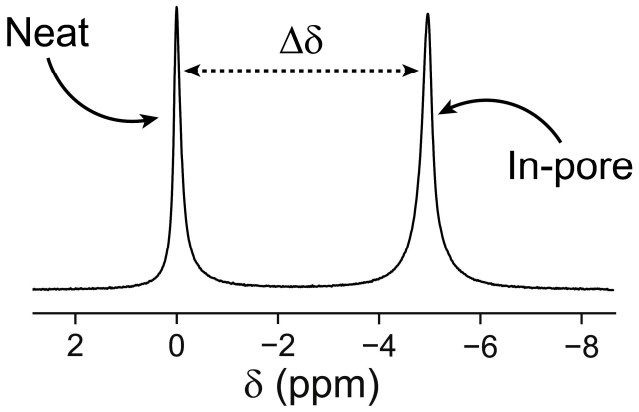

Figure 2.6. Illustration of a typical NMR spectrum for an electrolyte adsorbed within a microporous carbon. Species adsorbed within the pores, referred to as in-pore species, are shifted to a more negative chemical shift relative to neat electrolyte.

Further insight into pore structure can also be gained by analysing the chemical shift difference between the bulk adsorbate resonance and the resonance of species adsorbed within the carbon pores. This difference is commonly referred to as Δδ. As highlighted by Cervini *et al.*, Δδ is multifaceted, being influenced by a number of structural and chemical factors that are difficult to isolate.[10] Electronic structure density functional theory (DFT) calculations have been performed on a series of graphene-like fragments of varying geometries, with the induced magnetic response at points in space surrounding these fragments being determined to help isolate the different contributions towards Δδ.[22,34,132] The magnetic response of the carbon under an applied field causes guest species occupying regions close to the graphene-like fragments to experience a nucleus-independent chemical shift (NICS). Forse *et al.*[22] showed that the NICS was largest near the surface of the aromatic fragment, decaying as the distance from the ring-plane increased. Extending the size of the aromatic domain was also shown to significantly increase the NICS, and it was demonstrated that fragments arranged in slit-pore arrangements gave rise to increased NICS, with narrower pores exhibiting larger NICS. It was also shown that the curvature of the graphene-like fragment influenced the NICS, with concave

surfaces giving a larger NICS due to diamagnetic field overlap, and convex surfaces exhibiting smaller NICS (relative to that of the planar fragment). Moran *et al*.[132] demonstrated how the extended aromaticity of graphene-like fragments influences ring currents, with modelled polybenzoid hydrocarbons exhibiting large variation in the NICS at a distance of 1 Å across the fragment surface. However, it was also shown that the NICS averages to a single value at distances relevant to adsorption (> 3 Å). The NICS induced by aromatic surfaces is by far the largest contributor towards Δδ, however factors such as chemical exchange[7,10,133] and changes to the local environment of the adsorbate[18,37] (*e.g.,* distortion of the adsorbate solvation environment) may also contribute.

Taking a recorded Δδ from an NMR spectrum of an activated carbon and inferring structural information for the material is theoretically possible but presents immense challenges due to the multifaceted nature of Δδ. Recently, Xing *et al*. have developed a method to determine carbon pore size distributions using ^{1}H MAS NMR spectra of adsorbed water.[32] The approach involves the acquisition of ^{1}H MAS NMR spectra for water-saturated porous carbons and converting it into a pore-size distribution based on several assumptions: (i) the carbon pores are modelled as slit-shaped pores formed by circumcoronene molecules; (ii) Δδ for the adsorbed water is attributed to the NICS induced by the carbon surface that can be equivalently described by the DFT model for a circumcoronene slit-pore; (iii) water molecules rapidly exchange and occupy all regions between circumcoronene molecules up to a defined cut-off region above the molecule surface (conventionally 3 Å); and (iv) water molecules exist in a slow-exchange regime without interactions between adsorbates, making Δδ dependent only upon the NICS which is inherently related to pore size.[32] Following this method, the pore size distribution can be determined from the Δδ values of ^{1}H MAS NMR spectra, and has been shown to give reasonable agreement with values determined from gas sorption data.[10,134] This methodology is promising, but the assumptions require further validation. Future work should focus on evaluating the use of circumcoronene as the model fragment and incorporating weighted averages for NICS values to better account for preferential water adsorption at the carbon surface.[135]

A related NMR approach was also developed by Forse *et al*. to estimate carbon domain sizes for porous carbon materials.[36] Experimental Δδ values are recorded, then a lattice simulation method is used to calculate theoretical Δδ values for a series of modelled structures. The simulations are characterised by the following: (i) individual carbon pores can be modelled as slit-pores and the in-pore NICS values are calculated using DFT, (ii) free energies determined

by MD simulations are used to describe the adsorption thermodynamics of molecules within the slit-pores, (iii) the pore size distribution of the model is matched to experimental data derived by gas sorption, and (iv) a simulated NMR experiment is performed in the fast-exchange regime to give a simulated Δδ value. The simulation is iteratively repeated using varying carbon domain sizes, with Δδ being compared to experimental values allowing an estimation of the carbon domain size. This approach has indicated that TiC-CDCs vacuum annealed at higher temperatures have larger domains that those at lower temperatures, ranging from coronene-sized domains (diameter ≈ 0.75 nm) up to dicircumcoronene-sized (diameter ≈ 1.8 nm) domains.[36] Liu *et al*. have recently implemented this methodology for a large series of porous carbons in conjunction with experimental PDF measurements (specifically the decay of the pairwise C-C correlations), highlighting the relation between decreasing domain size and increased specific capacitance when utilised as supercapacitor electrodes.[99] However, it is important to note that the approaches by Liu *et al.* and Xing *et al*. make the underlying assumption that a slit-pore can accurately represent the porosity of the carbon. *In actu*, microporous carbon materials exhibit significant disorder and defects within their graphitic domains (as illustrated by the fullerene-like model by Harris) and exhibit contributions to Δδ outside of the NICS.

2.5 Carbon structure and electrochemical performance

One of the main limitations for supercapacitors is their relatively low energy density compared to other electrochemical storage devices. As such, most research in this field has focused on developing new electrode materials with increasing energy densities. Conventional development of supercapacitor electrodes has focused on the synthesis of materials with increasingly large SSAs (2000-3000 $m^2\ g^{-1}$), giving rise to increased capacitances following Equation 2.6.[136] However, Chmiola *et al*. proposed a new avenue towards increased capacitances, highlighting the importance of the relative sizes of micropores and adsorbates.[23] Prior to this work, the traditional view was that reductions in pore size would decrease the SSA, reducing the capacitance.[90] Contrary to this assumption, it was shown that the capacitance of a series of TiC-CDCs with a 1.5 M NEt_4BF_4-ACN electrolyte experienced an anomalous increase in capacitance as pore size decreased below 1 nm. This 'turning point' in capacitive behaviour seemingly aligned with pore dimensions becoming narrower than the solvated cation and anion diameters (1.30 nm and 1.16 nm, respectively).[137] This phenomenon has been rationalised by the partial desolvation or distortion of ion solvation spheres, which allows ions to move closer

to the electrode surface, reducing charge separation and enhancing capacitance. This hypothesis is corroborated by MD simulations of supercapacitors, wherein the extent of desolvation or decoordination of the ion has been shown to have a significant impact upon the local charge stored on the electrode surface.[19] The influence of pore size over capacitance in the absence of a solvent has also been investigated using ionic-liquid electrolyte TiC-CDC cells.[138] Here, it was shown that the measured capacitance was largest as the pore diameter approached the dimensions of the cation and anion, but decreased sharply as the pore width narrowed beyond this point.

Often, reported correlations between pore width and capacitance are exemplified by normalising the capacitance against the SSA (or pore volume), effectively deconvoluting the two contributions towards capacitance.[23,138,139] However, Centeno *et al*. state that the anomalous increase in capacitance with respect to decreasing pore size is a result of inaccuracies when determining SSA using gas-sorption for microporous carbons.[140] By normalising the capacitance by the surface area of pore sizes that are strictly relevant to adsorption (*i.e.,* larger than the ionic radius), the increase in capacitance with respect to pore size was no longer observed. However, it is worth noting that in the work by Chmiola *et al*., the anomalous increase in capacitance was still observed without SSA normalisation. Recent studies have also reported a lack of correlation between pore size and capacitance,[99,141–143] with computational investigations determining only minor increases in capacitance.[144] These contrasting results strongly indicate that other structural variables are in effect.

Recently, Liu *et al*. reported a strong correlation between structural disorder in the electrodes and capacitance.[99] More disordered carbons with smaller graphitic domains were shown to exhibit higher capacitances. This was attributed to increased localisation of charge across smaller domains, leading to stronger electrolyte-electrode interactions and a more efficient storage of ions.[145] Furthermore, it was suggested that smaller domains exhibit a higher concentration of topological defects which have been suggested to increase capacitive performance.[146] They propose that variations in carbon disorder were the main contribution towards the trend reported by Chmiola *et al*., although a contribution from pore size could not be entirely neglected.[23]

2.6 Pore structure and electrolyte behaviour

Recently, studies have shown that specific ion properties, such as solvation strength, solvated ionic radii, and bare nucleus radii can influence adsorption phenomena within microporous

carbons.[10,147–151] This influence has important implications for charged systems (*e.g.,* supercapacitors and CDI devices) as it is anticipated that the influence of specific ion properties extends to electrosorption behaviour. Ionic properties have become increasingly relevant following studies that identified three distinct mechanisms by which electrode charge can be balanced within an EDLC: counter-ion adsorption, ion exchange, and co-ion expulsion.[2,16,29,64] It is expected that the precise charging mechanism exhibited by a particular system will be strongly influenced by the spontaneous adsorption behaviour of electrolytes.

Intuitively, the minimum pore width that can be accessed by ions is determined by their ionic radii, with micropores narrower than the bare ion size being inaccessible. However, this situation is considering the total desolvation of the ion, an energetically unfavourable and highly improbable situation. Practically, ionic species in aqueous and organic electrolytes are solvated, causing the solvated radius of the ion relative to the pore dimensions to influence adsorption behaviour.[148] To a first approximation, it may be expected that solvated ions that are larger than the pore size are barred from adsorbing. Importantly, however, solvation shells are labile and can distort and/or partially desolvate in order to access energetically favourable environments.[147] The rigidity of the solvation radius of the ion is intrinsically related to the strength of the ion-solvent interaction, thus careful selection of ion-solvent pairings allows the tailoring of the solvation properties and its corresponding adsorption behaviour.

There have been numerous theoretical studies investigating the relation between adsorption behaviour and solvation properties. MD simulations by Williams *et al.*[147] showed that the insertion of the relatively charge-diffuse pertechnetate (TcO_4^-) anion (in aqueous solution) into a graphene oxide slit-pore exhibits a decrease in free energy and a decrease in its hydration number. This is attributed to a partial desolvation of the anion, effectively reducing its solvation radius to enter the slit-pore and adsorb to the carbon surface. Conversely, charge-dense anions (SO_4^{2-}, I^-, and Cl^-) exhibited increased free energies upon insertion, with the free energy minimum at the mouth of the slit-pore becoming more pronounced for more weakly hydrating anions. The energetic penalty towards insertion for the strongly solvated species is attributed to the high energetic cost for the ion to shed or distort its first, or in wider pores, its second hydration shell.[149,150] Thus, for ions where the energetic penalty outweighs the energetic gain from adsorption, there is a significant restriction towards pore insertion, suppressing the in-pore ion population. Kondrat and Kornyshev[25,26,152] termed this an ionophobic system, wherein the pores are ion-deficient prior to charging. Mean-field theory models proposed that image charges from charged micropore surfaces facilitate denser packing of counter-ions into co-ion

deficient micropores during charging. This model is supported by MD simulations of carbon nanotube micropores of various sizes in an ionic liquid.[153] The increased capacitance observed by Chmiola *et al.* for carbons with micropores smaller than the solvated electrolyte ions is attributed to the formation of this superionic state within the pores.[16,23,154] Monte Carlo simulations have shown that the charge dynamics of initially ionophobic pores are favourable, charging via an unrestricted counter-ion adsorption mechanism.[25,152] In contrast, ionophilic systems (systems with larger ion concentrations within the pores) exhibit slow, diffusion-like charge dynamics due to overfilling. However, ionophilic systems typically exhibit increased capacitances for microporous carbons comprising larger pores (> 1 nm) where barriers towards insertion are minimised.[155]

Ionic mobility has also been shown to influence electrochemical performance within supercapacitors. Capacitance studies on aqueous sulphate-salt electrolytes within an activated carbon electrode (1.36 nm average pore width) showed that the most hydrating cation (Li^+) maintained the majority of its capacitance as scan rate was increased (1 mV s^{-1} to 10 mV s^{-1} and then to 100 mV s^{-1}).[17] Conversely, more charge diffuse and more mobile cations (Na^+ and K^+) exhibited a large drop in capacitance, with their respective CVs exhibiting resistive profiles. These differences were attributed to the limited mobility of the strongly hydrated Li^+ cations, which are assumed to remain near the electrode/electrolyte interface during discharge. This proximity enables the rapid reformation of the EDL in the subsequent charging cycle.

2.7 Modelling supercapacitance within microporous electrodes

For supercapacitors, the formation of the EDL is the key principle by which charge is stored. As such, a detailed understanding of its formation and its structure is required to progress the understanding of supercapacitance. Several existing models describe this interface with varying degrees of complexity.

The simplest model is that proposed by Helmholtz,[42] wherein the surface charge of the planar electrode is neutralised by a layer of oppositely polarised electrolyte ions. The Gouy-Chapman model built upon the Helmholtz model by recognising that ions are not rigidly bound to the electrode surface. Subsequently, a diffuse layer in which the ions are distributed following the Boltzmann equation was implemented. The Stern model[156] modified the Gouy-Chapman model by combining the compact ion layer from the Helmholtz model with the diffuse layer of the Gouy-Chapman model. The compact ion layer, or the Stern layer, accounted for the finite size of ions, limiting the approach to the electrode surface to the order of the ionic radii.

The Stern model was later modified by Grahame as to account for species penetrating beyond the Stern layer.[157] The region beyond the Stern layer is typically occupied by solvent molecules, but ionic species with partially desolvated or distorted solvation shells can also access this region. Ions that have penetrated the Stern layer and are in direct contact with the electrode are referred to as specifically adsorbed ions. The Stern-Grahame model defines three distinct planes: (1) the inner Helmholtz plane (IHP), intersecting the centres of ions specifically adsorbed to the electrode surface; (2) the outer Helmholtz plane (OHP), crossing the centres of solvated ions at their closest approach to the electrode; and (3) the diffuse layer, as described by the Gouy-Chapman model. The Bockris, Devanthan, and Müller (BDM)[158] model builds upon the Stern-Grahame model by incorporating a strong dipole-determined alignment of solvent molecules closest to the charged surface. Subsequent layers of solvent molecules exhibit diminishing alignment with increasing distance from the surface (**Figure 2.7**).

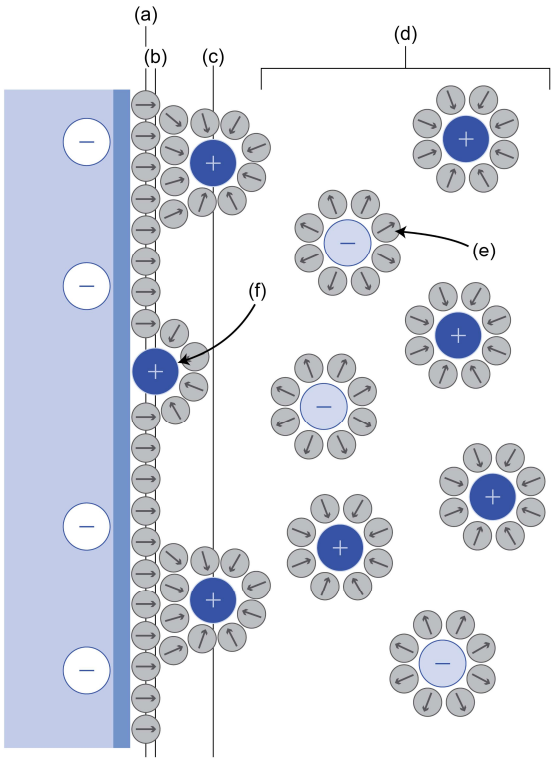

Figure 2.7. Schematic illustration of an electric double-layer on a planar electrode using the BDM model. (a) Solvent molecules adsorbed to the surface of the electrode exhibit a fixed, dipole-determined alignment (denoted by arrows). (b) The inner-Helmholtz plane (IHP), passing through the centre of specifically adsorbed ions, and (c) the outer-Helmholtz plane (OHP), passing through the centre of solvated ions at their closest approach to the electrode surface, are shown. (d) Beyond the OHP, the diffuse layer is displayed. Solvent molecules outside ion solvation shells and those adsorbed to the electrode are omitted for clarity. (e) Solvent molecules within solvation shell of ions are orientated according to ionic charge. (f) Specifically adsorbed ions may distort their solvation shell as to closer approach to the polarised electrode surface. Ion and solvent molecule sizes are not to scale.

For microporous carbons, it is important to consider the possibility of overlapping EDLs within narrow pores.[159] In the limit of pore dimensions, in which the EDLs overlap strongly, it can be assumed that there is a constant electrostatic potential within the pore space (otherwise referred to as the Donnan approach).[2] The modified Donnan approach (mD) by Biesheuvel *et al*.[159–161] incorporates a Stern layer into the EDL within micropores, and a nonelectrostatic attractive potential that accounts for ion adsorption independent of an applied electric field. This attractive potential is a well-known and well-documented phenomenon resulting from chemical effects,[133,162] electrostatic forces,[147,160] and capillary action.[2,135] Variants of the mD model have been shown to provide good agreement between theory and equilibrium data for salt adsorption in CDI devices, but significantly underestimated capacitance at low concentrations (often by an order of magnitude).[2,163,164] Recently, Simoncelli *et al*. showed that MD simulations at high concentrations could be used to parameterise an mD model, with extrapolated capacitances at lower concentrations giving improved agreement with experimental data.[164,165]

Advanced theoretical studies have also been performed to gain further insight into the precise structure of the EDL within micropores. Classical DFT calculations by Jiang *et al*.[166] and MD simulations by Feng *et al*.[167] showed an oscillatory variation in capacitance as slit-pore size was varied. This oscillatory behaviour was attributed to constructive and destructive superpositions of EDLs. The same phenomenon was later observed in spherical-pore models, with increased curvature magnifying the oscillatory behaviour.[168] Concave surfaces were also shown to give capacitances comparable to that of slit-pores, whereas convex surfaces gave increased capacitances due to its increased surface charge density.[145,165] These studies also suggested that correlations between pore size and capacitance increases could be masked by wide pore size distributions.

MD studies of ionic liquid electrolytes and planar electrodes showed that the charge across the IHP and OHP may exceed that of the electrode surface.[27,169] This results in the phenomenon of overscreening, wherein a layer of oppositely charged ions forms a second layer as to balance the excess charge in the first layer.[170] The overscreening effect may propagate away from the surface, forming several ionic layers with an alternating overall charge. MD simulations of ionic liquids within model microporous TiC-CDC structures derived from quenched MD simulations showed an absence of overscreening within confined environments.[19,20,113] This was attributed to the partial decoordination of ions within the pores (a process analogous to the desolvation of organic and aqueous electrolytes) limiting the formation of defined overscreening layers. These models reported capacitances in quantitative agreement with

experimental results, provided insight into ion-exchange charging mechanisms, and have shown that ions partition themselves among different adsorption sites with the most confined ions storing charge more efficiently.[19]

Overall, further work is required to gain a better understanding of the complex ion-electrolyte structure within microporous carbons, particularly those within a charged environment. Several models created show promise, but extensive comparison to experimental data is required to fully validate their predictions. As such, there is an increasing demand for experimental techniques that can accurately determine the behaviour of these environments.

2.8 Experimental methods for characterising charge storage mechanisms

A variety of experimental methods have been developed and employed to study the mechanisms of charge storage within supercapacitors. Measurements from surface force balance (SFB) experiments[171,172] and atomic force microscopy (AFM)[173,174] have evidenced layering effects at charged planar surfaces, giving good agreement with the models proposed by simulations, as discussed above. *In situ* dilatometry measurements have also been used to measure electrode expansion and contraction during charging, with expansion being attributed to ions filling pores, and contraction being due to ion expulsion.[175] Hantel *et al*. observed an asymmetric expansion at positive and negative polarisations for a TiC-CDC electrode, indicating different adsorption behaviour. However, these techniques are unable to determine specific adsorption mechanisms within porous materials.

One technique that can provide insight into adsorption mechanisms within these complex materials is electrochemical quartz crystal microbalance (EQCM). EQCM has been a powerful technique for observing electrolyte-electrode interfaces and has recently been applied to study supercapacitors.[176–179] EQCM comprises a thin piezoelectric quartz crystal positioned between two electrodes. An alternating electric field is applied across the crystal causing it to exhibit vibrational motion at a resonance frequency that is dependent upon the loaded mass upon the crystal. By casting supercapacitor electrodes onto the quartz crystal and measuring the frequency of the crystal as electrolyte is adsorbed, the precise changes in mass as a function of ion adsorption can be measured, providing insight into ion adsorption processes.[176,180] Work by Levi *et al.* showed that ion desolvation occurred upon pore insertion for the highly solvated Li^+ ions within an aprotic propylene carbonate electrolyte.[176] Further studies upon ionic liquid electrolytes within microporous carbons showed stark differences in the charging mechanism between the different polarities, with cations being the sole active species in charge balance

under negative polarisation, and both ions partaking in charge balance under a positive polarisation. These experiments also revealed size-determined ion-sieving effects, and illustrated how varying the voltage range can alter the charge storage mechanism.[177,180] In this study, it was shown that the electrode mass change was minimal at low charge densities, indicating an ion-exchange mechanism, whereas under a higher charge density, the measured mass change corresponded with a purely counter-ion adsorption mechanism. Solvation numbers of various anions and cations for aqueous electrolytes within confined micropores were also calculated.[177] However, these calculations assume that charge is balanced exclusively via counter-ion adsorption.

Recently, electrochemical impedance spectroscopy (EIS), otherwise known as ac-electrogravimetry, paired with EQCM (or ac-EQCM) has aided in the deconvolution of species involved in charge-balancing.[179,181,182] For each set of experimental data, theoretical ac-electrogravimetric models are constructed from various combinations of the electrolyte species (*i.e.*, cations, anions, and solvent molecules). Experimental data is then compared to each theoretical fit to isolate contributions from individual species. This approach was recently implemented by Lé *et al*. in a study on supercapacitors comprising vertically aligned graphene nanosheet electrodes and various propylene carbonate electrolytes, revealing ion-specific effects on electrosorption mechanisms and exchange kinetics.[182]

In situ infrared (IR) spectroelectrochemistry, also referred to as attenuated total reflectance-surface-enhanced infrared adsorption spectroscopy (ATR-SEIRAS), has also been used to study ion behaviour within microporous carbons.[183] This technique utilises the enhanced IR adsorption intensity of molecules adsorbed to surfaces in order to distinguish adsorbed and bulk species. Furthermore, the IR adsorption of the individual electrolyte components can be distinguished from one another, allowing individual adsorption behaviour to be determined. *In situ* ATR-SEIRAS measurements performed on supercapacitors comprising ionic liquids and TiC-CDC electrodes showed a decrease in the adsorption intensity for both anions and cations during charging.[184] This was attributed to ions penetrating deep into the carbon pores, entering undetectable regions due to the carbon particle blocking the IR signal. Ion exchange mechanisms have also been revealed for ionic liquids within polarised carbon nanofibres.[185]

*In situ s*mall-angle X-ray scattering (SAXS) experiments show a decreased intensity following the infiltration of electrolyte into electrode pores.[181] SAXS studies have shown that pores that are inaccessible in an unpolarised electrode can be irreversibly filled with electrolyte when polarised.[186,187] Ion confinement behaviour within micropores has also been investigated by

combining *in situ* SAXS and Monte Carlo simulations, showing increased ion confinement and increased in-pore ion concentrations upon electrode polarisation.[188–190] *In situ* small-angle neutron scattering (SANS) has also been used to study the electrosorption of ions in carbon micropores of varying sizes for organic and aqueous electrolytes. Yushin *et al*. reported enhanced ion adsorption within narrow micropores (< 1 nm) under an applied potential.[191,192] Notably, diffraction-based methods are able to detect adsorption behaviour as a function of pore size, with larger pores giving smaller changes in adsorption intensity and vice versa. Thus, these methods can provide information on the local environments in which the adsorbed species occupy.

NMR spectroscopy is another powerful technique that has been used to observe and quantify electrolyte behaviour within microporous carbons. NMR spectroscopy is non-invasive and element-specific, allowing the tracking of individual electrolyte species. Furthermore, the technique is sensitive to changes in local structure, allowing changes in solvation structure to be monitored. These intrinsic properties have been used to study the underlying chemistry of lithium-ion batteries,[193] dendrite formation,[194–196] intercalation within graphitic electrodes,[197] and solid electrolyte interphase (SEI) formation.[198,199] NMR spectroscopy has also been used extensively in the study of supercapacitor devices. For microporous carbon electrodes, the phenomenon of ring current shifts (discussed later) allows adsorbed species to be distinguished from bulk species, enabling the quantitative measurement of electrolyte adsorption behaviour. Cycled electrodes that have been extracted from the cell (*ex situ* experiments) have been used in magic angle spinning (MAS) NMR experiments. This method provides high resolution spectra and enables more sophisticated measurements; however, the electrode voltage cannot be measured during the acquisition of NMR spectra, and self-discharge must be mitigated.[13] *Ex situ* measurements have provided insight into the charging mechanisms of various organic electrolytes, indicating that an ion exchange mechanism is in effect.[99,200] *Ex situ* measurements have also been used to study factors affecting ionic mobility and charge storage mechanisms in supercapacitors comprising room temperature ionic liquids.[40,64]

An alternative approach is that of *in situ* NMR spectroscopy measurements, wherein specially designed cells are cycled within the detection coil.[201,202] *In situ* experiments allow for a known potential (or current) to be applied throughout the electrode during NMR experiments, providing detailed insight into electrolyte electrosorption behaviour. Typically, *in situ* experiments are performed using a constant applied voltage, with NMR spectra being acquired following the electrochemical equilibration of the system.[13] However, as discussed in later

sections, *in situ* NMR spectroscopy experiments cannot benefit from MAS, drastically reducing the resolution. Moreover, metallic components required to cycle the cell often give rise to additional broadening effects. A study by Griffin *et al.*[29] used *in situ* NMR spectroscopy to study supercapacitors comprising activated carbon electrodes and tetraethylphosphonium tetrafluoroborate (PEt_4-BF_4) salt dissolved in acetonitrile. Both the cations and anions could be observed using ^{31}P and ^{19}F NMR, respectively (**Figure 2.7**). Under a positive polarisation, an ion-exchange mechanism was observed, whereas under a negative polarisation, a counter ion adsorption mechanism was observed. Interestingly, despite the different mechanisms, the total in-pore ionic charge was determined to balance the electronic charge in both electrodes. The precise rationale behind the difference in the electrosorption mechanisms under opposing polarities in this system is unknown and requires further investigation.

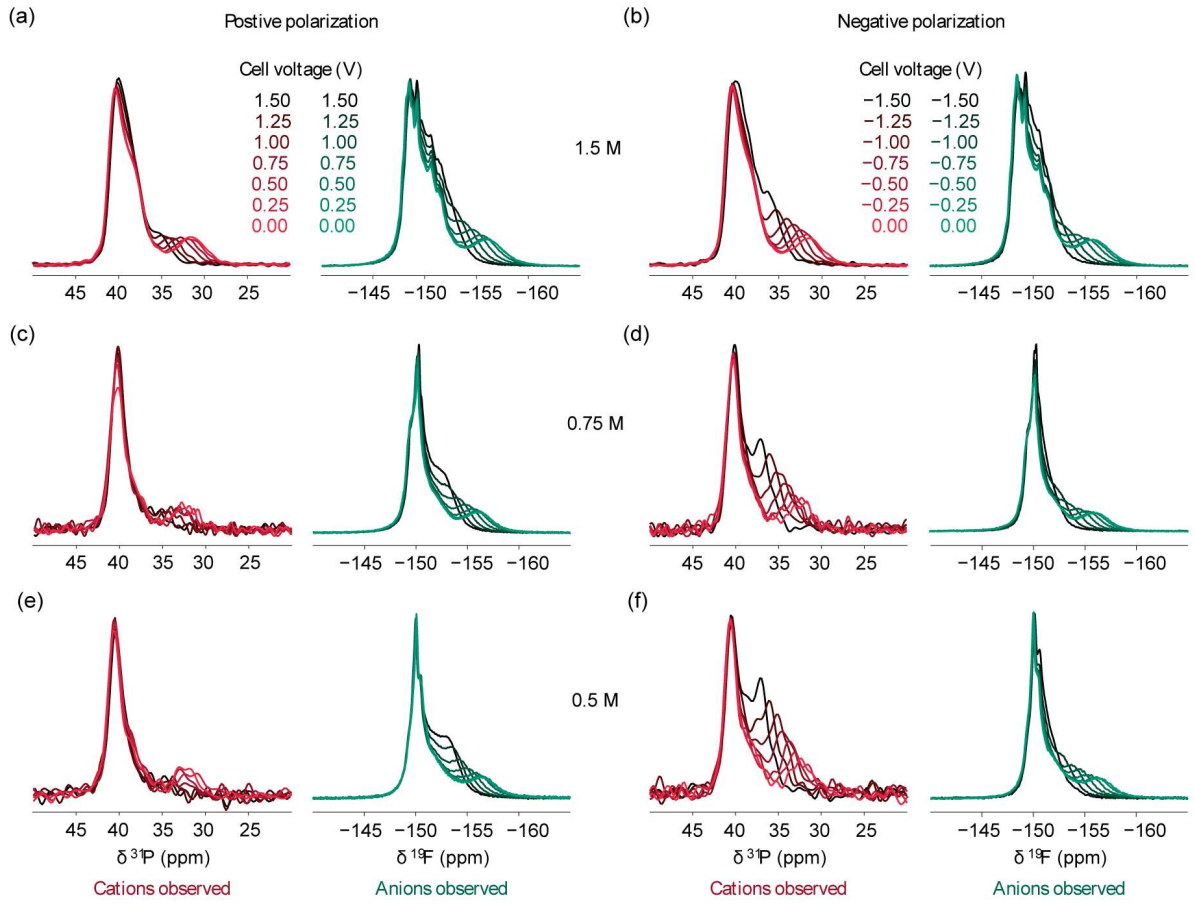

Figure 2.7. *In situ* ^{31}P and ^{19}F NMR spectra of individual supercapacitor electrodes held at set applied voltages. Spectra recorded for electrolytes within (a,c,e) positively polarised and (b,d,f) negatively polarised activated carbon electrodes are shown. Electrolyte concentrations are (a,b) 1.5 M, (c,d) 0.75 M, and (e,f) 0.5 M. In-pore anion intensities increase for positively polarised electrodes, whereas in-pore cation intensities increase for negatively polarised electrodes. Figure adapted from Ref. [29].

NMR studies have indicated that specific ion properties can influence the electrosorption mechanism.[10,24,31,37] *In situ* and *ex situ* NMR studies on the analogous tetraethylammonium tetrafluoroborate ($TEABF_4$ or NEt_4BF_4) electrolyte showed a greater ion-exchange character under a negative polarisation relative to PEt_4BF_4.[31,200] *In situ* ^{19}F NMR studies on $TFSI^-$ salts in ACN revealed a significant co-ion desorption mechanism at negative voltages, a stark contrast to the counter-ion adsorption mechanisms observed in the BF_4^- salts.[16] The contrasting electrosorption behaviour between the two electrolytes indicates substantial differences in $TFSI^-$ and BF_4^- adsorption behaviour, with further investigation being required to fully understand this. Within the same work by Griffin *et al*., it was found that a co-ion desorption mechanism was promoted by changing the cation from the relatively small Li^+ and Na^+ cations to the larger tetrabutylammonium cation (NBu_4^+). As such, it was inferred that the ion size relative to the pore dimensions influenced the electrosorption behaviour. This observation was corroborated by *in situ* NMR studies on aqueous electrolytes by Luo *et al*.[37] In the absence of an applied voltage, no in-pore ^{19}F resonance was observed. However, under an applied positive voltage exceeding +0.4 V, an in-pore resonance appeared and grew in a manner consistent with counter-ion adsorption. This behaviour was attributed to the strongly solvated F^- anions being restricted from inserting into the narrow micropores, yet under a positive potential the F^- would experience an electrostatic force that was sufficiently large as to encourage partial desolvation and adsorption. This phenomenon emphasised the importance of solvation properties in ultra confined microporous environments, with further work being required to elucidate the effects of ion-solvent interactions on electrosorption mechanisms, and particularly how these effects vary between aqueous and organic electrolytes.[13]

This thesis aims to advance the understanding of ion-solvent interactions and their influence on adsorption behaviour in aqueous electrolytes using NMR spectroscopy and DFT calculations. The specific objectives are to:

- Elucidate the impact of cation and anion solvation properties on spontaneous wetting and ion adsorption behaviour, with consideration of the potential influence of water ions in these systems.
- Understand how carbon micropore structure influences spontaneous ion adsorption behaviour and the local solvation environment of ions.
- Identify the preferred electrosorption mechanism of selected aqueous electrolytes using *in situ* NMR spectroscopy, correlating these findings with their spontaneous adsorption behaviour and electrochemical performance.

- Address the challenges associated with calculating NMR parameters using planewave DFT calculations on periodic graphene-like systems and to propose methodology to overcome these limitations.

Chapter 3

Nuclear magnetic resonance spectroscopy

Nuclear magnetic resonance (NMR) spectroscopy is the primary characterisation technique used within this thesis. This chapter outlines key principles of the technique and then delves into specific theoretical aspects relevant to studying ion adsorption in porous materials.

3.1 A quantum mechanical description of nuclear spin

3.1.1 Spin operators and spin states

The wavefunction, Ψ, is a mathematical description of the quantum state of an isolated system. It is a complex-valued probability amplitude from which possible measurement outcomes can be derived. Ψ can be factorised into spin-based and spatial-based components.[203]

$$\Psi = \psi_{\text{spin}}\psi_{\text{space}} \tag{3.1}$$

Since NMR spectroscopy detects nuclear spin, the following discussion on spin theory focuses on ψ_{spin}. The spin properties of a nucleus can be extracted by enacting spin-operators upon ψ_{spin}. A consistent set of spin-operators for a single-spin system are defined by:

$$\hat{\mathbf{I}}^2 = \hat{I}_x^2 + \hat{I}_y^2 + \hat{I}_z^2 \tag{3.2}$$

where $\hat{\mathbf{I}}^2$ is the operator for the squared magnitude of the nuclear spin, and $\hat{I}_x$, $\hat{I}_y$, and $\hat{I}_z$ are the operators for the *x*-, *y*-, and *z*-components of nuclear spin, respectively.[204] $\hat{\mathbf{I}}^2$ commutes with one of these directional components, which by convention is the *z*-magnetisation operator:

$$\left[\hat{\mathbf{I}}^2, \hat{I}_z\right] = 0 \tag{3.3}$$

$\hat{\mathbf{I}}^2$and $\hat{I}_z$ can therefore be defined by a set of common eigenfunctions:

$$\begin{aligned}\hat{\mathbf{I}}^2\psi_{I,m} &= I(I+1)\hbar\psi_{I,m}\\ \hat{I}_z\psi_{I,m} &= m\hbar\psi_{I,m}\end{aligned} \tag{3.4}$$

It is common convention when dealing with these expressions for $\hbar$ to be dropped (*i.e.*, assumed to be incorporated into the operator) and for the Dirac notation (*i.e.*, the bra-ket notation) to be used for the sake of simplicity.[203] As the wavefunction describing this system is an eigenfunction of $\hat{\mathbf{I}}^2$ and $\hat{I}_z$, the expectation values of these operators are given by:

$$\begin{aligned}\langle\hat{\mathbf{I}}^2\rangle &= \frac{\int \psi^*_{I,m}\hat{\mathbf{I}}^2\psi_{I,m}\mathrm{d}\tau}{\int \psi^*_{I,m}\psi_{I,m}\mathrm{d}\tau} = \langle\psi_{I,m}|\hat{\mathbf{I}}^2|\psi_{I,m}\rangle = I(I+1)\\ \langle\hat{I}_z\rangle &= \frac{\int \psi^*_{I,m}\hat{I}_z\psi_{I,m}\mathrm{d}\tau}{\int \psi^*_{I,m}\psi_{I,m}\mathrm{d}\tau} = \langle\psi_{I,m}|\hat{I}_z|\psi_{I,m}\rangle = m\end{aligned} \tag{3.5}$$

where $I(I+1)$ describes the magnitude of the nuclear spin angular momentum squared, $|\mathbf{I}|^2$, and m denotes the z-component of the nuclear angular momentum. I takes non-negative values which are either integers or half-integers, with NMR active nuclei having a value of $I > 0$, and m exists as values between I and $-I$ with a difference of 1 between each possible value. Thus, for an isolated nucleus, the z-component is quantised exactly within one of $2I+1$ states. As the wavefunction (or quantum state) is normalised, $\langle\psi_{I,m}|\psi_{I,m}\rangle = 1$, the z-component of the nuclear spin can be represented in its matrix form as:

$$\hat{I}_z = \begin{pmatrix} \langle\psi_{I,m}|\hat{I}_z|\psi_{I,m}\rangle & \langle\psi_{I,m}|\hat{I}_z|\psi_{I,m-1}\rangle & \cdots & \langle\psi_{I,m}|\hat{I}_z|\psi_{I,-m}\rangle \\ \langle\psi_{I,m-1}|\hat{I}_z|\psi_{I,m}\rangle & \langle\psi_{I,m-1}|\hat{I}_z|\psi_{I,m-1}\rangle & \cdots & \langle\psi_{I,m-1}|\hat{I}_z|\psi_{I,-m}\rangle \\ \vdots & \vdots & \ddots & \vdots \\ \langle\psi_{I,-m}|\hat{I}_z|\psi_{I,m}\rangle & \langle\psi_{I,-m}|\hat{I}_z|\psi_{I,m-1}\rangle & \cdots & \langle\psi_{I,-m}|\hat{I}_z|\psi_{I,-m}\rangle \end{pmatrix} \tag{3.6}$$

The expression can then be evaluated to give the values of m:

$$\hat{I}_z = \begin{pmatrix} I & 0 & \cdots & 0 \\ 0 & I-1 & \cdots & 0 \\ \vdots & \vdots & \ddots & \vdots \\ 0 & 0 & \cdots & -I \end{pmatrix} \tag{3.7}$$

For spin I = ½ nuclei, the $m = +\frac{1}{2}$ and $m = -\frac{1}{2}$ states are often referred to as the $|\alpha\rangle$ and $|\beta\rangle$ Zeeman eigenstates, respectively, and provide the projection of the spin angular momentum onto the magnetic field.[203,204] Importantly, a single nuclear spin is not restricted to a single state, with $|\psi_{\text{spin}}\rangle$ comprising a superposition of all possible states, with their relative contributions being given by superposition coefficients, c_m.

$$|\psi_{\text{spin}}\rangle = \sum_m c_m |\psi_{I,m}\rangle \tag{3.8}$$

The coefficients satisfy the normalisation condition $\sum_m c_m^* c_m = 1$, where $c_m^* c_m$ is the relative probability of the system returning an eigenvalue corresponding to m after being operated on by $\hat{I}_z$. Assuming a spin of I = ½, where m is equal to $+\frac{1}{2}$ or $-\frac{1}{2}$, $|\psi_{I,m}\rangle$ can be represented as:

$$\begin{gathered} \hat{I}_z|\alpha\rangle = +\tfrac{1}{2}|\alpha\rangle\,, \quad \hat{I}_z|\beta\rangle = -\tfrac{1}{2}|\beta\rangle \\ |\psi_{I,m}\rangle = c_\alpha|\alpha\rangle + c_\beta|\beta\rangle \end{gathered} \tag{3.9}$$

with the expectation value for $\hat{I}_z$ being:

$$\langle \hat{I}_z \rangle = \langle \psi_{I,m}|\hat{I}_z|\psi_{I,m}\rangle = \tfrac{1}{2} c_\alpha^* c_\alpha - \tfrac{1}{2} c_\beta^* c_\beta \tag{3.10}$$

The remaining components of the angular momentum, $\hat{I}_x$ and $\hat{I}_y$, do not commute with $\hat{I}_z$, and $|\psi_{I,m}\rangle$ is not an eigenfunctions of either $\hat{I}_x$ or $\hat{I}_y$, having the following effects on $|\alpha\rangle$ and $|\beta\rangle$:

$$\begin{aligned} \hat{I}_x|\alpha\rangle &= +\tfrac{1}{2}|\beta\rangle\,, \quad \hat{I}_x|\beta\rangle = +\tfrac{1}{2}|\alpha\rangle \\ \hat{I}_y|\alpha\rangle &= +\tfrac{i}{2}|\beta\rangle\,, \quad \hat{I}_y|\beta\rangle = -\tfrac{i}{2}|\alpha\rangle \end{aligned} \tag{3.11}$$

with the corresponding expectation values of $\hat{I}_x$ and $\hat{I}_y$ being given by:

$$\begin{aligned} \langle \hat{I}_x \rangle &= \langle \psi_{I,m}|\hat{I}_x|\psi_{I,m}\rangle = \tfrac{1}{2} c_\alpha^* c_\beta + \tfrac{1}{2} c_\beta^* c_\alpha \\ \langle \hat{I}_y \rangle &= \langle \psi_{I,m}|\hat{I}_y|\psi_{I,m}\rangle = \tfrac{i}{2} c_\beta^* c_\alpha - \tfrac{i}{2} c_\alpha^* c_\beta \end{aligned} \tag{3.12}$$

3.1.2 Isolated nuclear spins in a static magnetic field

The energy, E, of a single isolated spin under a static magnetic field is derived by solving the Schrödinger equation by operating upon the wavefunction, $|\psi_{I,m}\rangle$, with the Hamiltonian that describes the energy of the system, $\hat{\mathcal{H}}$:

$$\hat{\mathcal{H}}|\psi_{I,m}\rangle = E|\psi_{I,m}\rangle \tag{3.13}$$

The total Hamiltonian of the system is complex, comprising a multitude of degrees of freedom and interactions. Consider a simple system with a single isolated spin in the static magnetic field of an NMR experiment, $\boldsymbol{B}_0$, with a magnitude of B_0. Conventionally, when considering an NMR experiment, the z-axis is defined by the orientation of $\boldsymbol{B}_0$. In such a system, a dominant interaction emerges known as the Zeeman interaction. The Hamiltonian for the Zeeman interaction is defined as:

$$\hat{\mathcal{H}}_z = -\gamma\hbar B_0\hat{I}_z \tag{3.14}$$

where γ is the gyromagnetic ratio of the nucleus and $\hat{I}_z$ is the z-component of the spin magnetisation. As the z-axis is defined by the orientation of $\boldsymbol{B}_0$, the quantity $-\gamma B_0$ is defined to be the Larmor frequency, ω_0, the angular frequency at which the spin magnetisation precesses about B_0. The Zeeman Hamiltonian can then be described in terms of frequency:

$$\hat{\mathcal{H}}_z = \omega_0\hbar\hat{I}_z \tag{3.15}$$

Recall that $|\psi_{I,m}\rangle$ is an eigenfunction of $\hat{I}_z$, giving the eigenvalue m:

$$\hat{I}_z|\psi_{I,m}\rangle = m|\psi_{I,m}\rangle \tag{3.16}$$

allowing the Zeeman Hamiltonian to be represented as:

$$\hat{\mathcal{H}}_z|\psi_{I,m}\rangle = -\gamma\hbar B_0 m|\psi_{I,m}\rangle \tag{3.17}$$

with the energies of the eigenstates being obtained by substituting equation (3.17) into the Schrödinger equation (Equation 3.13), giving:

$$E = -\gamma\hbar B_0 m = \omega_0 \hbar m \tag{3.18}$$

The energy difference between the eigenstates is proportional to the applied magnetic field and the gyromagnetic ratio, making NMR spectroscopy effectively isotope-specific as ω_0 is unique to a given nucleus at a given field strength. Assuming that γ is positive, operating with the Zeeman Hamiltonian upon the eigenstates of a spin $I = ½$ system gives the Zeeman eigenstates:

$$\begin{aligned} \hat{\mathcal{H}}_z|\alpha\rangle &= -\gamma\hbar B_0 \hat{I}_z|\alpha\rangle = -\tfrac{1}{2}\gamma\hbar B_0|\alpha\rangle = +\tfrac{1}{2}\omega_0\hbar|\alpha\rangle \\ \hat{\mathcal{H}}_z|\beta\rangle &= -\gamma\hbar B_0 \hat{I}_z|\beta\rangle = +\tfrac{1}{2}\gamma\hbar B_0|\beta\rangle = -\tfrac{1}{2}\omega_0\hbar|\beta\rangle \end{aligned} \tag{3.19}$$

Here, the transition energy, ΔE, between the two spin states is equal to $|\omega_0\hbar|$ (Figure 3.1).

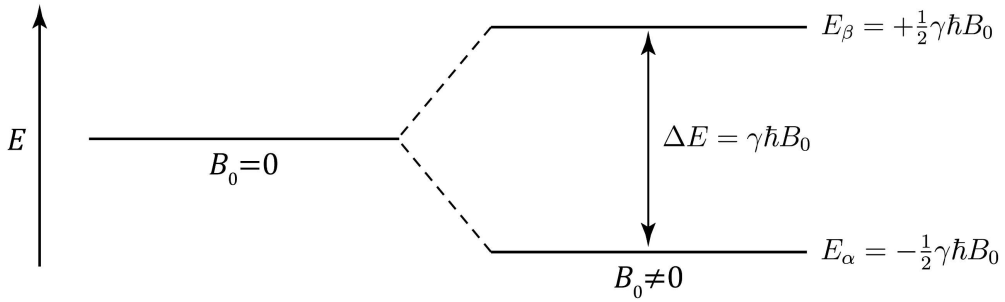

Figure 3.1. The Zeeman energy splitting between the spin states of spin *I* = ½ nuclei under an applied field assuming that $\gamma > 0$.

For a sample comprising non-interacting spin $I = ½$ nuclei under an applied field, each spin-system exists as a superposition of the two eigenstates, $|\alpha\rangle$ and $|\beta\rangle$. When the sample is at thermal equilibrium, the statistical occupancy of the Zeeman eigenstates follows a Boltzmann distribution, reflecting the probabilities of individual spins existing in the $|\alpha\rangle$ and $|\beta\rangle$ states:

$$\frac{p_\beta}{p_\alpha} = \exp\left(\frac{-\Delta E}{k_B T}\right) = \exp\left(\frac{-\omega_0\hbar}{k_B T}\right) \tag{3.20}$$

where p_α and p_β are the populations (number of nuclei) in each spin state, k_B is the Boltzmann constant, and T is the absolute temperature.[205] The population distribution, or statistical mixture of the eigenstates, is dependent upon both the nucleus and the applied magnetic field through its dependency on ω_0. A preferential occupation of the lower energy state is expected, with a greater population of the magnetic moments across the sample aligning with the applied field, resulting in a net magnetisation aligned with $\boldsymbol{B}_0$. As $\boldsymbol{B}_0$ defines the z-axis, this net

magnetisation along the z-axis, M_z, can be represented by the sum of the z-components of each spin within the sample multiplied by γ:

$$M_z = \gamma\hbar\langle\hat{I}_z\rangle^{(1)} + \gamma\hbar\langle\hat{I}_z\rangle^{(2)} + \cdots \gamma\hbar\langle\hat{I}_z\rangle^{(N-1)} + \gamma\hbar\langle\hat{I}_z\rangle^{(N)} \tag{3.21}$$

where N is the total number of spins within the sample.[206] The magnitude of the bulk magnetisation is proportional to the Larmor frequency, with nuclei of greater gyromagnetic ratios inducing greater magnetic moments. As $c_\alpha^* c_\alpha$ and $c_\beta^* c_\beta$ denote the probability of obtaining the $|\alpha\rangle$ and $|\beta\rangle$ states, respectively, the probabilities can be summed to find the number of spins which occupy these states upon measurement. The corresponding populations of the $|\alpha\rangle$ and $|\beta\rangle$ states are therefore given by:

$$\begin{aligned} p_\alpha &= c_\alpha^{*(1)} c_\alpha^{(1)} + c_\alpha^{*(2)} c_\alpha^{(2)} + \cdots c_\alpha^{*(N-1)} c_\alpha^{(N-1)} + c_\alpha^{*(N)} c_\alpha^{(N)} \\ p_\beta &= c_\beta^{*(1)} c_\beta^{(1)} + c_\beta^{*(2)} c_\beta^{(2)} + \cdots c_\beta^{*(N-1)} c_\beta^{(N-1)} + c_\beta^{*(N)} c_\beta^{(N)} \end{aligned} \tag{3.22}$$

The net z-magnetisation can then be expressed using an ensemble averaged value of $\langle\hat{I}_z\rangle$, or by using the population difference between the two states:

$$M_z = \tfrac{1}{2}\gamma\hbar\left(p_\alpha - p_\beta\right) \tag{3.23}$$

The energy difference between the Zeeman eigenstates is much smaller than the energies of other interactions, such as random thermal motion. As a result, the overall population difference between the two states is relatively small, making NMR an inherently insensitive technique. Following Equation 3.20, raising the magnetic field strength and decreasing the temperature give rise to an increased population difference, improving sensitivity.

3.2 The vector model

Thus far, the net magnetisation of a non-interacting ensemble of spins has been defined using the quantum mechanical description. From this, a classical picture of NMR spectroscopy illustrating the behaviour of the net magnetisation can be used to explain key concepts within the theory.

3.2.1 Bulk magnetisation and precession

Assume the sample comprises non-interacting spin $I = ½$ nuclei, as was the case in section 3.1.2. In the absence of an applied field, the magnetic moments are randomly oriented as the energies of the different orientations are degenerate (**Figure 3.2**). Under a static, uniform field aligned along the z-axis (*i.e.*, $B_0 \neq 0$), the spin-systems will preferentially occupy the lower energy $|\alpha\rangle$ state aligned with the field. An equilibrium is eventually reached through a process called relaxation; a phenomenon revisited in later sections. Note that, the individual magnetic moments are not fully aligned with B_0. Instead, a greater population of $|\alpha\rangle$ relative to $|\beta\rangle$ is in effect, resulting in a bulk magnetisation orientated along the z-axis, M_z, as detailed in section 3.1.2. Additionally, as the energy for all orientations of the x- and y-components of nuclear spin are degenerate for this system, it can be assumed that these components cancel out, leaving M_z as the sole component describing the equilibrium magnetisation vector for the sample, $\boldsymbol{M}_0$.

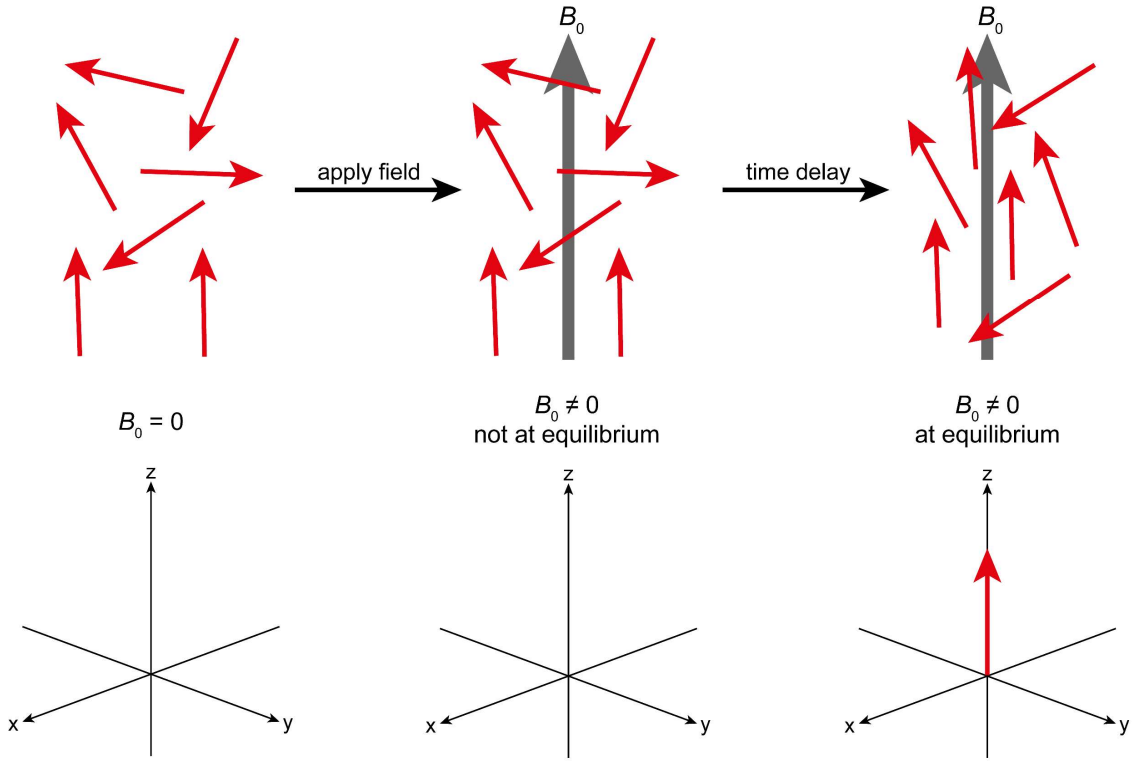

Figure 3.2. Graphical depiction of the random orientation of the individual spins resulting in no net magnetisation. Once an external field, $\boldsymbol{B}_0$, is applied, no immediate change is observed, but the energetic preference for aligned magnetic moments results in a gradual population preference, giving a net magnetisation aligned with the external field. Transverse magnetisation components are degenerate, cancelling out resulting in no net magnetisation in the *xy*-plane.

Once equilibrium has been reached, $\boldsymbol{M}_0$ exhibits a fixed magnitude, M_0, and direction. However, assuming that the bulk magnetisation vector is tipped away from the z-axis by an angle equal to β, the magnetisation would then be observed to precess about the z-axis at a rate equal to the Larmor frequency, ω_0, while maintaining the angle β (**Figure 3.3**).[206,207] By tipping $\boldsymbol{M}_0$ away from $\boldsymbol{B}_0$, an xy-component of magnetisation is introduced into the system. Assuming β is the tip angle towards the x-axis, the net x-component of the magnetisation vector, M_x, is given by:

$$M_x = M_0 \sin(\beta) \tag{3.24}$$

The x-component precesses about the z-axis at ω_0, evolving into a combination of x- and y-components with respect to time, as described by:

$$\begin{aligned} M_x &= M_0 \sin(\beta) \cos(\omega_0 t) \\ M_y &= -M_0 \sin(\beta) \sin(\omega_0 t) \end{aligned} \tag{3.25}$$

These x- and y-components of $\boldsymbol{M}_0$ are critical in the NMR experiment as they facilitate the detection of the magnetic behaviour by the detector coil, with the transverse magnetisation components cutting the detector coil during precession, inducing a measurable current across the detector coil.[206]

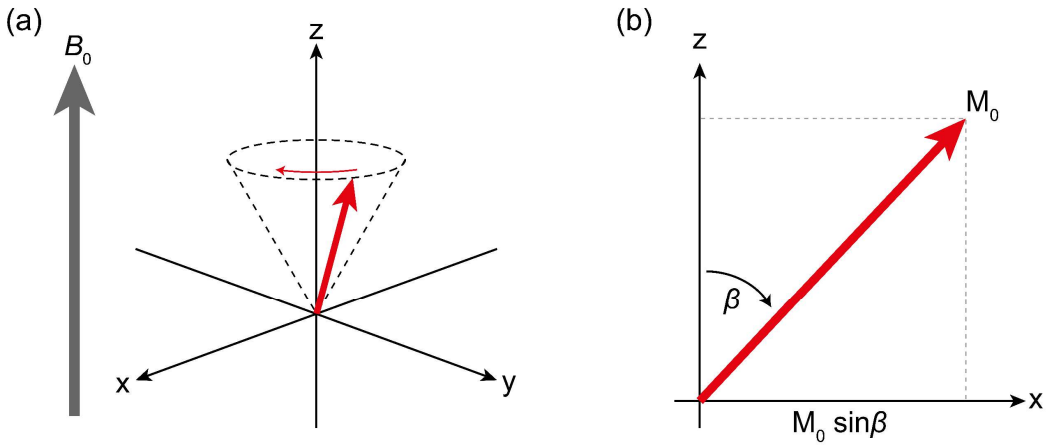

Figure 3.3. (a) The precessional motion of the magnetisation vector once it is tilted away from the z-axis (*i.e.,* the applied field) assuming that $\gamma > 0$, resulting in $\omega_0 < 0$. (b) Tilting of the magnetisation vector ($\boldsymbol{M}_0$) by a tilt angle of β towards the x-axis creates a transverse magnetisation component, the magnitude of which is defined by Equation 3.24.

3.2.2 Radiofrequency pulses and the rotating frame

One of the key principles of NMR experiments is to rotate $\boldsymbol{M}_0$ away from its equilibrium position and to measure the magnetic response of the sample. Typically, a rotation away from the z-axis, β, is achieved by introducing a magnetic field in the xy-plane, $\boldsymbol{B}_1$, via a pulse of electromagnetic radiation. The orientation of $\boldsymbol{B}_0$ is fixed, and typically $B_0 \gg B_1$. Therefore, to rotate $\boldsymbol{M}_0$ away from $\boldsymbol{B}_0$ the phenomenon of resonance must be used. The frequency of the electromagnetic radiation pulse, ω_{rf}, is set to be close to the Larmor frequency, ω_0, typically existing within the radiofrequency (*r.f.*) regime. In the static laboratory frame, the *r.f.* pulse comprises two counter-rotating magnetic fields of frequencies $\pm\omega_{\mathrm{rf}}$ (**Figure 3.4**). Classically, the reference frame of the vector model is changed here from the static laboratory frame to the rotating frame, a frame of reference rotating about the z-axis at an angular frequency of ω_{rf}. Within this rotating frame, the component of the *r.f.* pulse with frequency ω_{rf} appears stationary, whereas the component with frequency $-\omega_{\mathrm{rf}}$ rotates at $-2\omega_{\mathrm{rf}}$ relative to the rotating frame. By using the rotating frame, only the stationary component of the *r.f.* pulse is considered, with the quickly rotating component being neglected (**Figure 3.4**).[206,208]

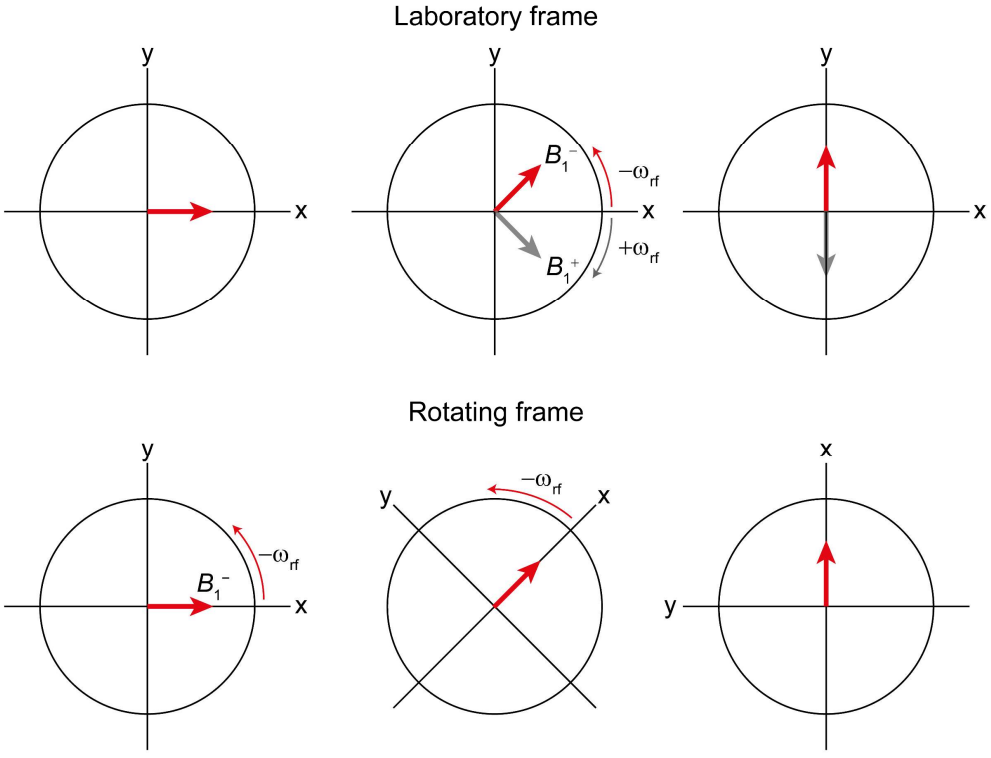

Figure 3.4. Simplistic illustrations of the two counter-rotating components of the radiofrequency field within the Laboratory frame. The bottom row shows the rotating frame axis system, wherein the axis rotates at the same frequency as one of the components (here the frame rotates at $-\omega_{\mathrm{rf}}$).

Within the rotating frame, the apparent Larmor precession, or offset frequency, is given by:

$$\Omega = \omega_0 - \omega_{\mathrm{rf}} \tag{3.26}$$

where ω_0 is the Larmor frequency and ω_{rf} is the frequency of the *r.f.* pulse. By extension, the apparent magnetic field strength within the rotating frame, ΔB, can be defined as:

$$\Delta B = -\frac{\Omega}{\gamma} \tag{3.27}$$

The term $\Delta \boldsymbol{B}$ is referred to as the reduced field in the rotating frame (**Figure 3.5a**). For a system under B_0 being hit with an *r.f.* pulse along the *x*-axis (*i.e.,* under B_1), the effective field that the Larmor precession acts about within the rotating frame, B_{eff}, is given by:

$$B_{\mathrm{eff}} = \sqrt{(B_1)^2 + (\Delta B)^2} \tag{3.28}$$

The orientation of $\boldsymbol{B}_{\mathrm{eff}}$ in relation to $\Delta \boldsymbol{B}$ is typically referred to as the tilt angle, θ, and is determined using simple trigonometric identities. Equation 3.28 underpins the concept of resonance within the NMR experiment, as by minimising the offset frequency, Ω, the effect of ΔB is reduced, resulting in B_{eff} being influenced by B_1 despite $B_0 \gg B_1$.[204,206]

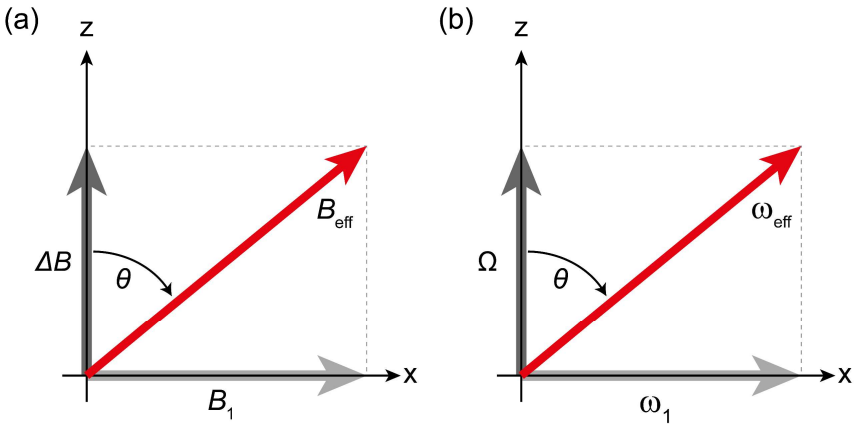

Figure 3.5. Illustrations showing (a) the relation between the effective field (B_{eff}), the reduced field (ΔB), the applied field (B_1), and the tilt angle (θ) within the rotating frame and (b) the analogous relation described in terms of frequency.

Assuming the *r.f.* pulse is on-resonance, where $\Omega = 0$, the effective field is shown to align along the *x*-axis with size ω_1 and $\theta = 90°$ (**Figure 3.5b**). The motion of $\boldsymbol{M}_0$ under $\boldsymbol{B}_1$ is relatively straightforward, with $\boldsymbol{M}_0$ being rotated from the *z*-axis into the *yz*-plane

(**Figure 3.6a-b**). The extent of the vector nutation is typically denoted by the flip angle, β, which is defined as:

$$\beta = \omega_1 \tau_1 \tag{3.29}$$

where τ_1 is the pulse duration. The angle through which the magnetisation is rotated can be tailored by altering the duration of the *r.f.* pulse or the power applied across the *r.f.* coil (as governed by $\omega_1 = -\gamma B_1$). Conventionally, pulses are described by their direction and their flip angle (*e.g.,* $90°_x$, where $\beta = 90°$ and the pulse is along the *x*-axis). In practice, the *r.f.* pulse cannot be on-resonance with multiple Larmor frequencies. In these instances, a hard pulse can be applied where B_1 is sufficiently large as to orientate $\boldsymbol{B}_{\text{eff}}$ close to the *x*-axis despite $\theta \neq 90°$. The pulse may be considered non-selective if:

$$\omega_1 \gg |\Omega| \text{ or } B_1 \gg |\Delta B| \tag{3.30}$$

As $\omega_1 \gg |\Omega|$, ω_{eff} is approximately equal to ω_1 despite $\theta \neq 90°$. Consequently, for spectrometers with larger B_0 values, and assuming that $|\Omega|$ is due to chemical shift differences, more power must be used to create an *r.f.* pulse so that B_1 satisfies the above condition.[206] Immediately following the application of the *r.f.* pulse, the magnetisation vector will begin to precess in the *xy*-plane (**Figure 3.6c**) about $\boldsymbol{B}_{\text{eff}}$, which in the absence of $\boldsymbol{B}_1$ will be orientated along $\Delta\boldsymbol{B}$. Assuming in this instance that $\gamma < 0$, and that the receiver reference frequency = ω_1, the precession through the transverse plane about $\Delta\boldsymbol{B}$ in the rotating frame is given by:

$$\begin{aligned} M_x &= -M_0 \sin(\beta) \sin(\Omega t) \\ M_y &= -M_0 \sin(\beta) \cos(\Omega t) \end{aligned} \tag{3.31}$$

The frequency of this precession is detected by the transverse magnetisation as it cuts through the detector coil, inducing a current. This current is measured to give an electrical signal known as the free induction decay (FID). To detect both the *x*- and *y*-components of the transverse magnetisation using a single detector coil, quadrature detection is implemented. Here, the output from one coil is fed into two mixers with receiver phases that are phase shifted by 90° from one another. The real and imaginary components are then used as the complex input of a Fourier transform (FT), converting the time-domain FID into a frequency-domain NMR

spectrum. The process of rotating the equilibrium magnetisation about a flip angle and measuring the magnetic response in the form of an FID is known as a pulse-acquire experiment.

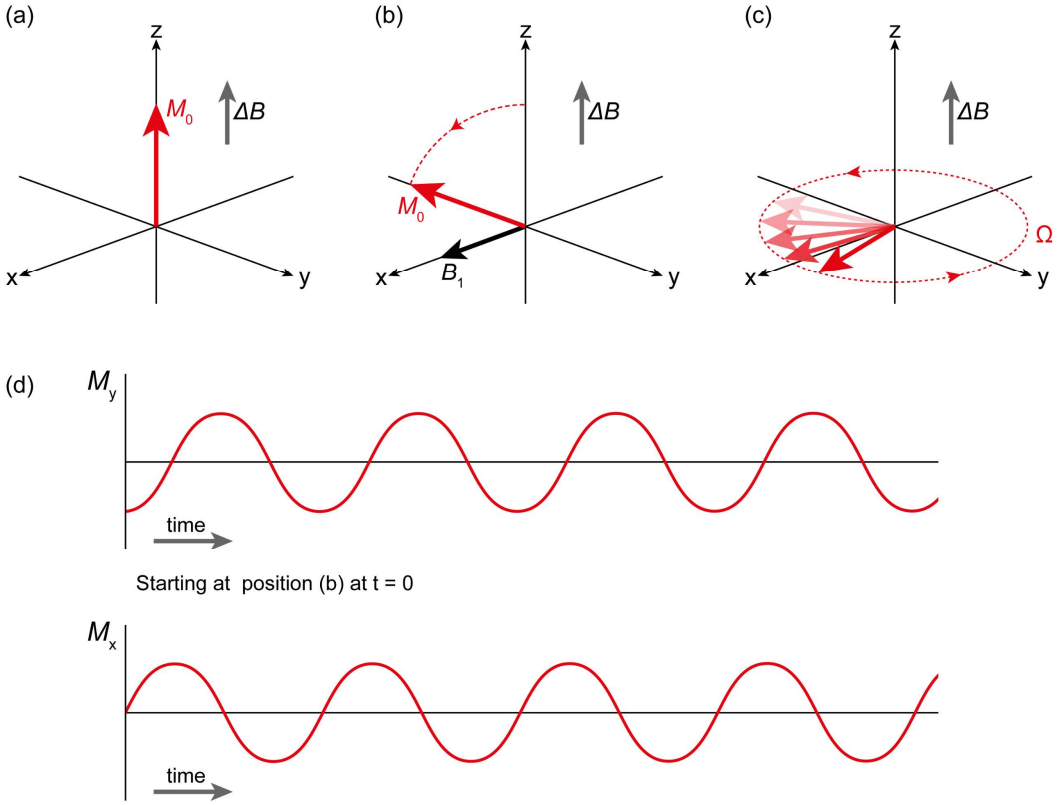

Figure 3.6. The vector model description of a simple 90°$_x$ experiment within the rotating frame. (a) Initially, a net magnetisation forms that is aligned with the effective field, Δ***B***. (b) A 90° excitation pulse, $\boldsymbol{B}_1$, is applied along the *x*-axis, flipping the magnetisation along the −*y*-axis, generating transverse magnetisation. (c) Once $\boldsymbol{B}_1$ is no longer applied, the magnetisation begins to precess in the *xy*-plane at the offset frequency, Ω. (d) The evolution of the *x*- and *y*-components of the magnetisation with respect to time are also shown, starting with the $\boldsymbol{M}_0$ along -*y*, as shown in (b), and rotating in an anticlockwise fashion (*i.e.*, a positive rotation following the right-handed axis set).

3.2.3 Free induction decay and relaxation

Notably, the FID changes with respect to time, with the precessional motion and orientation of the magnetisation vector being reliant upon time-dependent relaxation processes that return the system to a state of thermal equilibrium. This relaxation process typically comprises two processes: spin-lattice (or longitudinal) relaxation and spin-spin (or transverse) relaxation. Longitudinal relaxation relates to the process in which the *z*-component of the equilibrium magnetisation vector $\boldsymbol{M}_0$, M_z, returns to thermal equilibrium following a nutation away from the *z*-axis. The time constant for the spin-lattice relaxation is denoted by T_1, and the response of M_z towards equilibrium along the *z*-axis following a perturbation is given by:

$$M_z(t) - M_0 = [M_z(0) - M_0]e^{-\frac{t}{T_1}} \tag{3.32}$$

where M_0 is the equilibrium magnetisation, $M_z(t)$ is the z-component of magnetisation at t, $M_z(0)$ is the magnetisation in the z dimension following perturbation, and t is the time elapsed following the pulse. Assuming $\boldsymbol{M}_0$ is aligned along the x-axis, setting the time between pulse-acquire experiments, otherwise referred to as the recycle delay, D_1, to $D_1 \geq 5T_1$ results in a good recovery of M_z following perturbation, with $\geq 99.3\%$ of M_z being recovered (**Figure 3.7**).[204] T_1 relaxation times are varied, typically on the order of milliseconds or seconds, but can be up to several minutes or hours depending upon the strength of nuclear spin interactions and dynamical processes that contribute towards the realignment of the magnetisation along the applied field.

Transverse relaxation relates to the decoherence of the transverse magnetisation following perturbation due to the decay of the FID. Variations in the local magnetic environment and spin dynamics contribute towards the transverse relaxation time constant, T_2, with the decay in coherence being described by:

$$M_{xy}(t) = [M_{xy}(0)]e^{-\frac{t}{T_2}} \tag{3.33}$$

where $M_{xy}(0)$ is the transverse component of the bulk magnetisation.

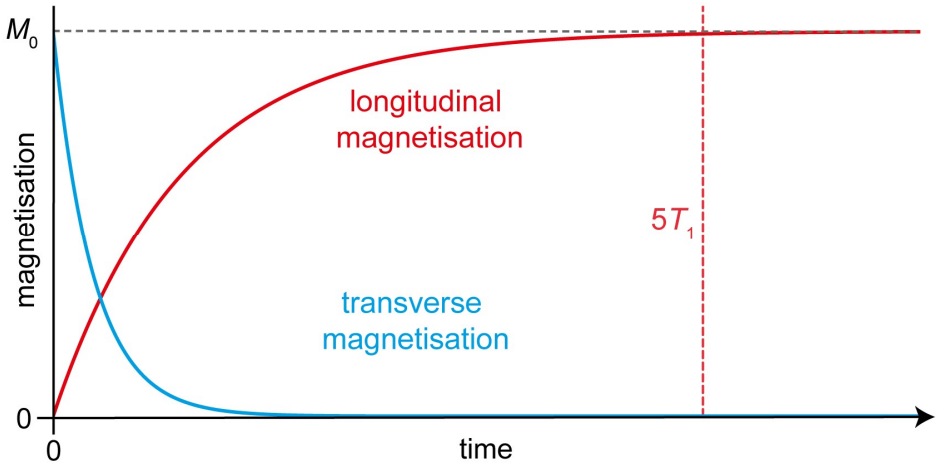

Figure 3.7. A plot showing the exponential decays of the transverse and longitudinal magnetisation with respect to time. The *z*-magnetisation returns to its maximum value at thermal equilibrium, whereas the transverse magnetisation decays to zero. At $D_1 = 5T_1$, 99.3% of M_0 has been recovered.

Transverse relaxation influences the lineshape of the resonances in NMR spectra, with shorter T_2 values giving shorter FIDs, resulting in broader resonances in the frequency domain. The full-width half-maximum, W, of the resonance for a non-interacting system is given by:

$$W = \frac{1}{\pi T_2} \tag{3.34}$$

As described by Equation 3.31, the *x*- and *y*-components are equal to zero when $\beta = 0$, thus it is always the case that $T_1 \geq T_2$. For solids, $T_1 \gg T_2$ as the spins are held in place, increasing the decoherence of transverse magnetisation due to differences in the local magnetic environment, whereas in solution it is possible for $T_1 \approx T_2$ due to the increased mobility of the nuclei averaging out variations in the local magnetic environments, resulting in a sustained coherence of transverse magnetisation. The FID (*i.e.,* the transverse magnetisation) and its decay is given by:

$$S(t) = S(0)[\cos(\Omega t) + i\sin(\Omega t)]e^{-\frac{t}{T_2}} = S(0)e^{i\Omega t}e^{-\frac{t}{T_2}} \tag{3.35}$$

This signal can then be Fourier transformed into the frequency-domain, giving a complex frequency domain signal comprising real and imaginary components. Conventionally, the NMR spectrum is the real component of this signal giving an adsorptive Lorentzian lineshape. The Fourier transformed signal can be summed cumulatively and in practical NMR experiments it is common practice to run multiple pulse-acquire experiments. Running N experiments, conventionally referred to as transients, increases the signal proportionally with N, whereas the random background noise increases proportionally with $\sqrt{N}$, thus the signal-to-noise ratio (SNR) $\propto \sqrt{N}$. It is important to wait for the system to return to thermal equilibrium between pulse-acquire experiments ($D_1 \geq 5T_1$, as detailed above) to ensure the consistent perturbation of $\boldsymbol{M}_0$ for each transient.

3.3 Interactions in NMR

The discussion thus far has assumed a simple non-interacting spin system under a static magnetic field, investigating fundamental mechanisms related to the relaxation and response of magnetisation following perturbation through an *r.f.* pulse. Here, the discussion details fundamental interactions, both within and between spin systems that influence the behaviour of these nuclear magnetic moments.

3.3.1 Tensors and magnetic shielding

As $\omega_0 \propto \gamma$, it could be assumed that all nuclei of a particular isotope will precess at the same frequency, giving rise to a single resonance in the NMR spectra. Practically, this is not the case, as the nuclei are experiencing additional magnetic fields aside from B_0, giving rise to numerous resonances that are offset from ω_0. If $B_0 \neq 0$, electrons within the orbitals of nuclei circulate about $\boldsymbol{B}_0$, inducing a weak local magnetic field, $\boldsymbol{B}_i$, that is proportional to the applied field. $\boldsymbol{B}_i$ can either oppose $\boldsymbol{B}_0$, referred to as a diamagnetic field that results in a shielding effect, or align with $\boldsymbol{B}_0$, augmenting the applied field with a paramagnetic field in a deshielding effect. The effective magnetic field experienced by the nucleus, B_{eff}, is given by:

$$B_{\text{eff}} = B_0 - B_i = B_0(1 - \sigma) \tag{3.36}$$

where σ is the shielding constant for the nucleus, comprising both diamagnetic and paramagnetic components. As a result of nuclear shielding, the observed precession frequency for a given spin is given by:

$$\omega_{\text{obs}} = -\gamma B_{\text{eff}} \tag{3.37}$$

Equations 3.36 and 3.37 show that the observed resonance frequency for a nucleus in an atom is always reduced relative to that of a bare nucleus stripped of its electrons, and that nuclei occupying different local electronic environments will exhibit different resonance frequencies. It is inconvenient to measure exact values for σ due to the small difference between B_{eff} and B_0. Instead, it is common practice to define the chemical shift, δ, in terms of the difference between the Larmor frequency of the nucleus of interest, ω_{obs}, and that of a reference nucleus, ω_{ref}.

$$\delta = 10^6 \left(\frac{\omega_{\text{obs}} - \omega_{\text{ref}}}{\omega_{\text{ref}}} \right) \tag{3.38}$$

The chemical shift increases as σ decreases, thus δ is considered a deshielding parameter, whereby a larger chemical shift denotes a stronger B_{eff} experienced by the nucleus. Conventional reference compounds are inert, soluble, and give strong simple resonances (*e.g.,* tetramethylsilane for ^{1}H and ^{13}C NMR). In actuality, the electron density surrounding nuclei is rarely spherical, often exhibiting anisotropy with respect to the direction of the applied

magnetic field. When the electron density is non-uniform, it leads to chemical shift anisotropy (CSA). In such cases, the shielding constant is best described by a second-rank tensor:[208]

$$\boldsymbol{\sigma} = \begin{pmatrix} \sigma_{xx} & \sigma_{xy} & \sigma_{xz} \\ \sigma_{yx} & \sigma_{yy} & \sigma_{yz} \\ \sigma_{zx} & \sigma_{zy} & \sigma_{zz} \end{pmatrix} \tag{3.39}$$

By continuing the convention of $\boldsymbol{B_0}$ being aligned with the *z*-axis in the laboratory frame, the induced shielding field is described by:

$$\boldsymbol{B}_i = -\boldsymbol{\sigma B_0} = -\begin{pmatrix} \sigma_{xx} & \sigma_{xy} & \sigma_{xz} \\ \sigma_{yx} & \sigma_{yy} & \sigma_{yz} \\ \sigma_{zx} & \sigma_{zy} & \sigma_{zz} \end{pmatrix} \cdot \begin{pmatrix} 0 \\ 0 \\ B_0 \end{pmatrix} = \begin{pmatrix} -\sigma_{xz}B_0 \\ -\sigma_{yz}B_0 \\ -\sigma_{zz}B_0 \end{pmatrix} \tag{3.40}$$

Here the terms $-\sigma_{xz}B_0$, $-\sigma_{yz}B_0$, and $-\sigma_{zz}B_0$ relate to the induced field components in the *x*-, *y*-, and *z*-axis of the laboratory frame, respectively, showing how $\boldsymbol{B}_i$ can be orientated in any given direction relative to $\boldsymbol{B}_0$. Notably, tensors are often symmetric, and even in cases of asymmetrical tensors, the antisymmetric contributions have no effect on the NMR spectrum, asides from inducing relaxation. In such instances, a set of axes can be selected such that the shielding tensor for the nucleus becomes diagonal (**Figure 3.8**). This orientation is described using a principal axis system (PAS) that is fixed in orientation with respect to the molecule:

$$\boldsymbol{\sigma}_{\mathrm{PAS}} = \begin{pmatrix} \sigma_{XX} & 0 & 0 \\ 0 & \sigma_{YY} & 0 \\ 0 & 0 & \sigma_{ZZ} \end{pmatrix} \tag{3.41}$$

where σ_{XX}, σ_{YY}, and σ_{ZZ} are the principal components of the tensor and $\boldsymbol{\sigma}_{\mathrm{PAS}}$ is diagonal. In isotropic solutions, where nuclei undergo rapid tumbling rates, the isotropic magnetic shielding, σ_{iso}, is observed:

$$\sigma_{\mathrm{iso}} = \tfrac{1}{3}(\sigma_{XX} + \sigma_{YY} + \sigma_{ZZ}) \tag{3.42}$$

and the corresponding isotropic resonance frequency, ω_{iso}, is given by:

$$\omega_{\mathrm{iso}} = -\gamma B_0(1 - \sigma_{\mathrm{iso}}) \tag{3.43}$$

For systems where the nuclei are not undergoing rapid tumbling, and by extension their shielding tensor components are not motionally averaged, the situation becomes more complex.

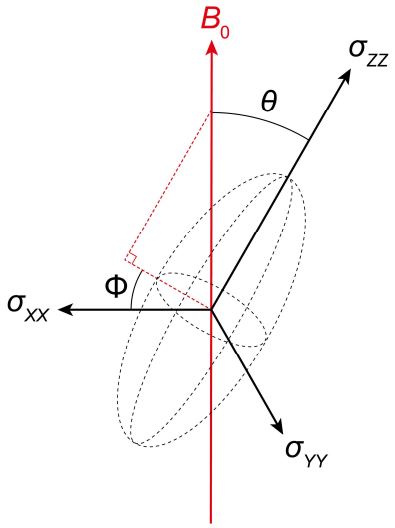

Figure 3.8. A schematic of an ellipsoid representing the magnetic shielding tensor on a principal axis system (PAS). The polar angles θ and Φ that define the orientation of the PAS relative to B_0 are also shown.

Consider a crystalline solid in which the molecules are orientated along the same axis with respect to the applied magnetic field. In this instance, a single σ (and by extension δ) is observed for the sample. Changing the orientation of the sample (*i.e.,* rotating the PAS) relative to $\boldsymbol{B}_0$ will alter the shielding tensor as described by:

$$\sigma = \sigma_{XX} \sin^2\theta \cos^2\Phi + \sigma_{YY} \sin^2\theta \sin^2\Phi + \sigma_{ZZ} \sin^2\theta \tag{3.44}$$

where θ and Φ are polar angles describing the orientation of the tensor with respect to $\boldsymbol{B}_0$ (**Figure 3.8**). Within a powdered crystalline material, the molecules occupy various orientations giving rise to a superposition of the orientationally dependent chemical shifts in the observed NMR spectrum. The observed superposition of the orientationally-dependant resonances is termed a powder pattern. The shape of the pattern is dependent upon the magnetic shielding tensor, with the turning points of the pattern coinciding with the principal shielding components and their respective chemical shifts (**Figure 3.9**). In the standard convention, the principal components of the shielding tensor are ordered as $\sigma_{ZZ} \geq \sigma_{YY} \geq \sigma_{XX}$.[209] However, from this point forward, the Haeberlen convention[210] will be used, which defines the principal components as follows:

$$|\sigma_{ZZ} - \sigma_{\text{iso}}| \geq |\sigma_{XX} - \sigma_{\text{iso}}| \geq |\sigma_{YY} - \sigma_{\text{iso}}| \tag{3.45}$$

It is often useful to describe shielding tensors using both the principal components and parameters such as the shielding anisotropy, ζ, and the shielding asymmetry, η. These parameters are defined as:[203,209]

$$\zeta = \sigma_{ZZ} - \sigma_{\text{iso}} \tag{3.46}$$

$$\eta = \frac{\sigma_{YY} - \sigma_{XX}}{\zeta} \tag{3.47}$$

The total shielding tensor for an axially asymmetric system ($\sigma_{YY} \neq \sigma_{XX}$, $\therefore \eta > 0$) is therefore given by:[210]

$$\sigma = \sigma_{\text{iso}} + \tfrac{\zeta}{2}[(3\cos^2\theta - 1) + \eta(\sin^2\theta \cos 2\Phi)] \tag{3.48}$$

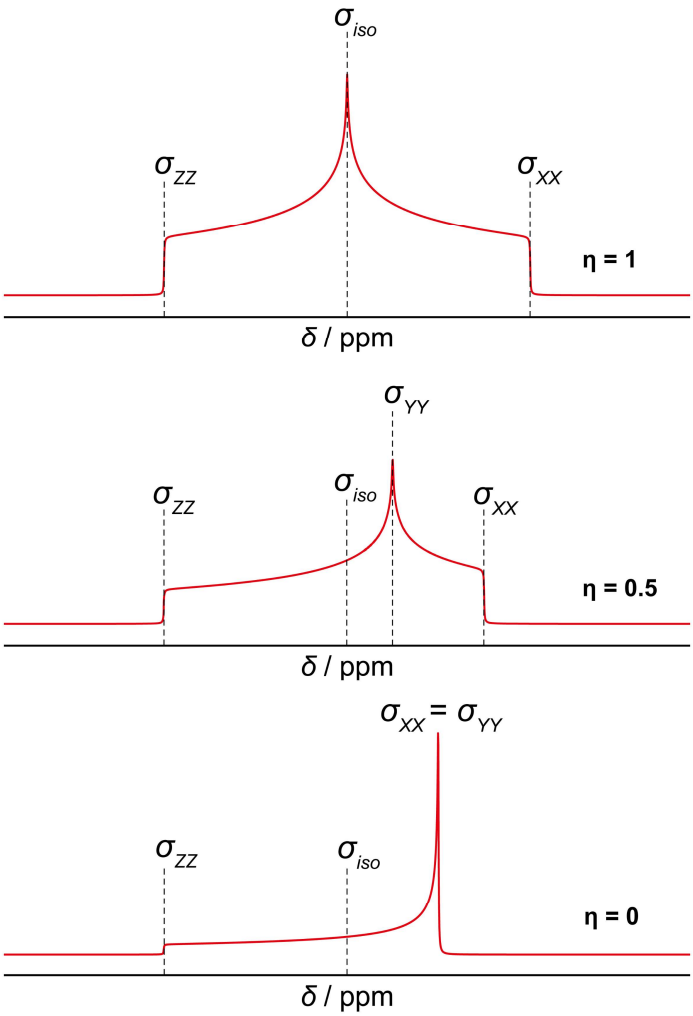

Figure 3.9. Illustration of chemical shift anisotropy (CSA) powder patterns of polycrystalline samples. The shielding asymmetry and relative axial shielding tensor values are shown.

3.3.1.1 Ring current shielding

As detailed above, the circulation of electrons under an applied field generates an induced field that alters the effective magnetic field interacting with the nucleus of interest. Notably, this circulation is particularly influential in aromatic (4n+2 π-electron) systems, with highly delocalised π-electrons readily circulating about the π-orbitals under $\boldsymbol{B}_0$. This motion induces a significant diamagnetic moment that opposes the applied field, with the correlated ring current induced field, $\boldsymbol{B}_\pi$, shielding nuclei above and below the ring, and deshielding nuclei in the plane of the aromatic ring (**Figure 3.10a**). One such example is the aromatic compound benzene (C_6H_6). Under an applied magnetic field, the π-electrons circulate in a diatropic motion, inducing a diamagnetic field that deshields the hydrogen atoms in the plane of the ring (*i.e.*, an increase in B_{eff}) (**Figure 3.10b**). By extension, nuclei that are situated above and below the plane of the benzene molecule will experience a significant shielding effect. This situation is observed clearly in the molecule *trans*-15,16-dimethyl-15,16-dihydropyrene, where the aromatic protons are deshielded (8.1 ppm to 8.7 ppm) and the methyl protons are shielded (−4.3 ppm).[207]

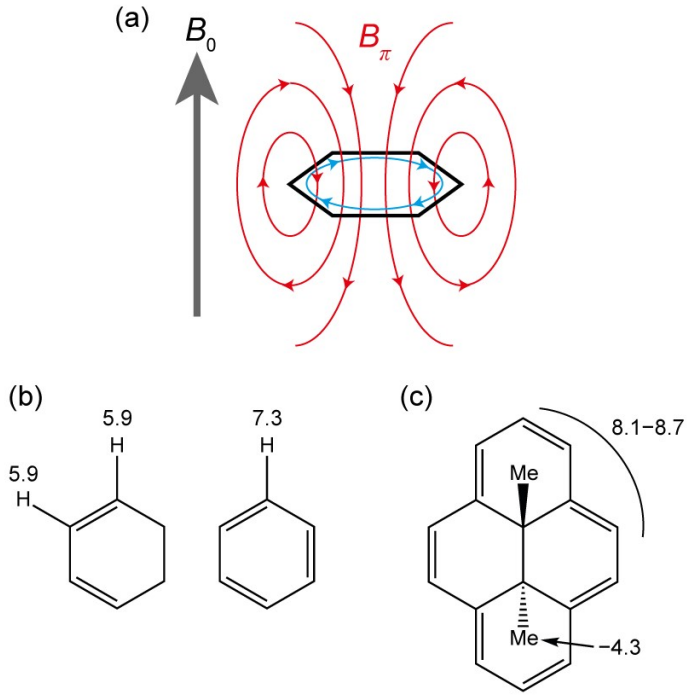

Figure 3.10. (a) Illustration showing the circulation of the π electrons (blue arrows) within an aromatic ring and the resulting induced magnetic field, B_π (red field lines). (b) ^{1}H Chemical shifts (in ppm) reported for cyclohexa-1,3-diene and benzene show a marked difference due to ring current shielding. (c) *trans*-15,16-dimethyl-15,16-dihydropyrene ^{1}H chemical shifts for the ring current deshielded methyl protons and the ring current shielded aromatic protons. Chemical shift values are taken from Ref. [207].

The ring current induced field is localised, with field strength being inversely proportional to the cubed distance from the ring-plane ($B \propto r^{-3}$). Consequently, this "neighbouring group" shielding effect proves to be a powerful analytical tool, allowing the identification of nuclei occupying the local environment of aromatic groups via their chemical shifts. This allows for the identification of both intramolecular and intermolecular nuclei that are near the aromatic group. Fundamentally, increasing the extent of conjugation, and by extension the number of delocalised π-electrons, will induce a stronger field resulting in a greater extent of shielding or deshielding for neighbouring nuclei. Additionally, antiaromatic structures (with 4n π-electrons) exhibit paratropic ring currents, circulating in the opposing direction to aromatic structures and inducing paramagnetic fields. However, the inherent instability of many antiaromatic compounds and stability of aromatic compounds causes diamagnetic shielding to be the predominant ring current effect that is observed in materials.

3.3.2 Spin-spin coupling

Information can be gained by considering the interactions between the electronic properties of nuclei and the magnetic field, but there is another source of extremely valuable information encoded within most NMR spectra. By considering how multiple nuclei interact with each other within the sample, known as spin-spin or internuclear couplings, it is possible to gain further insight into the chemical environments of the nuclei.

3.3.2.1 Dipolar coupling

Nuclear spins within a system can interact through space with neighbouring nuclei, in which the two nearby magnetic dipole moments can directly couple. The interaction for two coupled heteronuclear spins can be described by a traceless and axially symmetric tensor, d_{ij}^{PAS}, of which the PAS z-axis is parallel to the internuclear vector, $\vec{R}_{ij}$, resulting in an orientation-dependent splitting parameter, ω_{ij}, defined by:

$$\omega_{ij} = -d_{ij}^{\mathrm{PAS}} \cdot \frac{1}{2}\left(3\cos^2\Theta_{ij} - 1\right) \tag{3.49}$$

where Θ_{ij} describes the orientation of $\vec{R}_{ij}$ with respect to $\boldsymbol{B}_0$, and d_{ij} is the dipolar coupling constant:

$$d_{ij}^{\mathrm{PAS}} = \hbar\left(\frac{\mu_0}{4\pi}\right)\frac{\gamma_i\gamma_j}{{r_{ij}}^3} \tag{3.50}$$

where $\hbar$ is the reduced Planck constant, μ_0 is the permittivity of vacuum, r_{ij} is the internuclear separation between the two spins, i and j, and the gyromagnetic ratios of the two nuclei are given by γ_i and γ_j (**Figure 3.11**).

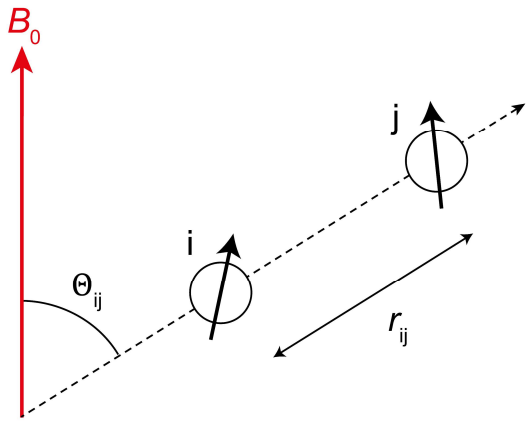

Figure 3.11. Schematic showing the key parameters that determine the dipolar interaction between two nuclear spins, i and j.

For homonuclear spin systems, an additional contribution corresponding to a "flip-flop" interaction (or the flipping of both spins i and j through a zero-quantum transition) is required due to the energy equivalence of the i_+j_- and i_-j_+ spin states (*i.e.*, $E_{i_-\rightarrow i_+} = E_{j_+\rightarrow j_-}$), giving the adjusted splitting parameter:[204,211]

$$\omega_{i,j}^{\mathrm{homo}} = -d_{ij}\cdot\frac{3}{4}\left(3\cos^2\Theta_{ij} - 1\right) \tag{3.51}$$

Importantly, the dipolar coupling interaction is (i) anisotropic, due to its dependence upon Θ_{ij}, (ii) localised, as $\omega_{ij} \propto {r_{ij}}^{-3}$, and (iii) strongest between nuclei with large gyromagnetic ratios. In solution-state NMR, ω_{ij} is motionally averaged to zero by fast isotropic tumbling, akin to the CSA interaction. However, in solids, dipolar coupling is generally retained, broadening NMR resonances. For a pristine crystallite with an isolated pair of spin $I = ½$ heteronuclei, i and j, and a fixed molecular orientation, the resulting spectra for both nuclei will display a doublet at frequencies equal to $\omega_0 \pm \omega_{ij}$ due to the alignment and antialignment of the neighbouring magnetic moment relative to $\boldsymbol{B}_0$. The magnitude of the frequency splitting is orientationally dependent, which, like chemical shift anisotropy, drastically affects the resonance shape for polycrystalline powder samples that comprise a distribution of

orientations. Assuming ω_{ij} is the only internuclear spin interaction, the NMR spectrum of the polycrystalline powder sample containing a full range of orientations will be a Pake-Doublet,[212] where the outer edges correspond to the $\Theta_{ij} = 0°$ and the intense 'horns' to $\Theta_{ij} = 90°$ (**Figure 3.12**). Solid samples comprise many nuclear spins that couple to one another, introducing dipolar interactions of myriad orientations and internuclear distances. The observed resonance for polycrystalline solids is typically an amalgamation of these interactions, giving a broadened lineshape following a Gaussian distribution.

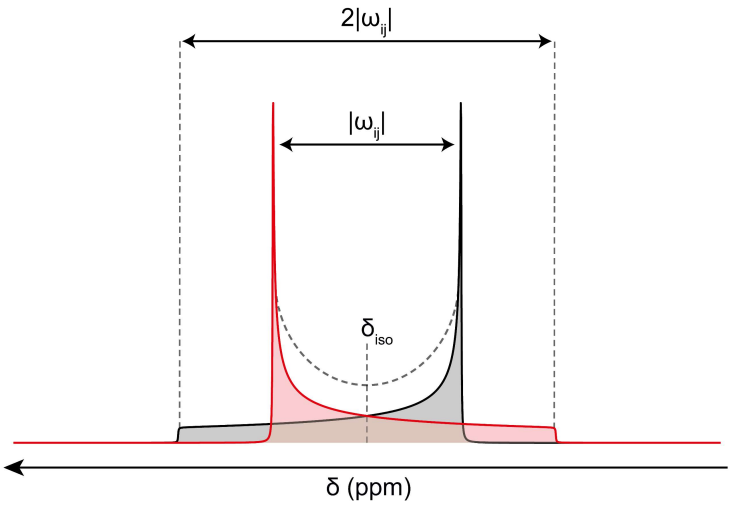

Figure 3.12. Model NMR spectrum showing the observed powder pattern (Pake-Doublet) of a polycrystalline sample comprising exclusively i-j spin pairs, with the contributions from aligned and anti-aligned spins depicted.

3.3.2.2 Scalar coupling

Nuclei that share a bond can undergo an additional indirect spin-spin interaction known as scalar coupling (or *J*-coupling); an interaction mediated by the shared electron density between the nuclear spins. This "through-bond" interaction is very weak, often on the order of a few Hz, requiring high spectral resolutions to observe features caused by this interaction. Typically, scalar coupling interactions are rarely resolved for solid samples as broadening from stronger interactions (*e.g.,* CSA and dipolar coupling) and field inhomogeneity reduce the spectral resolution beyond the level required to observe scalar coupling. In solution-state NMR, the broadening from larger, orientationally dependent interactions are removed, allowing scalar coupling features to be resolved. Consequently, *J*-coupling proves to be a vital interaction for solution-state NMR, providing ample information regarding local bonding structures. With that being said, the weak scalar interaction is still present within solid samples. Thus, even if it

cannot be resolved in conventional pulse-acquire 1D NMR spectra, it can still be exploited to transfer magnetisation, or even observed using select two-dimensional NMR experiments.[213]

3.3.3 Quadrupolar coupling

The discussion thus far has centred around spin $I = ½$ nuclei that exhibit a symmetric charge distribution and an orientation independent interaction between nuclei and their local electric field gradient (EFG). For nuclei of spin $I > ½$, there is an asymmetric charge distribution across the nucleus which is described by a nuclear electric quadrupole moment (EQM). This can be represented as the second rank tensor, $\boldsymbol{Q}$:

$$\boldsymbol{Q} = \begin{pmatrix} Q_{xx} & Q_{xy} & Q_{xz} \\ Q_{yx} & Q_{yy} & Q_{yz} \\ Q_{zx} & Q_{zy} & Q_{zz} \end{pmatrix} \tag{3.52}$$

The asymmetry in the nuclear charge distribution gives rise to an orientationally dependent interaction with the local EFG. The local EFG is described in terms of a PAS by the second rank tensor, $\boldsymbol{q}_{\mathrm{PAS}}$:

$$\boldsymbol{q}_{\mathrm{PAS}} = \begin{pmatrix} q_{XX} & 0 & 0 \\ 0 & q_{YY} & 0 \\ 0 & 0 & q_{ZZ} \end{pmatrix} \tag{3.53}$$

where $|q_{ZZ}| \geq |q_{YY}| \geq |q_{XX}|$ and $\mathrm{Tr}\{\boldsymbol{q}_{\mathrm{PAS}}\} = 0$, giving an isotropic average of zero. Consequently, the motional averaging of molecules in solution effectively averages out quadrupolar coupling. Generally, the interaction between the EQM and the EFG is described in terms of its magnitude (in frequency units) through the nuclear quadrupole coupling constant, C_{Q}:

$$C_{\mathrm{Q}} = \frac{e^2 Q q_{ZZ}}{h} \tag{3.54}$$

and a dimensionless quadrupolar asymmetry parameter, η_{Q}:

$$\eta_{\mathrm{Q}} = \frac{q_{XX} - q_{YY}}{q_{ZZ}} \tag{3.55}$$

For a site of cubic symmetry, where the EFG is spherically symmetric ($|q_{ZZ}| = |q_{YY}| = |q_{XX}|$), $C_\mathrm{Q} = 0$ and the nucleus can be treated equivalently to a spin I = ½ system. The strength of the quadrupolar interaction for spin I > ½ nuclei within an asymmetric EFG is larger than all other interactions (several MHz) aside from the Zeeman interaction. The effect of this interaction is often described as a perturbation of the distinct Zeeman energy levels (**Figure 3.13**).

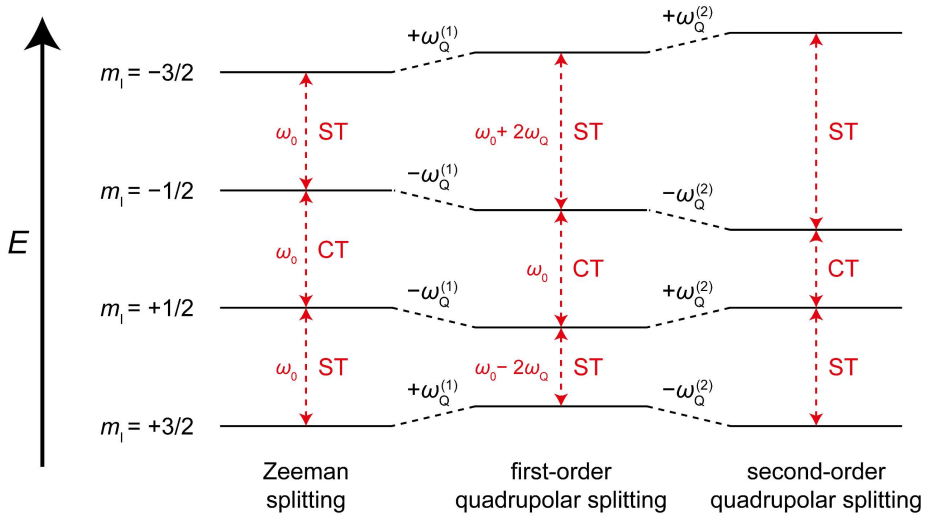

Figure 3.13. Energy level diagram showing the effect of the quadrupolar interaction on the Zeeman energy levels for a spin *I* = 3/2 nucleus. The first-order quadrupolar interaction does not affect the central transition (CT), whereas the second-order quadrupolar interaction modifies all transitions.

For a quadrupolar nucleus of spin I, where I is a half-integer, the system has $2I + 1$ Zeeman states, resulting in $2I$ allowed single-quantum transitions, where $\Delta m_I = \pm 1$. The quadrupolar interaction perturbs the Zeeman energy levels, resulting in distinct transition frequencies that can be categorised into two types of single-quantum transitions: (i) The central transition (CT) between the states $m_I = ½ \leftrightarrow -½$, with a frequency difference that, to first order, is approximately equal to ω_0, and (ii) satellite transitions (ST) that occur at frequencies shifted from ω_0 following the first-order expression $\omega^{(1)}_{(m_I-1)\leftrightarrow m_I} = (2m_I - 1)\omega^{(1)}_\mathrm{Q}$, where $\omega^{(1)}_\mathrm{Q}$ is the first-order quadrupolar splitting parameter, defined as:[203,214]

$$\omega^{(1)}_\mathrm{Q} = \frac{\omega^\mathrm{PAS}_\mathrm{Q}}{2}\left[(3\cos^2\theta - 1) + \eta_\mathrm{Q}(\sin^2\theta\cos 2\Phi)\right] \tag{3.56}$$

and $\omega^\mathrm{PAS}_\mathrm{Q}$ is given by:[215]

$$\omega^\mathrm{PAS}_\mathrm{Q} = \frac{3\pi C_\mathrm{Q}}{2I(2I-1)} \tag{3.57}$$

For a pristine crystallite of quadrupolar nuclei with half integer spins, the observed NMR spectrum will exhibit $2I$ resonances: one central transition at the Larmor frequency and $2I-1$ satellite resonances. As with chemical shift anisotropy and dipolar coupling, the orientational dependence of $\omega_{\mathrm{Q}}^{(1)}$ broadens the satellite transition resonances for powdered crystallite samples. In contrast, the central transition remains sharp and is unaffected by this broadening.

Larger EFGs relative to the Zeeman interaction give rise to a weaker second-order perturbation that influences all transitions, including the CT. The frequency splitting due to second order quadrupolar coupling, $\omega_{\mathrm{Q}}^{(2)}$, is inversely proportional to ω_0 and comprises an isotropic component and two orientationally dependent anisotropic components that can be described using Legendre polynomials ($P_n(\cos\theta)$):

$$\omega_{\mathrm{Q}}^{(2)} \propto \frac{1}{\omega_0}[AP_0(\cos\theta) + BP_2(\cos\theta) + CP_4(\cos\theta)]$$

$$P_0(\cos\theta) = 1$$

$$P_2(\cos\theta) = \frac{1}{2}(3\cos^2\theta - 1) \qquad (3.58)$$

$$P_4(\cos\theta) = \frac{1}{8}(35\cos^4\theta - 30\cos^2\theta + 3)$$

where A, B and C are spin- and transition-dependent coefficients.[214] Half-integer spin systems experiencing a second order quadrupolar perturbation will exhibit a broadened CT due to the orientational dependence of $\omega_{\mathrm{Q}}^{(2)}$. The STs are also broadened by $\omega_{\mathrm{Q}}^{(2)}$, however, systems exhibiting second-order perturbations will inherently have very large values for $\omega_{\mathrm{Q}}^{(1)}$, broadening the STs often to the point where the CT becomes the only remaining feature of the spectrum that can be identified. Importantly, the isotropic component of the second order quadrupolar coupling contributes towards δ_{iso} alongside the contribution of magnetic shielding.

3.3.4 Bulk magnetic susceptibility effects

Magnetic susceptibility, χ, is a dimensionless quantity that describes the magnetic response of a material when under an applied field. For samples where $\chi \neq 0$, a net magnetisation, $\boldsymbol{M}$, is induced within the material that is proportional to the applied field, $\boldsymbol{H}_0$.[216] The magnetisation of the material is either diamagnetic ($\chi < 0$) or paramagnetic ($\chi > 0$) and is given by:

$$\boldsymbol{M} = \boldsymbol{\chi}_{\mathrm{V}} \cdot \boldsymbol{H}_0 \tag{3.59}$$

where $\boldsymbol{\chi}_{\mathrm{V}}$ is the volume susceptibility tensor. A simplified model (**Figure 3.14**) is adopted here to discuss the effect of the bulk magnetic susceptibility (BMS) on an observed nucleus within a magnetically susceptible sample where $\boldsymbol{\chi}_{\mathrm{V}}$ is isotropic.[217–219]

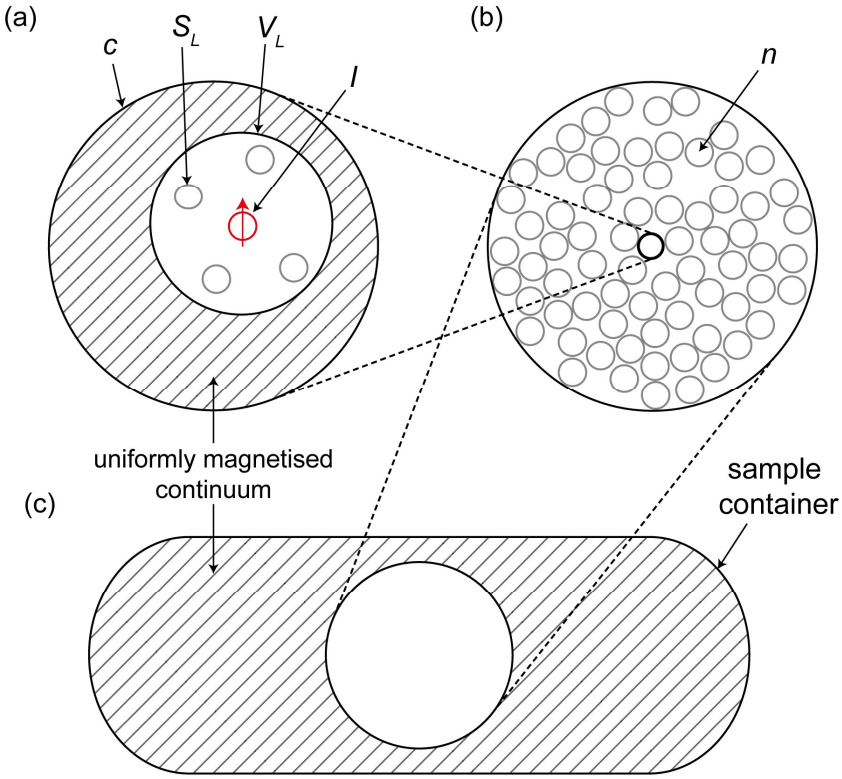

Figure 3.14. Model of a polycrystalline sample comprising spherical crystallites, based on the model by Kubo *et al*. (Ref. [217]). (a) A crystallite, *c*, of volume V_C containing the observed nucleus, *I*, is shown. A Lorentz sphere, V_L, is defined about the nucleus containing neighbouring magnetic centres, S_L. The magnetic susceptibility of the region outside of *I* and S_L, and inside V_L is assumed to be zero. The remainder of the crystallite is modelled as a uniformly magnetised continuum that contributes an intra-particle BMS shielding contribution. (b) *n* neighbouring crystallites are illustrated within a second Lorentz sphere. The neighbouring crystallites are considered as point dipoles, $\boldsymbol{\mu}_n$, that interact with *I* via dipolar coupling. (c) This sphere is sufficiently large as to converge the interactions across its volume. The remainder of the sample is considered uniformly magnetised, giving an inter-particle BMS shielding contribution.

Assume that the observed nucleus, I, exists within a spherical crystallite, c, of uniform $\boldsymbol{\chi}_{\mathrm{V}}$ at the position $\boldsymbol{r}$. A spherical region, termed the Lorentz sphere,[220] V_L, is then defined about I with dimensions substantially smaller than the crystallite volume, V_c, yet sufficiently large as to converge the shielding interactions from adjacent magnetic centres, S_{L}, within the Lorentz

sphere to a single term, $\boldsymbol{\sigma}_{\mathrm{L}}$. The remaining volume of V_{c} surrounding V_{L} is then subdivided into i spherical volumes, V_i, that are uniformly-magnetised, each inducing a magnetic dipole moment, $\boldsymbol{\mu}_i$, when under an applied field as defined by:[221]

$$\boldsymbol{\mu}_i = V_i \cdot \boldsymbol{M} \tag{3.60}$$

The first term of the BMS effect is the sum of the dipolar interaction between the nucleus and $\boldsymbol{\mu}_i$.[216,219] The projection along $\boldsymbol{H}_0$ of the demagnetising dipolar field, $\boldsymbol{h}_{\mathrm{D},i}$, due to $\boldsymbol{\mu}_i$ evaluated at the nucleus is given by:

$$h_{\mathrm{D},i} = \frac{\mu_i}{|\boldsymbol{r} - \boldsymbol{r}_i|^3}(3\cos^2\theta_i - 1) \tag{3.61}$$

where μ_i is the magnitude of the magnetic dipole, $|\boldsymbol{r} - \boldsymbol{r}_i|$ is the distance from the nucleus to the centre of V_i, and θ_i is the angle between the nucleus-dipole vector and $\boldsymbol{H}_0$.[221–223] $h_{\mathrm{D},i}$ can be defined for each point across the particle, with the sum of these terms defining the shape-dependent contribution to the demagnetising field experienced by the nucleus, $\boldsymbol{H}_{\mathrm{D}}(\boldsymbol{r})$, that modifies the Larmor frequency.[216,220,221,224] For spherical particles that are uniformly magnetised, $\boldsymbol{H}_{\mathrm{D}}(\boldsymbol{r})$ is homogenous and orientationally independent.[225] For ellipsoidal geometries, $\boldsymbol{H}_{\mathrm{D}}(\boldsymbol{r})$ is homogenous, but dependent upon the orientation of $\boldsymbol{H}_0$. In both instances, the nucleus experiences an intra-particle BMS shift due to $\boldsymbol{H}_{\mathrm{D}}(\boldsymbol{r})$, but no line broadening. Homogenously magnetised samples of arbitrary shape exhibit an inhomogeneous, orientationally dependent $\boldsymbol{H}_{\mathrm{D}}(\boldsymbol{r})$, giving rise to a BMS shift and line broadening that are dependent upon the particle alignment relative to $\boldsymbol{H}_0$.[226] For a powdered sample of non-spherical particles, the intra particle BMS effect causes an inhomogeneous broadening due to the random orientation of the crystallites.

The long-range component of the BMS effect (*i.e.,* inter-particle interactions) can be considered analogously to intra-particle interactions. This component is treated as the sum of inter-particle dipolar interactions, where adjacent particles are considered as point dipoles (assuming a sufficiently large distance from the nucleus) (Equation 3.60). As with the intra-particle BMS interaction, a Lorentz sphere is defined about the initial particle, within which the dipolar contributions from n adjacent particles converge, giving $\boldsymbol{\sigma}_n$. The remaining particles outside the Lorentz sphere that make up the sample volume, k, are considered as point dipoles, $\boldsymbol{\mu}_k$, each inducing a demagnetising field. The components of the induced dipolar fields

projected along the applied field, $h_{\mathrm{D},k}$, are summed to give the inter-particle BMS interaction.[219] This is effectively achieved by treating the remaining volume outside of the Lorentz sphere as a magnetic continuum. The inter-particle BMS effect results in a variation of the demagnetising field throughout a non-spherical particle regardless of sample homogeneity. This variation is dependent upon the position within the sample, the $\boldsymbol{\chi}_{\mathrm{V}}$ of the crystallite, and the sample orientation relative to $\boldsymbol{H}_0$.[219] Practically, polycrystalline samples typically comprise particles of myriad geometries, volumes, and orientations. As such, significant BMS line broadening is expected, giving lineshapes resembling a complex amalgamation of powder-pattern-like features that changes with sample orientation.[222,223,227]

Thus far, only isotropic $\boldsymbol{\chi}_{\mathrm{V}}$ systems have been discussed; however, it is common for $\boldsymbol{\chi}_{\mathrm{V}}$ to be anisotropic ($\Delta\boldsymbol{\chi}_{\mathrm{V}}$). A typical example of susceptibility anisotropy is found in aromatic systems, in which the ring current induces a stronger magnetic field when the ring-plane is perpendicular to the applied field as opposed to when it is parallel ($\chi_{\perp} > \chi_{\parallel}$). $\Delta\boldsymbol{\chi}_{\mathrm{V}}$ introduces further broadening within polycrystalline samples as the strength of the magnetic moment exhibits an additional orientational dependence with respect to the applied field.[216,221,228] It is therefore useful to separate $\boldsymbol{\sigma}_{\mathrm{BMS}}$ into two components, an isotropic BMS term ($\boldsymbol{\sigma}_{\mathrm{IBMS}}$), characterised by the mean of the principal values, and an anisotropic BMS term ($\boldsymbol{\sigma}_{\mathrm{ABMS}}$), described by the deviation from the mean. For solutions, BMS broadening is typically very small (< 1 Hz) due to isotropic motional averaging, and in solids the broadening from other interactions (*e.g.*, CSA and quadrupolar coupling) often eclipses broadening arising from susceptibility effects. However, for static solutions within susceptible solids of varying geometries, and for suspensions of disordered solids, the shifts and broadening due to BMS can be significant when studying the nuclei of both solvent and solutes.[29,31,209]

3.4 Experimental techniques in NMR spectroscopy

3.4.1 Magic angle spinning

For solution-state NMR spectroscopy, many of the interactions discussed above are isotropically averaged due to fast molecular tumbling. For solids, however, the orientational dependencies of the CSA, dipolar coupling, scalar coupling, first-order quadrupole interactions, and BMS interactions give complex resonances that are often difficult to interpret. Fortunately, the anisotropic contributions of these interactions exhibit the same $3\cos^2\theta - 1$ (*i.e.,* the second Legendre polynomial) orientational dependence relative to the alignment of

the applied field. By setting θ to 54.736°, or the magic angle, the orientational dependency term cancels out, effectively averaging out anisotropic nuclear interactions. Rapidly spinning a sample about an axis of rotation, θ_R, set to 54.736° from $\boldsymbol{B}_0$ (**Figure 3.15**) ensures that the average crystallite orientation is at the magic angle:[204]

$$\frac{1}{2}(3\cos^2\theta - 1) = \frac{1}{2}(3\cos^2\theta_R - 1)(3\cos^2\beta - 1) \qquad (3.62)$$

For effective averaging of anisotropic interactions, the spinning speed of the sample must exceed the magnitude of the interaction. If this condition is not met, the interaction will not be fully averaged out, resulting in a powder pattern lineshape with spinning sidebands. These sidebands will be spaced at integer multiples of the spinning frequency from the isotropic chemical shift

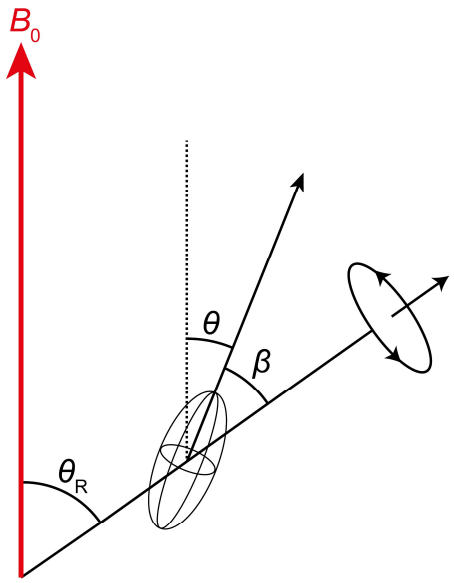

Figure 3.15. Schematic of angles relevant to magic angle spinning (MAS). θ_R is the angle at which the sample is rotated.

Commercial magic angle spinning (MAS) rotors are available in a range of sizes, with smaller internal volumes exhibiting faster spinning rates. Typical spinning speeds range between 5-30 kHz, values less than the frequencies of the first-order quadrupole interaction (several MHz), dipolar interactions between "high-gamma" nuclei (*e.g.,* ^{1}H and ^{19}F homonuclear coupling, where $d_{ij}^{PAS} > 30$ kHz)[210], and high field CSA interactions for high-electron count nuclei (*e.g.,* ^{195}Pt, ^{207}Pb, and ^{117,119}Sn).[203] Consequently, these interactions are only partially averaged by MAS. Furthermore, the second order quadrupolar interaction is only partially dependent upon

the second Legendre polynomial, with the remaining components persisting during MAS experiments leading to a partial averaging.[215]

As detailed in section 3.3.4, IBMS interactions arising from particle and sample shape, and interparticle interactions for particles of arbitrary geometries, can be treated analogously to magnetic dipole-dipole interactions of a fixed magnitude. As such, MAS averages out IBMS line broadening.[221,222] For samples with anisotropic susceptibilities (*e.g.,* aromatic molecules, where $\chi_{\perp} > \chi_{\parallel}$ due to ring current-induced fields), the strength of the dipole moment is dependent upon the orientation of the susceptibility tensor relative to the applied field. Consequently, isotropic reorientation from MAS fails to average ABMS interactions to zero and the line broadening from this interaction persists.[221]

3.4.2 Decoupling

On occasion, the strength of a dipolar coupling may be greater than the MAS spinning rate, preventing the interaction from being averaged out. Fortunately, both heteronuclear and homonuclear inter-nuclear couplings (both dipolar and scalar) can be removed through decoupling. For two coupled nuclear spins, I and S, the magnetic field perturbation generated by all neighbouring S nuclei upon I can be averaged by continually flipping the orientations of S. This continual motion effectively averages out the populations of the S spins aligned and anti-aligned with $\boldsymbol{B}_0$ resulting in a single averaged perturbation experienced by I, effectively decoupling I from S. For heteronuclear nuclei, the simplest way to decouple the nuclei is by applying a continuous radio-frequency wave (CW) at the Larmor frequency of the nucleus that is not being observed.[210,229,230] Practically, for a simple decoupling 90° pulse-acquire experiment observing the nucleus I that is coupled to S, a 90° pulse is applied that perturbs I, then during its subsequent FID, a continuous wave at the Larmor frequency of S is applied as the FID of I is recorded (**Figure 3.16a**). An alternative approach is to use a two-pulse phase modulation (TPPM)[231,232] decoupling pulse, a technique developed due to inherent losses in decoupling efficiency at high MAS when using CW.[232–234] TPPM decoupling comprises a train of pulses of equal magnitude, but with alternating phase sign (**Figure 3.16b**). Homonuclear decoupling provides a greater challenge than heteronuclear decoupling as the observed nucleus can easily be affected by the decoupling *r.f.* pulse targeting the coupled nucleus, effectively perturbing the observed nuclei during the acquisition of the FID. Homonuclear decoupling experiments therefore use weaker, more selective pulses in conjunction with complex

decoupling sequences, in which brief windows are included where the decoupling pulse is stopped, allowing the FID to be recorded.

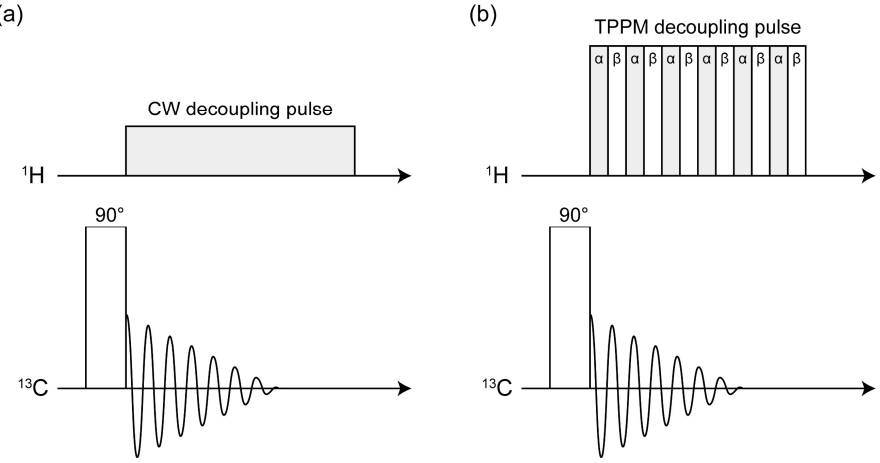

Figure 3.16. Schematics for simple experiments that acquire ^{1}H-decoupled ^{13}C spectra using (a) a continuous wave (CW) decoupling pulse and (b) a two-pulse phase modulation (TPPM) pulse train. In the TPPM train, a shallow offset angle is defined (*e.g.,* 15°), and pulses α and β apply this offset with alternating phase.

3.4.3 Cross-polarisation

Cross-polarisation (CP)[235] experiments are routinely used to greatly increase the sensitivity of low-γ, low abundance nuclei, I, that are coupled to high-γ, high abundance nuclei, S. This enhancement is achieved via a transfer of magnetisation from I onto S that is mediated by the dipolar interaction. Notably, aside from poor sensitivity, low-γ nuclei exhibit longer T_1 relaxation times as the dipolar interaction, which is inherently weak for these systems, heavily contributes towards the rate at which the net magnetisation realigns with the applied field.[204] The transferral of magnetisation from I to S effectively causes the necessary recycle delay to depend on the T_1 for I and not the T_1 for S, greatly reducing the recycle delay and allowing a greater number of transients to be recorded within a given time. CP experiments begin with an initial 90° pulse applied to I, which if we assume is about the y-axis, results in a detectable magnetisation along the x-axis. Immediately following this, an *r.f.* pulse is applied along the x-axis, suppressing the free evolution of transverse magnetisation and effectively 'locking' the magnetisation of I along $\boldsymbol{B}_1$. This field is referred to as a spin-locking pulse. Using a second frequency channel, a second spin-locking pulse is applied along the x-axis at the frequency of S for the same duration as the spin-locking pulse upon I, the duration of which is termed the contact time (CT). Once both spins are locked along the same axis, magnetisation transfer can occur via dipolar coupling (**Figure 3.17**).

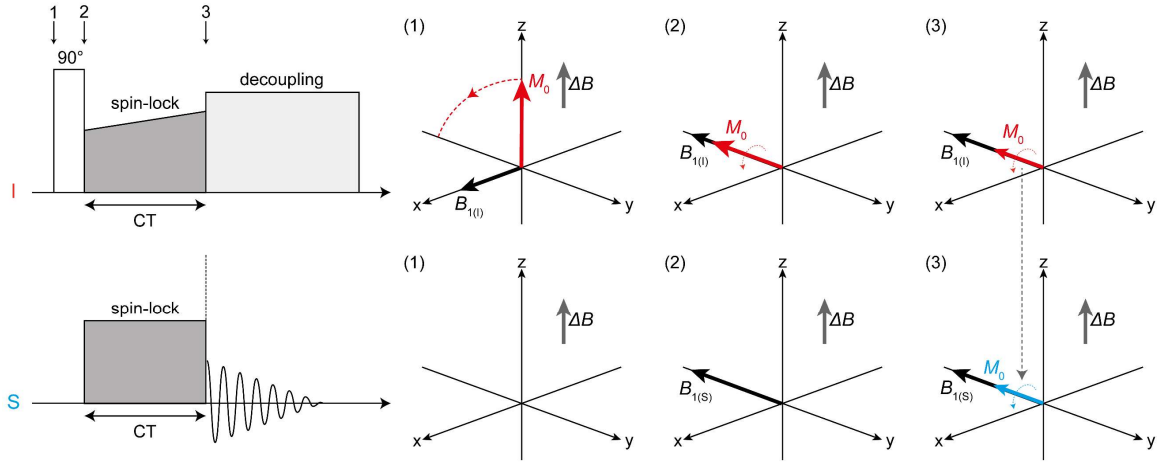

Figure 3.17. The pulse sequence for the cross-polarisation (CP) experiment. A 90° excitation pulse is applied along the *x*-axis, followed by a spin-lock pulse along the −*y*-axis. A gradient amplitude spin-lock pulse is shown for nucleus *I*. Illustrations of the vector model depiction of the net magnetisation for *I* (in red) and *S* (in blue) are shown. The equilibrium magnetisation for the low abundance nuclei is not shown for the sake of simplicity.

For static samples, the Hartmann-Hahn condition must be met for optimal magnetisation transfer during CT:[236,237]

$$\begin{aligned} \omega_{1I} &= \omega_{1S} \\ \gamma_I B_{1I} &= \gamma_S B_{1S} \end{aligned} \tag{3.63}$$

For experiments combining MAS and CP, the magnetisation transfer is affected by the time-dependence of dipolar coupling, modifying the Hartmann-Hahn condition:[238]

$$\begin{aligned} \omega_{1I} &= \omega_{1S} \pm n\omega_R \\ \gamma_I B_{1I} &= \gamma_S B_{1S} \pm n\omega_R \end{aligned} \tag{3.64}$$

where ω_R is the MAS rate and n is an integer (typically, $n = 1$ or 2). It is common practice for a decoupling pulse to be applied to I during the acquisition of the FID of S as to prevent broadening from heteronuclear dipole-dipole couplings. A ramped amplitude spin locking pulse is also typically used for I as to satisfy the matching conditions for a range of crystallites within polycrystalline solids.[239] As magnetisation transfer during the CT is mediated by the heteronuclear dipolar interaction, the extent of cross-polarisation is dependent upon inter-nuclear distances. As such, CP experiments are non-quantitative, as the intensity of the resonance is proportional to the magnitude of the dipolar coupling. However, the distance-

dependence of the magnetisation transferral provides valuable insight into structural properties and dynamical behaviour.

3.4.4 Spin echo experiments

Another essential building block in NMR pulse sequences is the Hahn echo or spin echo experiment.[240] Here, spins are initially perturbed following a 90° pulse to generate transverse magnetisation. Following perturbation, the individual spins precess about $\boldsymbol{B}_0$ according to their individual offset frequencies, Ω, determined by individual spin interactions.

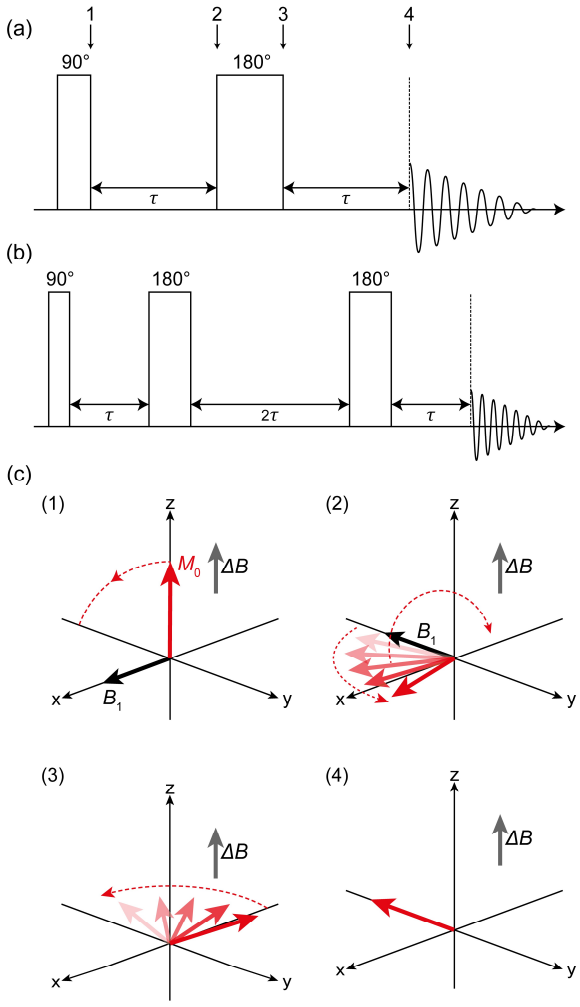

Figure 3.18. The pulse sequences for the (a) Hahn-echo and (b) a double-echo experiment. (c) Illustrations of the vector model description of the net magnetisation at different time intervals within the Hahn-echo experiment. At time interval (1), the magnetisation is tipped 90°, generating transverse magnetisation. Immediately following the pulse differences in precessional frequencies causes decoherence of the transverse magnetisation. After a time-delay of τ (2), an inversion pulse is applied, flipping the transverse magnetisation by 180° (3). After another time delay of τ (4) the spins regain coherency, and the FID is acquired. The double-echo experiment repeats the inversion pulse 2τ after the initial inversion pulse with acquisition after a further delay equal to τ.

Over a given period, referred to as the delay time, τ, the different offset frequencies will result in phase differences given by Ω/τ and an overall loss of transverse magnetisation. A 180° inversion pulse is then applied, changing the phase of the spins to $(2\pi - \Omega/\tau)$, which after τ, will result in a refocussing of the spins along the magnetisation vector following the initial 90° pulse (*i.e.,* phase of 2π, or 0) (**Figure 3.18**).[205,207]

For a simple 90° pulse-acquire experiment, a delay must be left between the acquisition of the FID and the excitation pulse as to avoid detecting a transient response in the receiver coil from the excitation *r.f.* pulse (*i.e.,* allowing the coil to "ring down"). This delay prevents acquisition of the FID immediately following excitation, leading to a loss of signal intensity, and potentially leading to a distortion of the baseline. The Hahn echo experiment circumvents these issues, as the receiver delay is effectively included within the second τ delay following the excitation pulse.[204] Another advantage of the Hahn echo experiment is that it is selective, with resonances correlated with spins flipped by an angle $\neq$ 90° being suppressed as they are not refocussed by the inversion pulse. This is particularly useful for suppressing background noise as nuclei outside the centre of the *r.f.* coil experience a weaker B_1 due to its field inhomogeneity and are subsequently perturbed by shallower flip angles. By performing a series of inversion pulses (*e.g.* double-echo experiments or the DEPTH experiment[241,242]) the selectivity towards spins perturbed by a true 90° flip angle is enhanced. Notably, not all spins regain coherence due to transverse relaxation, resulting in a slight loss of signal compared to a simple 90° excitation experiment, a theme discussed in the next section.

3.4.5 Relaxometry

The spin-lattice relaxation constant, T_1, is conventionally measured by an inversion recovery experiment,[243,244] or a saturation recovery experiment.[245,246] Inversion recovery experiments 'invert' the bulk magnetisation by perturbing it with a 180° excitation pulse and then allow it to return to thermal equilibrium over a recovery period, τ_R. A 90° excitation pulse is then applied, transferring the 'recovered' magnetisation onto the *xy*-plane, with the recorded signal intensity being given by:

$$S(\tau_R) = S_0\left(1 - 2e^{-\frac{\tau_R}{T_1}}\right) \tag{3.65}$$

where S_0 is the signal intensity following a total relaxation of the bulk magnetisation. T_1 values can be estimated by performing measurements with varying τ_R values and constructing a plot

of $S(\tau_R)$ against τ_R and fitting it to Equation 3.65 (**Figure 3.19**). Inversion recovery experiments require $\tau_R \geq 5T_1$ as to allow $\geq 99.3\%$ of the magnetisation to return to thermal equilibrium between each transient. As such, inversion recovery experiments are impractical when observing nuclei with long T_1 values (*e.g.,* solids or small molecules with fast tumbling rates). Saturation recovery experiments overcome this limitation as the bulk magnetisation is forced into an isotropically distributed (or 'saturated') state prior to the recovery period through the application of a train of 90° excitation pulses with alternating phase. As the magnetisation does not need to return to thermal equilibrium prior to signal acquisition, the recycle delay can be set to 0, although care must be taken not to overheat the coil as the train is applied. The signal recovery in a saturation recovery experiment is given by:

$$S(\tau_R) = S_0\left(1 - e^{-\frac{\tau_R}{T_1}}\right) \tag{3.66}$$

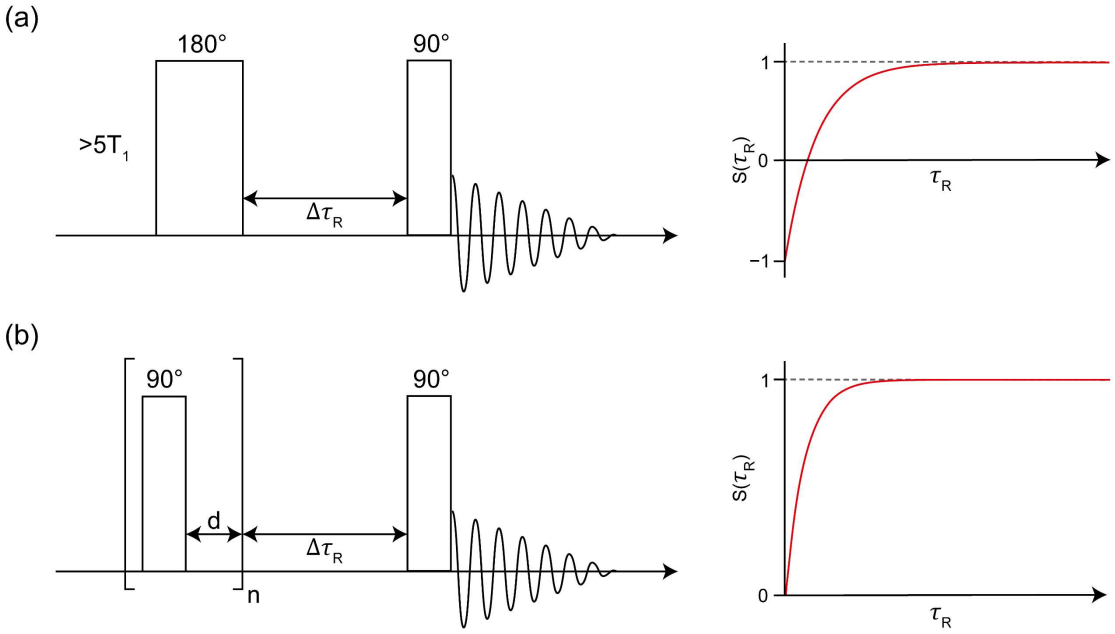

Figure 3.19. Pulse sequences for the (a) inversion recovery and (b) saturation recovery experiments. Corresponding fits for the signal intensity as a function of recovery time are also illustrated, with (a) and (b) fitting to Equations 3.65 and 3.66, respectively.

To measure the spin-spin relaxation constants, inhomogeneous contributions towards the decoherence of transverse magnetisation, T_2^i, (*e.g.,* an inhomogeneous applied field and/or distribution of chemical shifts) must be separated from homogenous contributions, T_2 (*e.g.,* dynamical, electronic, and internuclear coupling effects). The overall observed spin-spin relaxation constant, T_2^*, is a combination of these two contributions, given by:[204,206]

$$\frac{1}{T_2^*} = \frac{1}{T_2} + \frac{1}{T_2^i} \tag{3.67}$$

Notably, decoherence due to T_2^i is dependent upon the location of the nucleus within the inhomogeneous applied field. If it can be assumed that the nucleus exists within the same inhomogeneous region of the field throughout the experiment, the inversion pulse of the Hahn echo experiment will fully recover the dephasing due to T_2^i. Importantly, the signal lost from decoherence due to T_2 relaxation will not be recovered by the inversion pulse. T_2 can therefore be measured by performing Hahn echo experiments with varying delay times, τ, and plotting the recorded signal intensity against τ (**Figure 3.20**).

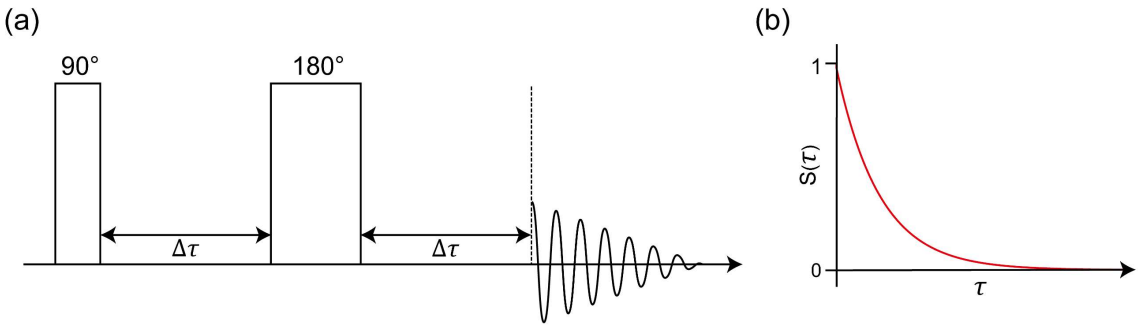

Figure 3.20. (a) Pulse sequences for the variable delay Hahn echo experiment for the measurement of spin-spin relaxation constants. (b) Simulated fit to Equation 3.68, showing the decay of signal intensity as the delay time increases.

Due to further factors inducing decay during an echo experiment, such as diffusion within an inhomogeneous field or homonuclear dipolar coupling, the true value of T_2 (*i.e.*, true random non-reversible relaxation) is practically impossible to measure in solids. Thus, an approximated value, T_2', is instead determined by fitting experimental data to:[207]

$$S(\tau) = S_0 e^{-\frac{\tau}{T_2'}} \tag{3.68}$$

The spin-lattice relaxation time constant for the decay of the spin-locked magnetisation vector aligned along the weak $\boldsymbol{B}_1$ field in the rotating frame of reference back towards its equilibrium state aligned along the effective field, $\boldsymbol{B}_0$, is denoted by $T_{1\rho}$. $T_{1\rho}$ values for high-γ nuclei, $T_{1\rho}^I$, are typically measured by an experiment comprising a 90° excitation pulse followed by a spin locking pulse of incremental durations, τ, and recording the FID signal intensity as a function

of τ (**Figure 3.21**).[204,247] $T_{1\rho}^{I}$ is then derived by fitting an equation analogous to that used to derive T_2 (Equation 3.68):[204]

$$S(\tau) = S_0 e^{-\frac{\tau}{T_{1\rho}}} \tag{3.69}$$

where S_0 is the signal intensity recorded when $\tau = 0$.

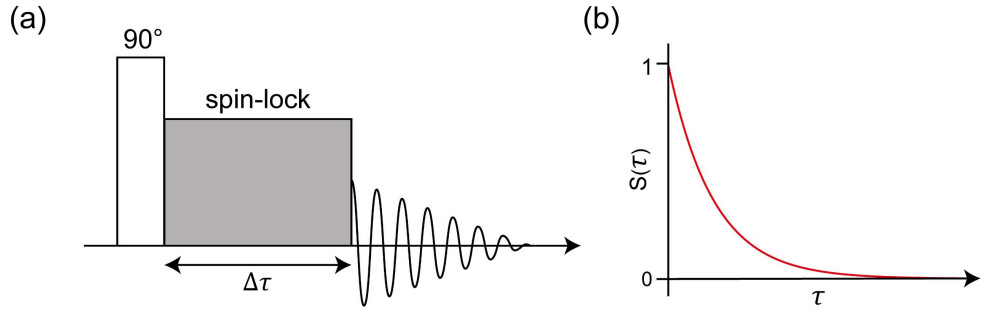

Figure 3.21. (a) Pulse sequence of a simple experiment to measure $T_{1\rho}$ where the duration of the spin-lock pulse, τ, is varied. (b) Simulated fit to Equation 3.69, showing the decay of signal intensity as the spin-lock pulse duration increases.

3.4.6 Chemical exchange averaging in NMR

Nuclei that exhibit considerable mobility between distinct magnetic environments within the timescale of NMR measurements can exhibit significant perturbations in their resonance lineshape. Consider a simple two-site exchange system, in which nuclear spin systems may exchange between two chemical environments, A and B, and the exchange rate for the forward (A → B) and reverse (B → A) processes are denoted by k_1 and k_{-1}, respectively. The free precession of transverse magnetisation following excitation, $M_{xy}(t)$, (and by extension the FID signal decay, $S(t)$) can be described for a single site as a Bloch equation (Equation 3.35).[248] This can be extended to an isolated two-site system, in which the nuclei remain in their individual sites (A or B), with the transverse magnetisation of the two sites being given by:[249]

$$M_{xy}(t) = M_{xy}^{\mathrm{A}}(0) e^{i\Omega_{\mathrm{A}} t} e^{-\frac{t}{T_{2,\mathrm{A}}}} + M_{xy}^{\mathrm{B}}(0) e^{i\Omega_{\mathrm{B}} t} e^{-\frac{t}{T_{2,\mathrm{B}}}} \tag{3.70}$$

where T_2 is the spin-spin relaxation constant, and Ω_{A} and Ω_{B} are the offset frequencies within the rotating frame at sites A and B, respectively. For an ensemble of spin-systems exchanging between inequivalent magnetic environments (A and B), when a spin-system 'hops' from A to

B it will precess at a different rate to the spins remaining in site A (*i.e.,* $\Omega_A \neq \Omega_B$) (**Figure 3.22a**). When the spin returns to site A, it is out of phase with the ensemble that remained exclusively within site A. The decoherence of the transverse magnetisation is therefore dependent upon both the spin-spin relaxation rates of the distinct sites, and the exchange rate between the two sites. The adapted Bloch-McConnell equation introduces the 'hopping' between sites A and B using kinetic rate equations for the exchange process. By defining site A as the reference frame ($\Omega_A = 0$) and $\Delta\Omega$ as $\Omega_B - \Omega_A$, the free precession of transverse magnetisation including chemical exchange is given by:[250–252]

$$M_{xy}(t) = M_{xy}^{A}(0)e^{\left(-\frac{1}{T_{2,A}} - k_1\right)t} + M_{xy}^{B}(0)e^{\left(i\Delta\Omega - \frac{1}{T_{2,B}} - k_{-1}\right)t} \tag{3.71}$$

In the slow regime, where the spins predominantly exist within either site A or site B, and $k_{ex} \ll |\Delta\Omega|$ (where $k_{ex} = k_1 + k_{-1}$), two defined resonances at Ω_A and Ω_B are observed. Assuming that $k_1 = k_{-1}$, the linewidth broadening due to chemical exchange in the slow regime, W_S, is given by:

$$W_S = \frac{k_1}{\pi} = \frac{1}{\pi\tau_1} \tag{3.72}$$

where τ_1 is the average lifetime of the spin at a given site. When $k_{ex} \gg |\Delta\Omega|$, the fast exchange causes the spins to experience an effective local field, determined by the relative fractional populations, p, at the two sites ($\Omega_{avg} = p_A\Omega_A + p_B\Omega_B$).

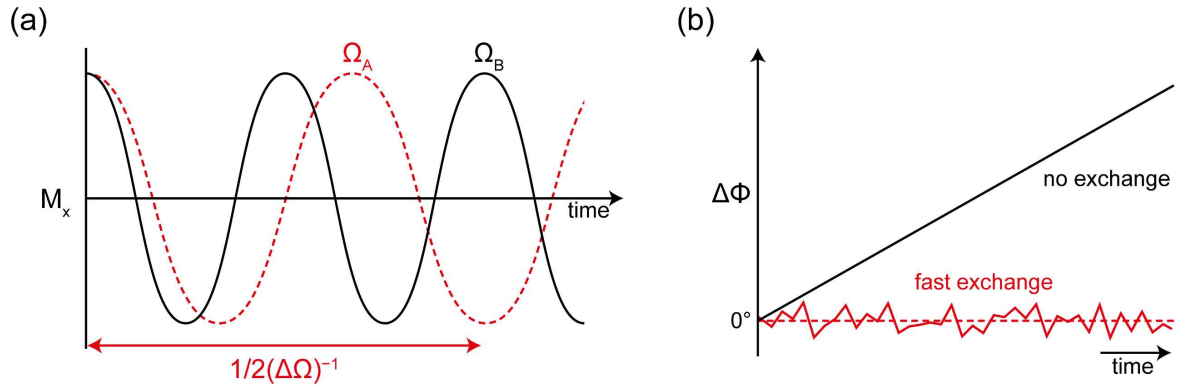

Figure 3.22. (a) The accumulation of phase difference between spins in site A and B. Separate signals from sites A and B are only detected provided an appreciable phase difference, ΔΦ, is built. (b) Time dependence of ΔΦ for spins undergoing fast chemical exchange and in the absence of chemical exchange. Under fast exchange an average ΔΦ of 0° is observed, giving a resonance peak at one frequency value in the NMR spectrum.

The extent of spin dephasing due to chemical exchange decreases as k_{ex} increases beyond $|\Delta\Omega|$, as when chemical exchange occurs, $\Delta\Omega$ changes sign, and the accumulation of phase difference, $\Delta\Phi$, reverses (**Figure 3.22b**).[207] Therefore, if exchange is occurring before an observable $\Delta\Phi$ is measured, the averaging between the two sites becomes more complete, and a single resonance is observed (**Figure 3.23**).

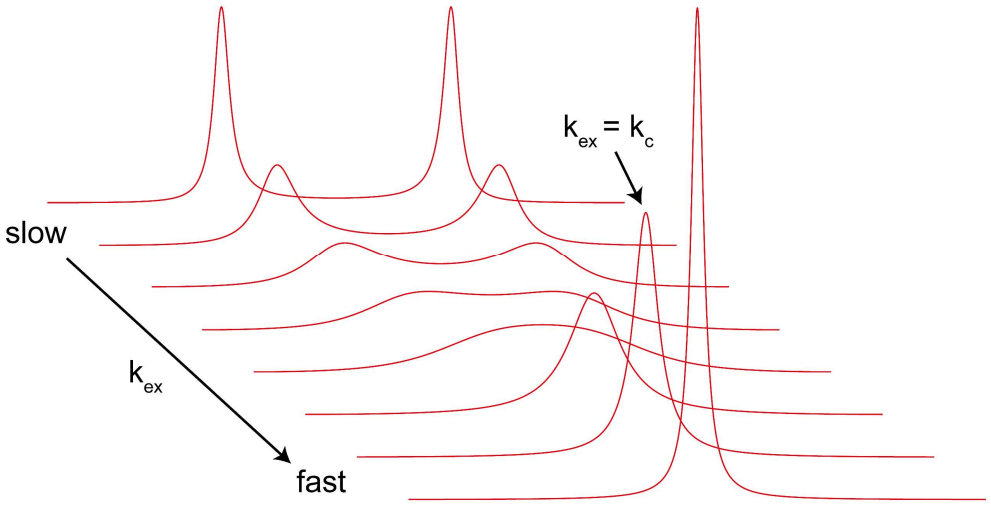

Figure 3.23. Simulated NMR spectra for a pair of nuclei undergoing chemical exchange between two sites. The exchange rate, k_{ex}, between the two sites increases from top to bottom and the spectra where $k_{ex} = k_c$ is indicated.

The broadening due to chemical exchange in the fast regime, W_F, is determined by:

$$W_F = \frac{\pi|\Delta\Omega|^2}{2k} \tag{3.73}$$

and the boundary between the slow-intermediate and intermediate-fast exchange regimes is defined by a coalescence rate, k_c, given by:[206]

$$k_c = \frac{\pi|\Delta\Omega|}{\sqrt{2}} \approx 2.2|\Delta\Omega| \tag{3.74}$$

where rates exceeding k_c are in the fast regime, and rates less than k_c are within the slow regime. At $k_{ex} = k_c$, a single broad resonance at Ω_{avg} is observed. As $\Delta\Omega$ is rarely larger than ~10kHz at high fields, only relatively slow exchange processes can be observed using NMR.[207] For asymmetric exchange systems, where either $k_1 \neq k_{-1}$ or $p_A \neq p_B$, the resonance lineshapes are unevenly broadened. If $p_A > p_B$ and $k_1 > k_{-1}$, the minor resonance (B) would

be significantly broader, as statistically, a larger proportion of species observed within site B during the measurement will have occupied site A and have experienced the dephasing effect.

3.4.7 Two-dimensional correlation experiments

One-dimensional (1D) NMR experiments have been discussed thus far, in which *r.f.* pulses are used to create transverse magnetisation, from which an FID is detected and subsequently Fourier transformed to give a one-dimensional spectrum in the frequency domain. Two-dimensional (2D) NMR experiments are a key subset of NMR techniques, where the resulting spectra are represented in two frequency domains, f_1 and f_2, with the signal intensity being displayed as a contour plot. Conventional 2D NMR experiments comprise four stages: (i) a preparation period, in which an excitation pulse is applied generating observable magnetisation, (ii) an evolution period, t_1, during which the magnetisation freely precesses, (iii) a mixing period, in which the magnetisation that has evolved during t_1 is transferred to neighbouring interacting spins via a series of *r.f.* pulses and delays, and (iv) a detection period, during which the FID of the magnetisation is detected in the second time dimension, t_2. The evolution during t_1 is indirectly observed in t_2 as the initial intensity of the NMR signal at the beginning of detection period is modulated by both the free evolution during t_1 and during the mixing period, t_m. As such, the evolution of the signal in the indirect dimension is measured by repeating the experiment with incrementally increasing values of t_1. A two-dimensional Fourier transformation is then performed, giving a 2D NMR spectrum in which cross-peaks are seen for spin pairings that have undergone a transferral of magnetisation during the mixing step. Care must be taken when setting up 2D NMR experiments due to the extensive quantities of data and long acquisition times associated with recording data for an indirect dimension, hence minimal spectral widths and sampling of the FID are often recommended. Another important consideration is that the indirect dimension does not filter out frequencies outside of the spectral width (unlike direct dimensions, in which filters suppress these frequencies), but instead will 'fold' the resonances around back onto the spectra. Hence, for 2D MAS NMR experiments, it is important that the spectral width of the indirect dimension is a multiple of the spinning rate so that the spinning sidebands lie atop the centreband.

3.4.7.1 Two-dimensional exchange spectroscopy (EXSY)

The dynamic exchange of nuclei between distinct magnetic environments can be indirectly observed using 2D exchange spectroscopy (EXSY) NMR experiments.[253,254] Conventionally,

a 90° excitation pulse is applied to generate transverse magnetisation followed by an evolution period of t_1. A second 90° pulse is then applied, returning the remaining transverse magnetisation back along the z-axis, where the magnetisation is stored for a mixing period, t_m, during which exchange between different sites occurs. A final 90° pulse is then applied to generate observable transverse magnetisation that is detected in t_2 (**Figure 3.24**).

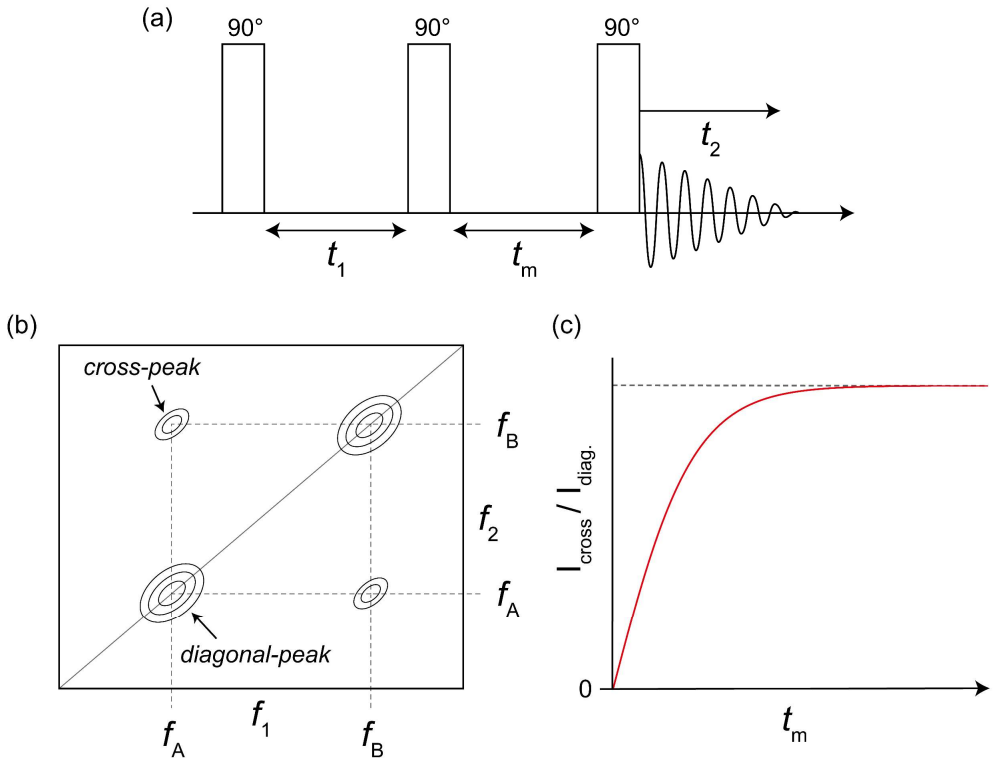

Figure 3.24. Pulse sequences for (a) a 2D EXSY experiment. (b) Illustration of a 2D NMR spectra produced from an EXSY experiment. (c) Simulated fit of Equation 3.75 used for the determination of the kinetic rate of exchange for the measured exchange process from the EXSY experiment.

Species that do not undergo chemical exchange will precess at identical frequencies, giving $f_1 = f_2$ across the two frequency domains and the diagonal components of the Fourier transformed 2D spectra. Nuclei that undergo exchange during t_m will precess at different rates ($f_1 \neq f_2$).[255] By identifying cross-peaks in the 2D spectra, nuclei that undergo chemical exchange between magnetically distinct environments can be mapped.[204] For a simple two-site exchange model, the exchange rate, k_c, can be estimated by fitting the cross-peak/diagonal-peak integrals to:[16]

$$\frac{I_{\text{cross}}}{I_{\text{diag.}}} = \tanh(k_c t_m) \tag{3.75}$$

where I_{cross} is the cross-peak intensity and $I_{\mathrm{diag.}}$ is the diagonal-peak intensity. Typically, chemical systems comprise myriad environments and exchange rates. As such, fits containing numerous exchange rates have been modelled to better describe complex exchange processes within well-defined systems.[7,10]

3.5 Computational calculation of NMR parameters

NMR theory outlined thus far shows that the assignment of solid-state NMR spectra can pose significant challenges owing to the sheer quantity of anisotropic nuclear interactions. Typically, the elucidation of these complex spectra can be aided by computationally predicting NMR parameters for systems of interest and comparing these parameters to experimental spectra. To determine these parameters, the electronic structure and the energy of the system must be calculated. Many of these calculations are performed using density functional theory (DFT) to determine the electronic ground state of a system by solving the Schrödinger equation.

3.5.1 Electronic structure calculations

The time-independent Schrödinger equation takes the general form:

$$\hat{\mathcal{H}}\psi(\boldsymbol{r}) = E\psi(\boldsymbol{r}) \tag{3.76}$$

where $\hat{\mathcal{H}}$ is the Hamiltonian operator, E is the energy of the system and $\psi(\boldsymbol{r})$ is the wavefunction of the ground state. $\hat{\mathcal{H}}$ contains information regarding the kinetic, $\hat{T}$, and potential, $\hat{V}$, energies for all particles within a system and can be represented in atomic units as:[256]

$$\hat{\mathcal{H}} = \hat{T}_{\mathrm{e}} + \hat{T}_{\mathrm{n}} + \hat{V}_{\mathrm{en}} + \hat{V}_{\mathrm{ee}} + \hat{V}_{\mathrm{nn}} \tag{3.77}$$

where $\hat{T}_{\mathrm{e}}$ is the kinetic energy of the electrons, $\hat{T}_{\mathrm{n}}$ is the kinetic energy of the nuclei, $\hat{V}_{\mathrm{en}}$ is the potential energy of the attractive electrostatic nuclei-electron interactions, with $\hat{V}_{\mathrm{ee}}$ and $\hat{V}_{\mathrm{nn}}$ describing the potential energies of the repulsive electrostatic electron-electron and nuclei-nuclei interactions, respectively.[257] The $\hat{V}_{\mathrm{ee}}$ term is particularly problematic as the wavefunction of each electron cannot be determined independently; instead, it must be solved while simultaneously considering the wavefunctions of all other electrons. This interdependence creates a many-bodied problem that lacks a closed-form solution. However,

by implementing approximations and leveraging computational methods, meaningful and useful solutions can be obtained, providing valuable insights. Equation 3.77 can be simplified by decoupling the nuclear terms from the electronic terms using the Born-Oppenheimer approximation.[258] The approximation considers nuclei as stationary from the perspective of electrons, and electron motion as instantaneous from the perspective of the nuclei due to the significant differences between the mass (three orders of magnitude) of the nuclei and the electrons. Therefore, under the Born-Oppenheimer approximation, $\hat{T}_{\mathrm{n}} = 0$ and $\hat{V}_{\mathrm{nn}}$ does not need to be explicitly determined as it will not affect the electronic wavefunction. Thus, the electronic-Hamiltonian, $\hat{\mathcal{H}}_{\mathrm{e}}$, can be defined by:

$$\hat{\mathcal{H}}_{\mathrm{e}} = \hat{T}_{\mathrm{e}} + \hat{V}_{\mathrm{en}} + \hat{V}_{\mathrm{ee}} \tag{3.78}$$

The solution of the time-independent Schrödinger equation using $\hat{\mathcal{H}}_{\mathrm{e}}$ is the electronic wavefunction, ψ_{e}, giving the electronic energy of the system, E_{e}. Here, ψ_e is considered as a function of the electron positions. The electronic wavefunction corresponding to the lowest E_{e} is termed the ground state.[256] Notably, the wavefunction itself cannot be directly observed, but the probability that N electrons exist at a particular set of coordinates $(\boldsymbol{r}_1, \ldots, \boldsymbol{r}_N)$ can be measured, with the probability being given by $\psi_i^*(\boldsymbol{r})\psi_i(\boldsymbol{r})$.[259] A related quantity is the electron density, $\rho(\boldsymbol{r})$, which defines the probability of finding an electron at a position r, and is given by:

$$\rho(\boldsymbol{r}) = 2\sum_{i}^{N} \psi_i^*(\boldsymbol{r})\psi_i(\boldsymbol{r}) \tag{3.79}$$

where the factor of 2 accounts for electrons of opposing spin occupying the same electron wavefunction, as defined by the Pauli exclusion principle. Fundamental theorems by Kohn and Hohenberg showed that each unique configuration of atoms has a unique $\rho(\boldsymbol{r})$, and that the ground-state energy derived from the Schrödinger equation is a unique functional of $\rho(\boldsymbol{r})$.[260]. It was also shown that the electron density that minimises the energy of the overall functional is the true electron density that corresponds to the full solution of the Schrödinger equation. However, the precise form of the unique functional that accurately calculates E is unknown, with the electronic energy of the system being defined as:[256]

$$E(\psi_i) = E_{\mathrm{known}}(\psi_i) + E_{\mathrm{XC}}(\psi_i) \tag{3.80}$$

where E_{known} defines the energetic components that can be described analytically, comprising electron kinetic energies and the coulombic interactions for electron-nuclei, electron-electron, and electron-nuclei pairings. These interactions are typically referred to as "classical" interactions. The remaining term of the energy functional, E_{XC}, is the exchange-correlation functional which defines all quantum mechanical effects outside E_{known}, such as spin-related enhancements and reductions to the probability of electron-electron approach due to the Pauli exclusion principle.[261] Kohn and Sham showed that ψ_i, and by extension the energy of the ground state, can be determined by solving a set of single electron equations:[262]

$$\left[-\frac{\hbar}{2m}\nabla^2 + V_{en}(\boldsymbol{r}) + V_{\text{HT}}(\boldsymbol{r}) + V_{\text{XC}}(\boldsymbol{r})\right]\psi_i(\boldsymbol{r}) = \varepsilon_i\psi_i(\boldsymbol{r}) \tag{3.81}$$

where the first term is the kinetic energy of each electron, $V_{en}(\boldsymbol{r})$ is the potential due to electron-nuclei interactions, $V_{\text{HT}}(\boldsymbol{r})$ is the Hartree potential due to coulombic repulsion between the electron of interest and the electron density of the system, $V_{\text{XC}}(\boldsymbol{r})$ defines the exchange-correlation contributions, and ε_i is the orbital-energy of the particle state ψ_i. To determine the electronic energy of the system, $V_{\text{XC}}(\boldsymbol{r})$ must be approximated (see later) and an initial value of $\rho(\boldsymbol{r}')$ is predicted, giving a trial value of $V_{\text{HT}}(\boldsymbol{r})$ following:

$$V_{\text{HT}}(\boldsymbol{r}) = e^2\int\frac{\rho(\boldsymbol{r}')}{|\boldsymbol{r}-\boldsymbol{r}'|}d\boldsymbol{r}' \tag{3.82}$$

where e is the elementary charge. As the kinetic energy and $V_{en}(\boldsymbol{r})$ can be analytically determined, the single particle wavefunction, ψ_i, for the "guess" can be calculated following Equation 3.82. The corresponding electron density defined by the calculated ψ_i is then compared to the trial value and if the values are the same then the system is in the ground-state electron density and the total electronic energy can be calculated. If the trial $\rho(\boldsymbol{r})$ and calculated $\rho(\boldsymbol{r})$ are different then a new trial $\rho(\boldsymbol{r})$ is selected and the process is repeated until $\rho(\boldsymbol{r})$ becomes self-consistent.

For the self-consistency method to be successful in determining the ground-state energy of the system, an accurate approximation of $V_{\text{XC}}(\boldsymbol{r})$ must be used. The true form of $V_{\text{XC}}(\boldsymbol{r})$ is complex, comprising myriad quantum mechanical interactions as well as correcting the unphysical self-interaction component of $V_{\text{HT}}(\boldsymbol{r})$.[256] As such, $V_{\text{XC}}(\boldsymbol{r})$ is unknown for all systems besides a uniform electron gas, where the exchange-correlation functional can be derived quantitatively and is equivalent across all regions of space. The derived exchange-

correlation functional of a uniform electron gas allows the construction of approximations of $V_{\mathrm{XC}}(\boldsymbol{r})$ for real systems, with the simplest being the local density approximation (LDA). Here, $V_{\mathrm{XC}}(\boldsymbol{r})$ is approximated as that determined for a homogenous electron gas of equivalent electron density at each point in space. The implementation of the LDA approximation completely defines the Kohn-Sham equation, and the self-consistent determination of the ground state energy can be achieved. LDA can accurately describe regions in which $\rho(\boldsymbol{r})$ remains relatively consistent but cannot provide accurate information about regions close to nuclei. As such, many other exchange-correlation functionals have been constructed to better describe the electronic density of the system. Generalised gradient approximation (GGA) functionals use both the local electron density and the local gradient of electron density about a position in space, often providing a better approximation of $\psi_i(\boldsymbol{r})$. The inclusion of physical information beyond local electron density can take various forms, resulting in many unique functionals that yield slightly different ground-state properties. A commonly used GGA functional is the Perdew-Burke-Ernzerhof (PBE) functional.[263]

3.5.1.1 Basis sets and the planewave approach

The Kohn-Sham DFT approach enables the calculation of the electronic wavefunctions for a system. However, solving the Kohn-Sham equations becomes increasingly complex as the number of atoms and electrons grows. This challenge is particularly pronounced in extended systems with periodic structures, such as solids, where it becomes unfeasible to implement this approach to obtain a direct solution. Instead, for solids, the electronic wavefunctions are typically approximated as a linear combination of a set of predefined basis functions, ϕ_i:

$$\psi(\boldsymbol{r}) \approx \sum_{i=1}^{N} \alpha_i \phi_i(\boldsymbol{r}) \tag{3.83}$$

where α_i is the expansion coefficient. When using this approximation, the calculation of interest is now finding the values of α_i that define the electronic wavefunctions using the specified basis set of functions.[256] Basis sets are commonly constructed from a series of atom-centred atomic orbitals that are individually calculated, the linear combination of which defines the molecular orbitals. In practice, the molecular orbitals are commonly defined by a linear combination of Gaussian functions, vastly increasing computational efficiency.[264] The choice of basis set is system-dependent, with different basis sets providing increased accuracy and

efficiency. For solids, the large number of atomic orbitals in the system makes this approach inefficient. Instead, a non-localised planewave approach is typically utilised for periodic systems. Here, the primitive unit cell of the solid is defined with periodic boundary conditions. Importantly, the atomic positions and therefore the electron density, $\rho(\boldsymbol{r})$, is periodic, as described by Bloch's theorem.[265,266]

$$\rho(\boldsymbol{r}) = \rho(\boldsymbol{r} + \boldsymbol{R}) \tag{3.84}$$

where $\boldsymbol{r}$ is a position in real space and $\boldsymbol{R}$ is the product of the real lattice vector, a, and an integer. The electronic wavefunction of a periodic system can then be expressed as the product of a cell-periodic function and a planewave term:[267]

$$\psi_{n,\boldsymbol{k}}(\boldsymbol{r}) = e^{i\boldsymbol{k}\cdot\boldsymbol{r}} u_{n,\boldsymbol{k}}(\boldsymbol{r}) \tag{3.85}$$

where $u_{n,\boldsymbol{k}}$ is a periodic function with the same periodicity as the unit cell, $\boldsymbol{k}$ is the wave vector, which describes the spatial periodicity of the electron's wavefunction in reciprocal space, i represents the imaginary unit, and n indexes the n^{th} electronic state. The cell-periodic term, $u_{n,k}(\boldsymbol{r})$, can be expanded using a basis set comprising a discrete set of plane waves:[256,265]

$$u_{\boldsymbol{k}}(\boldsymbol{r}) = \sum_{\mathrm{G}} c_{\mathrm{G}} e^{i\mathbf{G}\cdot\boldsymbol{r}} \tag{3.86}$$

where the summation is over all reciprocal lattice vectors defined by $\mathbf{G} = m_1 b_1 + m_2 b_2 + m_3 b_3$, where b_n are primitive wavevectors for the reciprocal lattice, and m_n are integers. The set of vectors defined by $\mathbf{G}$ can also be represented in terms of the crystal lattice vectors in real space, $\boldsymbol{a_n}$, where $\mathbf{G} \cdot \boldsymbol{a_n} = 2\pi m_n$. The electronic wavefunction can therefore be defined by combining Equations 3.85 and 3.86, giving:[268]

$$\psi_{n,\boldsymbol{k}}(\boldsymbol{r}) = \sum_{\mathbf{G}} c_{\boldsymbol{k}+\mathbf{G}} e^{i(\boldsymbol{k}+\mathbf{G})\cdot\boldsymbol{r}} \tag{3.87}$$

where $c_{\boldsymbol{k}+\mathbf{G}}$ are Fourier coefficients of the reciprocal lattice vector. In principle, determining the wavefunction for a single 'k-point' involves the summation of an infinite number of planewaves across infinite primitive lattices due to the limitless nature of $\mathbf{G}$. In practice, a discrete selection of planewaves is made. The calculated kinetic energy, E_k, at $\boldsymbol{k}$ is given by:[256]

$$E_k = \frac{\hbar^2}{2m}|\boldsymbol{k} + \mathbf{G}|^2 \tag{3.88}$$

where m is the electron mass. The planewave basis set is truncated to include planewaves of kinetic energies less than a defined cut-off energy, E_{cut}. This introduces a finite number of planewaves at the cost of introducing error into the calculation of the total energy. Increasing E_{cut} increases the number of planewaves, which reduces error but incurs increased computational costs. However, as wavefunctions of higher kinetic energies hold less physical relevance, the total energy of the system will begin to converge to a stable value as E_{cut} is incrementally increased.[265,269] The electronic wavefunction and the true electron density of the system is given by the integral of all possible values of $\boldsymbol{k}$. However, determining the electronic wavefunctions for every value of $\boldsymbol{k}$ would be computationally expensive. Furthermore, many $\boldsymbol{k}$ values that are within close proximity to one another within reciprocal space will present similar electronic wavefunctions. As such, the general approach is to approximate the integral as a sum of select $\boldsymbol{k}$ values.

Markedly, $\psi_{\boldsymbol{k}}$ is unique only up to the reciprocal lattice, causing all unique values of $\boldsymbol{k}$ to exist within the reciprocal space of the primitive unit cell, the first Brillouin zone. Therefore, it is common practice when modelling solids for a finite selection of *k*-points to be sampled across a regularly spaced Monkhorst-Pack grid within the first Brillouin zone.[270] The calculated total energy is then determined for grids of increasingly dense *k*-point sampling until convergence is achieved. Ideally, an optimally converged *k*-point mesh density and cut-off energy are determined for each system of interest; however, it is often the case that chemically analogous systems are treated with generalised parameters to increase efficiency. Another consideration when defining the density of the *k*-point mesh is related to the change in total energy as a function of *k*-space, with sharp band structures (a hallmark of semiconductors and semi-metals) requiring fine meshes to accurately describe the electronic structure of the periodic system.[265,269]

A further complication that arises when considering materials with small band-gaps is the phenomenon of "band-sloshing", where states near the Fermi level shift above and below it between each iteration of the self-consistency field cycle, preventing convergence.[271,272] The simplest solution is to use extremely fine *k*-point matrices, although there is no variational principle governing the convergence of the total energy with respect to the *k*-point density.[273]

An alternative approach is to implement electronic smearing, in which a fictitious electronic temperature is applied that smooths the sharp discontinuity around the Fermi energy, improving sampling accuracy and reducing the number of required *k*-points.[271,274] It is important to note that DFT is fundamentally a ground-state theory, as such electronic temperature smearing should be viewed as a convergence parameter and should be reduced wherever possible once convergence has been achieved.

3.5.1.2 Pseudopotentials and projector augmented waves

The discussion in the previous section details the use of energy cut-offs to vastly reduce computational expense. This approach limits the inclusion of planewaves that oscillate on short length scales within real space, such as those that would be required to describe core electrons within atoms. These electrons are particularly costly, and from a physical standpoint, are often unimportant in terms of chemical interactions. As such, it is common practice in planewave methods to approximate the properties of core electrons in a way that would reduce the number of planewaves required to describe the system. This is often achieved by implementing pseudopotentials, mathematical descriptions that replace the electron density of core electrons with a smoothed density that matches various important physical properties of the true core.[256] In calculations, the properties of the core electrons are generally fixed to these approximations across all calculations, giving rise to the title of the approach: the frozen-core approximation.[275] An amended wavefunction, or pseudowavefunction, that omits the core electrons and accurately describes the valence electrons is used in conjunction with the frozen-core approximation to provide a relatively computationally inexpensive method of approximating the total electron density of the system.

Pseudopotentials often define minimum energy cut-offs that should be used in the calculation, with pseudopotentials that require high energy cut-offs being termed ‘hard’, and those with low cut-offs being considered ‘soft’. The most widespread predefined pseudopotentials are the ultra-soft pseudopotentials (USPP) by Vanderbilt, as they have been shown to be accurate across a wide range of systems while being computationally inexpensive as they function at very low cut-off energies.[276] Importantly, excluding (or vastly simplifying) core electron wavefunctions from the calculation inhibits the determination of accurate NMR parameters, as it is often the case that these electrons are crucial in accurately describing the magnetic response of the system.[277] The projector augmented wave (PAW) approach by Blöchl[278] proposes that

the all-electron wavefunction and a well-behaved pseudo-wavefunction, $\tilde{\psi}$, are linked by a linear transformation, $\hat{T}$:

$$\psi = \hat{T}\tilde{\psi} \tag{3.89}$$

In principle, the PAW approach transforms rapidly oscillating core electron wavefunctions into smooth wavefunctions that are computationally inexpensive. Pickard and Mauri[277] built upon PAW, introducing the gauge-including projector augment wave (GIPAW) approach in which the all-electron magnetic response of the system is calculated. The key development upon PAW is that a phase factor proportional to the magnetic field is included within translational operators. GIPAW therefore facilitates the determination of fields induced by the current response of the electrons, providing simulated chemical shifts within real space for periodic systems.

3.5.2 Geometry optimisation

The discussion thus far has emphasised the relation between the position of atomic species, the total electronic structure of the system, and the magnetic parameters of the system. Subtle differences in the atomic position can subsequently lead to variances in the calculated parameters. It is therefore imperative that the atomic positions, either defined by the user or derived from a separate analytical technique, such as X-ray diffraction or neutron diffraction, accurately describe the system of interest. Erroneous inputs, either human or systematic (such as the inability for X-ray diffraction to distinguish proton positions or the fact that DFT simulations are performed at 0 K compared to experimental temperatures), can be minimised by implementing a geometry optimisation step.

The geometry optimisation calculation iteratively acts to minimise the forces and strains exerted upon the atoms, and ultimately the total energy across the input structure by systematically varying atomic positions and unit cell parameters. The Broyden-Fletcher-Goldgarb-Shanno (BFGS) quasi-Newton algorithm is preferred among DFT packages, as it allows geometry optimisations to be performed at fixed external stress values.[279] Preconditioning the unit cell with a geometry optimisation step often ensures that the total energy of the system is at its minimum, greatly improving the accuracy of calculated physical quantities relative to their experimental values. However, if structural parameters have been precisely defined by experimental techniques, it is often better to fix these parameters while

allowing the remaining parameters to adjust so that a better agreement between calculated and experimental data is achieved.

3.5.2.1 Dispersion inaccuracy and semi-empirical dispersion correction schemes

As detailed above, the precise density functional that underpins DFT is unknown and is approximated using gradient-corrected density functionals. While these approximations are often able to accurately describe hydrogen bonding, they fail to accurately describe dispersion interactions.[280] One such example is that of π–π interactions, where binding energies are frequently overestimated and the resultant intermolecular equilibrium distances are underestimated.[281,282] To correct for this underestimation, semi-empirical dispersion correction (SEDC) terms can be implemented in which dispersion energy terms are added to the total energy of the system. Popular correction terms developed by Grimme *et al*. often take the form of C_6R^{-6}, where R is the interatomic distance and C_6 are dispersion coefficients.[283] The total energy of the system accounting for a dispersion correction, $E_{\mathrm{DFT+D}}$, can be generally represented as follows:[281]

$$E_{\mathrm{DFT+D}} = E_{\mathrm{DFT}} + E_{\mathrm{disp.}} \tag{3.90}$$

where E_{DFT} is the total energy from the DFT calculation and $E_{\mathrm{disp.}}$ is the energy from the dispersion correction term. The decision as to whether SEDC should be implemented for the system of choice should be made on a system-by-system basis. Flexible materials that comprise chemical environments exhibiting strong dispersive forces will be heavily influenced by the implementation of SEDC schemes, often providing different atomic positions and cell lattice parameters when geometry optimised with and without SEDC. Thus, it is best practice to fine-tune the geometry optimisation process as to carefully cultivate the best agreement between calculated and experimental results.

3.5.3 Calculating NMR parameters

Using DFT, the magnetic response of the electrons within the system can be determined, allowing the corresponding magnetic parameters to be defined. Perhaps the most important parameter for NMR is magnetic shielding which arises from magnetically induced currents within the system. The calculated magnetic shielding tensor, $\boldsymbol{\sigma}^{\mathrm{DFT}}$, is typically defined for each nucleus within the given unit cell. Following diagonalisation into a PAS, the principal

components can be used to define the isotropic magnetic shielding, $\sigma_{\mathrm{iso}}^{\mathrm{DFT}}$, in addition to the anisotropic, ζ^{DFT}, and asymmetric, η^{DFT}, terms. For quadrupolar nuclei, the electric field gradient and the corresponding quadrupolar parameters, such as the quadrupolar coupling constant, $C_{\mathrm{Q}}^{\mathrm{DFT}}$, can be calculated.[267] To check the accuracy of the calculated magnetic shielding, the isotropic component must be converted into an isotropic chemical shift value that can be compared to experimental data. This is typically achieved by modelling several reference compounds that have well-known experimental isotropic chemical shifts, $\delta_{\mathrm{iso}}^{\mathrm{exp}}$, and share similar structural properties to the system of interest. A plot of $\delta_{\mathrm{iso}}^{\mathrm{exp}}$ against $\sigma_{\mathrm{iso}}^{\mathrm{DFT}}$ for defined nuclear sites can then be fitted to a linear relationship which takes the form:

$$\delta_{\mathrm{iso}}^{\mathrm{exp}} = \sigma_{\mathrm{iso}}^{\mathrm{ref}} - \sigma_{\mathrm{iso}}^{\mathrm{DFT}} \tag{3.91}$$

where $\sigma_{\mathrm{iso}}^{\mathrm{ref}}$ is the reference shielding used to interconvert between isotropic chemical shifts and isotropic magnetic shielding values. Notably, the magnetic shielding tensor can be determined for any point within the unit cell, allowing the magnetic response in the free space surrounding the nuclei to be mapped. $\delta_{\mathrm{iso}}^{\mathrm{DFT}}$ values calculated for these points in space are referred to as nucleus-independent chemical shifts (NICS), a useful parameter to compare to experimental NMR data for adsorbed species.[34,131]

Chapter 4

Studying specific ion effects on spontaneous adsorption in porous carbons using NMR spectroscopy

4.1 Introduction

As detailed in Chapter 2, porous carbons are an important class of materials used in various industrial and scientific applications such as energy storage, filtration, and catalysis.[1–6] These materials can exhibit high internal surface areas (> 2000 m^2 g^{-1}), with pore sizes ranging from the microporous (< 2 nm diameter) to the mesoporous (2-50 nm) regime, depending on the precursor and synthesis method.[7–11] Porous carbons also typically exhibit high electrical conductivity due to extensive conjugation of aromatic carbon rings throughout their structures.[12,13] These properties make porous carbons particularly desirable for electrochemical devices and processes involving adsorption and/or electrosorption of specific molecules and ions, such as capacitive deionisation (CDI) and supercapacitors.[2,8,14–17]

An understanding of how adsorbate species behave within microporous networks must be obtained to optimise porous carbons for specific applications. Theoretical modelling has provided insight into the behaviour of guest species within microporous networks, with studies highlighting the importance of specific ion properties, relative pore and ion dimensions, and the solvation properties of solvents and solutes.[6,10,18–22] The behaviour of spontaneously adsorbed species has been shown to have significant implications for the charging mechanisms in electrochemical devices.[10,16,23–26] The charge storage mechanism and kinetics of porous carbon/electrolyte combinations are influenced by the ionophobicity or ionophilicity. These terms, introduced by Kondrat *et al*. that denote the proclivity for adsorbate species to enter the

pores before charging, have also been shown to influence the charge storage mechanism and charging kinetics of electrochemical devices.[25–27]

Chapter 2 introduced the use of NMR spectroscopy as a highly sensitive probe of the behaviour of adsorbates within carbon micropores.[7,13,28,29,70] The phenomenon of ring current shielding induced by the conjugated aromatic surface allows for the distinction between adsorbed and non-adsorbed species to be made.[30,31] The magnitude of the ring current-induced NICS can be influenced by pore size, with the effect of proximity to the pore wall being extensively studied both theoretically and experimentally.[18,22,32–34] Furthermore, the domain size and homogeneity of the graphene-like fragments making up the carbon pore structure have also been shown to influence the NICS.[22,32,34–36] Overall, the magnitude $\Delta\delta$ is multifaceted, with the magnitude being determined by the NICS as well as other factors such as ion dynamics, electrolyte concentration, and specific ion effects.[7,10,33] The study of ion behaviour within carbon micropores using NMR spectroscopy has focused mainly on organic systems due to the extensive use of organic electrolytes in electrochemical devices.[13,16,24] However, there is an increasing interest in aqueous systems owing to their relevance in capacitive deionisation and developments in electrical storage devices continuing to push for more sustainable cell components.[38,39] Prior studies on porous carbons have investigated the confinement of aqueous alkali-metal salts within different carbon materials and the relevance of ion-water interactions for select electrolytes.[10,24,40]

The work in this chapter details a systematic NMR study investigating spontaneous ion adsorption behaviour across a series of aqueous alkali metal salt solutions within a set of model PCMs with different pore size distributions. Anion and cation properties are shown to influence the spontaneous adsorption behaviour of electrolyte species within microporous carbons, with the exact behaviour of these species being dictated by the complex interplay of various factors. Solvation strength and pore structure are also investigated, with results demonstrating their role in determining the adsorption behaviour of aqueous electrolyte species within a confined microporous environment. Ion-specific effects on species distribution within micropores are presented, with fundamental differences in ion partitioning stability and solvation behaviour being investigated.

4.2 Experimental details

4.2.1 Materials

Electrolytes were prepared using LiCl (Thermofisher Scientific, 98%), $LiClO_4$ (Sigma Aldrich, > 99%), Li_2SO_4 (Sigma Aldrich, > 99%), lithium bis(trifluoromethane)sulphonimide (LiTFSI) (Tokyo Chemical Industries, > 98%), NaCl (Thermofisher Scientific, 99%), $NaClO_4$ (Sigma Aldrich, > 98%), Na_2SO_4 (Thermofisher Scientific, 99%), NaTFSI (Tokyo Chemical Industries, > 98%), CsCl (Thermofisher Scientific, 99.9%), and tetraethylammonium chloride (NEt_4Cl) (Sigma Aldrich, > 99%). Activated carbon cloths (ACCs) ACC-5092-10, ACC-5092-15, and ACC-5092-20 (hereafter referred to as ACC-20, ACC-15, and ACC-20) were supplied by Kynol, and YP-50F activated carbon was supplied by Kuraray Europe. Porous carbon samples were dried overnight under a vacuum at 60 °C inside a Schlenk tube. Dried porous carbon (13 mg) was packed into zirconia magic angle spinning (MAS) rotors with an outer diameter of 3.2 mm. Care was taken during this step to minimise damage to the macroscopic structure of the porous carbon. Electrolyte solutions were injected in 2.5 μL increments into the rotors via microsyringe (capacity of 10 μL), allowing sufficient time for the solution to disperse throughout the carbon pore network between acquisitions. A polytetrafluoroethylene plug was packed into the cavity within the rotor cap to prevent excess electrolyte from accessing this region. Mass loss due to the microsyringe bore removing sample during solution additions was found to be negligible. Volumetric additions of solution were limited by the adsorption limit of the sample, with visibly wet samples (*i.e.,* the pooling of electrolyte on the sample surface) not being subjected to MAS, restricting the maximum added volume of solution to between 22.5 μL and 25.0 μL per 13 mg of porous carbon.

4.2.2 Material characterisation

The pore properties of the carbon materials and electrodes under investigation were determined by Prof. Volker Presser at Saarland University through nitrogen gas adsorption-desorption isotherms using an Autosorb iQ instrument (Quantachrome Instruments; currently under Anton-Paar) at liquid nitrogen temperature (−196 °C). Before analysis samples underwent outgassing at 300 °C for 24 h. The Brunauer-Emmett-Teller (BET) method,[122] applied through ASiQwin software (Quantachrome Instruments), was used to compute the specific surface area (SSA). The SSA and the distribution of pore sizes were also determined by employing the

quenched-solid density functional theory (QSDFT).[124] Scanning electron microscopy (SEM) images were acquired by Dr Sara Baldock at Lancaster University.

X-ray Photoelectron Spectroscopy (XPS) measurements were performed by Dr Kacper Polus at the University of Manchester using an ESCA2SR spectrometer (ScientaOmicron GmbH) using monochromated Al Kα radiation (1486.6 eV, 20 mA emission at 300 W, 1 mm spot size) with a base vacuum pressure of ~$1 \cdot 10^{-9}$ mbar. Charge neutralisation was achieved using a low energy electron flood source (FS40A, PreVac). Survey spectra were measured using 150 eV pass energy, and core levels with 50 eV pass energy. Binding Energy scale calibration was performed using C-C in the C 1s photoelectron peak at 284.8 eV. Analysis and curve fitting was performed using Voigt-approximation peaks using CasaXPS.[284]

Chemical analyses were performed by Prof. Volker Presser at Saarland University to determine the content of carbon, hydrogen, nitrogen, sulphur (CHNS), and oxygen in the ACC samples. Analyses were performed using an Elementar vario Micro Cube for CHNS analysis and an Elementar rapid OXY cube for oxygen determination. For CHNS analysis, samples were weighed into tin boats with a certain amount of WO_3 pressed to remove air and then placed directly into the autosampler of the vario Micro Cube. For oxygen analysis, samples were weighed into silver boats. Air was removed by pressing and then placed directly into the autosampler of the rapid OXY cube. The CHNS analyser was calibrated using sulphanilamide (25 mg) with known percentages of C, H, N, and S. The oxygen analyser was calibrated using benzoic acid (3 mg) with known oxygen content. Calibration measurements were repeated five times.

Solid-state NMR experiments were performed using a 400 MHz Bruker Avance III HD WB spectrometer, operating at a magnetic field strength of 9.4 T. The MAS spinning rate was 5 kHz. For each sample, the recycle interval was set to exceed $5T_1$, with the experimental value for T_1 being measured via saturation recovery experiments. 90° pulse lengths were calibrated in each experiment to ensure quantitative spectra. ^{1}H, ^{7}Li, ^{19}F, ^{23}Na, and ^{133}Cs NMR spectra were recorded using a single-pulse sequence, with the number of scans varying between 32 and 4096, dependent on the signal-to-noise ratio of each species within the porous carbons. 90° pulse lengths ranged between 2 μs to 6.5 μs, and recycle intervals ranged from 5-14 s (^{1}H), 5-20 s (^{7}Li), 3 s (^{19}F), 0.25-1.50 s (^{23}Na), and 4-18 s (^{133}Cs). 2D EXSY experiments were acquired with 8 scans for each increment of t_1. In the indirect dimension, the spectral width was set to 4 kHz to minimise the number of t_1 increments required, and the States-TPPI protocol was used to achieve sign discrimination.[231] For ^{7}Li EXSY spectra, the recycle interval and 90° pulse

length were set to 5 s and 3.9 μs, respectively. ^{1}H spectra were referenced relative to the CH_3 resonance of alanine (1.2 ppm). ^{7}Li, ^{23}Na, and ^{133}Cs spectra were referenced relative to neat 1 M aqueous solutions of their corresponding alkali metal salts (0.0 ppm in each instance).

4.2.3 Computational details

DFT calculations were performed using the Gaussian 16.0 package.[285] Geometries were optimised using the B3LYP exchange correlation functional with the 6-31G(d) basis set.[18,132] The Grimme-D3 dispersion correction scheme was also implemented.[286] NMR parameters were calculated using the gauge-independent atomic orbital (GIAO) method.

4.3 Results and discussion

4.3.1 NMR spectra of aqueous electrolyte adsorbed within a microporous carbon

Data presented here was acquired in the absence of an applied voltage to investigate spontaneous adsorption behaviour. Preliminary experiments were performed using 1 M aqueous lithium chloride (LiCl) as a model electrolyte to demonstrate the principles of observing adsorbate behaviour within microporous carbons using NMR spectroscopy. Initial MAS NMR studies were performed on YP-50F, a well-characterised and commercially available activated carbon derived from coconut shells. For all experiments, a known mass of carbon was packed into a MAS rotor and loaded with a known volume of 1 M aqueous LiCl via microsyringe. **Figure 4.1** shows the ^{7}Li MAS NMR spectrum of YP-50F (13 mg) soaked with 1 M aqueous LiCl (20 μL). This experiment was performed using a simple 90° pulse-acquire experiment. The ^{7}Li MAS NMR spectrum is referenced to the spectrum of the neat 1 M LiCl solution, such that the resonance of the neat solution is set to 0 ppm.

The ^{7}Li MAS NMR spectrum of the soaked carbon exhibits three distinct resonances: (i) a sharp resonance centred about 0 ppm, (ii) a broader resonance at a more negative chemical shift (−5.86 ppm), and (iii) a very broad resonance between 0 ppm and −5.86 ppm. The resonance at 0 ppm corresponds to electrolyte species occupying chemical environments that are similar to that of the referenced neat electrolyte solution, an environment referred to as ex-pore. The resonance at −5.86 ppm is assigned to species existing within the confines of the microporous carbon structure, or in-pore species. These species experience a reduced effective field due to ring current-induced diamagnetic fields.

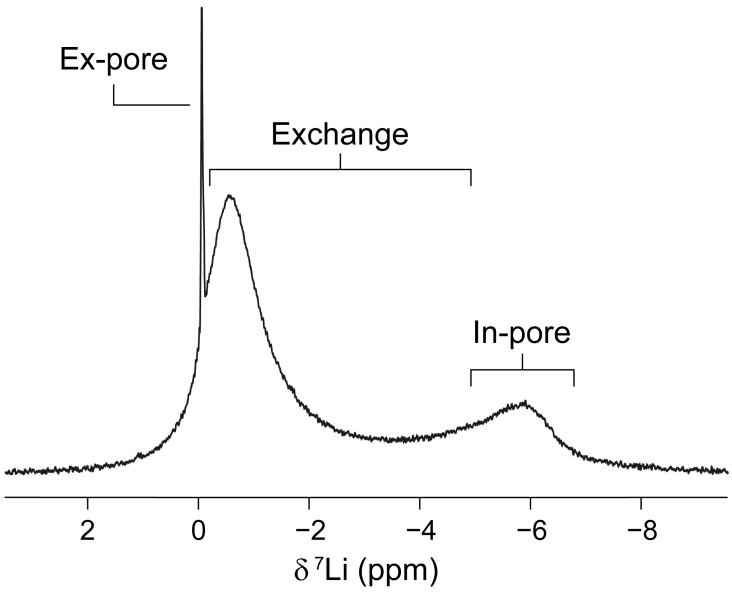

Figure 4.1. ^{7}Li MAS NMR spectrum (9.4 T, MAS rate = 5 kHz) of YP-50F (13 mg) loaded with aqueous 1 M LiCl (20 µL). Resonances correlated to free *ex-pore* cations, confined *in-pore* cations, and cations undergoing exchange between the in-pore and ex-pore environments are indicated.

As detailed in Section 3.3.1.1, the induced field from aromatic ring currents is localised, being inversely proportional to the cubed distance. As such, the magnitude of the ring current shift is only experimentally relevant when observed using NMR across several Å, the dimensions of a typical micropore. Consequently, ex-pore species do not experience ring current shifts as the shielding from this phenomenon diminishes across distances exceeding micropore dimensions. This interaction allows NMR spectroscopy to distinguish in-pore and ex-pore species. A useful parameter related to this phenomenon is Δδ, defined as:

$$\Delta\delta = \delta_{\text{in-pore}} - \delta_{\text{neat}} \tag{4.1}$$

where $\delta_{\text{in-pore}}$ is the chemical shift of the in-pore resonance and δ_{neat} is the chemical shift of the neat electrolyte. The magnitude of Δδ in the ^{7}Li spectra has a value of −5.86 ppm which is similar to values reported for other aqueous lithium-salt-based electrolytes adsorbed within YP-50F.[133] Provided the electrolyte volume loaded within the carbon is known, the cation populations within each environment can be determined by integrating the in-pore and ex-pore ^{7}Li resonances, giving insight into cation adsorption behaviour. Furthermore, as this effect is nucleus-independent, any NMR-active species can be monitored following the same approach, including water molecules using ^{1}H NMR and certain anionic species (*e.g.,* fluorinated species using ^{19}F NMR spectroscopy).

Notably, the in-pore resonance was significantly broader than the ex-pore resonance (FWHMs > 1 ppm and < 0.1 ppm, respectively). This broadening is attributed to YP-50F exhibiting a range of micropore geometries, giving rise to several local magnetic environments that the Li^+ cations can occupy. A minor contribution to the broadening is also expected from ABMS contributions from the carbon particles and the sample shape, however the extent of this line broadening is assumed to be obscured by broadening from wide pore-size distributions and various surface geometries that create a range of magnetically distinct in-pore environments. The broad resonance between 0 ppm and −5.86 ppm is assigned to lithium cations undergoing intermediate-to-fast exchange between different magnetically distinct in-pore environments, and between the in-pore and ex-pore environments. This exchange results in the cations experiencing an averaged effective field, giving a broad resonance between the chemical shifts of the in-pore and ex-pore resonances. Similar assignments of this exchange region have been reported for aqueous electrolytes adsorbed within YP-50F,[133] for water adsorbed within various PDCs,[10] and for YP-50F loaded with 1 M tetraethylammonium (TEA^+) tetrafluoroborate (BF_4^-).[7] These assignments have been further supported in the literature by 2D EXSY NMR experiments, with cross-peaks between the exchange region and the ex-pore peaks and between exchange and in-pore peaks being observed.[7,133] The presence of this broad exchange region can cause challenges when attempting to gain quantitative information on adsorbate populations through signal integration, particularly when MAS cannot be implemented (*e.g.,* for *in situ* measurements of electrochemical devices) and the resonances become substantially broadened. As such, for quantitative investigations of adsorption behaviour using NMR spectroscopy, a system exhibiting a reduced exchange character is desirable.

4.3.2 Carbon fibres and chemical exchange between micropore environments

A series of commercially available activated carbon cloths were characterised and investigated for use as a potential model activated carbon due to their ease of use and abundancy. The ACC-5092 series by Kynol (Germany), hereafter referred to as ACC, has been extensively characterised within the literature (**Table 4.1**). Chemical analyses were performed to determine the carbon, hydrogen, nitrogen, sulphur, and oxygen (CHNS-O) content in the ACC samples. **Table 4.2** shows that the carbon content decreased as the SSA decreased, with ACC-10 having the lowest carbon content (89±0.3%) and ACC-20 having the largest carbon content (96±0.9%).

Table 4.1. Calculated and experimentally derived structural properties for YP-50F and the ACC series. (a) Particle diameter refers to the fibre width for the ACC series.

Sample	SSA BET / $m^2 g^{-1}$	SSA QSDFT / $m^2 g^{-1}$	Pore volume / $cm^3 g^{-1}$	Avg. pore width / nm	Particle diameter / μm	Ref.
YP-50F	~1730	-	0.85	0.6 – 1.1	~5	[7,29,99]
ACC-20	2070	1876	0.81	0.89	~12[(a)]	[94]
ACC-15	1478	1550	0.56	0.68	~12[(a)]	[94]
ACC-10	916	1032	0.34	0.59	~12[(a)]	[287]

Table 4.2. CHNS-O analysis data for ACC-20, ACC-15, and ACC-10 samples.

Element	Percentage elemental composition		
	ACC-10	ACC-15	ACC-20
C	89.0±0.3	92.1±0.5	96.0±0.9
H	1.0±0.1	0.9±0.1	0.7±0.1
N	Not detected	Not detected	Not detected
S	Not detected	Not detected	Not detected
O	9.8±0.2	5.7±0.2	2.3±0.2

Oxygen was shown to be the second most common element, and neither nitrogen nor sulphur were observed within the limit of detection. The increase in oxygen content and decrease in carbon content as the SSA increases is assigned to greater activation periods being required to create wider pores/larger surface areas, during which it is assumed that oxygen is present and actively decomposing graphitic carbon into CO_2 and forming oxygen-based functionalities (*e.g.,* phenols, lactones, pyrones) throughout the carbon structure. The elemental composition of the ACC series surfaces was also characterised using XPS analysis. **Figure 4.2** shows that, to a first approximation, ACC-10 and ACC-20 exhibit the same elemental compositions. The surface of ACC-15 was shown to have an increased carbon content as well as a reduced oxygen and nitrogen content relative to ACC-10 and ACC-20.

The XPS elemental composition differs from the CHNS-O elemental compositions, suggesting that the elemental composition of the surface, up to a sampling depth of ~10 nm as determined by XPS, and the bulk elemental composition, as determined by CHNS-O analysis, are different. The exact reasons for these differences are not well understood and require further investigation. However, for the purposes of this work, both the XPS and the CHNS-O elemental compositions will be considered when considering observed trends for adsorbate-adsorbent interactions and behaviours.

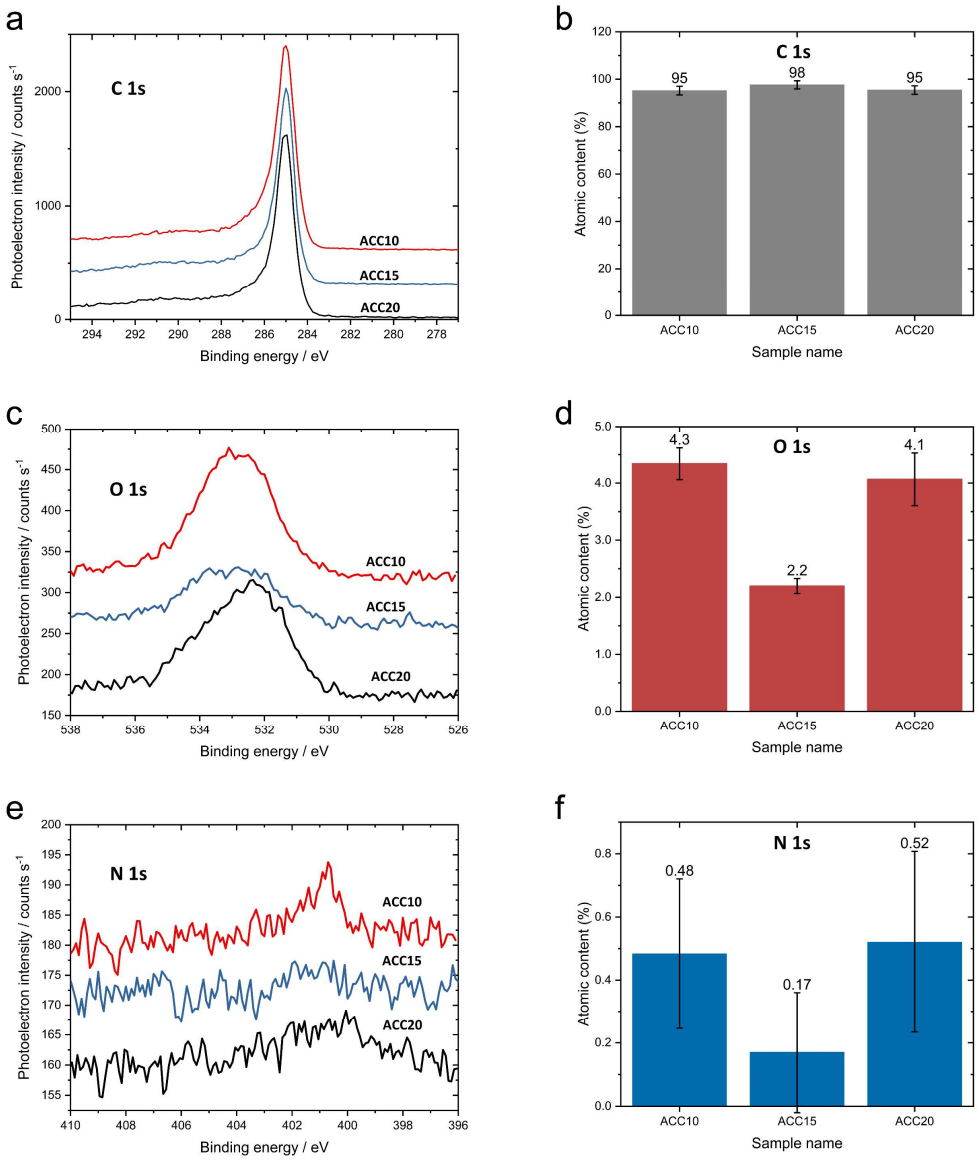

Figure 4.2. X-ray photoelectron spectroscopy data acquired for the dried ACC-5092 activated carbon cloths. (a, b) C 1s, (c, d) O 1s, and (e, f) N 1s data and percentage atomic contents are shown. C 1s analysis (a, b) shows that the ACC series exhibits similar quantities of heteroatoms within the predominantly carbonaceous structure. Oxygen (c,d) and nitrogen (e,f) populations of ACC-15 are markedly less than that of ACC-20 and ACC-10.

^{7}Li MAS NMR experiments were also performed on ACCs loaded with 1 M LiCl and compared to that acquired for YP-50F. **Figure 4.3** shows the recorded ^{7}Li NMR spectrum for (a) YP-50F and (b) ACC-20 (13 mg) loaded with 1 M LiCl (20 µL). ACC-20 is shown to have a narrow and symmetrical in-pore resonance centred about −5.5 ppm. The narrow resonance is characteristic of a narrow pore size distribution, with adsorbates residing within magnetically equivalent in-pore environments. A substantial reduction in exchange character is observed in the ACC-20 spectrum compared to that of YP-50F.

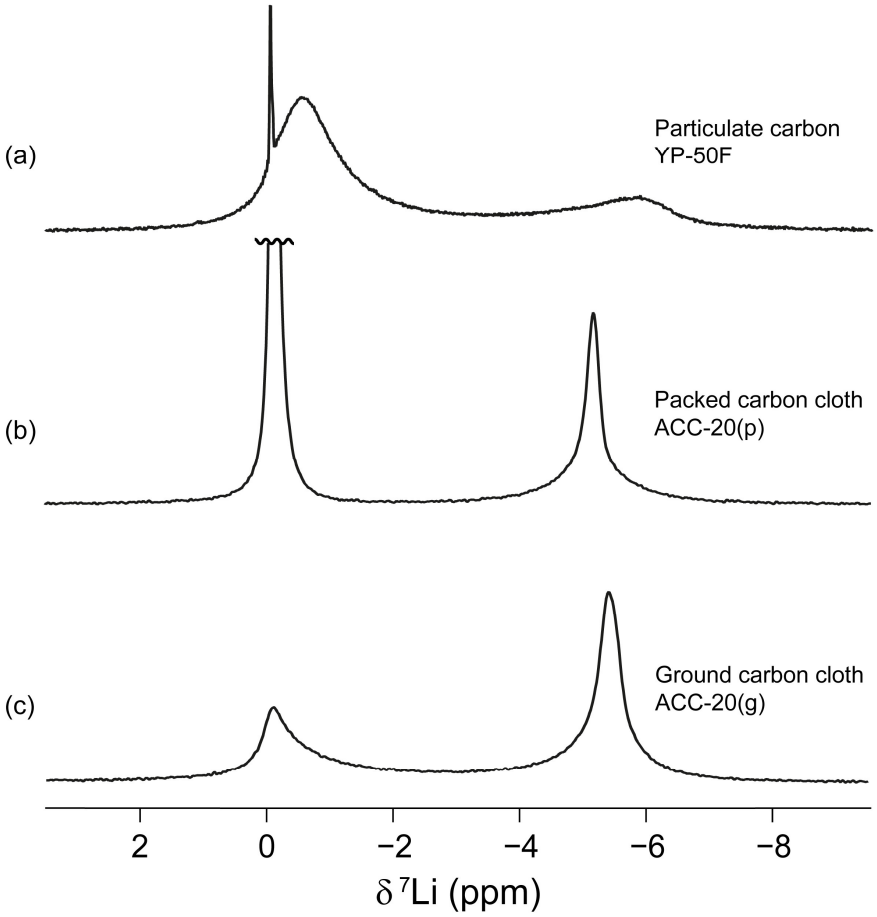

Figure 4.3. ^{7}Li MAS NMR spectra of activated carbons (13 mg) loaded with aqueous 1 M LiCl (20 µL). The spectra shown are for (a) YP-50F, (b) rotor-packed carbon cloth, and (c) ground carbon cloth.

As detailed by Cervini *et al.*, the small particle size of YP-50F facilitates a fast exchange rate at the interfacial region where in-pore to ex-pore exchange takes place, resulting in a significant exchange peak in the spectrum.[10] The activated fibres are approximately twice as large in two dimensions, and effectively infinite along the fibral axis (at least on the scale of random walk diffusion between the in-pore and ex-pore environment). It is therefore speculated that the fibral structure may act to suppress exchange between the in-pore and ex-pore along one dimension, significantly reducing the intensity of the exchange region in the NMR spectrum. To further investigate the exchange-suppressing characteristics of the fibral structure, samples of ACC-20 ground to varying extents using a pestle and mortar were characterised using scanning electron microscopy (SEM), loaded with electrolytes, and then studied using NMR spectroscopy. **Figure 4.4** shows scanning electron micrographs of three samples: (a) a sample of pristine ACC-20, (b) a sample packed into and then removed from a 3.2 mm MAS rotor, referred to as ACC-20(p), and (c) a sample ground for 30 minutes using a pestle and mortar, or ACC-20(g).

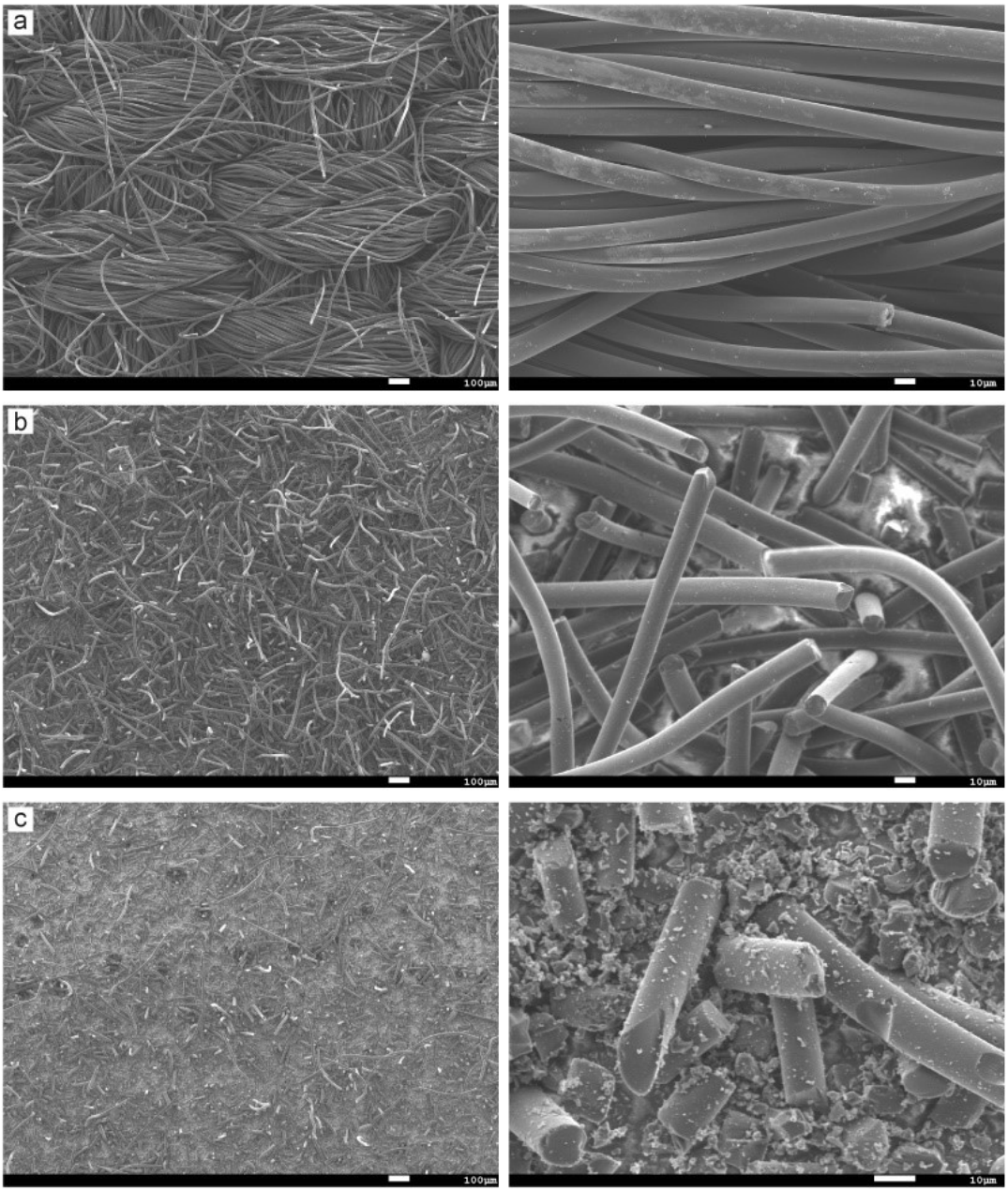

Figure 4.4. Scanning electron micrographs of ACC-20 at different magnifications. (a) A sample of pristine ACC-20, (b) a sample packed into, and removed from a 3.2 mm magic angle spinning (MAS) rotor, and (c) a sample ground using a mortar and pestle for 30 min.

SEM revealed that the ACC fibres remain unbroken following rotor-packing and unpacking. As such, the behaviours observed using packed samples in MAS NMR experiments are inferred to be relevant to the behaviours of the pristine cloth. On the other hand, grinding using a pestle and mortar was shown to break down the fibres into particles, with particle sizes ranging from approximately 3 µm to 20 µm. **Figure 4.3** shows the 1D ^{7}Li MAS NMR spectra of (b) ACC-20(p) and (c) ACC-20(g) loaded with 1M LiCl, both with a loaded mass of 13 mg and a loaded

volume of 20 µL. A broad resonance emerged in the spectrum of ACC-20(g) that was not observed in ACC-20(p), indicating a reduced suppression of exchange between the in-pore and ex-pore environments in the ground sample. ^{7}Li 2D EXSY[253,254] experiments were also performed on ACC-20(g) and ACC-20(g) (carbon mass of 13 mg, loading volume of 25 µL) to probe the chemical exchange of the cation between the in-pore and ex-pore environments.

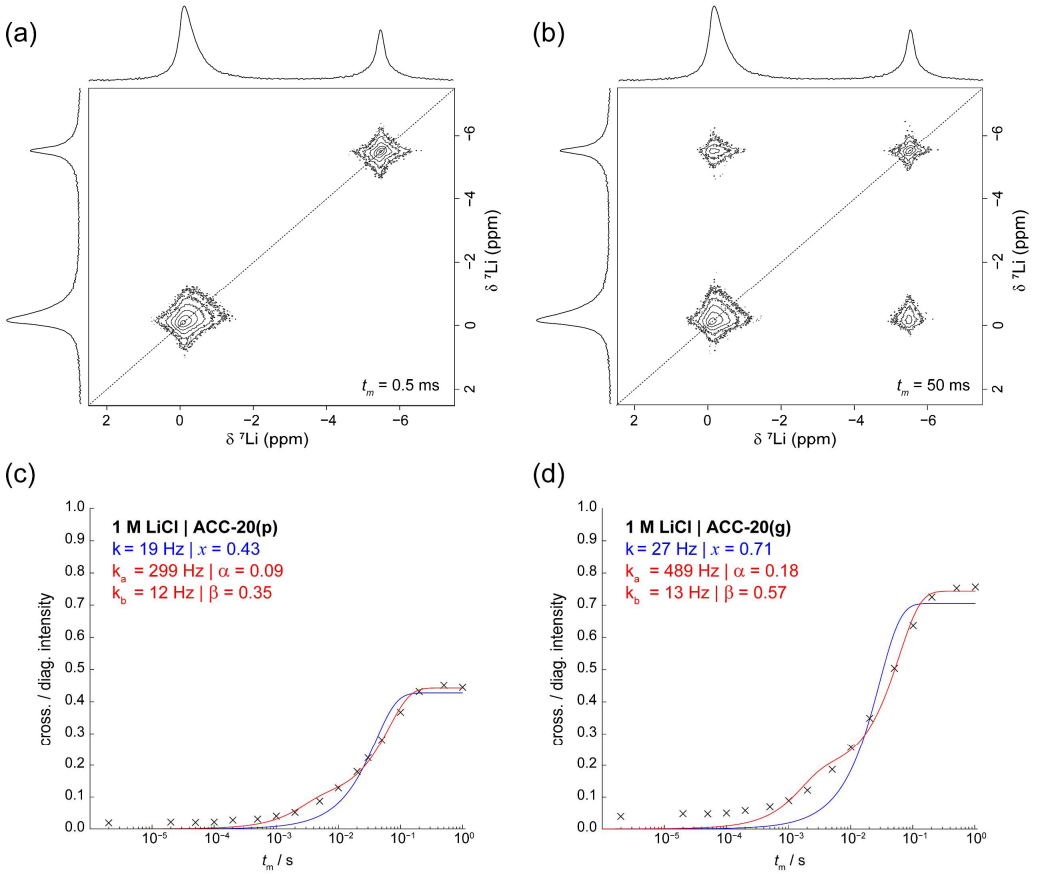

Figure 4.5. ^{7}Li 2D EXSY MAS NMR spectra of ACC-20 soaked with 1 M LiCl aqueous electrolyte (25 µL) recorded with mixing times of (a) 0.5 ms and (b) 50 ms. The cross-peak/diagonal-peak intensity ratio as a function of t_m are shown for (c) ACC-20(p), a sample cut directly from the cloth, and (d) ACC-20(g), a sample that was ground using a mortar and pestle for 30 min prior to packing. Fits used to determine exchange rates from Equation 4.2 ($I_{cross}/I_{diag.} = x \cdot \tanh(kt_m)$) and Equation 4.3 ($I_{cross}/I_{diag.} = \alpha \cdot \tanh(k_a t_m) + \beta \cdot \tanh(k_b t_m)$) are displayed in blue and red, respectively.

Figure 4.5a shows the 2D EXSY spectrum acquired with a mixing time, t_m, of 0.5 ms, where only diagonal peaks are observed. These diagonal resonances correlate to cations that exist within the same environment before and after the duration of t_m. No major cross-peaks between the in-pore and ex-pore resonances were observed, indicating negligible chemical exchange has occurred between the two sites during t_m. As t_m was increased to 50 ms (**Figure 4.5b**), clear cross-peaks were observed between the in-pore and ex-pore environments,

showing that lithium cations were moving from the in-pore to the ex-pore environment (or *vice versa)* during t_m. As detailed previously in Section 3.4.7.1, exchange rates for the in-pore to ex-pore exchange can be estimated by conducting a series of 2D EXSY spectra with incrementally increasing values of t_m. The exchange rate constant for in-pore to ex-pore exchange, k, was estimated following:

$$a_{cross}/a_{diag.} = x \cdot \tanh(kt_m) \quad (4.2)$$

where x is a fitting parameter. **Figure 4c** and **Figure 4d** show the cross-peak to diagonal-peak intensity ratio as a function t_m for the fibrous sample and the ground sample, respectively. The fit using Equation 4.2 (marked in blue in **Figure 4c-d**) gives poor agreement for both datasets, indicating a complex exchange process comprising multiple components. Following the approach by Fulik *et al*.,[7] exchange rate constants for a rapid in-pore to ex-pore exchange, k_a, and a slow diffusion between different in-pore environments, k_b, were estimated by fitting the cross-peak intensity, a_{cross}, and the diagonal peak intensity, $a_{diag.}$, to:[7,16]

$$a_{cross}/a_{diag.} = \alpha \cdot \tanh(k_a t_m) + \beta \cdot \tanh(k_b t_m) \quad (4.3)$$

where α and β are fitting parameters. The two-component rate equation (marked in red in **Figure 4c-d**) provided a significantly improved fit to the experimental data, indicating that both a slow and a fast exchange rate process are in effect. The fit for the fibrous sample (**Figure 4.5c**) demonstrated significantly reduced in-pore to ex-pore exchange compared to the ground sample (**Figure 4.5d**), with estimated k_a values of 299 Hz and 489 Hz, respectively. This difference in exchange rate is also reflected in the single-rate fit, with k values of 19 Hz and 27 Hz, respectively. Seemingly, the fibrous microstructure acts to reduce k_a, which is interpreted to be due to diffusion along the length of the fibre being unlikely to result in an in-pore to ex-pore exchange as the particle size in this dimension is exceedingly large (> 300 μm). As such, the diffusion of cations that influences the NMR spectrum is inferred to be effectively limited to a radial dimension perpendicular to the axis of the fibre. Sample ACC-20(p) also exhibited a slight reduction in the rate of in-pore diffusion compared to ACC-20(g), with k_b values of 12 Hz and 13 Hz, respectively, although this difference may be attributed to error in the fits. Notably, the fitting parameter x increased from 0.43 to 0.71 (**Figure 4.5c**) after the sample was ground. Similar increases were also observed for both α (0.09 to 0.18) and β (0.35 to 0.57) in the two-component fit (**Figure 4.5d**). The increases indicate that a greater proportion

of ^{7}Li species undergo exchange in ACC-20(g) compared to ACC-20(p), further demonstrating that the fibral structure of ACC-20(p) inhibits in-pore to ex-pore exchange.

Importantly, the estimated exchange rates are an amalgamated value correlating to an average of complex intramolecular diffusion and in-pore to ex-pore exchange.[16] As such, the calculated exchange rates should only be taken as an indicator of the timescale of the exchange processes as to enable the inexact comparison of exchange rates for different systems. Additionally, experimental data with long t_{m} values do not precisely align with the fits due to differences in longitudinal relaxation times between the in-pore and ex-pore environments, and the complex reality of the dynamic processes that are occurring over multiple time- and length-scales.

4.3.3 Effect of loading volume on electrolyte partitioning

To ensure the quantitative measure of the population of electrolyte species across and to gain insight into adsorption behaviour as a function of loading volume, a series of volumetric loading experiments were performed. In these experiments, electrolyte was sequentially added to a sample of activated carbon and NMR spectra were acquired following each addition. ACC-20 was initially selected as the model carbon due to its improved spectral resolution relative to particulate-based activated carbons. **Figure 4.6a** shows ^{7}Li MAS NMR spectra of ACC-20 (13 mg) loaded with increasing volumes of aqueous 1 M LiCl solution. At low loading volumes of 2.5-7.5 μL, a single in-pore resonance is observed at –5.5 ppm, which grows with increasing loading volume. At a loading volume of 10 μL, an ex-pore resonance becomes visible at 0 ppm, the intensity of which increases with loading volume whereas the in-pore intensity plateaus. As the loading volume is increased, $\delta_{\text{ex-pore}}$ remains constant, whereas $\delta_{\text{in-pore}}$ shifts slightly to −5.2 ppm. This reduction of $\Delta\delta$ is attributed to a slight redistribution of the electrolyte ions towards the ex-pore reservoir as saturation occurs.[7,10] In addition, a small splitting is observed at a loading volume of 7.5 μL. This splitting was observed at similar loadings for other electrolytes. The precise origin of this splitting is unclear; however, it appears to be linked to the onset of saturation, introducing a slight redistribution of electrolyte ions, evident from the resonance intensities and the chemical shift of the in-pore resonance becoming less negative after saturation. This could result in the adsorbed ions occupying slightly different average in-pore environments before and after saturation.

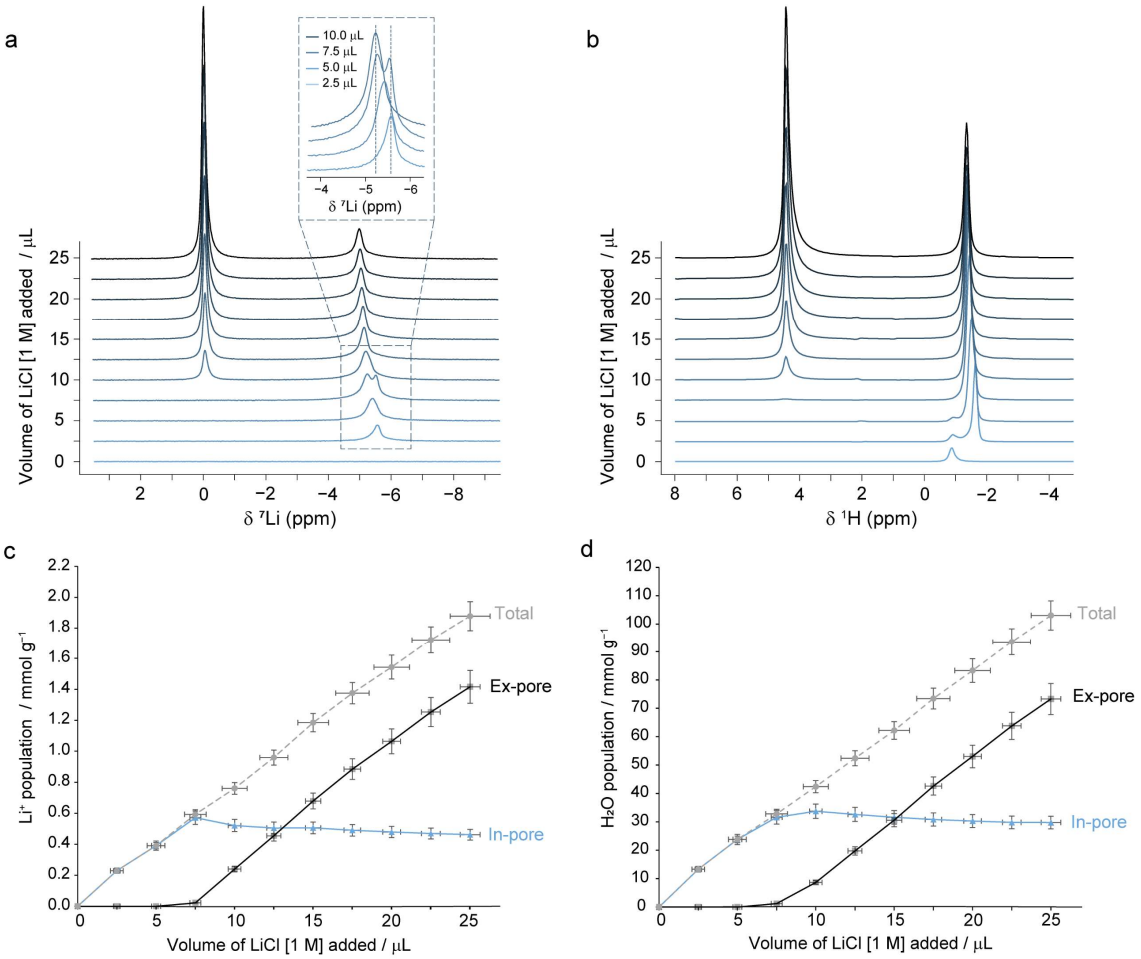

Figure 4.6. (a) ^{7}Li MAS NMR spectra and (b) ^{1}H MAS NMR spectra of ACC-20 (13 mg) recorded with increasing loading volumes of aqueous 1 M LiCl. Population distributions derived from the loading volume and the neat electrolyte concentration normalized by the carbon mass with respect to loading volume for (c) lithium ions and (d) water.

These observations agree with previous NMR adsorption studies, which typically show the in-pore environment is preferentially occupied at a low loading level until saturation is reached, after which the ex-pore environment begins to fill.[10,13] The saturation point between 7.5-10 µL is in line with the gas-sorption-derived pore volume of 0.81 $cm^3\ g^{-1}$ for ACC-20 (corresponding to 10.5 µL for 13 mg). ^{1}H MAS NMR experiments were also conducted following each addition, with the in-pore and ex-pore resonances being identified and integrated within the spectra to give the in-pore, ex-pore, and total populations of water molecules across the system. **Figure 4.6b** shows a minor in-pore water population (> 0.2 µL) persists after the drying of the carbon sample, evidenced by the minor resonance at −1 ppm at a loading of 0 µL. This small peak is seen for all samples prior to loading and is observed to shift to a more negative chemical shift following electrolyte loading. **Figure 4.6c-d** shows the in-pore, ex-pore, and total Li^+ and H_2O populations derived from the relationship between the integrated intensities of the in-pore

and ex-pore resonances of the ^{1}H and ^{7}Li MAS NMR spectra acquired at the different loading volumes. The ^{1}H MAS NMR spectrum at a loading of 0 µL was subtracted from the spectra of the loaded volumes to give a normalised total water population of 0 mmol g^{-1} prior to the addition of electrolyte. Measured Δδ values across the ^{1}H spectra were observed to be slightly larger (by approximately −0.6 ppm) than those observed in the ^{7}Li spectra across all loading levels. This was assumed to be due to free water molecules (*i.e.,* not within the hydration sphere of anionic or cationic species) freely accessing and exchanging with narrower, more shielded micropores that the bulkier solvated ^{7}Li cations could not access, shifting the average observed ^{1}H in-pore resonance to a more negative chemical shift.

For samples adsorbed within ACC-20, integrations between two defined chemical shifts were performed with relative ease as the in-pore and ex-pore peaks were sufficiently resolved. The inclusion or omission of the exchange region in the calculated integrals for well-resolved in-pore and ex-pore resonances was found to have negligible impact on the recorded integral (**Figure 4.7a**). Spinning side bands for the in-pore and ex-pore resonances were not included in the integrations as their inclusion was also found to have a negligible impact on the ratios between the in-pore and ex-pore environments. The recorded integrals of less resolved in-pore and ex-pore resonances were taken from the mid-point between the chemical shifts for the two environments as the weighting of the region between the two sites appears evenly distributed between the two resonances to a first approximation. **Figure 4.7b** demonstrates this scenario, showing the ^{23}Na MAS NMR spectrum acquired for ACC-20 (13 mg) loaded with 1 M NaCl (22.5 µL).

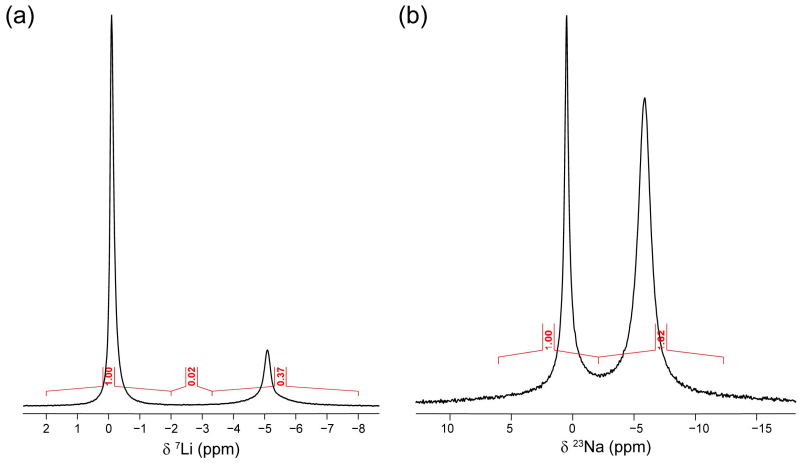

Figure 4.7. ^{7}Li MAS NMR of 22.5 µL 1 M LiCl solution soaked within ACC-20 (13 mg). The location of where the integrals were taken from for this spectrum are highlighted in red, with the weighting of each also being displayed. (b) ^{23}Na MAS NMR of 22.5 µL 1.0 M NaTFSI solution soaked within ACC-20 (13 mg). The exchange region was included in the integration of the in-pore and ex-pore resonances.

4.3.4 Specific ion effects on electrolyte partitioning

A number of studies have previously reported anion- and cation-specific effects on the adsorption behaviour of aqueous electrolytes within porous carbons, a well-known phenomenon detailed in prior literature.[10,24,288] In the current study, a series of aqueous alkali metal electrolytes (lithium-, sodium-, and caesium-based salts) were systematically investigated to probe the influence of these effects. $TFSI^-$, Cl^-, ClO_4^-, and SO_4^{2-} salts were selected to sample a range of anions with different solvation strengths.[37,289,290]

For each electrolyte, ^{1}H MAS NMR spectra and the corresponding cation MAS NMR spectra (*e.g.,* ^{7}Li, ^{23}Na, and ^{133}Cs) were acquired, and the resonances were integrated. Recorded integrals were referenced to the integral of the in-pore resonance measured at a loading of 2.5 µL. The total integral (*i.e.,* the sum of the referenced in-pore and ex-pore resonance integrals) was plotted against the loading volume for each electrolyte, and the linearity of the relationship was used to qualitatively assess if all loaded species were observed. **Figure 4.8** shows the calculated cation populations, derived from the loading volume and the neat electrolyte concentration, against the total integral of the cation resonances for each electrolyte. An ideal linear relationship between the total integral and the cation population (referenced to an arbitrary integral of 1.0 at a cation population of 2.5 µmol) is indicated by the red line.

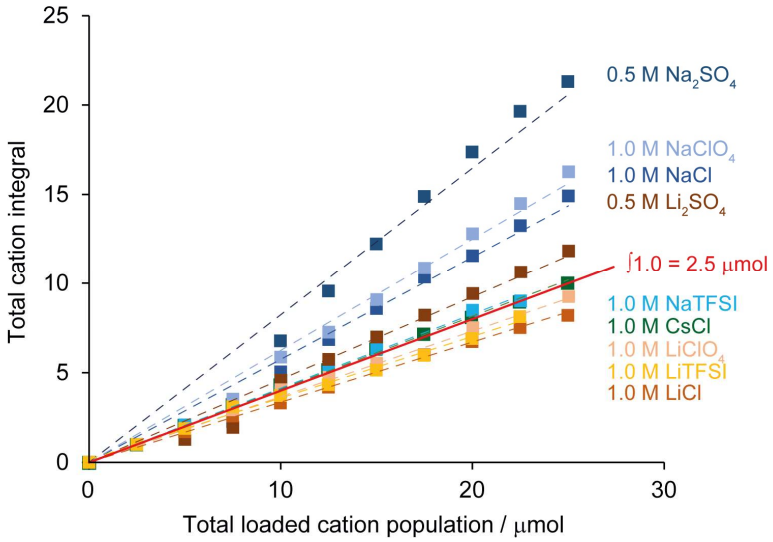

Figure 4.8. Recorded total cation integral against the total cation population determined from the loaded volume. Linear trends are indicated by the dashed lines for each electrolyte. An ideal linear relationship between the total integral loading volume (referenced to 1.0 at a cation population of 2.5 µmol) is indicated by the red line.

The systems containing 0.5 M Na_2SO_4, 1.0 M NaCl, 1.0 M $NaClO_4$, and 0.5 M Li_2SO_4 exhibited steeper gradients compared to other electrolytes and the theoretically ideal

correlation. This behaviour is attributed to these electrolytes "salting out" at lower loading levels (<7.5 μmol of cations), leading a significant portion of the cations to form a solid crystalline phase. In the solid phase, the resonance signals of the cations are substantially broadened, making them undetectable in the integrated regions. It is inferred that, in these systems, H_2O is preferentially adsorbed into the pores and the cations remain in the ex-pore environment, resulting in the crystallisation of the electrolyte salt. As more electrolyte is added and the in-pore environment becomes saturated with H_2O, a clear linear relation emerges between the measured cation integral and the total loaded cation population. This behaviour is attributed to the redissolution of the crystalline salt following further electrolyte addition, which allows the previously unobserved crystalline ex-pore cations to become detectable. Since the total integrals are referenced to the integral recorded at 2.5 μL, the electrolytes that exhibited salting out at that loading volume show steeper gradients relative to the ideal once the crystalline cations have redissolved. Among these, Na_2SO_4 demonstrated the greatest underestimation from the ideal linear relationship before in-pore saturation and exhibited the steepest gradient afterward. This aligns with the greater tendency for Na_2SO_4 to salt out within aqueous media, as predicted by its position in the Hofmeister series.[289,291]

From the measured populations, the molar ratio of Li^+ cations per H_2O molecule, χ, was calculated following:

$$\chi = n_{\text{cation}}/n_{H_2O} \tag{4.5}$$

where n_{cation} is the cation population and n_{H_2O} is the population of water molecules determined from the integration of the in-pore and ex-pore resonances. The exact concentrations cannot be confidently assigned as the precise pore volume that each species occupies is unknown and can only be approximated. The cationic molar ratio, χ, facilitates a less ambiguous description of population behaviours. The cationic molar ratio of the in-pore environment and the ex-pore environment were calculated using the populations derived from the integration of their respective peaks in the ^1H and ^7Li MAS NMR spectra. The total cationic molar ratio, χ_{total}, across the system was also determined, and was calculated following:

$$\chi_{\text{total}} = \left(n_{\text{cation}}^{\text{in-pore}} + n_{\text{cation}}^{\text{ex-pore}}\right)/\left(n_{H_2O}^{\text{in-pore}} + n_{H_2O}^{\text{ex-pore}}\right) \tag{4.6}$$

The in-pore, ex-pore, and total cationic molar ratios were calculated for each loading volume across each of the studied aqueous electrolytes. The cationic molar ratio of the neat electrolyte

solution, χ_{neat}, was calculated following Equation 4.5 using cation and water molecule populations calculated from the masses used to make up the stock solutions of electrolyte. For each electrolyte, χ_{total} was compared to χ_{neat}, with equivalent values indicating that all loaded species are observed and that the populations are quantitatively measured. **Figure 4.9** shows the calculated cationic molar ratios for ACC-20 (13 mg) at different loadings of 1 M LiCl. The total cationic molar ratio gives good agreement with the neat cationic molar ratio, demonstrating that the observable electrolyte species added during loading are all accounted for. All electrolytes studied in this work show good agreement between χ_{neat} and χ_{total}.

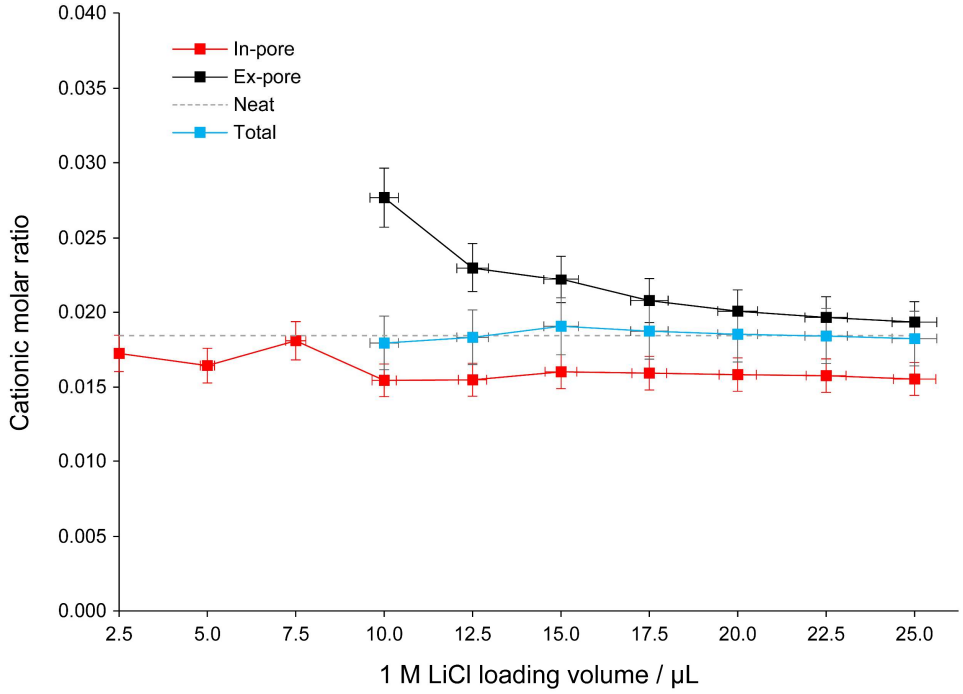

Figure 4.9. Cationic molar ratios calculated from ^{7}Li MAS NMR spectra of ACC-20 (13 mg) loaded 1 M LiCl. The total cationic molar ratio has good agreement with the neat solution cationic molar ratio.

Figure 4.10 shows $\chi_{in\text{-}pore}$ for ACC-20 soaked with aqueous lithium salt solutions, normalised by χ_{neat}. After saturation of the in-pore environment (> 10 µL), the ratio $\chi_{in\text{-}pore}/\chi_{neat}$ for 1 M LiCl is shown to maintain a value of 0.85±0.06 across subsequent loadings, indicating that the in-pore ion concentration is lower than that of the neat solution. This suggests that the carbon exhibits weakly ionophobic behaviour towards this electrolyte. For 0.5 M Li_2SO_4 (**Figure 4.10**), $\chi_{in\text{-}pore}/\chi_{neat}$ is more reduced, with a value of 0.42±0.03. This indicates that the carbon is more ionophobic toward Li_2SO_4 compared to LiCl.

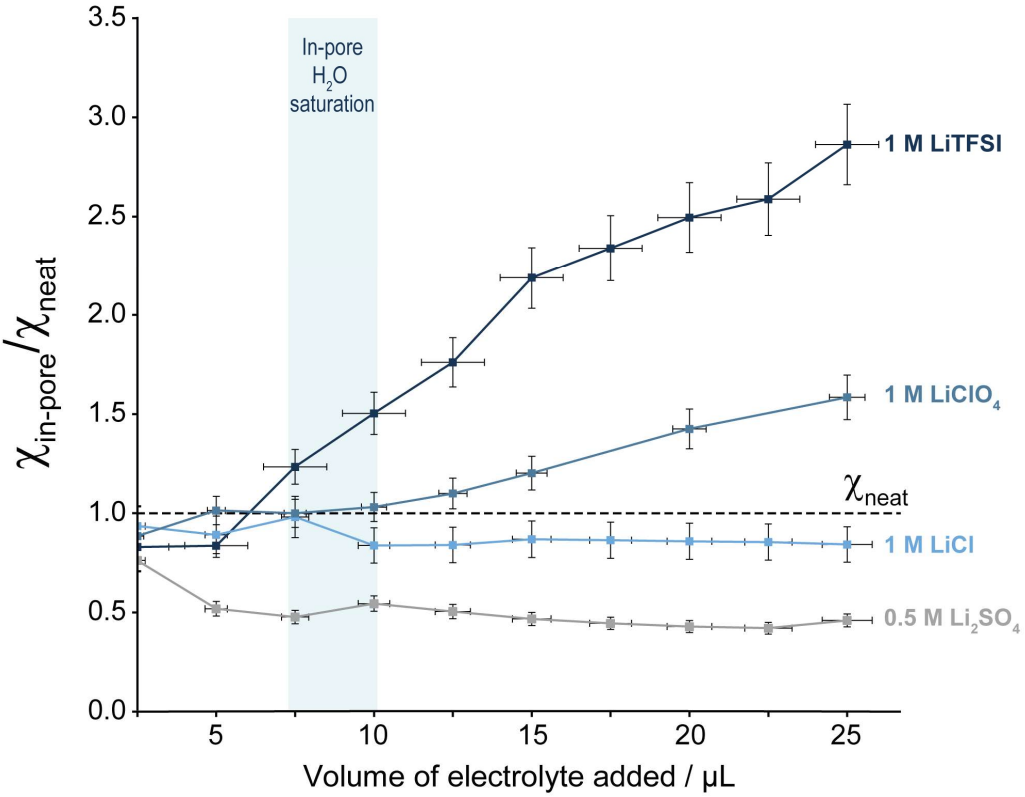

Figure 4.10. Calculated in-pore cationic molar ratios, $\chi_{in\text{-}pore}$, normalised by the neat cationic molar ratio, χ_{neat}, as a function of loading volume for aqueous solutions of 1 M LiTFSI, 1 M $LiClO_4$, 1 M LiCl, and 0.5 M $Li2SO_4$ soaked within 13 mg of ACC-20. 0.5 M Li_2SO_4 was used to maintain a consistent ionic strength concerning Li^+.

In contrast, for 1 M $LiClO_4$ and 1 M LiTFSI (**Figure 4.10**), $\chi_{in\text{-}pore}/\chi_{neat}$ is > 1, showing that the carbon is ionophilic towards these electrolytes when the loading volume exceeds the saturation volume. Interestingly, for the ionophilic systems, the in-pore cation population continues to increase with each addition of electrolyte, whereas the in-pore H_2O population reaches a maximum population at ~10.0 µL. Thus, for ionophilic systems, $\chi_{in\text{-}pore}$ is volume-dependent within the range of loading volumes studied here, a behaviour that has not been reported in prior studies. This highlights an important difference in pore-wetting behaviour between ionophilic and ionophobic systems, which should be considered when conducting quantitative NMR measurements, as the observed ion and solvent populations may not accurately represent those that would be observed in an excess of electrolyte.

To further explore specific cation effects on the adsorption behaviour, electrolyte species populations were measured for a series of sodium- and caesium-based electrolytes. **Figure 4.11** shows $\chi_{in\text{-}pore}/\chi_{neat}$ calculated at a loading level of 22.5 µL for a wider series of aqueous alkali salt solutions as measured by ^{1}H, ^{7}Li, ^{23}Na, and ^{133}Cs MAS NMR spectroscopy. This loading

level corresponds to the maximum electrolyte volume possible in the MAS NMR experiment without risking significant electrolyte leakage and spinning instability.

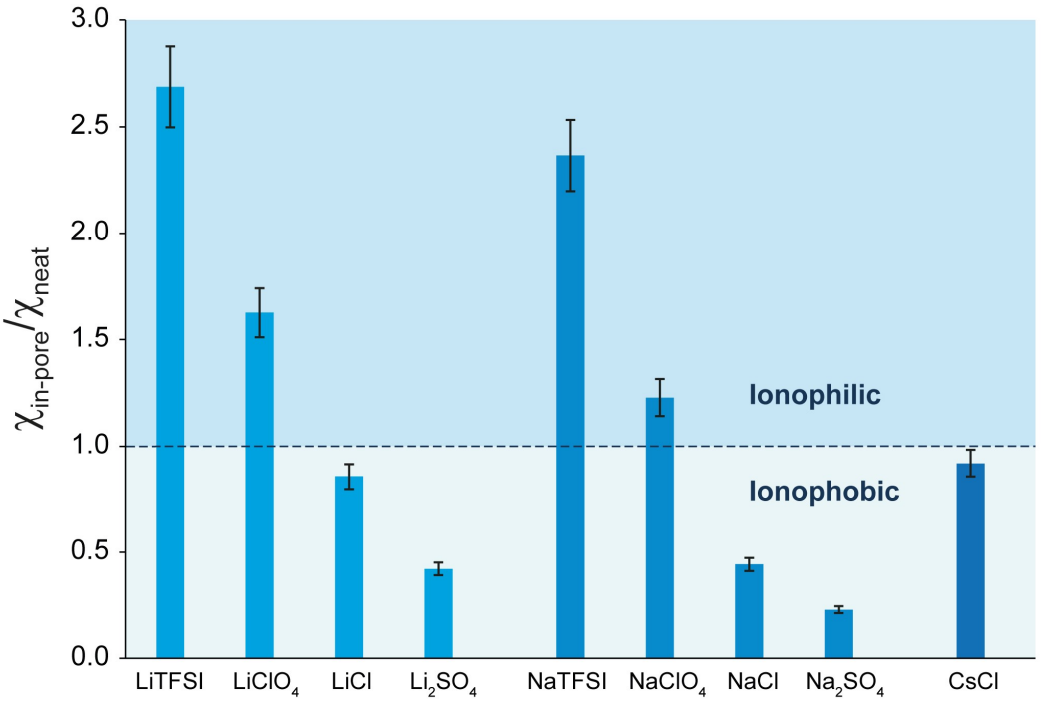

Figure 4.11. Calculated ratios between the in-pore cationic molar ratio, $\chi_{in\text{-}pore}$, and the neat cationic molar ratio, χ_{neat}, for a series of ACC-20 cloth samples (13 mg) soaked with 22.5 µL of aqueous alkali-metal electrolytes.

The Li^+ and Na^+ salts follow the same trend shown in **Figure 4.10** and prior work by Luo *et al.*,[24] with ACC-20 being the most ionophilic towards cations of $TFSI^-$ salts, and $\chi_{in\text{-}pore}/\chi_{neat}$ decreasing towards ionophobic character as the anion solvation strength increases. Between Li^+ and Na^+, there is a systematic decrease in $\chi_{in\text{-}pore}/\chi_{neat}$ whereby the carbon is slightly more ionophobic towards Na^+ salts than their Li^+ counterparts. However, the specific cation effects appear smaller than the specific anion effects. For CsCl, ACC-20 shows slightly more ionophilic character than LiCl. These observations are consistent with previous work on polymer-derived carbons soaked with the same electrolytes.[10]

The variation in $\chi_{in\text{-}pore}/\chi_{neat}$ for the studied electrolytes points to fundamental differences in pore-wetting behaviour. This behaviour relates to theoretical models predicting significant free energy barriers for strongly hydrated ions entering micropores.[147,150,292] The magnitude of the free energy barrier depends on factors including the relative size of pores and hydrated ions, and the ion-H_2O interaction strength.[149,293] For the sake of comparison, **Table 4.3** summarises reported hydration enthalpies, ΔH_{hyd},[294,295] and Gibbs free energies, ΔG_{hyd},[296] as qualitative indicators of the ion-H_2O interaction strength. Also listed are Gibbs free energies of transfer at

the organic solvent (nitrobenzene) to water interface, $\Delta G_{tr}^{O\rightarrow W}$, and the inner hydration sphere diameters, d_{hyd}, of various ions.[297]

Table 4.3. Experimentally determined values for the absolute standard molar enthalpies of hydration, ΔH_{hyd},[294] molar Gibbs free energies of hydration, ΔG_{hyd},[296] and standard Gibbs energies of transfer of ions from nitrobenzene to water, $\Delta G_{tr}^{O\rightarrow W}$,[297] quoted for the individual ions at 298.15 K. Hydrated ion diameters, d_{hyd}, reported by Marcus are also provided.[298]

Ionic species	ΔH_{hyd} / kJ mol^{-1}	ΔG_{hyd} / kJ mol^{-1}	$\Delta G_{tr}^{O\rightarrow W}$ / kJ mol^{-1}	d_{hyd} / nm
Li^+	–531	–475	–38.2	0.42
Na^+	–416	–365	–34.2	0.47
Cs^+	–283	–250	–15.4	0.63
SO_4^{2-}	–1035	–1080	-	0.76
Cl^-	–367	–340	–38.2	0.64
ClO_4^-	–246	–430	–7.9	0.74

The cation-specific effects on spontaneous electrolyte adsorption observed here agree well with trends observed in previous work[10] and broadly correlate with the known properties of the cations studied (**Table 4.3**). For Li^+ and Na^+, although the hydrated ion diameters of 0.42 nm and 0.47 nm are smaller than the ACC-20 average pore size (0.89 nm), these ions are known to exhibit strongly held second hydration spheres that resist distortion or rearrangement, leading to significant free energy barriers upon entry to sub-nanometre pores.[150,292] The larger diameter of Na^+ is consistent with the slightly suppressed in-pore population of the sodium salts compared to their lithium-based counterparts. While Cs^+ has a larger hydrated ion diameter (0.63 nm), it is a weakly hydrated ion, as evidenced by the smaller ΔH_{hyd} and ΔG_{hyd}. Calculated radial distribution functions show minimal evidence of a second hydration sphere, resulting in a smaller effective diameter and more ionophilic behaviour compared to that observed for Li^+ and Na^+.[10,299]

The anion-specific effects can be partially rationalised in the same way, whereby the magnitude of the hydrated ion diameter and free energy of hydration for SO_4^{2-} would be expected to restrict pore entry. As SO_4^{2-} preferentially resides outside the pores, electrostatic anion-cation interactions will suppress the in-pore cation population, as observed here by NMR. For Cl^-, which has a smaller hydrated ion diameter and less negative ΔH_{hyd} and ΔG_{hyd}, ionophobic behaviour is also observed but to a lesser extent than for SO_4^{2-}. In contrast, ACC-20 displays ionophilic behaviour towards ClO_4^- and TFSI salts. For ClO_4^-, despite having a large hydrated ion diameter of 0.74 nm, the lower absolute ΔH_{hyd} suggests a weak ion-H_2O interaction.

Additionally, the more negative ΔG_{hyd} indicates a significant entropic contribution to the hydration structure. The change to the hydration environment upon adsorption is difficult to predict; however, the small $\Delta G_{tr}^{O \rightarrow W}$ indicates that this anion is significantly more hydrophobic than the other ions studied and suggests that it may have more favourable ion-surface interactions within the carbon pores, which are non-polar to a first approximation. This helps to explain why adsorption may be favoured over residence in the ex-pore electrolyte.

It is noteworthy that simulations have predicted that the adsorption of the chemically similar TcO_4^- anion within a 0.68 nm pore is indeed energetically favoured.[147] For $TFSI^-$, the hydration energies have not been reported to the best of our knowledge, although density functional theory (DFT) calculations suggest that this anion is strongly hydrophobic with a positive ion-H_2O interaction energy.[82] This helps to explain why the $TFSI^-$ salts are the most readily adsorbed of the electrolytes studied. It also noted that aqueous $TFSI^-$ salts have been shown to exhibit lower contact angles on graphitic surfaces than more strongly solvated salts such as fluorides and chlorides, further pointing towards the hydrophobic properties of the former.[300,301]

While the adsorption behaviour of the cations directly observed by NMR can be partially rationalised based on specific anion and cation effects, for aqueous systems, it is also important to consider the potential of zero charge of the carbon surface and the possibility for self-ionisation of water, which generates hydroxide and hydronium ions. These ions can contribute to charge-balancing within both the in-pore and ex-pore environments. Consequently, it is unreasonable to assume that the adsorption properties of both salt ions are the same, and the precise populations of the unobserved (anionic) species in aqueous systems cannot necessarily be inferred from the measured cation populations. **Figure 4.12** shows the measured change in pH (ΔpH) of the neat electrolyte upon the addition of ACC-20 (10 wt%) in relation to $\chi_{in\text{-}pore}/\chi_{neat}$. For all electrolytes studied, the pH of the ex-pore electrolyte increases to give a basic solution. The precise origins of these pH effects are complex and not well understood, with possible contributions from imbalanced local anion and cation populations and electrolyte-surface interactions requiring careful consideration.[6,11,24,133] However, the magnitude of ΔpH appears to be linked to the cationic and anionic properties of the electrolyte, with more ionophilic electrolytes (higher $\chi_{in\text{-}pore}/\chi_{neat}$) resulting in larger pH changes. This suggests that the change in pH is at least in part linked to the relative accessibility of the electrolyte ions to the in-pore environment, with salts containing more hydrophobic anions, such as ClO_4^- and $TFSI^-$, giving larger pH changes.

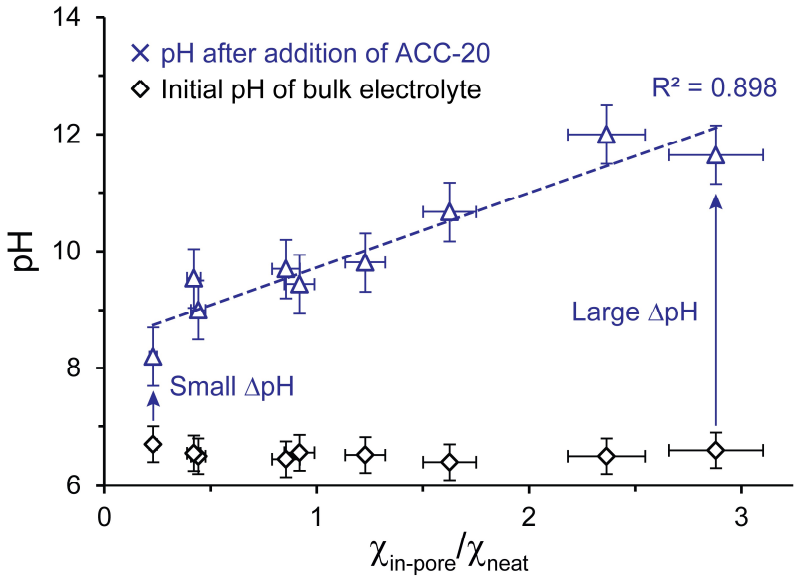

Figure 4.12. In-pore cationic molar ratios normalised by the neat electrolyte concentration, $\chi_{in\text{-}pore}/\chi_{neat}$, against the initial pH and the pH following the addition of 10 wt% ACC-20 for different electrolytes.

These results are consistent with observations in the recent work by Lyu *et al*., in which a large increase in pH was observed for 1 M LiTFSI aqueous electrolyte following the addition of the microporous carbon YP-50F.[133] The pH change observed by Lyu *et al*. was attributed to H_3O^+ adsorption driven by the surface basicity of the carbon pores, as characterised by XPS and Boehm titration, resulting in an increased uptake of $TFSI^-$ relative to Li^+. This imbalance in cation and anion populations has been previously observed, however the role of water self-ionisation was not discussed.[24,302] To gain further insight, ^7Li and ^{19}F MAS NMR spectra were acquired to determine cation and anion partitioning behaviour.

Figure 4.13 shows cationic and anionic molar ratios (both normalised by the neat cationic molar ratio) for ACC-20 loaded with incremental volumes of 1 M LiTFSI. An increased uptake of the $TFSI^-$ relative to Li^+ is observed, showing good agreement with observations in other studies.[24,133,302] A potential contribution to the observed pH effect, alongside surface basicity attracting hydronium ions, is the differing pore accessibilities between anionic and cationic species. It is inferred that weakly hydrated species such as $TFSI^-$ may readily enter the confined pore environment, whereas the insertion of more solvated species such as Li^+ is relatively suppressed. This creates an 'accessibility-driven ionic charge imbalance' between the in-pore and ex-pore environments. The pore-accessibility-determined excess negative charge within the pore is proposed to be balanced by an increased uptake of H_3O^+, with the excess positive charge outside the pore balanced by OH^-, giving rise to the measured increase in pH of the ex-pore solution.

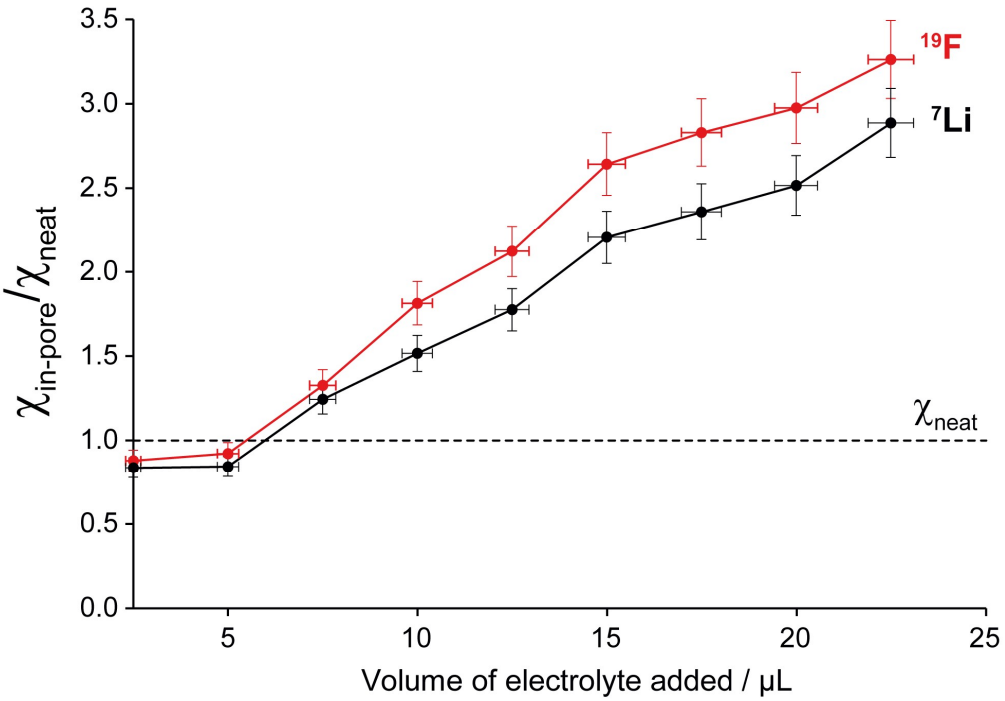

Figure 4.13. In-pore anionic and cationic molar ratios normalised by the neat electrolyte concentration, $\chi_{in\text{-}pore}/\chi_{neat}$, against loading volume. Anion and cation populations are derived from integrations of ^{19}F and ^{7}Li MAS NMR spectra, respectively.

To further probe the pH behaviour, an electrolyte comprising a weakly solvated cation, tetraethylammonium (NEt_4^+), and a strongly solvated anion, chloride (Cl^-) was investigated. Markedly, a decrease in the bulk electrolyte pH ($\Delta pH = -1.5$) was initially observed upon the addition of ACC-20 to a 1 M aqueous solution of NEt_4Cl. This decrease is tentatively assigned to an increased uptake of the weakly hydrated NEt_4^+ cation relative to Cl^-, resulting in an increased uptake of OH^-, decreasing the observed pH of the bulk solution. Interestingly, however, the pH of the bulk solution began to increase following its initial decrease, giving a ΔpH of +2.0 after 30 minutes. This indicates the presence of competing interactions, with further investigation being required to fully elucidate the complex mechanisms that are in effect.

Overall, differences in pore accessibility are proposed to partially contribute towards observed pH changes for the bulk solution upon the addition of activated carbon alongside contributions from the protonation of the carbon surface. However, it is acknowledged that an initial protonation of the basic carbon functionalities across the pore surface by H_3O^+ species may drive preferential anion insertion and suppress cation insertion. Overall, our results show that pH changes are a general phenomenon for aqueous salt solutions adsorbed on microporous carbons. Adsorption-driven dissociation of solvent H_2O molecules represents an important

difference compared to organic electrolyte solutions, which should be considered when making quantitative measurements of adsorption and charge-balancing.

4.3.5 Pore size effects on electrolyte ion partitioning

Figure 4.14a shows $\chi_{in\text{-}pore}/\chi_{neat}$ for the chloride salts soaked on ACC-20, ACC-15, and ACC-10, which have average micropore diameters of 0.89 nm, 0.68 nm, and 0.59 nm, respectively (**Table 4.1**).

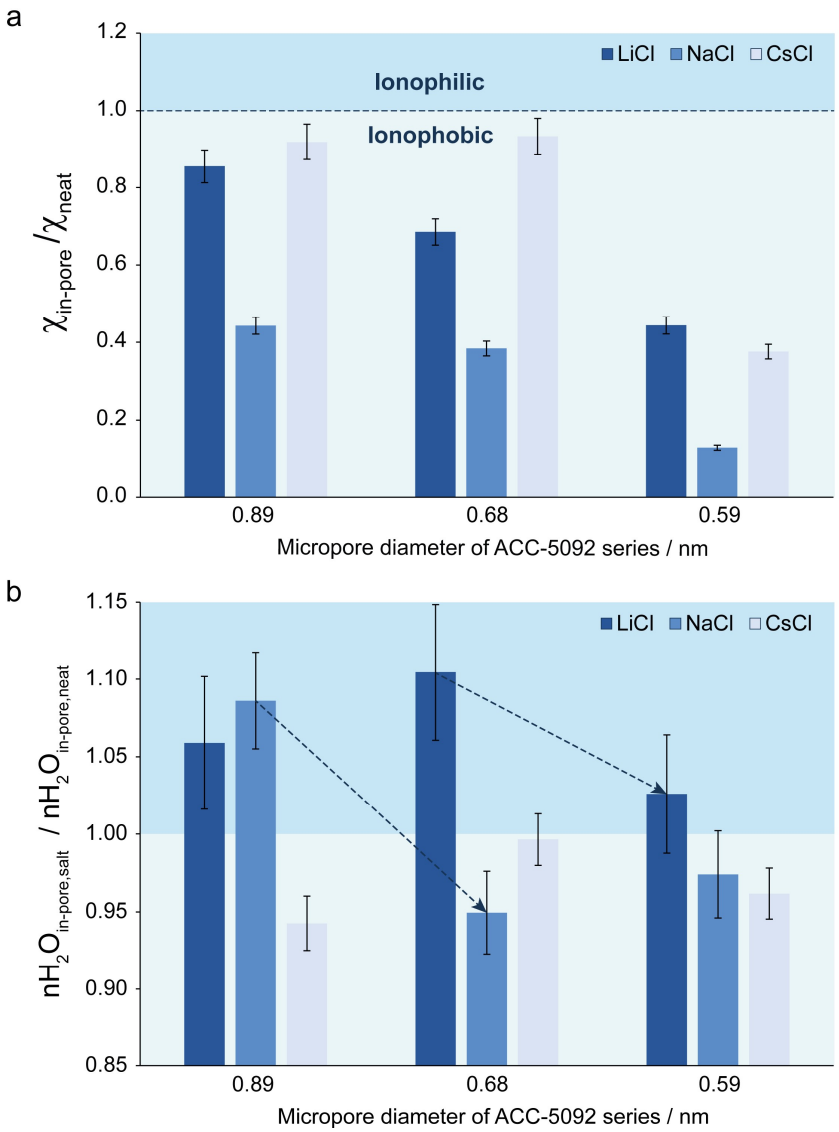

Figure 4.14. (a) In-pore cationic molar ratios calculated from MAS NMR for a loading of 22.5 µL normalised by cationic molar ratio for the respective neat solutions. The dotted line indicates the boundary between ionophilic and ionophobic behaviour. (b) In-pore H_2O populations of chloride salt electrolytes within the ACC-5092 series normalised by the in-pore H_2O population of neat water, represented by the colour boundary. Arrows denote abrupt drops in in-pore H_2O population with reducing pore width that result in a change from the > 1 regime towards the <1 regime.

Each system is ionophobic ($\chi_{in\text{-}pore}/\chi_{neat}$ <1), indicating positive adsorption energy irrespective of pore width in this range, which is consistent with results from other studies.[10,24,293] Each carbon is most ionophobic towards NaCl, indicating that Na^+ has the highest adsorption energy. This is attributed to Na^+ having a larger first hydration sphere relative to Li^+.[10,299,303–305] For LiCl, $\chi_{in\text{-}pore}/\chi_{neat}$ decreases continuously with decreasing pore width, whereas NaCl and CsCl show abrupt steps between pore widths of 0.68 nm and 0.59 nm. Calculated RDFs show that Li^+ and Na^+ have pronounced second hydration spheres (diameters of ~0.80 nm and ~0.88 nm, respectively),[10] which will become progressively more distorted with decreasing pore width, whereas the strongly hydrated inner hydration sphere is inferred to be maintained across all pore environments. In contrast, Cs^+ has a weaker second hydration sphere, so it appears that the inner hydration sphere dominates the adsorption properties. $\chi_{in\text{-}pore}/\chi_{neat}$ for CsCl is maintained between ACC-20 and ACC-15, indicating that the hydration structure of Cs^+ is not sensitive to the change in pore width from 0.89 nm to 0.68 nm despite its relatively large solvated diameter of 0.64 nm.[10] This behaviour is attributed to the relatively weak hydration strength of Cs^+ facilitating the distortion of its second hydration shell, enabling Cs^+ to readily insert into both 0.89 nm and 0.68 nm micropores.[295,306]

Figure 4.14b shows that, within ACC-20 (0.89 nm), the in-pore H_2O population for 1 M LiCl and NaCl solutions is greater than that of pure H_2O, suggesting changes in the packing arrangement of water within the pores.[307] This rearrangement is consistent with the high charge density of Li^+ and Na^+ forming structure within the pores, a behaviour ascribed to ionic kosmotropes, termed by Collins and Washbough.[291,305,307–311] This behaviour agrees with observations under applied potential by Levi *et al.*, whereby strongly hydrated cations (such as Li^+ and Na^+) readily bring large quantities of coordinated H_2O molecules with them into the in-pore environment. However, this observed behaviour depends upon sufficiently large pore dimensions to avoid a significant free energy barrier toward inserting the hydrated ions into the pore.[176,177]

For CsCl, **Figure 4.12b** shows a reduced in-pore H_2O population relative to pure H_2O. This behaviour is consistent with the 'structure-breaking' properties of chaotropes, such as Cs^+ which are more prone to partial desolvation and can therefore occupy space inside the pores which H_2O molecules could otherwise occupy.[177,291,308,312–315] **Figure 4.14b** also shows that as the average pore size is reduced from 0.89 nm to 0.68 nm, the pore-volume-normalised in-pore population, $\rho_{in\text{-}pore}$, for H_2O in the NaCl system decreases, suggesting a substantial alteration to the solvent-solute behaviour. Further reduction in pore size to 0.59 nm results in Li^+ and Na^+

exhibiting in-pore H_2O populations closer to neat H_2O. This suggests that, within increasingly confined environments, the influence of kosmotropic cations over H_2O rearrangement is effectively suppressed by decreasing pore widths as increasingly large free energy barriers towards adsorption restrict the adsorption of fully solvated kosmotropic ions.[305]

The adsorption behaviour of LiCl $\chi_{in\text{-}pore}$ and NaCl $\chi_{in\text{-}pore}$ across the ACC-5092 series indicate that a pore-width dictated, ion-specific restriction towards cation adsorption is in effect. As these differences are not observed for the weakly solvated, chaotropic Cs^+, it is inferred that the effect of pore-width on $\chi_{in\text{-}pore}$ for Na^+ and Li^+ correlates with the strong solvation-affinity of the kosmotropic cations. This phenomenon is well-documented within supercapacitor literature, where the ionic solvation energy can exceed the free energy barrier towards adsorption, preventing the distortion of the hydration sphere. In such instances, when the solvation radii approach pore diameters, a significant limitation on the accessibility of narrow microporous environments occurs.[90,137,306,316] Additionally, CHNS-O data (**Table 4.2**) and XPS results (**Figure 4.2**) show variation in the oxygen content across the ACC series; however, no strong correlation is observed between the surface content or bulk elemental composition and electrolyte partitioning behaviour.

4.3.6 Specific ion effects on Δδ

Figure 4.15a shows Δδ values recorded for chloride electrolytes and pure water soaked within the ACC-5092 series. For all NMR active nuclei studied across the alkali metal-chloride series (^1H, ^7Li, ^{23}Na, and ^{133}Cs), Δδ increases as the average pore width decreases. This can be partially ascribed to electrolyte species occupying regions of increasingly overlapping ring current induced shielding as pore size decreases.[22] A further contribution to the increasing Δδ across the series is the average domain size of the carbon, with larger domains inducing stronger ring current shifts.[13] Consequently, activated carbons with a lower degree of activation and lower pore volumes may have larger graphitic domains, giving larger Δδ for observed adsorbates. As noted above, CHNS-O results and XPS data indicate differences in the oxygen content across the ACC series (**Table 4.2** and **Figure 4.2**). As such, it is expected that variations in surface group functionalization may also contribute to observed differences in Δδ. ^1H Δδ values for each electrolyte and neat H_2O are similar across the ACC-5092 series. This indicates that in each system, H_2O molecules access similar regions of the microporous structure in each carbon, irrespective of the cationic species present. As ^1H Δδ is dominated by the ring current shielding induced by the carbon surface, it can be used as a probe for the magnitude of the

shielding induced by each carbon. Thus, the change in ^{1}H Δδ of −0.75 ppm observed as pore size is reduced from 0.89 nm to 0.68 nm and again from 0.68 nm to 0.59 nm is ascribed to both the narrowing of the pore structure and variations in the carbon domain size.

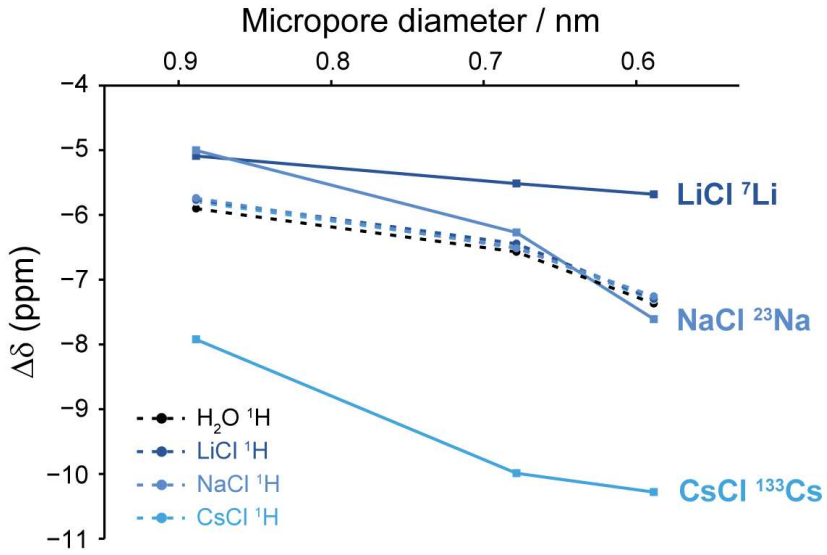

Figure 4.15. (a) Δδ values calculated from $\delta_{in\text{-}pore}$ and $\delta_{ex\text{-}pore}$ from ^{1}H, ^{7}Li, ^{23}Na, and ^{133}Cs MAS NMR spectra against the average pore width of the activated carbon cloths. Values are taken from a loading volume of 22.5 µL for deionised water and 1 M aqueous solutions of LiCl, NaCl, and CsCl soaked in ACC samples with different average pore sizes, *d*. ACC-20 (*d* = 0.89 nm), ACC-15 (*d* = 0.68 nm), and ACC-10 (*d* = 0.59 nm).

The ^{7}Li Δδ values show the least variation concerning pore diameter. Computational predictions by Sasikumar *et al.* show that the NICS is the dominant contributor towards ^{7}Li Δδ.[18] As such, the reduced ^{7}Li Δδ relative to ^{1}H Δδ across the carbons studied suggests that the strongly solvated Li^{+} cations are restricted from entering narrower, more shielded regions of the in-pore environment that free H_2O molecules can occupy. Na^{+} within ACC-20 exhibits a similar Δδ to Li^{+}. However, ^{23}Na Δδ increases by more than ^{7}Li Δδ for decreasing pore diameter (**Figure 4.15a**). The preferential adsorption of ions into larger pores,[10,13] and $\boldsymbol{\rho}_{in\text{-}pore}$ of the cationic species for NaCl being less than that of LiCl across the ACC-5092 series (**Figure 4.16**) indicates that the larger ^{23}Na Δδ observed is not due to Na^{+} occupying narrower pore environments.

Instead, the larger increase in ^{23}Na Δδ with respect to decreasing pore size is ascribed to contributions independent of ring current shielding, such as the distortion of the Na^{+} solvation shell during pore-insertion and the increased polarizability of Na^{+} relative to Li^{+}.[18,317] To further investigate the role of hydration on Δδ, DFT calculations were performed on isolated sodium cations and their immediate hydration environments.

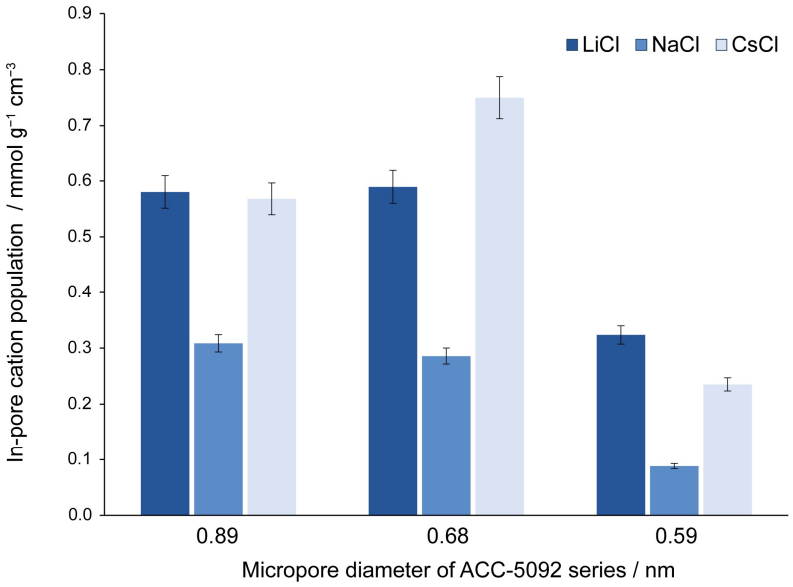

Figure 4.16. Pore-volume normalised in-pore cation populations for 1 M LiCl, 1 M NaCl, and 1 M CsCl within ACC-20, ACC-15, and ACC-10.

To study these effects, water molecules were removed one at a time, starting from a fully hydrated configuration, their geometries were then reoptimized and magnetic parameters were calculated.[18] **Table 4.4** shows isotropic magnetic shielding tensors and their respective chemical shifts for a sodium cation in different solvation environments calculated using DFT. δ_{iso} was given by:

$$\delta_{\mathrm{iso}} = 10^6 \cdot \left(\frac{\omega_n - \omega_{n=4}}{\omega_{n=4}}\right) \tag{4.4}$$

where ω_n is the precession frequency for a sodium with n water molecules in its hydration shell, and $\omega_{n=4}$ is the precession frequency for a sodium ion with 4 water molecules in its solvation sphere. ω_n was determined following:

$$\omega_n = -\gamma B_0 \left(1 - \frac{\sigma_{\mathrm{iso}}}{10^6}\right) \tag{4.5}$$

Where γ (MHz·T^{-1}) is the gyromagnetic ratio, B_0 (T) is the applied field strength, and σ_{iso} (ppm) is the calculated isotropic shielding tensor for sodium. The calculated chemical shifts suggest that ^{23}Na δ_{iso} is indeed sensitive to the solvation structure of Na^+, with desolvation shifting ^{23}Na $\delta_{in\text{-}pore}$ to a more negative chemical shift, increasing $\Delta\delta$. Similar trends were observed for models of Li^+, Rb^+, and Cs^+ by Sasikumar *et al.*[18] For weakly solvated ionic species entering narrow pores, the solvation sphere can be altered to enter otherwise inaccessible environments. This is a well-known phenomenon within the confines of

microporous environments.[4,19,37,137,150,177,299] DFT predictions by Sasikumar *et al*. detail a significant increase in Δδ for partially desolvated aqueous Cs^+ cations (−13.0 ppm) compared to those that are fully hydrated (−3.2 ppm).[18] This increase in ^{133}Cs Δδ is attributed to a significant change in $\delta_{in\text{-}pore}$ as water molecules are removed from the local environment, changing the local electronic environment and enabling a closer approach for Cs^+ to the pore wall.[18,37]

Table 4.4. DFT calculated isotropic magnetic shielding values σ_{iso} and the corresponding isotropic chemical shifts, δ_{iso}, for a sodium cation with varying degrees of hydration (arbitrarily referenced to $n H_2O$ = 4 ^{23}Na σ_{iso}).

nH_2O	^{23}Na σ_{iso} (ppm)	^{23}Na δ_{iso} (ppm)
4	564.0	0.0
3	573.2	−17.7
2	587.3	−35.4
1	605.1	−49.6
0	622.7	−58.8

The experimental ^{133}Cs Δδ value of CsCl within ACC-20 (−7.9 ppm) is larger than the predicted ^{133}Cs Δδ for a fully hydrated Cs^+ cation held at the carbon surface (−3.2 ppm).[18] This is attributed to partial desolvation of a proportion of Cs^+ cations upon pore entry. The dominant contribution to ^{133}Cs Δδ may be the removal of a water molecule from the local ^{133}Cs chemical environment, with a secondary contribution arising from the closer proximity to the pore wall.[18] It is also possible that a proportion of adsorbed Cs^+ across the ACC-5092 series are partially desolvated as ^{133}Cs Δδ is systematically larger than ^{7}Li Δδ and ^{23}Na Δδ.

A concomitant increase in ^{133}Cs Δδ and Cs^+ $\boldsymbol{\rho}_{in\text{-}pore}$ (**Figure 4.15a** and **Figure 4.16**) is observed as pore width is reduced from 0.89 nm to 0.68 nm following the change from ACC-20 to ACC-15. This is attributed to Cs^+ occupying more shielded in-pore environments within ACC-15 due to its narrower pores (and possibly larger domains) and a greater proportion of the pores exhibiting sufficiently large free energy barriers towards insertion as to promote the distortion of Cs^+ hydration spheres compared to micropores in ACC-20.

As the pore width is reduced from 0.68 nm to 0.59 nm, a slight increase in ^{133}Cs Δδ (−10.0 ppm to −10.3 ppm) and a significant decrease in CsCl $\boldsymbol{\chi}_{in\text{-}pore}$ (0.0178 to 0.0070) is observed (**Figure 4.15a**). It is inferred that the reduction in pore width to 0.59 nm induces a dramatic change in the behaviour of the CsCl system, incurring a significant resistance to pore insertion that was

not experienced within pore dimensions ≥ 0.68 nm. This is proposed to be due to a proportion of pore diameters becoming sufficiently narrow, and the free energy barrier towards insertion becoming sufficiently large, as to prevent the insertion of even partially dehydrated Cs^+. The well-known concentration dependence of ^{133}Cs δ has also been considered and is inferred to partially contribute to observed changes in ^{133}Cs Δδ (**Figure 4.17**).[10,318]

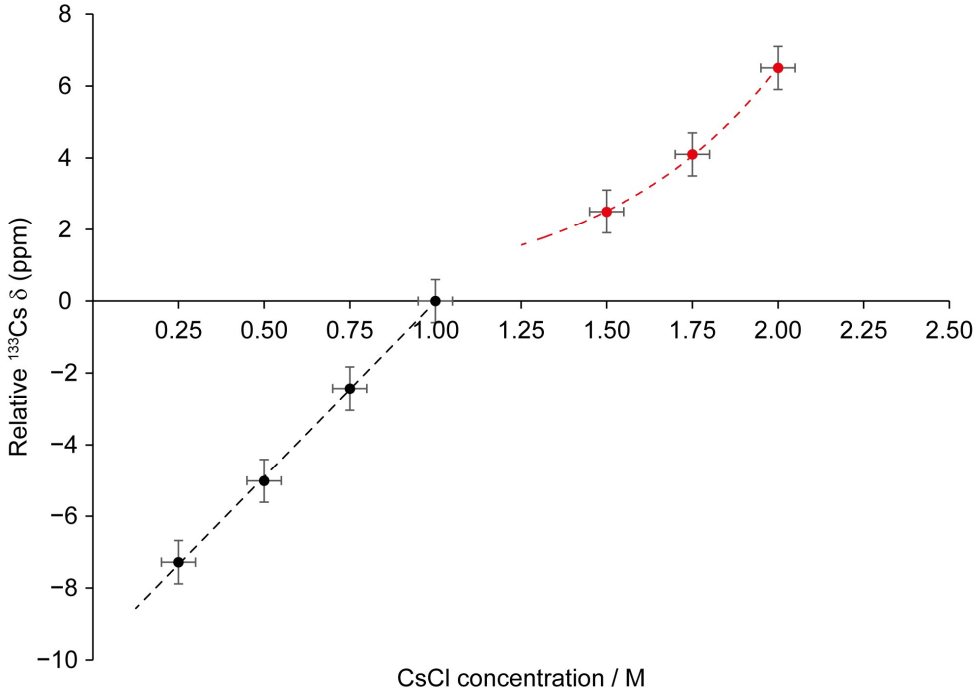

Figure 4.17. Recorded δ values from solution-state ^{133}Cs NMR spectra taken from CsCl solutions with a range of concentrations. δ values are referenced to the isotropic chemical shift recorded for 1 M CsCl.

4.3.7 Summary and outlook

Anion and cation properties have been shown to influence the spontaneous adsorption properties of ionic species and solvent molecules within porous carbons, with the precise behaviour arising from the interplay between different, and sometimes competing, factors. A key influence is the intrinsic solvation properties of the ionic species (kosmotropic/chaotropic character), with anion and cation behaviour being heavily influenced by their respective interactions with water molecules, as well as the interactions between the hydrated species and the microporous carbon structure. These ion-specific hydration effects influence the extent of ionophilicity or ionophobicity exhibited by the microporous environment and give rise to substantial differences regarding their adsorptive behaviour. For ionophilic systems, the arrangement of in-pore cations with respect to loading volume indicates an increased density of ionic species within the pore. However, it is noted that the anion population distribution has

not been quantified. Hence, the density of ionic species within the micropores remains relatively ambiguous for most electrolytes.

Ionophilic and ionophobic in-pore environments have been shown to behave fundamentally differently concerning loading volume, particularly regarding the stability of the population distribution as a function of electrolyte loading. This highlights that, for similar carbon-to-electrolyte ratios, ionophilic systems should be considered as volume-dependent systems following the saturation of their in-pore environment with water. In contrast, ionophobic systems can be considered volume-independent following saturation. This behaviour may change in systems containing a large excess of electrolytes, with ionic distribution becoming volume-independent for sufficiently large volumes. Solvation strength appears to influence $\Delta\delta$, and measurements of this parameter have helped to rationalise the ion and solvation behaviour in different systems.

NMR spectroscopy has been shown to provide insight into the mechanistic behaviour of electrolyte species within complex microporous carbonaceous environments. The role of the hydration sphere and ionic solvation strength is paramount in influencing the behaviour of these systems, with future investigations being required to elucidate the role of different solvents. A better understanding of the role that the local microporous structure has over the adsorption behaviour of the ionic species is required to develop optimised energy storage devices. Particularly, carefully tailoring microporous carbon properties and selecting specific ionic species within them will allow for sophisticated devices with myriad specialist applications.

Chapter 5

Studying specific ion effects on electrosorption behaviour using *in situ* NMR spectroscopy

5.1 Introduction

Results outlined in Chapter 4, along with recent studies in the literature, have demonstrated through NMR spectroscopy that specific electrolyte ion properties influence spontaneous adsorption behaviour within microporous carbons.[10,24] Theoretical models further suggest that the distribution of ionic species across the porous network prior to charging may have a marked effect on the charge-balancing mechanisms and, consequently, the electrochemical performance of supercapacitor devices. However, the quantification of electrosorption behaviour in relation to specific electrolyte ion properties is still lacking. Systematic studies employing advanced characterisation techniques are needed to provide deeper insight into the mechanisms underlying supercapacitance.

Several studies have demonstrated the use of NMR spectroscopy to probe the charging mechanisms of supercapacitor devices. However, many of these studies were performed *ex situ*, with the supercapacitor device being charged to a given voltage, disassembled to obtain the charged electrode, and then characterised using NMR spectroscopy.[64] The primary advantage of the *ex situ* approach is the ability to use magic angle spinning, vastly improving spectral resolution. However, the approach is inherently limited to observing equilibrium states, and performing extended measurements of a given system (*i.e.,* over hundreds of cycles) becomes exceedingly laborious. Moreover, the *ex situ* approach is inherently invasive, potentially resulting in a rearrangement of electrolyte species or solvent evaporation between the point of cell disassembly and NMR acquisition.

An alternative approach for characterising electrosorption behaviour is through *in situ* NMR spectroscopy. Here, spectra are acquired on working supercapacitor devices, allowing the observation of non-equilibrium states and avoiding issues associated with cell disassembly. Additionally, *in situ* experiments are more time efficient than *ex situ* experiments, as a single cell can be assembled and studied at different charge states and over several cycles. However, *in situ* NMR spectroscopy can only be performed using static samples which results in a significant reduction in spectral resolution due to the absence of magic angle spinning. *In situ* NMR spectroscopy has been developed and implemented extensively by Grey *et al*. to study electrosorption behaviour within supercapacitors comprising organic electrolytes.[16,29,31,35,64,99,201] In these studies, cells with laterally offset electrodes were used to study an electrode at a known polarisation independently from its oppositely charged counter-electrode. These studies have provided quantitative insight into charge-balancing mechanisms and how they vary with respect to the applied potential. Aqueous supercapacitors have also been studied using *in situ* NMR spectroscopy, albeit to a much lesser extent. Luo *et al*. showed that the strongly-solvated electrolyte ions of aqueous 0.8 mol kg^{-1} NaF within a PDC electrode (average pore diameter of 0.58 nm) existed predominantly outside of the pore, requiring a "gating voltage" of 0.4 V to drive a partial desolvation and subsequent insertion into the in-pore environment.[13,37] This study highlighted the importance of the relation between ion-solvent interactions and porous carbon structure for the adsorption and electrosorption of electrolytes. However, a complete understanding of this relationship is currently lacking, with further work being required to better understand the role of ion-solvent interactions on electrosorption mechanisms.

The results detailed by this chapter address the practical challenges associated with the study of aqueous supercapacitors using *in situ* NMR spectroscopy and the steps taken to ensure the acquisition of quantitative insights into charging behaviour. *In situ* NMR experiments acquired over stepped voltages and during simultaneous electrochemical cycling are presented. *In situ* ^{23}Na NMR spectra are acquired for electrolytes prepared from the weakly solvated NaTFSI (1 M) and the strongly solvated Na_2SO_4 (1 M) to probe the effect of ion-solvation interaction strengths upon electrosorption behaviour. *In situ* ^{19}F NMR spectra were also acquired for NaTFSI, allowing both the anion and cation behaviours to be probed during cycling. The charge-balancing mechanism is shown to vary distinctly between the two systems, with the spontaneously ionophobic system exhibiting a preference towards co-ion expulsion, and the spontaneously ionophilic system exhibiting a preference towards counter-ion insertion.

Interesting chemical shift changes are also reported for the ^{19}F and ^{23}Na in-pore resonance for 1 M NaTFSI, where under an applied voltage, the in-pore resonance shifts to a more negative chemical shift than that acquired at 0 V. These findings were corroborated using a stacked electrode setup in an *in situ* NMR experiment, wherein two distinct in-pore resonances are observed that shift in opposing directions with respect to the applied voltage.

5.2 Experimental details

5.2.1 Electrode and electrolyte materials

Activated carbon cloths and aqueous electrolytes detailed in Section 4.2.1 were prepared following the same procedure. Additional aqueous electrolyte solutions were prepared from lithium trifluoromethanesulfonate (LiOTf) (Sigma Aldrich, > 99%) and sodium trifluoromethanesulfonate (NaOTf) (Sigma Aldrich, > 99%).

5.2.2 Sample preparation

Activated carbon cloths were dried overnight under vacuum at 60 °C inside a Schlenk tube before electrodes were cut from the material. Electrodes were weighed and paired to within a tolerance of ±0.01 mg, and all electrodes were soaked in an excess of aqueous electrolyte solution for 12 h prior to electrochemical analysis or NMR spectroscopy experiments.

5.2.3 NMR parameters

NMR experiments were performed using a 400 MHz Bruker Avance III HD WB spectrometer, operating at a magnetic field strength of 9.4 T. For each sample, T_1 was determined using saturation recovery experiments and 90° pulse lengths were calibrated in each experiment to ensure quantitative spectra. ^{1}H, ^{7}Li, ^{19}F, and ^{23}Na NMR spectra were typically referenced to neat 1 M aqueous solutions of their corresponding electrolyte salts (0.0 ppm in each instance) unless otherwise specified.

5.2.3.1 MAS NMR experiments

^{1}H, ^{7}Li, ^{19}F, and ^{23}Na MAS NMR spectra were acquired using a double-channel HX 3.2 mm MAS probe at 9.4 T. Simple pulse-acquire experiments were performed for all nuclei. ^{1}H spectra were acquired using an 80 W pulse for 4.5 μs and a relaxation delay of 5 seconds, with 32 transients being recorded per spectrum. ^{7}Li spectra were acquired using a 120 W pulse for

4.5 μs and a relaxation delay of 2 seconds, with 64 transients being acquired per spectrum. ^{19}F NMR spectra were acquired using a 120 W pulse for 5.2 μs and a relaxation delay of 3 seconds, with 64 transients being acquired per spectrum. Finally, ^{23}Na NMR spectra were acquired over 128 transients using a 140 W pulse for 4.9 μs and a relaxation delay of 1.5 seconds.

5.2.3.2 In situ NMR experiments

^{7}Li, ^{19}F, and ^{23}Na *in situ* NMR spectra were acquired using a Bruker/ePROBE HX double resonance wide-bore static probe using a solenoid coil with an inner diameter of 10 mm. Coils with different numbers of turns were required to tune to the Larmor frequencies of specific nuclei of interest. *In situ* cells were orientated so that the electrode surface was aligned parallel to the applied field. ^{7}Li NMR spectra were acquired for mock *in situ* cells (*i.e.,* no wires connected to probe contacts) using a pulse-acquire experiment, with 320 transients being acquired using a relaxation delay of 5 seconds and an optimised 90° pulse of 200 W for 13 μs. A pulse-acquire experiment was also used for *in situ* ^{23}Na NMR experiments, with spectra being acquired over 32 transients using an optimised 90° pulse of 11 μs at 140 W, and a relaxation delay of 1 s for all samples. A double-echo pulse sequence was used to acquire *in situ* ^{19}F NMR spectra to reduce background signals arising from components within the probe and/or cell. Pulse durations of 20 μs and 40 μs at a power of 140 W were applied for the 90° and 180° pulses, respectively. A 14 second relaxation delay was implemented, and the spectra were acquired over 16 transients. Deconvolution of static NMR spectra was performed using the DMFit software.[319] A single peak was fitted to the in-pore resonance, whereas several peaks were used to fit the ex-pore resonance due to sharp features arising from BMS shifts and the broad exchange peak between the in-pore and ex-pore resonance. Gaussian: Lorentzian ratios and peak positions were allowed to correct freely to give the best fit between the simulated and experimental spectra.

5.2.4 Electrochemical characterisation

Ex situ and *in situ* electrochemical measurements were performed using a Biologic VSP potentiostat and Biologic SP-150 potentiostat, respectively. *Ex situ* data was obtained using a two-electrode configuration within Swagelok cells, comprising stainless steel current collectors (316L grade), a filter paper separator (Whatman, grade 1, 180 μm thickness), and a stainless-steel spring to maintain good contact between components. *In situ* electrochemical measurements were carried out inside the static probe using commercial *in situ* cells (NMR

service and ePROBE, internal cavity of the cell is rectangular with a length of 15 mm, a diameter of 6 mm, and a depth of 1 mm) containing gold mesh current collectors (Thermofisher Scientific, 0.064 mm diameter wires, 99.9%). Polytetrafluoroethylene (PTFE) sheet spacers (2 × 0.5 mm thickness) were added to the cell cavity to ensure good contact between the components. A two-electrode configuration was used for the *in situ* devices, with the electrodes being laterally offset by 1.5 cm so that the anode and cathode could be studied independently of one another by positioning a single electrode within the radiofrequency coil of the probe.[31] For all experiments, one electrode was studied with its polarity being reversed to study the effect of opposing voltages.

Cyclic voltammetry (CV) experiments and galvanostatic charge-discharge (GCD) experiments were performed on *in situ* and *ex situ* cells using a potential window of 0.0 V to 0.8 V. The specific capacitance of the working electrode, C_s, was determined following $C_s = 2C_T/m_w$, where m_w is the average mass of the two electrodes and C_T is the total capacitance across the cell, given by $C_T = I/(\Delta V/\Delta t)$, where I is the applied current and $\Delta V/\Delta t$ is the GCD discharge gradient. Reported C_s values were determined from GCD curves acquired using an applied current density of 0.1 A g^{-1}.

In situ cells were conditioned through *in situ* CV experiments at 100 mV s^{-1} (30 cycles), 10 mV s^{-1} (20 cycles), and 1 mV s^{-1} (10 cycles) prior to NMR data acquisition to ensure reproducible capacitive behavior. *In situ* NMR spectra were recorded for cells held at set voltages and cells undergoing dynamic cycling (cyclic voltammetry experiments). For cells held at defined voltages between 0.0 V and ±0.8 V, NMR data acquisition commenced once the change in current response of the cell was below 0.01 mA s^{-1} following the application of the voltage. For experiments involving simultaneous cyclic voltammetry and NMR data acquisition, spectra were collected at predetermined voltage intervals. To ensure minimal spectral changes between transients caused by variations in the applied voltage, a sufficiently slow scan rate of approximately 0.1 mV s^{-1} was used, allowing for the acquisition of multiple transients under similar charge states, and improving the signal to noise ratio of the NMR spectra.

5.3 Results and discussion

5.3.1 *In situ* NMR cell design

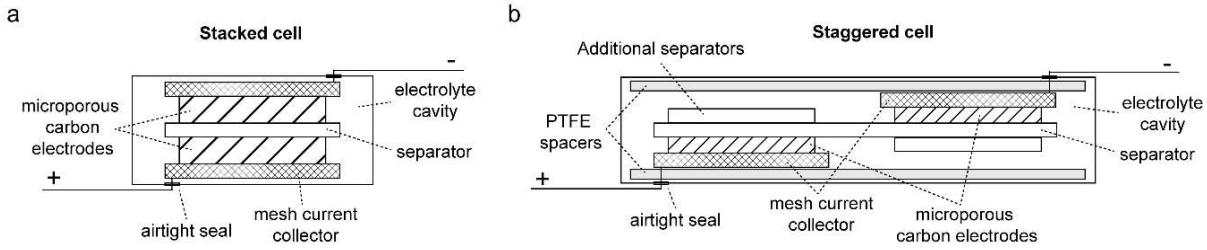

Figure 5.1. Schematic of the (a) stacked and (b) staggered *in situ* supercapacitor cell geometries.

Conventionally, supercapacitors are constructed using a stacked electrode arrangement (**Figure 5.1a**), wherein electrodes are aligned atop each other as to minimise the distance between the electrode surfaces. However, as outlined in previous studies by Grey *et al*., the stacked arrangement causes both electrodes to be positioned within the NMR coil, causing both electrodes to be observed simultaneously during *in situ* NMR experiments.[16,31,35,201] This geometry prevents the independent observation of electrosorption behaviour within an electrode of a defined polarisation as resonances from both electrodes are detected simultaneously. Typically, to avoid the detection of both electrodes, the electrodes are laterally offset from each other (**Figure 5.1b**).[31] This geometry allows for one electrode to be positioned within the solenoid coil of the probe, with the other electrode being positioned outside the region of detection, allowing an electrode of a defined polarisation to be independently observed. A further consideration for the design of the *in situ* cell is the use of mesh current collectors in place of a metallic foil, as a metallic foil will block the radiofrequency pulse from reaching the sample, preventing nuclear spins from being perturbed.

The cell geometry shown in **Figure 5.1** was housed within the commercially available PEEK cell manufactured by ePROBE. The depth of the internal cavity required the insertion of additional spacers to ensure sufficient contact between the components, preventing high resistive character in the electrochemical data. For cells containing ACC-20 electrodes, two 0.5 mm thick PTFE spacers were required. The need for the relatively thick spacers is inferred to be due to the poor contact between the fibrous surface of the ACC-20 electrode and the mesh current collectors. Additional pieces of filter-paper separator were soaked with electrolyte and added above the electrodes to further improve the internal contact between components and to provide a reservoir of electrolyte close to the electrode surface.

Figure 5.2 shows *in situ* cyclic voltammograms that were acquired at a scan rate of 10 mV s^{-1} for cells comprising ACC-20 soaked with 1 M NaTFSI using (a) a stacked electrode arrangement and (b) a staggered electrode arrangement. The electrochemical performance of the stacked *in situ* cell is comparable to that acquired using a Swagelok cell, demonstrating a quasi-rectangular shape that is typical of supercapacitors (see Chapter 2). A deviation from the desired rectangular cyclic voltammogram is observed for the staggered cell. This is inferred to be due to the increased separation between the electrodes resulting in an increased resistance and the generation of a weaker electric field.

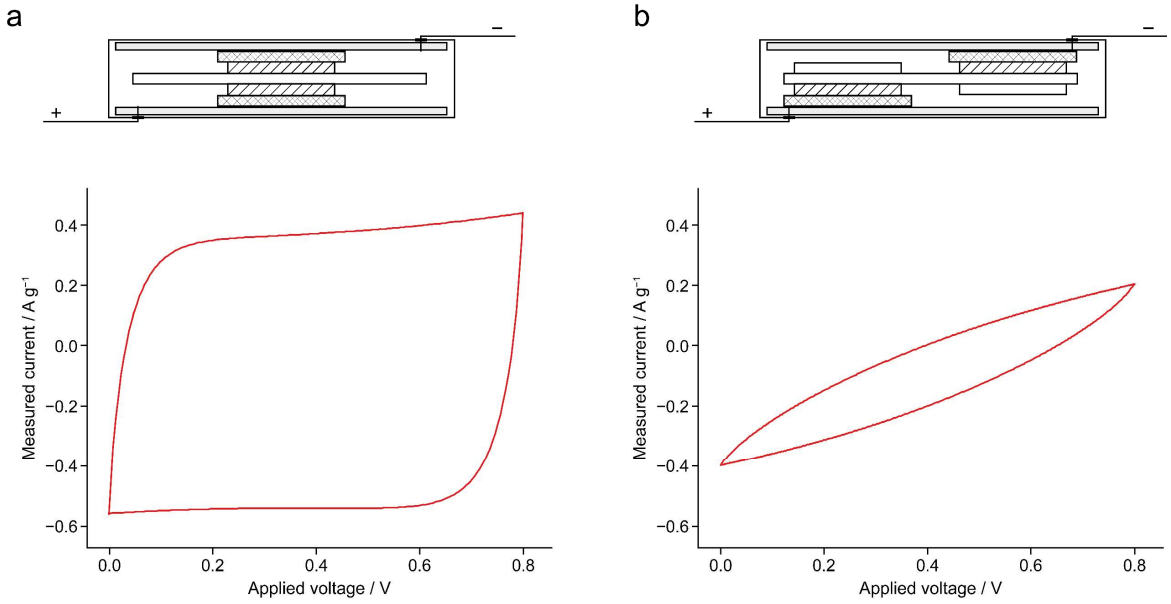

Figure 5.2. Schematic representation of cell geometry and the corresponding cyclic voltammograms (10 mV s^{-1}) acquired for (a) stacked and (b) staggered *in situ* cells comprising 1 M NaTFSI soaked ACC-20 electrodes, gold mesh current collectors, a filter paper separator, and PTFE spacers. Cycle number 20 is shown in each case.

Wang *et al*. demonstrated that a less-resistive cyclic voltammogram could be achieved by using an overlaid geometry, wherein the electrode is positioned at the opposing end to the wire cavity and an extended current collector is used.[31] However, for this system, minimal differences in the CV data were observed between the two geometries. As such, the staggered arrangement displayed in **Figure 5.2b** was utilised to minimise the amount of current collector used for each cell.

Figure 5.3 demonstrates that reducing the scan rate from 10 mV s^{-1} to 1 mV s^{-1}, results in a more rectangular CV curve. This change suggests that the cycling behaviour can be returned to that of an ideal capacitor through slower cycling. This is assumed to be due to resistive contributions from ion mobility (*i.e.,* ions being unable to move in response to the applied

voltage within the timeframe of the voltage sweep) being minimised, with slower scan rates allowing ions to efficiently pack to balance the charge applied across the electrode surfaces. A specific capacitance of ~115 F g^{-1} is estimated using the discharge current at 0.0 V from the 1 mV s^{-1} cyclic voltammogram. This is in relatively good agreement with capacitance values in the literature for cells comprising ACC-20 electrodes and aqueous sodium-based electrolytes.[94]

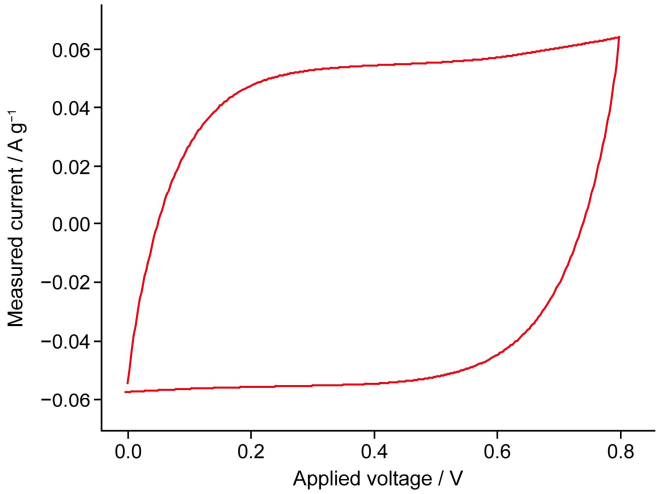

Figure 5.3. Cyclic voltammogram (Cycle number 20 acquired at 1 mV s^{-1}) acquired for the staggered *in situ* cell comprising 1 M NaTFSI soaked ACC-20 electrodes, gold mesh current collectors, a filter paper separator, and PTFE spacers.

Both *in situ* cell geometries (**Figure 5.2**) were cycled at scan rates of 1 mV s^{-1}, 10 mV s^{-1}, and 100 mV s^{-1}. All cells exhibited good cycle stability, showing no observable loss of capacitance over the first 50 cycles. Over a prolonged period, the aqueous solvent was found to evaporate, resulting in the recrystallisation of the electrolyte salt. For the bare *in situ* cell, the solvent was found to evaporate over a time-scale relevant to *in situ* NMR measurements, resulting in a gradual reduction in the intensity of the measured electrolyte resonances during extended experiments and the eventual failure of the cell. This issue was counteracted by using a silicone sealant and PTFE tape to seal the edges of the PEEK cell, reducing the rate of evaporation and allowing *in situ* cells to be cycled reproducibly for approximately 2-3 weeks.

5.3.2 Considerations for *in situ* NMR on aqueous supercapacitors

Before conducting *in situ* NMR experiments, a series of control experiments were performed to determine factors that will impact the observed NMR spectra. Firstly, preliminary studies investigating the difference in spectral resolution between static and spinning samples (due to practical limitations preventing the spinning of operating supercapacitor cells) were performed.

Samples were prepared by packing ACC-20 (13 mg) into a 3.2 mm rotor, and aqueous 1 M $LiClO_4$ (15 μL) was added via microsyringe. ^1H and ^7Li MAS NMR spectra were acquired using a simple pulse-acquire experiment at 9.4 T at spinning rates of 0 kHz and 5 kHz. Pulse durations were optimised to ensure a 90° pulse, and the relaxation delay, D_1, was optimised using a saturation recovery experiment, with D_1 being set to satisfy $D_1 > 5T_1$. The ^1H NMR spectra were referenced to the CH_3 resonance of alanine (1.2 ppm) and the ^7Li NMR spectra were referenced to neat 1 M $LiClO_4$ which was set to 0 ppm.

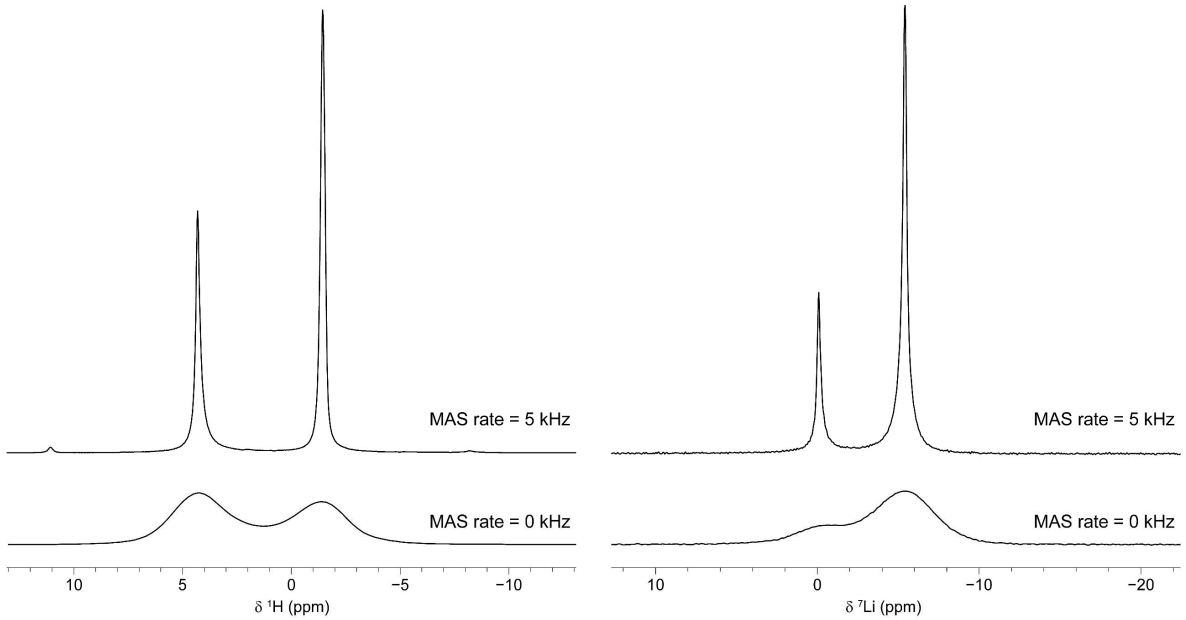

Figure 5.4. ^1H and ^7Li MAS NMR spectra acquired for ACC-20 (13 mg) loaded with 1 M $LiClO_4$ (15 μL) at MAS rates of 5 kHz and 0 kHz. Spinning side bands are denoted with asterisks.

Figure 5.4 shows ^1H (left) and ^7Li (right) NMR spectra acquired at spinning rates of 5 kHz (top) and 0 kHz (bottom). Ex-pore resonances are observed at 4.3 ppm and ~0.0 ppm, and the in-pore resonances are observed at −1.5 ppm and −5.4 ppm for the ^1H and ^7Li spectra, respectively. As the spinning rate is reduced from 5 kHz to 0 kHz, a significant broadening of the resonances is observed in both the ^1H and ^7Li spectra, resulting in a slight overlap of the in-pore and ex-pore peaks. This is due to the reintroduction of BMS effects into the static spectra that were removed by MAS averaging. Despite this broadening, the in-pore and ex-pore resonances can still be identified in the static spectra due to the good spectral resolution exhibited by ACC-20 (see Chapter 4). However, the overlap of the two sites makes a simple integration of the resonances difficult, complicating the determination of ion and solvent populations within the in-pore and ex-pore environments.

Mock cells comprising a pair of ACC-20 electrodes soaked with LiCl and various cell components were also investigated to isolate contributions from the cell geometry towards the spectral resolution. Static ^{7}Li NMR spectra were acquired for a mock cell comprising a pair of ACC-20 electrodes (each 8.0 mg and arranged in the stacked geometry) and a filter paper separator that were all soaked in 1 M LiCl for 12 hours. The cell was positioned inside the coil so that the electrode surfaces (*i.e.,* the largest cross-sectional area) were orientated parallel to the applied field as this orientation resulted in BMS shifts that maximised Δδ. Similar observations have been reported in studies on TiC-CDC electrodes.[35]

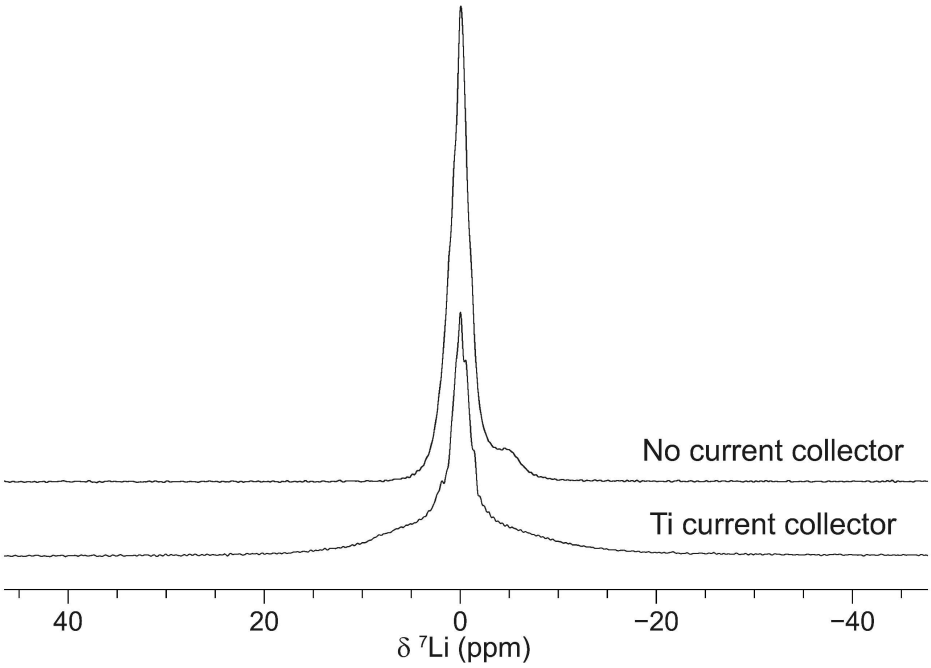

Figure 5.5. *In situ* ^{7}Li NMR spectra acquired for mock cells containing ACC-20 electrodes (2.75 mg each) soaked with 1 M LiCl, with and without the presence of a titanium mesh current collector.

Figure 5.5 shows the static ^{7}Li NMR spectrum acquired for the mock cell both with and without a titanium current collector. Firstly, for the cell without the current collector, the ex-pore resonance at ~0 ppm is shown to be substantially larger than the in-pore resonance at approximately −4.9 ppm. This is due to the excessive electrolyte volume in the cell components (*e.g.,* electrolyte-soaked separator and electrodes) and cell cavity relative to the total electrode pore volume. An additional contribution to the small size of the in-pore resonance relative to the ex-pore is the ionophobicity of ACC-20 pores towards LiCl (see Chapter 4). As observed in **Figure 5.4**, the resonances are broadened under static conditions, resulting in the large ex-pore resonance hiding a greater proportion of the small in-pore resonance. Thus, for a simple cell containing a separator, electrodes, and electrolyte, significant overlap between the in-pore and ex-pore peaks is observed, hindering the determination of ion populations within the two

environments. The reduction in resolution between the in-pore and ex-pore resonances is further compounded for ionophobic systems, wherein the relative intensity of the in-pore resonance is inherently reduced.

Figure 5.5 also shows the ^{7}Li spectrum acquired for the same mock cell with an added titanium mesh current collector. The spectrum of the cell containing the titanium mesh exhibits broader resonances which is inferred to arise from the BMS of titanium. The increased broadening from the titanium current collector hides the in-pore resonance that was previously observed at −4.9 ppm, preventing the determination of adsorption behaviour for this system. Therefore, when deciding on current collectors for *in situ* NMR experiments, it is important to select materials that exhibit a sufficiently small BMS so that the in-pore resonance is not obscured by broadening.

In addition to desirable magnetic properties, the current collector must exhibit stable electrochemistry with the electrolyte of choice across the applied voltage window. The combined requirements of a stable electrochemistry during cycling and desirable magnetic properties proved to be a challenging combination when selecting aqueous electrolyte-current collector pairings for *in situ* NMR experiments. The chloride electrolyte series (LiCl, NaCl, and CsCl) best demonstrate these challenges, as current collectors with magnetic susceptibilities that match the small diamagnetic susceptibility of the other cell components which enable the observation of the in-pore resonance (*e.g.,* Cu, Al, and Au) were found to exhibit poor cycling performance during cyclic voltammetry experiments, showing reduced capacitance and/or cell failure over extended cycling. This behaviour is attributed to faradaic reactions occurring between the electrolyte and the current collector. This was qualitatively confirmed through visual inspection of the cell components following extensive cycling, with cells that exhibited poor cycling stability displaying signs of corrosion (*e.g.,* a green solid on the surface of Cu current collectors, indicating the formation of $CuCl_2$, and the visible breakdown of Al into a white precipitate, signifying the formation of $AlCl_3$).[320]

For the aqueous chloride electrolytes, current collectors that exhibited good cycling stability (Ti and Ni) severely broadened the electrolyte resonances in the NMR spectra, preventing the in-pore population from being determined. As such, the electrosorption behaviour of aqueous chloride electrolytes could not be studied using *in situ* NMR as a suitable current collector was not identified. Further work is required to build a comprehensive library of suitable current collector-electrolyte pairings for use in *in situ* NMR studies to provide insight into the charging mechanisms of different electrolytes.

5.3.3 Investigating specific anion effects on electrosorption behaviour

The specific ion behaviour for spontaneous adsorption within porous carbons may influence the charging mechanisms under an applied potential.[2,16] To gain further insight into this, *in situ* ^{23}Na NMR spectra were recorded for cells comprising ACC-20 electrodes soaked with aqueous 1 M NaTFSI and aqueous 1 M Na_2SO_4 across a range of applied potentials (±0.8 V). Although the SO_4^{2-} anion populations were not quantified directly, it is possible to infer qualitative information about the charging mechanism from the observed behaviour of the cations.

The *in situ* cells were constructed using laterally offset electrodes to allow the observation of a single electrode environment. Additional PTFE separators were placed to ensure good contact between the electrode and the current collectors. All cells were cycled before *in situ* NMR spectra were acquired, running *in situ* cyclic voltammetry (CV) experiments at 100 mV s^{-1}, 10 mV s^{-1}, and 1 mV s^{-1} before acquisition. **Figure 5.6a** shows *in situ* CV curves acquired at a scan rate of 1 mV s^{-1} for cells comprising ACC-20 electrodes soaked with 1 M Na_2SO_4 and 1 M NaTFSI. The CV curves both present quasi-rectangular shapes with no peaks, indicating that no Faradaic reactions occur across the applied potential window. **Figure 5.6b** shows the galvanostatic charge-discharge (GCD) data recorded prior to NMR data acquisition for the same systems using a current density of 0.1 A g^{-1}. Specific capacitances of 107 F g^{-1} and 100 F g^{-1} were determined from the GCD discharge curves for cells comprising 1 M NaTFSI and 1 M Na_2SO_4, respectively. A large internal resistance is observed in both cells due to the staggered electrode arrangement.[31]

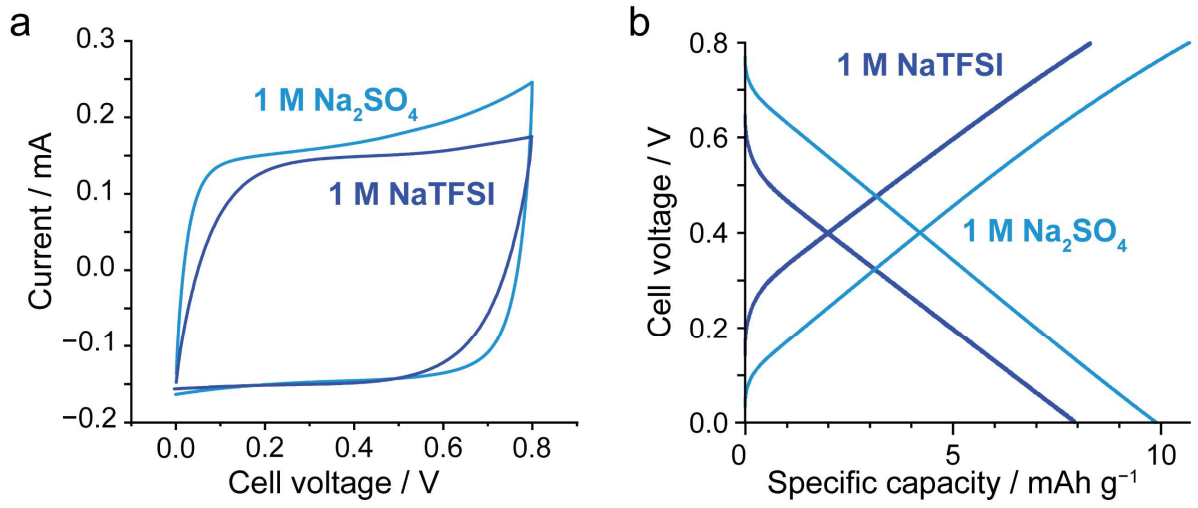

Figure 5.6. (a) Cyclic voltammograms (1 mV s−1, cycle 180) and (b) galvanostatic discharge curves (0.1 A g−1, cycle 180) recorded *in situ* for staggered symmetrical ACC-20 (2.73 mg per electrode) cells soaked with 1 M NaTFSI and 1 M Na2SO4.

No significant differences in C_s were observed between the 1 M NaTFSI and 1 M Na_2SO_4 cells, despite their differing electrolyte wetting properties. This suggests that the relationship between capacitance and ionophilicity/ionophobicity is not straightforward. While Kondrat *et al*. predicted differences in the charging dynamics between ionophobic and ionophilic systems, this study found no significant difference in the charging dynamics between the two systems.[25,154] However, due to the non-optimal cell geometry for *in situ* NMR, it is likely that other sources of electronic and ionic resistance dominate the charging dynamics.

Figure 5.7 shows ^{23}Na NMR spectra acquired at an applied voltage of 0 V for the *in situ* cells following cycling. The cell was oriented with the electrode surface parallel to the applied field, and only one electrode was positioned within the solenoid coil of the probe. The resulting spectra were referenced to the neat electrolyte solution at 0 ppm. Both spectra display two broad peaks corresponding to the in-pore and ex-pore environments, along with several additional features near the ex-pore peak attributed to BMS effects from the gold current collector and the irregular shape of the sample. Importantly, the introduction of these cell components does not hinder the identification of the in-pore and ex-pore resonances.

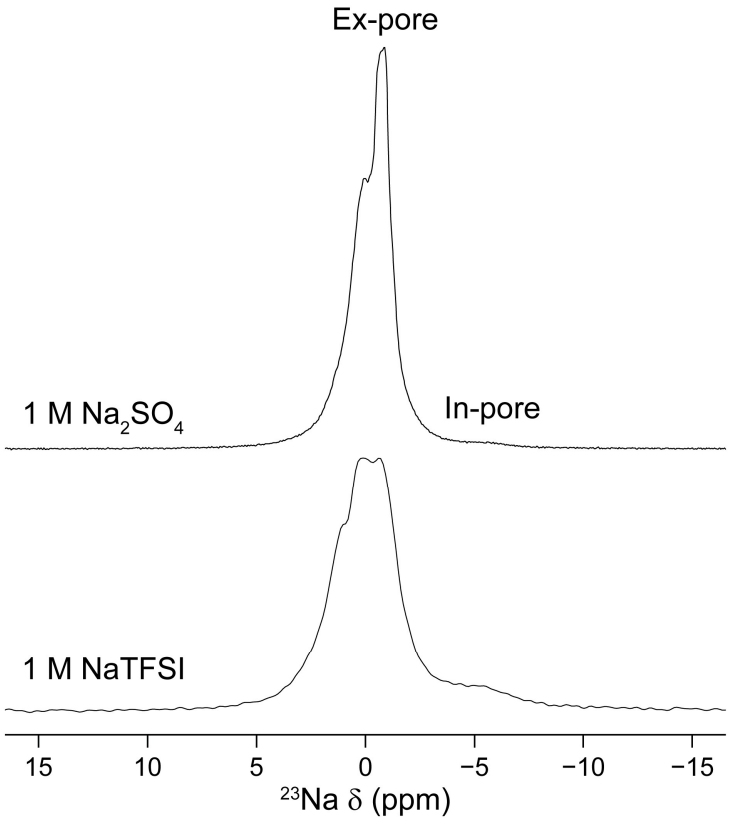

Figure 5.7. *In situ* ^{23}Na NMR spectra acquired for 1 M Na_2SO_4 and 1 M NaTFSI in the absence of an applied voltage. Cells comprise gold mesh current collectors, ACC-20 electrodes (2.73 mg each), PTFE spacers (2 × 0.5 mm), and a filter paper separator.

The in-pore resonances in the ^{23}Na NMR spectra for 1 M NaTFSI (−5.3 ppm) and 1 M Na_2SO_4 (−4.7 ppm) show significant differences in intensity relative to the ex-pore. This is attributed to the different spontaneous adsorption properties of the two electrolytes within ACC-20 (see Chapter 4), with the strongly ionophobic Na_2SO_4 giving a low-intensity in-pore peak and the ionophilic NaTFSI exhibiting an in-pore peak of greater intensity.[321] The *in situ* Δδ values deviate from values acquired for model systems under MAS, with ACC-20 (13 mg) loaded with electrolytes (15 μL) in the absence of an applied potential giving a Δδ of −6.2 ppm and −6.0 ppm for 1 M NaTFSI and 1 M Na_2SO_4, respectively. Additionally, the ex-pore resonance is shifted to a more negative chemical shift relative to the neat electrolyte (0 ppm), with NaTFSI shifting by −1.0 ppm and Na_2SO_4 shifting by −0.8 ppm. The observed differences in Δδ between the model spectra and the *in situ* spectra are attributed to subtle changes in the BMS arising from variations in electrode geometry and cell orientation. The effect of subtle differences in the BMS on the observed NMR spectra are demonstrated in **Figure 5.8**, in which the ^{23}Na NMR spectra for two different 1 M NaTFSI cells comprising the same components and electrode masses are shown.

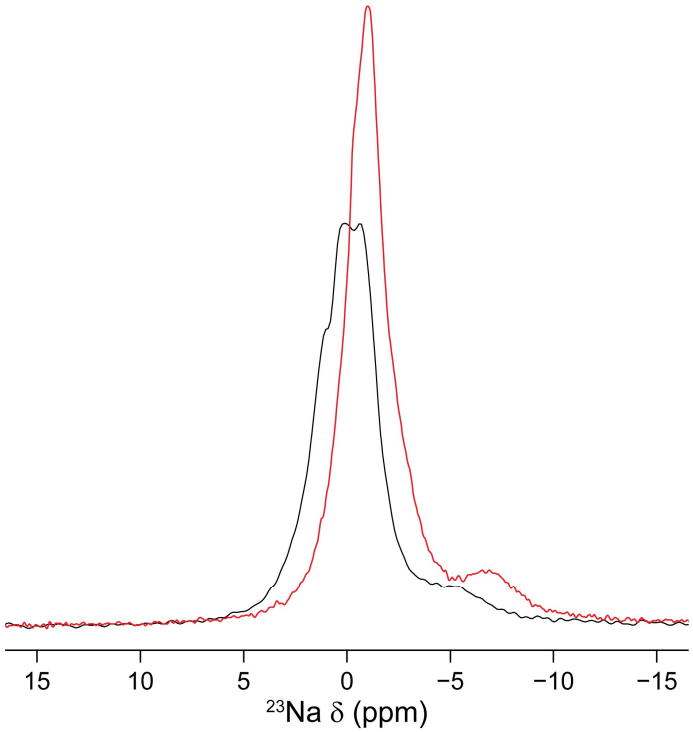

Figure 5.8. *In situ* ^{23}Na NMR spectra acquired at 0 V for different cells comprising 1 M NaTFSI, gold mesh current collectors, ACC-20 electrodes (2.73 mg each), PTFE spacers (2 × 0.5 mm), and a filter paper separator.

A quantitative analysis of populations cannot be determined due to ambiguity regarding the total volume soaked into the electrode and the loss of electrolyte during cell assembly.

However, a qualitative analysis of the population distribution can be performed. To determine the distribution of the cations between the in-pore and ex-pore environments, spectra were deconvoluted into simplified components. **Figure 5.9** shows the deconvolution of the ^{23}Na NMR spectra in **Figure 5.7**, wherein peaks are fitted to the broad in-pore and ex-pore resonances, the features due to BMS effects, and a region describing exchange between the in-pore and ex-pore environments. The chemical shift, peak intensity, peak width, and the ratio between the Gaussian and Lorentzian lineshape of the fitting peaks were allowed to vary freely as to provide the best fit between the simulated and experimental spectra. The integrals of the deconvoluted components of the ^{23}Na NMR spectra acquired at 0 V were set as reference values, against which the integrals of deconvoluted spectra acquired under applied voltages would be compared to determine electrosorption behaviour. For the deconvolution of a series of spectra acquired under different applied potentials, the spectrum acquired at 0 V was fitted first as this typically exhibited the best resolution of the in-pore resonance. The remaining spectra were then fitted using the initial fit of the 0 V spectrum as a point of reference.

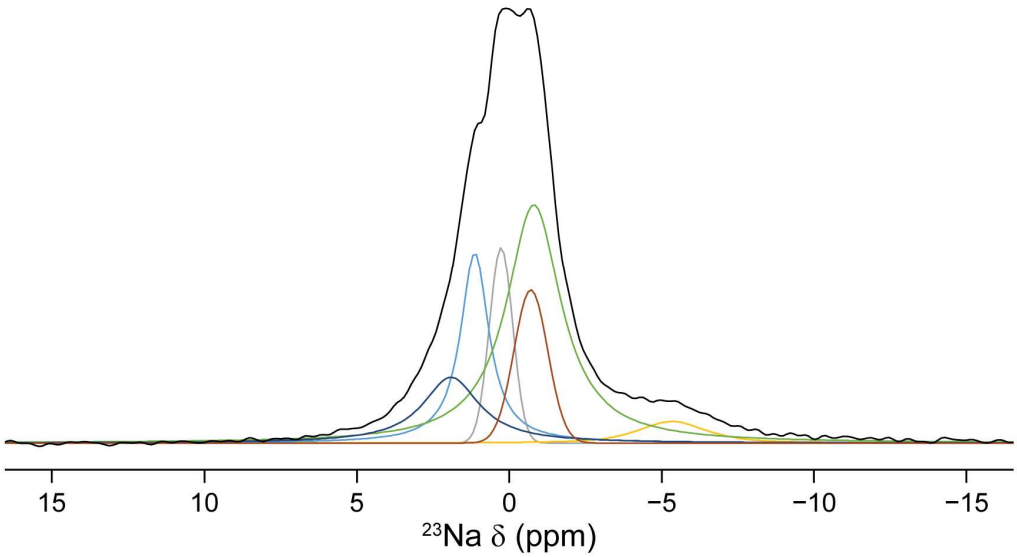

Figure 5.9. Deconvoluted *in situ* ^{23}Na NMR spectrum for a cell comprising 1 M NaTFSI acquired in the absence of an applied voltage.

5.3.3.1 Potential-driven changes in cation partitioning

To investigate changes in the Na^+ cation population distribution as a function of applied potential, ^{23}Na NMR spectra of a single electrode were acquired while the cell was held at set voltages.[29] Following the application of a voltage, the cell was allowed to rest until the current response of the cell stabilised (> 0.01 mA s^{-1}), after which NMR spectra were acquired. The acquired static ^{23}Na NMR spectra necessitated small adjustments in spectral phasing across

different applied voltages, which gave variations of up to ±25% in the deconvoluted in-pore population. Due to this phasing sensitivity, an error margin of ±25% has been incorporated into the determined populations.

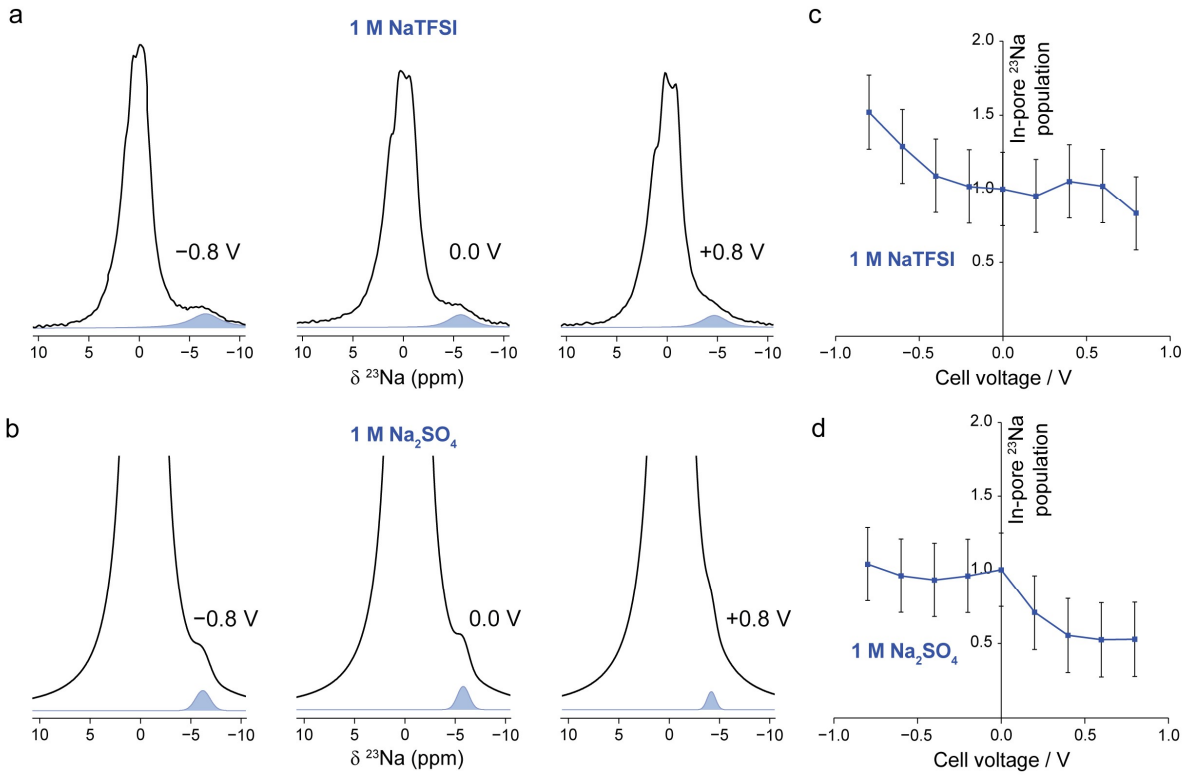

Figure 5.10. ^{23}Na NMR spectra recorded *in situ* for cells comprising (a) 1 M NaTFSI and (b) 1 M Na_2SO_4 at 0.0 V and ±0.8 V. Spectra for each electrolyte are shown on the same vertical scale. Calculated in-pore ion populations over a potential range of ±0.8 V are shown for (c) 1 M NaTFSI and (d) 1 M Na_2SO_4 cells. In-pore ion populations are referenced to the in-pore population recorded at 0 V and are derived from the integrals of the deconvoluted in-pore resonances shown in blue in (a) and (b).

Figure 5.10a-b show *in situ* ^{23}Na NMR spectra obtained at 0.0 V and ±0.8 V for the NaTFSI and Na_2SO_4 systems, respectively. The deconvoluted in-pore resonances are highlighted. Under a positive applied potential, an essentially unchanged in-pore ^{23}Na population was observed for the 1 M NaTFSI system (**Figure 5.10c**). This indicates that, under a positive applied potential, the adsorption of counter-ions into the pore is the dominant charge-balancing mechanism. Under a negative applied potential, the in-pore ^{23}Na population steadily increased as the voltage became increasingly negative, implying the preferential adsorption of Na^+ counter ions into the pores. Thus, a counter-ion adsorption mechanism appears to be the dominant charging mechanism across both polarities for the 1 M NaTFSI system. For 1 M Na_2SO_4, the in-pore ^{23}Na population under a negative polarization remains unchanged (**Figure 5.10d**). This suggests that the unobserved SO_4^{2-} anions are removed from the in-pore

environment via a co-ion expulsion mechanism to balance the charge across negatively polarized carbon surfaces. Under a positive voltage range, the ^{23}Na population ratio decreases as the voltage increases, indicating co-ion expulsion. Therefore, the preference for charge-balancing is implied to dominate across both electrode polarities.

The ionophobic properties of ACC-20 towards spontaneous Na^+ adsorption for Na_2SO_4 is seemingly reflected in the charge-balancing mechanism, with ion expulsion being preferred. The ionophilic 1 M NaTFSI system is also shown to follow a charging mechanism that results in an increased in-pore cation population. These results indicate that the inherent ionophilicity/ionophobicity of the electrolyte-porous carbon system in the absence of an applied potential influences the preference towards specific charge-balancing mechanisms within charged systems. Despite differing charging mechanisms, the similar specific capacitances for 1 M NaTFSI and 1 M Na_2SO_4 suggest the link between the charging mechanism and capacitance is complex and requires further work to fully understand.

To further validate the inferred electrosorption behaviour observed in the ^{23}Na NMR spectra, *in situ* ^{19}F NMR spectra acquired for the 1 M NaTFSI system. The same cell was used in both the ^{23}Na and ^{19}F NMR experiments, with both spectra being acquired in succession at set voltages. The double-echo pulse sequence was used to acquire ^{19}F NMR spectra to minimise background signal from components within the probe and the cell. **Figure 5.11a** shows the *in situ* ^{19}F NMR spectrum acquired for the 1 M NaTFSI cell at an applied voltage of 0 V. The spectrum is referenced to the neat solution of 1 M NaTFSI, with the in-pore and ex-pore resonances being observed at −4.3 ppm and −0.2 ppm, respectively. As with the *in situ* ^{23}Na NMR spectra, the observed $\Delta\delta$ differed from values measured for a model system ($\Delta\delta$ = −5.9 ppm) of ACC-20 (13 mg) loaded with 1 M NaTFSI (15 μL) due to BMS effects. The relative intensity of the in-pore resonance in the ^{19}F spectrum is significantly larger than that of the in-pore peak in the ^{23}Na spectrum. This is attributed to the use of the double-echo pulse, in which ex-pore nuclei that exist outside the centre of the solenoid coil are filtered out as they do not undergo a 90° flip-angle. Additionally, the ionophilic nature of the ACC-20|$TFSI^-$ system is inferred to contribute to the increased intensity of the in-pore peak relative to the ex-pore peak.

Figure 5.11b shows the recorded populations of the $TFSI^-$ anions and the Na^+ cations from the deconvoluted *in situ* ^{19}F and ^{23}Na NMR spectra. Under a positive applied potential, the ^{19}F in-pore population increases while the ^{23}Na in-pore population remains unchanged. Conversely, under a negative potential, the ^{19}F in-pore population stays the same, and the ^{23}Na in-pore population increases. The findings from the *in situ* ^{19}F NMR data are consistent with the *in situ*

^{23}Na NMR results, suggesting that a counter-ion adsorption is the primary charge-balancing mechanism for the ionophilic NaTFSI electrolyte.

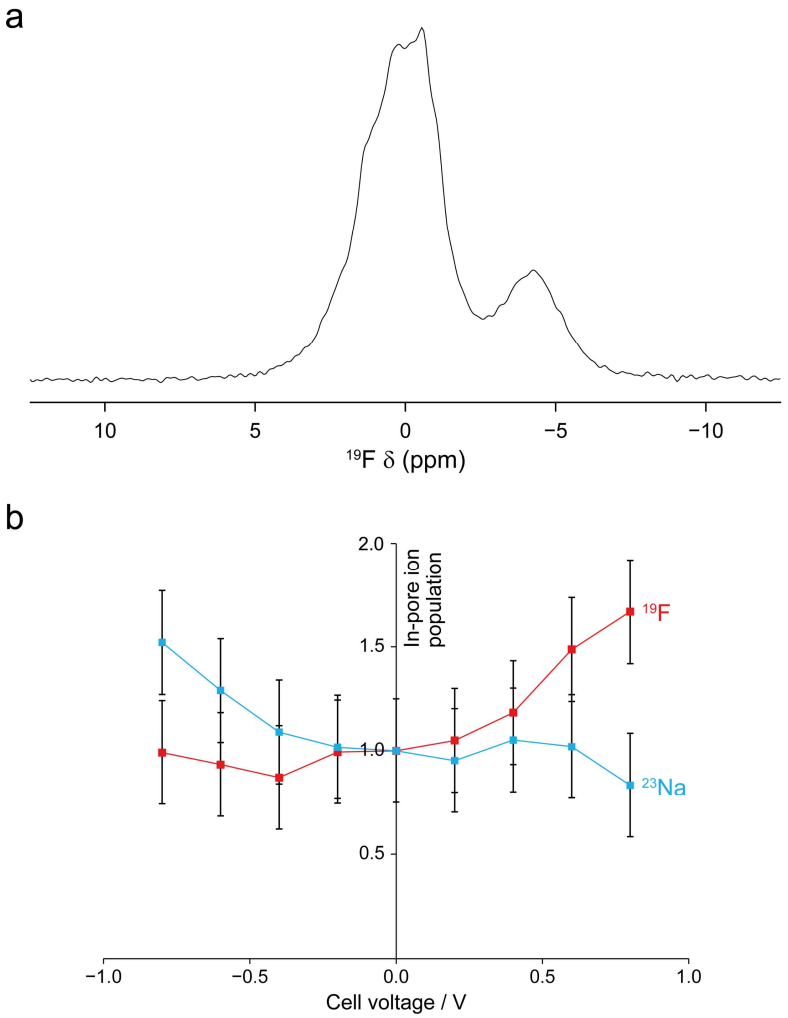

Figure 5.11. (a) ^{19}F NMR spectrum recorded *in situ* for cells containing 1 M NaTFSI. The spectrum was acquired using a double-echo pulse sequence at an applied voltage of 0 V. (b) Calculated in-pore anion and cation populations over a potential range of ±0.8 V are shown for the 1 M NaTFSI cell. In-pore ion populations are referenced to the in-pore population recorded at 0 V.

5.3.3.2 Potential-driven effect on Δδ

By examining the chemical shifts of in-pore and ex-pore resonances, insight into the effect of different electrode polarisations on local ion environments can be gained. **Figure 5.12a-b** shows overlaid *in situ* ^{19}F and ^{23}Na NMR spectra acquired for a cell comprising ACC-20 electrodes (each 2.73 mg) and aqueous 1 M NaTFSI that had been cycled prior to the acquisition of the NMR spectra. MAS NMR spectra (spinning rate of 5 kHz) for a model system of ACC-20 (13 mg) loaded with 1 M NaTFSI (22.5 µL) are also displayed for reference (**Figure 5.12c-d**). To enhance visual clarity, all spectra are referenced such that the ex-pore peak at 0 V is set to 0 ppm.

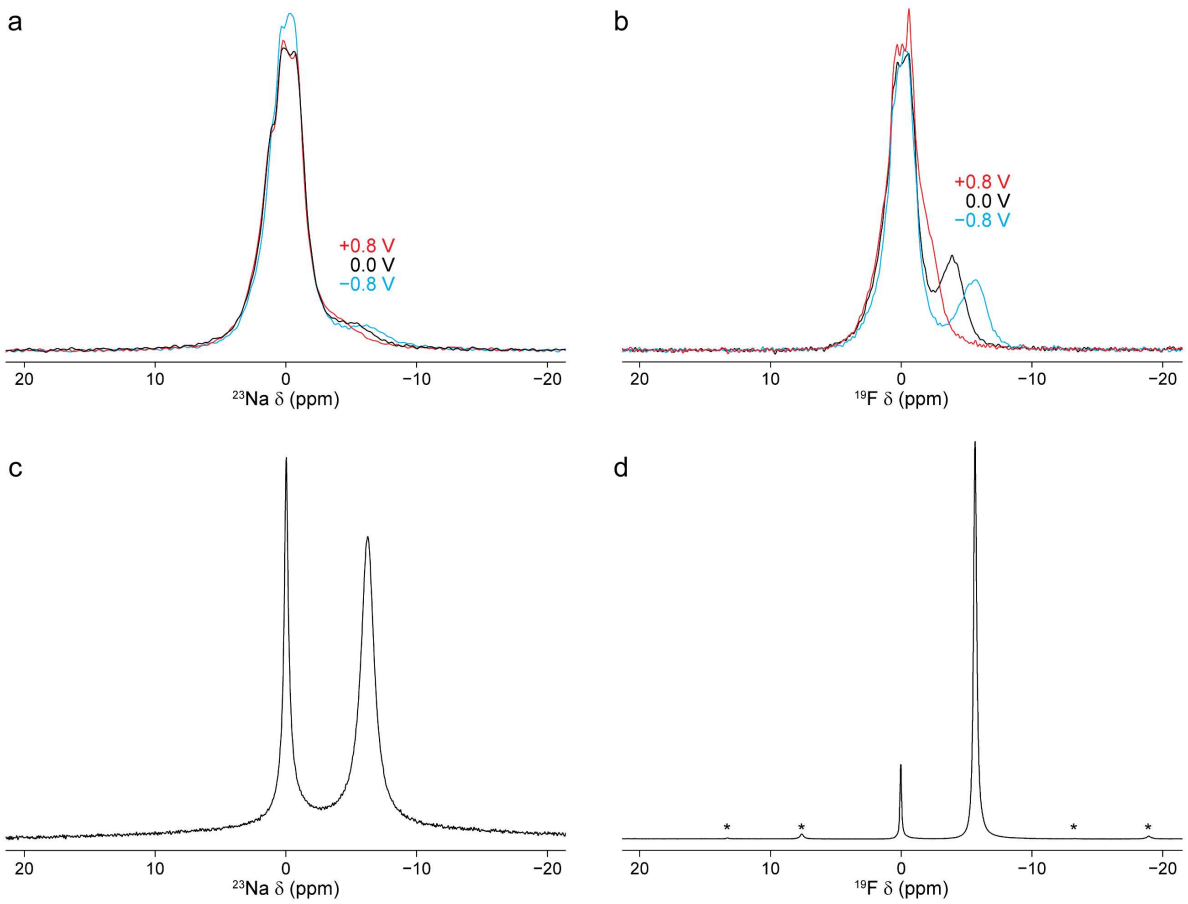

Figure 5.12. *In situ* (a) ^{23}Na and (b) ^{19}F NMR spectra at different applied voltages (0.8 V, 0 V, and −0.8 V) for a cycled cell comprising ACC-20 electrodes (2.73 mg each), aqueous 1 M NaTFSI electrolyte, gold mesh current collectors, PTFE separators (2 × 0.5 mm), and a filter paper separator. Both spectra are referenced such that the ex-pore resonance at 0 V is set to 0 ppm. (c) ^{23}Na and (d) ^{19}F MAS NMR spectra (MAS rate = 5 kHz) for ACC-20 (13 mg) loaded with aqueous 1 M NaTFSI (22.5 µL). MAS NMR spectra are referenced such that the ex-pore resonance is set to 0 ppm and spinning side bands are denoted with asterisks.

For both nuclei, the chemical shift of the ex-pore peak remains unchanged (0 ppm) as the applied voltage is increased from 0 V to +0.8 V. At 0 V, the *in situ* ^{19}F and ^{23}Na NMR spectra exhibit a Δδ of −3.9 ppm and −5.4 ppm, respectively (**Figure 5.12a-b**). These values are reduced compared to the Δδ values of the model system, where ^{19}F Δδ = −5.7 ppm and ^{23}Na Δδ = −6.3 ppm (**Figure 5.12c-d**), with these differences being attributed to BMS effects in the *in situ* NMR spectra that are absent in the model system. As a positive potential of +0.8 V is applied, the in-pore resonance in the ^{23}Na spectrum is observed to move to a less negative chemical shift, moving from −5.4 ppm to −4.1 ppm. A similar shift towards a less negative chemical shift is also seen for the in-pore resonance in the ^{19}F NMR spectra, shifting from −3.9 ppm to −2.4 ppm. Similar results have been observed in the *in situ* ^{19}F NMR study of

1.5 M PEt_4BF_4 in ACN using YP-50F supercapacitor electrodes.[29] Notably, the potential-driven changes in Δδ for both nuclei are considerably less pronounced than those observed for organic electrolytes and ionic liquids.[29,31,64]

To a first approximation, the reduction in Δδ as the potential becomes increasingly positive can be attributed to changes in ion-carbon distances during electrosorption, with ions moving away from the carbon surface and consequently experiencing reduced average shielding.[13] However, both ^{19}F Δδ and ^{23}Na Δδ are shown to decrease as the applied voltage becomes increasingly positive. Therefore, it is unlikely that changes in ion-carbon distance are the primary cause as it would imply the unexpected behaviour of both $TFSI^-$ and Na^+ ions moving away from the positively polarised surface. Instead, the chemical shift change of the in-pore resonance is attributed to changes in the electronic structure of the carbon surface, wherein charging to +0.8 V causes an accumulation of unpaired electrons on the carbon surface, leading to an increasingly paramagnetic contribution that deshields species near the carbon surface.[31,64] The reduction in Δδ during electrode polarisation has been previously reported in the literature[7,29,64,201,322] and DFT models corroborate contributions from increasing paramagnetism as a result of changes in the electronic structure of the carbon.[22,31]

Figure 5.12a-b also displays the spectra for the cell under a negative polarisation. The chemical shift of the ex-pore resonance in both the ^{19}F and ^{23}Na NMR spectra remains unchanged, regardless of the applied potential. At −0.8 V, the in-pore peak in the ^{23}Na NMR spectra is observed to move towards a more negative chemical shift, changing from −5.4 ppm at 0 V to −6.2 ppm at −0.8 V. A similar shift is observed for the in-pore resonance in the ^{19}F NMR spectra, moving from −3.9 ppm to −5.8 ppm. The observed increase in Δδ is not attributed to changes in the electronic structure of the carbon as charging, regardless of polarity, results in increased paramagnetic contributions.[13,29] An alternative explanation could be electrosorption-driven changes in the local chemical environment of the ions. Luo *et al*. showed in the *in situ* NMR study of NaF (0.8 mol kg^{-1}) within a small pore PDC that ^{19}F Δδ increased as the applied voltage was increased from 0.7 V to 1.0 V, with the in-pore peak shifting from −9 ppm to −25 ppm.[18,37,321] The increased deshielding was attributed to a voltage-gated partial desolvation of the F^- anion during pore-insertion. However, the magnitude of the diamagnetic shift observed in this work is considerably smaller than those observed by Luo *et al*., indicating that the shift may not be a result of partial desolvation.[37] Furthermore, Δδ is observed to increase for both Na^+ cations and $TFSI^-$ anions. Assuming that partial desolvation is indeed the cause for the diamagnetic shift, this would imply an unlikely scenario in which both $TFSI^-$ anions

and Na^+ cations are partially desolvated as they are electrosorbed into the pores of the negatively polarised electrode. Instead, an additional mechanism is inferred to be the dominant contribution towards the diamagnetic shift of the in-pore peaks under a negative polarisation.

For the 1 M NaTFSI system, the Na^+ in-pore resonance for the *in situ* cell at −0.8 V (−6.2 ppm, **Figure 5.12a**) lies at a chemical shift that is approximately equal to the chemical shift of the in-pore resonance of the model 1 M NaTFSI system under MAS (−6.3 ppm, **Figure 5.12c**). A similar observation is made for the $TFSI^-$ in-pore resonance, with a δ of −5.4 ppm for the *in situ* cell at −0.8 V (**Figure 5.12b**) and a δ of −5.7 ppm for the in-pore peak of the model system (**Figure 5.12d**). Thus, to a first approximation, it may seem that applying a voltage of −0.8 V causes the in-pore species within the cycled *in situ* cell to return to a local magnetic environment similar to that of the spontaneously adsorbed electrolyte. However, it is important to consider paramagnetic contributions from the negative polarisation of the electrode and BMS effects from the *in situ* cell components/electrode geometry. These contributions make comparison between Δδ values in the *in situ* NMR spectra and the model MAS NMR spectra complex.

Additional cells comprising 1 M NaTFSI and ACC-20 electrodes were constructed to verify the observed electrosorption-driven changes in the in-pore chemical shift. Since different electrode polarisations shift the in-pore resonances in opposite directions, a cell was assembled using a stacked electrode geometry (**Figure 5.2a**) to enable simultaneous observation of the in-pore environments of the oppositely polarised electrodes. The cell was cycled extensively between 0 V and 0.8 V prior to the acquisition of NMR spectra, exhibiting a quasi-rectangular shape in CVs recorded at 100 mV s^{-1}, 10 mV s^{-1}, and 1 mV s^{-1}, with a specific capacitance of ~115 F g^{-1} estimated from the discharge curve of the 10 mV s^{-1} cyclic voltammogram. **Figure 5.13** shows the *in situ* ^{19}F and ^{23}Na NMR spectra acquired for the stacked cell at different applied voltages. All spectra are referenced such that the ex-pore peak at 0 V is set to 0 ppm. At all applied voltages, the chemical shift of the ex-pore peak remains constant for both nuclei. When no voltage is applied, the ^{23}Na spectrum displays a single in-pore resonance at −6.2 ppm. Under an applied voltage of 0.8 V, the in-pore resonance splits into two distinct peaks: one shifted to −4.4 ppm (less negative) and the other shifted to −7.8 ppm (more negative). Based on the previous analysis of the staggered cell, the peak with the less negative shift is associated with the positively polarised electrode, while the more negative peak is linked to the negatively polarised electrode. Reversing the electrode polarity by applying a −0.8 V voltage also gives two in-pore peaks at −4.7 ppm −7.8 ppm in the ^{23}Na spectrum. The similar chemical shifts of

the two in-pore peaks across both polarisations show that the in-pore environment of the two electrodes are approximately equivalent, with the slight variations being attributed to subtle differences in the geometries and orientations of the electrodes giving rise to distinct BMS effects.

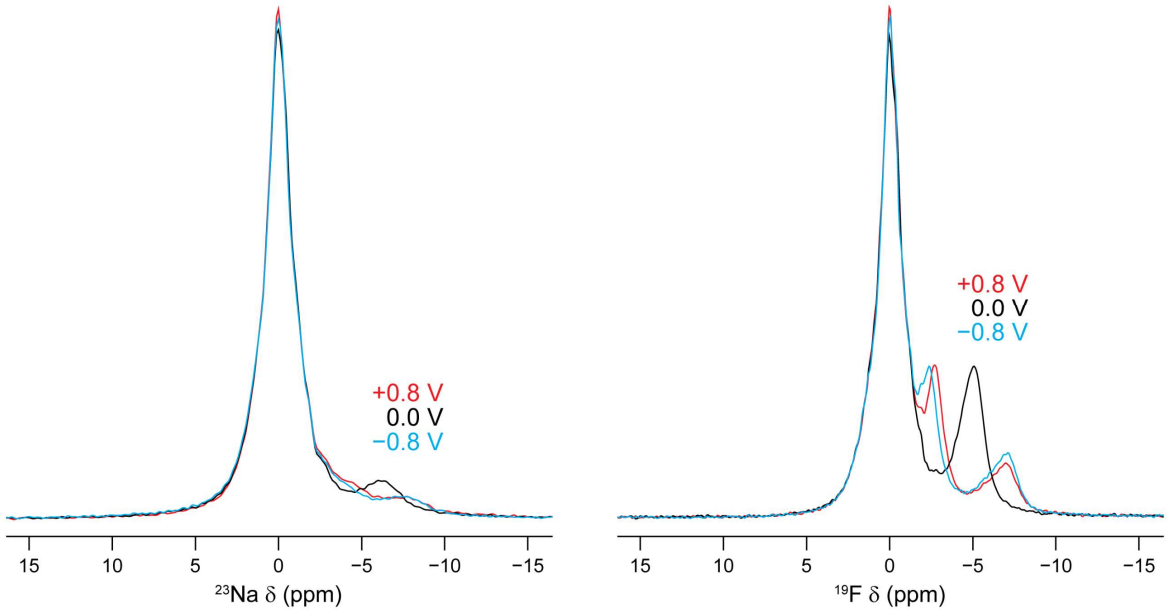

Figure 5.13. *In situ* (a) ^{23}Na and (b) ^{19}F NMR spectra acquired at different applied voltages (0.8 V, 0 V, and −0.8 V) for a cycled cell comprising ACC-20 electrodes (2.90 mg each) arranged in a stacked geometry, aqueous 1 M NaTFSI electrolyte, Au mesh current collectors, PTFE separators (2 × 0.5 mm), and a filter paper separator. Both spectra are referenced such that the ex-pore resonance at 0 V is set to 0 ppm.

Additionally, ^{19}F NMR spectra were recorded for the stacked cell under different voltages (**Figure 5.13**). At 0 V, a single in-pore resonance is observed at −5.1 ppm. Similar to the ^{23}Na NMR spectra, applying a voltage caused this resonance to split into two peaks: at 0.8 V, the chemical shifts are –2.4 ppm and −7.1 ppm, and at −0.8 V they are –2.7 ppm and −7.1 ppm. At 0 V, the single in-pore resonances exhibit Δδ values of −6.2 ppm and −5.1 ppm in the ^{23}Na and ^{19}F NMR spectra, respectively. These values are reduced relative to those observed in the model system of 1 M NaTFSI-soaked ACC-20, where ^{23}Na Δδ = −6.3 ppm and ^{19}F Δδ = −5.7 ppm (**Figure 5.12c-d**). For the negatively polarised electrode, the in-pore peaks shift to give Δδ values of −7.8 ppm for ^{23}Na and a −7.1 ppm for ^{19}F. Notably, these Δδ values are higher than those in the model system. This suggests that there are diamagnetic contributions causing the in-pore resonances of both anions and cations to shift to more negative chemical shifts than those observed at equilibrium under spontaneous adsorption conditions. However, as the

difference in Δδ between the model systems and the negatively polarised electrodes is relatively small (< 2 ppm), it is plausible that these differences are due to BMS effects.

Cells comprising different 1 M aqueous electrolytes were also investigated using the *in situ* NMR approach. *In situ* cells were assembled using electrolyte-soaked (12 hours) ACC-20 electrodes arranged in a staggered geometry. All cells were cycled between 0.0 V and 0.8 V using cyclic voltammetry experiments under scan-rates of 100 mV s^{-1}, 10 mV s^{-1}, and 1 mV s^{-1} prior to the acquisition of NMR spectra. **Figure 5.14a** shows the recorded *in situ* ^{23}Na Δδ values as a function of applied voltage, and **Figure 5.14b** shows the recorded *in situ* ^{19}F Δδ values. Several cells comprising 1 M NaTFSI were assembled and the recorded Δδ values for each cell are displayed. ^{23}Na NMR spectra for NaOTF could not be acquired due to poor resolution between the in-pore and ex-pore resonances, while *in situ* ^{7}Li NMR spectra for LiOTF could not be obtained due to probe tuning limitations.

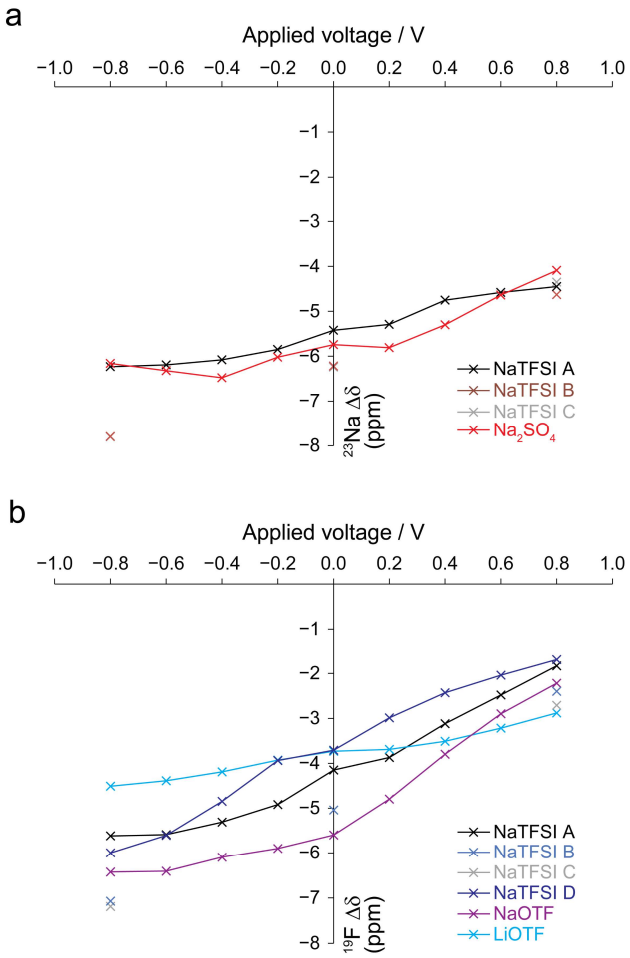

Figure 5.14. (a) ^{23}Na and (b) ^{19}F Δδ values as a function of applied potential for a range of 1 M aqueous electrolytes. Multiple cells comprising 1 M NaTFSI are displayed: (A) a staggered cell recorded at stepwise voltages, (B+C) the two stacked cell electrodes, and (D) a staggered cell undergoing simultaneous cycling.

Different electrolytes exhibit different values of Δδ at 0 V for both nuclei. These differences are attributed to (i) variations in adsorption behaviour among the electrolytes and (ii) cell-specific changes in BMS effects due to subtle variations in cell geometry and orientation relative to the applied field. These factors are difficult to separate, complicating direct comparisons of Δδ values between different systems.

For all electrolytes, MAS NMR spectra were also acquired for model systems comprising ACC-20 (13 mg) packed within a MAS rotor and loaded with electrolyte (22.5 μL) via microsyringe. Across all electrolytes, and for both nuclei, the Δδ value at 0 V was reduced by approximately 1-2 ppm compared to those obtained for the model systems. For the NaTFSI cells, where both ^{19}F and ^{23}Na *in situ* NMR spectra were acquired (A, B, and C, shown in **Figure 5.14a-b**), the difference between ^{19}F Δδ at 0 V and ^{19}F Δδ for the model system was equal to the difference between ^{23}Na Δδ at 0 V and ^{23}Na Δδ for the model system. Since both nuclei show similar differences in Δδ, it can be inferred that the differences between the measured Δδ of the *in situ* system at 0 V and the model system (*i.e.,* Δδ values under spontaneous adsorption conditions) are due to nucleus-independent shifts caused by the bulk magnetic susceptibility of the *in situ* cell components.

Figure 5.14a shows that for all electrolytes, the ^{23}Na Δδ value becomes less negative as the applied voltage becomes more positive, and more negative as the applied voltage becomes increasingly negative. Similarly, **Figure 5.14b** shows that ^{19}F Δδ exhibits the same trend as ^{23}Na Δδ with respect to the applied voltage. At −0.8 V, both ^{23}Na Δδ and ^{19}F Δδ for all electrolytes are within 1.5 ppm of the Δδ of the model system under spontaneous adsorption conditions. The observed electrosorption-driven behaviour of Δδ it is not attributed to the ionophilicity of the electrolyte, as the same behaviour is observed for both the ionophilic $TFSI^-$ anion and the ionophobic SO_4^{2-} anion. Furthermore, this behaviour is not specific to the Na^+ cation, as similar Δδ behaviour is observed in the ^{19}F NMR spectra for a cell comprising 1 M LiOTF.

It is important to note that this study focused on preconditioned cells, as opposed to other NMR studies that have used pristine cells (*i.e.,* cells that have not undergone electrochemical cycling). Consequently, it is tentatively proposed that the diamagnetic shift of the in-pore resonance, which is unique to this study, may result from extensive cycling before data acquisition. However, the exact mechanisms driving the diamagnetic shift of the in-pore peak in electrodes under a negative polarisation remain poorly understood and require further

investigation. An approach to further explore this phenomenon would be to compare the in-pore chemical shift of pristine cells with that of spontaneously adsorbed systems. This comparison would provide insight into the initial partitioning of ion within the electrodes. Subsequently, a systematic investigation could be conducted to analyse the in-pore chemical shift of the F^- anion during the first charge and discharge of the cell, and across subsequent cycles. Such an investigation could offer a deeper understanding of the nature of the diamagnetic shift.

5.3.3.3 In situ NMR during cycling using stacked cells

With the improved electrochemical response of the stacked cell design, it is possible to acquire *in situ* NMR spectra for a cell undergoing simultaneous dynamic cycling.[31] ^{19}F NMR spectra were acquired as a stacked-electrode cell comprising ACC-20 electrodes (2.4 mg each) soaked with aqueous 1 M NaTFSI was simultaneously cycled across a potential window spanning 0.0 V to 0.8 V at a scan rate of 0.104 mV s^{-1}, with spectra being acquired for two full cycles. The scan rate was determined by dividing the potential window into 0.1 V increments, across which 32 transients were acquired with a recycle delay of 30 s. As the cell voltage changes continuously, and the voltage increments are sizeable compared to the narrow voltage window of the aqueous electrolytes (0.8 V), changes in the spectra are observed between transients resulting in a slight spectral broadening. After the first two positive cycles, the polarity of the electrodes was reversed, and spectra were acquired for two complete cycles between 0.0 V and −0.8 V at a scan rate of −0.104 mV s^{-1}. Following the second negative cycle, additional spectra were recorded during two further positive cycles, followed by two more negative cycles. A total of 128 *in situ* ^{19}F NMR spectra were obtained for each full 0 V → ±0.8 V → 0 V cycle, with 8 full cycles being studied.

Figure 5.15a shows the cyclic voltammograms of the first cycles following the change in electrode polarisation and **Figure 5.15b** shows the CV curves for the subsequent cycle under the same electrode polarisation. All curves exhibit a quasi-rectangular shape that is indicative of capacitive behaviour. The CV curve of the first and the third positive cycles show a similar form, as do the first and the third negative cycles. A similar behaviour is shown by the subsequent cycles at a given polarisation, with the second and the fourth cycles exhibiting similar shapes in both the positive and negative voltage sweeps. This shows that the electrochemical performance under both positive and negative applied voltages is reproducible.

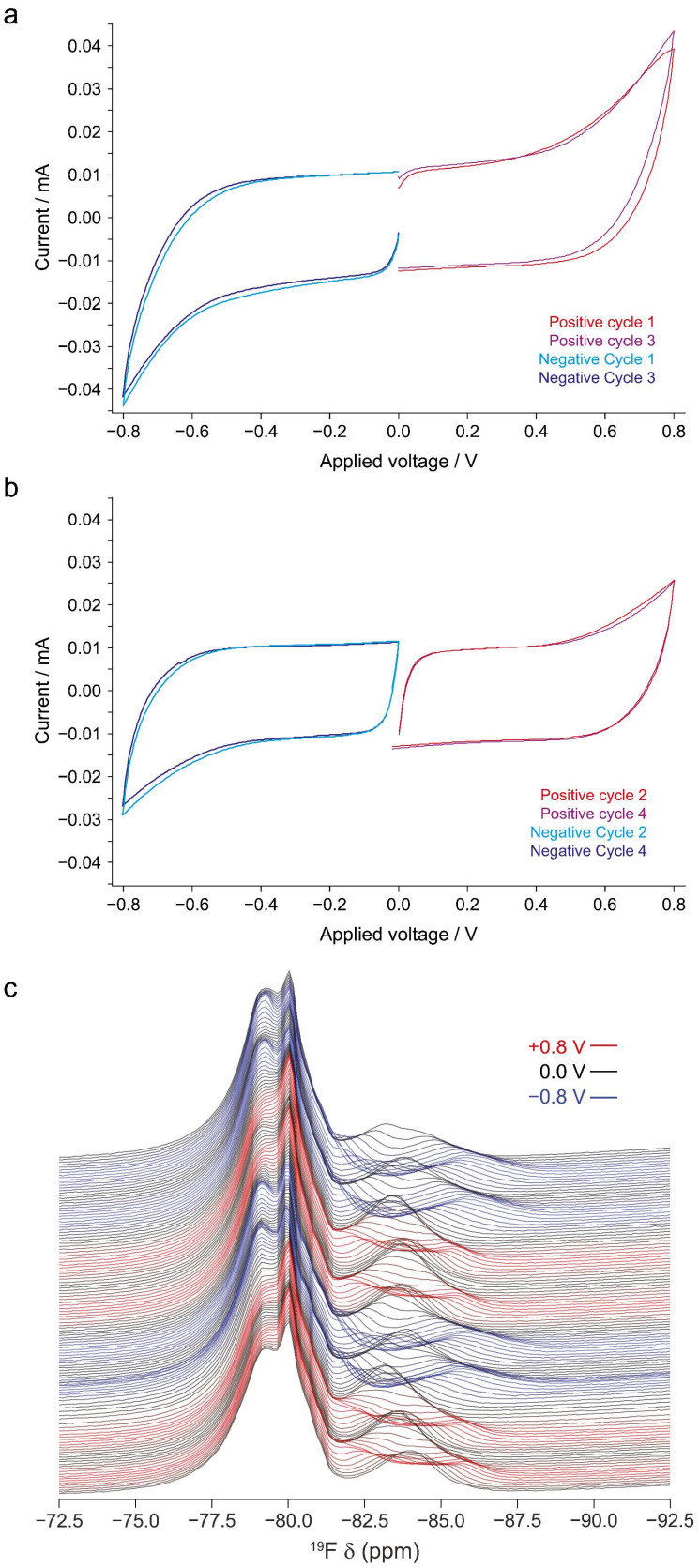

Figure 5.15. Cyclic voltammograms of positive and negative cycles at a scan rate of ±0.104 mV s^{-1} are shown, with data being separated to display the (a) initial cycles and (b) subsequent cycles following a change in the electrode polarisation. (c) Stacked *in situ* ^{19}F NMR spectra acquired during simultaneous cyclic voltammetry experiments.

The initial CV curves following a change in electrode polarisation show an increased current at larger applied voltages, resulting in a deviation from the rectangular shape. This feature denotes an increased resistance during cycling, with the sharp peak at high voltages being indicative of faradaic processes.[323] As such, this feature is attributed to the electrochemical oxidation/reduction of the carbon surface. The subsequent cycles following the initial polarisation of the electrodes (**Figure 5.15b**) exhibit a reduced resistive character and a more rectangular shape, indicating a subtle change in electrochemical performance between the initial and subsequent cycles.

Figure 5.15c shows the *in situ* ^{19}F NMR spectra acquired during cycling referenced to the CF_2 group of PTFE set to −122.3 ppm. The spectra acquired during dynamic cycling resemble those acquired under fixed voltages as shown in **Figure 5.13**. The overlaid spectra highlight the periodic changes in $\delta_{\text{in-pore}}$ in response to the applied voltage. At 0 V, a single in-pore resonance is observed, while under an applied voltage, the in-pore peak splits into two distinct resonances. Across all four positive cycles, the split in-pore resonances exhibit the same change in $\delta_{\text{in-pore}}$ relative to the applied voltage. As such, the $\delta_{\text{in-pore}}$ values for the two in-pore resonances at +0.8 V are found to be largely consistent, with the $\delta_{\text{in-pore}}$ of the positive electrode being −82.2±0.2 ppm and the $\delta_{\text{in-pore}}$ of the negative electrode being −85.6±0.2 ppm. In contrast, the $\delta_{\text{in-pore}}$ of the single resonance at 0 V is shown to differ between the initial and subsequent positive cycles, with the response of $\delta_{\text{in-pore}}$ at 0 V after the first and second positive cycles differing, and the response after the third and fourth positive cycles being inequivalent. Several factors may contribute to the change in $\delta_{\text{in-pore}}$, such as: (i) Electrosorption-driven changes in ion-surface distances, (ii) an EDL and subsequent stored surface charge that persists even after discharging back to 0 V, and (iii) electrochemical oxidation/reduction of the carbon surface altering its electronic structure. The reduced resistance observed in the second cycle compared to the first (as shown in **Figure 5.15b**) is attributed to less oxidation/reduction of the electrode surfaces during the second cycle as many groups susceptible to reduction/oxidation have undergone such reactions during the first cycle.

Under a negative applied voltage, the in-pore resonance also splits (**Figure 5.15c**), exhibiting similar changes in $\delta_{\text{in-pore}}$ as a function of applied voltage across all four cycles. A notable change in spectral phasing is observed following the first negative cycle which is seemingly self-corrected following the second negative cycle and during all subsequent negative cycles. At −0.8 V, the $\delta_{\text{in-pore}}$ of the positive electrode is −81.6±0.3 ppm and the $\delta_{\text{in-pore}}$ of the negative

electrode is −85.9±0.2 ppm. A slight variation in the shape of the in-pore resonance of the negative electrode (about −86 ppm) is observed between the first two negative cycles and the final two negative cycles. This transformation is attributed to a gradual change in spectral phasing across the extended duration of the experiment. Markedly, the change in the $\delta_{in\text{-}pore}$ of the positive electrode in response to a negative applied potential differs significantly from the changes observed during positive cycles. This discrepancy is partially attributed to variations in the BMS between the two electrodes.

The converged in-pore resonance at 0 V, which was shifted to a less negative chemical shift following the first two positive cycles, is shown to return to the initial chemical shift following the first negative cycle. This coincides with the first negative cycle reintroducing the increased resistive character, giving a CV curve similar to that of the first positive cycle (see **Figure 5.15a**). This behaviour indicates the return to the equilibrium state of the cell that is achieved following a prolonged rest period at 0 V. As with the positive cycles, the subsequent negative cycle shifts the in-pore peak at 0 V to a less negative chemical shift, with the corresponding cyclic voltammogram exhibiting a more rectangular shape, indicating reduced resistance. Thus, it is shown that the $\delta_{in\text{-}pore}$ of the converged in-pore resonance at 0 V is related to both the resistance during cycling and the number of cycles following the initial polarisation.

Figure 5.16 shows a contour plot of the *in situ* ^{19}F NMR spectra as a function of applied voltage for the 1 M NaTFSI cell under dynamic cycling. The variation of $\delta_{in\text{-}pore}$ (between −81 ppm and −87 ppm) generally corresponds with changes in the applied voltage. However, upon closer inspection of the contour plot, a slight lag is occasionally observed between the greatest change in $\delta_{in\text{-}pore}$ (with respect to $\delta_{in\text{-}pore}$ at 0 V) and the largest applied voltage (±0.8 V). During the first charge under a positive applied voltage, the in-pore resonance observed at 0 V centred about −84 ppm splits. The resonance corresponding to the negatively polarised electrode moves towards a more negative chemical shift, reaching its largest change at a chemical shift of −85.8 ppm at +0.8 V, exhibiting no lag. In contrast, the in-pore resonance of the positive electrode moves towards a less negative chemical shift, with a chemical shift of −82.3 ppm at +0.8 V. During the discharge the peak continues to shift to a less negative $\delta_{in\text{-}pore}$, reaching a value of −82.3 ppm at +0.7 V, demonstrating a lag of ~0.1 V between the applied voltage and the maximum change in $\delta_{in\text{-}pore}$. The subsequent cycle displays similar behaviour, with the in-pore environment of the negative electrode exhibiting no lag, and the positive electrode exhibiting a lag of ~0.1 V. This indicates subtle differences in the charging behaviour of the two electrodes. The polarity of the electrodes was then reversed through the application of a

negative voltage. During the negative cycles, the in-pore of the positively and negatively charged electrodes both exhibit a lag of ~0.1 V between the largest change in $\delta_{in\text{-}pore}$ and the largest applied voltage. This differs from the change in $\delta_{in\text{-}pore}$ observed across positive cycles. Further work is required to gain a better understanding of these differences.

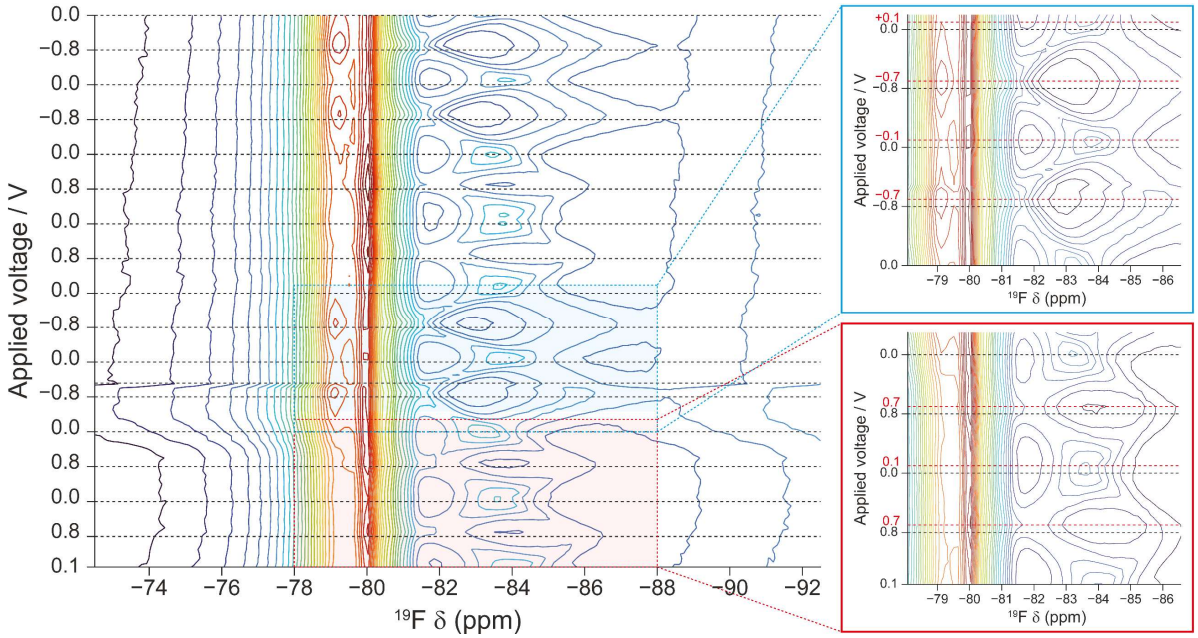

Figure 5.16. Contour plot of sequential *in situ* ^{19}F NMR spectra of both electrodes of a stacked supercapacitor cell comprising 1 M NaTFSI and ACC-20 electrodes (each 2.4 mg) undergoing simultaneous electrochemical cycling. During acquisition, cyclic voltammetry experiments were performed at a scan rate of 0.104 mV s^{-1} across a potential window of 0.8 V (between 0.0 V and ±0.8 V). 32 transients were acquired per 0.1 V interval using a recycle delay of 30 s, with a total of 16 1D experiments performed per charging cycle.

Further insight into the electrochemical response of $\delta_{in\text{-}pore}$ can be gained by examining the non-ideal cyclic voltammograms (**Figure 5.15a-b**). In the first positive cycle shown in **Figure 5.15a**, a positive voltage is applied, generating positive currents between the 0.0 V and 0.8 V. When the voltage reaches 0.8 V, the cell begins to discharge, and the applied voltage is gradually reduced. However, the current remains positive during the discharge, and thus the magnitude of the charge stored in each electrode continues to increase, until the applied voltage is reduced to approximately 0.7 V. Below 0.7 V, negative currents flow as the cell continues to discharge towards 0.0 V. As such, it is inferred that the changes of the in-pore chemical shift are not correlated with the applied voltage and instead are correlated with the magnitude of the charge stored across the electrodes. Wang *et al*. report similar observations with real-time *in situ* ^{19}F NMR measurements of a dynamically cycled supercapacitor cell comprising 1 M NEt_4BF_4/*d*ACN and YP-50F-PTFE (95:5 wt%) film electrodes.[31]

Unlike the charging cycle, the discharge displays a rectangular shape as the discharge curve concludes and the subsequent charging curve begins, resulting in a very narrow voltage window where negative currents are observed during the positive charging cycle. Interestingly, despite the fast change in the direction of current flow, the ^{19}F NMR spectra acquired during the discharge also exhibit a lag between $\delta_{in\text{-}pore}$ and the end of the discharge curve, with the minimum change in $\delta_{in\text{-}pore}$ relative to the $\delta_{in\text{-}pore}$ at 0 V being acquired at an applied voltage of 0.1 V. It is worth noting that the electrochemical data presented herein was acquired using a 2-electrode cell, limiting the analysis of electrode current responses. Indeed, the use of a 3-electode *in situ* cell would provide greater insight into the individual electrode contributions and the complex relationship between applied voltage and $\delta_{in\text{-}pore}$.

5.3.4 Summary and outlook

In this chapter, practical considerations regarding the application of *in situ* NMR spectroscopy for the study of aqueous supercapacitors have been presented. The influence of the electrode geometry within *in situ* cells on electrochemical performance was investigated and optimised for use in *in situ* NMR spectroscopy studies. The staggered electrode arrangement facilitates the separate study of the two electrodes using *in situ* NMR spectroscopy, while still demonstrating capacitive charging behaviour during cyclic voltammetry experiments. The effects of bulk magnetic susceptibility contributions from cell components and electrode geometry on the observed NMR spectra were also examined, as were the challenges of identifying electrochemically stable pairings between aqueous electrolytes and low-susceptibility current collectors.

In situ NMR spectroscopy experiments were conducted using aqueous electrolytes with contrasting spontaneous adsorption behaviours. Cells comprising ACC-20 electrodes soaked in the ionophilic 1 M NaTFSI electrolyte were compared to those soaked in the ionophobic 1 M Na_2SO_4 electrolyte. *In situ* ^{23}Na NMR spectra were obtained at set applied voltages and deconvoluted to determine the in-pore cation peak integral. By comparing the in-pore integral of the spectrum at 0 V with those under applied voltages, the charging mechanism of both systems were analysed. For 1 M NaTFSI, a cation adsorption mechanism is observed at the negative electrode, while an anion adsorption mechanism is inferred to take place at the positive electrode, as the in-pore cation population remained constant. In contrast, for 1 M Na_2SO_4, co-ion desorption occurs at both electrodes, with cations being expelled from the in-pore environment of the positive electrode, and anions being expelled from the pores of the negative

electrode. These findings suggest that the ionophilicity/ionophobicity of the electrolyte under spontaneous adsorption conditions influences the preference towards specific charge-balancing mechanisms. These observations were corroborated by *in situ* ^{19}F NMR spectroscopy of the 1 M NaTFSI cell, whereby an anion adsorption mechanism is observed at the positive electrode, and a constant anion population is observed at the negative electrode, indicating cation adsorption.

The potential-driven changes in the in-pore chemical shift for the aqueous NaTFSI electrolyte have been examined using *in situ* ^{19}F and ^{23}Na NMR spectroscopy. The results show that the in-pore peak of the positive electrode undergoes a paramagnetic shift under an applied voltage, consistent with previous studies. In contrast, the in-pore peak of the negative electrode exhibits a diamagnetic shift. Given that this behaviour is observed for both nuclei and that the magnitude of the shifts is relatively small, these changes are not attributed to the desolvation of ionic species. Similar findings for other aqueous electrolytes suggest that this behaviour is not due to specific ion properties of the NaTFSI electrolyte.

To further explore these shifts, stacked electrode configurations were used, allowing the simultaneous observation of the in-pore resonances for both the positive and negative electrodes. Under dynamic cycling conditions, the stacked arrangement enabled the simultaneous analysis of the response for both in-pore resonances. The position of the resonance at an applied voltage of 0 V was found to correlate with both the cycle number (whether initial or subsequent) and the resistance observed in the corresponding cyclic voltammograms. Further work is required to fully elucidate the mechanisms behind the diamagnetic shift of the in-pore resonance and the effect of extensive cycling prior to obtaining NMR spectra.

Chapter 6
Determining magnetic shielding parameters of extended aromatic materials using DFT

6.1 Introduction

Extended aromatic materials, such as graphene, porous disordered carbons, and carbon nanotubes, have garnered significant interest due to their wide range of applications. The breadth of applications of pristine graphene and graphene-like materials (*e.g.,* supercapacitors,[23,29,60,99] capacitive deionisation,[2,324] heterogeneous catalysis,[1,89,325] gas storage,[8] DNA sequencing[326]) arises from their distinctive electronic, thermal, and structural properties which can be tailored for use in specific applications (*e.g.,* specific surface areas, electronic band gaps, helicities, surface functionalisation). For many applications, guest species are introduced into the carbonaceous material that adsorb to the aromatic carbon surface, either spontaneously or in response to an external condition (*e.g.,* an applied voltage). For such applications, a complete understanding of the impact of the carbon structure (*e.g.,* defect sites, curvature, surface-functionalisation) and the adsorption behaviour of guest species within these materials is of primary importance to further develop the performance of these systems.

As detailed in prior chapters, NMR spectroscopy is an effective technique for the selective investigation of local carbon structure and guest-surface interactions for aromatic materials.[7,13,28,29,70,317,327–330] Importantly, the ring current-induced diamagnetic fields are localised, typically only extending to distances relevant to adsorption (*i.e.,* a few Ångstroms from the carbon surface). As such, species adsorbed to graphene-like surfaces typically exhibit chemical shifts that are reduced in frequency relative to non-adsorbed counterparts. Analysis of the magnitude of $\Delta\delta$ in experimental NMR spectra, and the line-shapes of shifted resonances,

can provide valuable insight into the local carbon structure and guest adsorption behaviour.[18,22,32–34] However, while the ring current-induced magnetic field is usually the dominant contribution to Δδ, chemical effects, dynamics, and other magnetic effects can also affect its magnitude.

As outlined in Chapter 2, the contribution of the ring current-induced shielding to Δδ can be determined through the calculation of the NICS using DFT. In recent years, NICS studies have been performed using sp^2-hybridised molecules, such as coronene, to model the graphene-like fragments that form the general structure of porous carbons.[22,34,132] Small surface domains and model slit-pores can be constructed from one or more fragments in suitable geometries and the ring current induced field in the vicinity can be probed. Moran *et al*. showed that the magnitude of the NICS increases as the number of carbons in the domain size increased and that the NICS is largely uniform at distances relevant to physical adsorption.[132] Forse *et al*. also demonstrated that decreasing the distance between parallel aromatic fragments introduces a greater overlap between the ring current induced fields, increasing the NICS experienced at positions between the two aromatic surfaces.[22] Kilymis *et al.* recently expanded upon this work, modelling larger graphitic fragments using a tight-binding model, showing a continued increase in the measured NICS with increasing domain size.[34] Notably, the aforementioned approaches modelled carbon fragments within an infinite vacuum, often referred to as a 'molecule-in-a-box' approach. As such, despite the successful tight-binding approach by Kilymis *et al*., there is an intrinsic limit to the size of fragment probed, and a molecular edge effect will always be present. This is particularly relevant for polyaromatic hydrocarbons as ring currents have been shown to circulate around the edge of the molecule, giving a sizeable contribution to the NICS even for the largest of fragments.[34,331,332]

An alternative method for determining the magnetic shielding parameters of aromatic materials is through periodic calculations in reciprocal space.[164,267,277,333] In previous studies, the GIPAW[277,334] method has been used to computationally study ^{13}C chemical shifts for pristine and defected single-walled carbon nanotubes.[335–338] Kibalchenko *et al*. used a similar approach to probe the NICS within the interior of infinitely periodic, non-metallic, single-walled nanotubes.[317] Planewave-based DFT calculations can also be performed on periodic graphene layers, proposedly providing insight into experimentally observed ^{13}C chemical shifts and the NICS induced by aromatic carbon domains in the absence of edge-effects. However, considerable issues with the convergence of magnetic shielding parameters of periodic graphene surfaces have been previously reported by Vähäkangas *et al.*[339] when using the

GIPAW method.[277] These issues are attributed to the vanishing electronic band gap of graphene, giving rise to an erratic and oscillatory convergence behaviour for magnetic shielding with respect to reciprocal space sampling density. Notably, other studies have not reported convergence issues when determining magnetic shielding parameters for graphene using periodic-boundary DFT calculations.[106,335,340,341] A detailed study on this convergence behaviour is currently lacking, but previous improvements in convergence have been attributed to the use of graphene supercells[106] and the thermal smearing of energy levels.[340]

Here, a detailed study of DFT NMR calculations on graphene is presented, highlighting complexities due to its unique electronic structure. The origin of previously observed convergence issues is identified and an approach for calculating converged magnetic parameters for graphene is outlined. Additionally, the behaviour of contested ring currents within a periodic graphene structure and their correlation with the NICS calculated above the ring-plane are discussed. Finally, the impact of introducing defect sites within the graphene surface on ring currents, chemical shifts, and ring current-induced chemical shifts is discussed.

6.2 Computational details

Fragment-based electronic structure computations on aromatic molecules were performed using Gaussian 16.0, with NMR shielding tensors being computed using the GIAO approach, with the B3LYP exchange correlation functional, and the 6-31G(d) basis set, following the approaches of Moran *et al*. and Forse *et al.*.[22,132] Periodic electronic structure computations on infinite graphene sheets employed a plane-wave density functional theory first-principles method, as implemented in the CASTEP v22.11 code. The Perdew-Burke-Erzernhof (PBE) nonhybrid GGA density functional, a plane-wave basis energy cut-off of 600 eV, and ultrasoft pseudopotentials were implemented.[263,342] The Grimme-D3 dispersion correction scheme was implemented for both periodic and cluster-based calculations.[286] All atomic positions and lattice parameters were relaxed, with convergence tolerances of 2×10^{-5} eV, 0.05 eV $Å^{-1}$, and 1×10^{-3} Å being implemented for the energy, force, and displacement, respectively. For defected graphene layers, the lattice parameter perpendicular to the ring-plane was fixed during geometry optimisation. NMR shielding tensors were calculated using the GIPAW approach.[277,333]

Graphene sheets were modelled using 3 × 3 × 1 supercells in order to allow probe molecules to be inserted within the periodic unit cells with sufficient separation between periodic repeats.[106] Monkhorst-Pack *k*-point grids of dimensions (*m, m*, 1) were used for the periodic

graphene sheets, where *m* was incrementally increased to achieve convergence of shielding parameters.[270] Calculations using *k*-grids of dimension (*m, m*, *n*) for *n* = 1, 3, 5, and 7 were also performed, with determined NMR parameters showing negligible differences between the integers of *n*. *k*-grids were centred about **Γ** and fractional offsets of the *k*-grids along the reciprocal lattice vectors parallel to the sheet-plane (k_x and k_y) were investigated. NMR parameters were converged as a function of both *k*-grid sampling density and plane-wave energy cut-off.

6.3 Results and discussion

6.3.1 Referencing magnetic shielding parameters

Calculated magnetic shielding tensors, σ, were converted to chemical shifts, δ, using a reference shielding obtained from periodic DFT calculations performed on a set of model compounds with well-known experimental chemical shifts (*L*-alanine, diamond, and benzene). ^{13}C NMR spectra of *L*-alanine were acquired using a 400 MHz Bruker Avance III HD WB spectrometer and referenced to tetramethylsilane (TMS) using literature values of the -CH_3 resonance (20.5 ppm).[343,344] In the acquired ^{13}C NMR spectra of *L*-alanine, the -CH and -C=O resonances appear at 51.1 ppm and 177.9 ppm, respectively. TMS-referenced ^{13}C chemical shifts for benzene (128.7 ppm)[340,345] and diamond (36.0 ppm)[341] were also taken from the literature. The conversion was performed using the equation of the linear fit between calculated magnetic shielding tensors and reported experimental chemical shifts for all reference compounds (**Figure 6.1**).

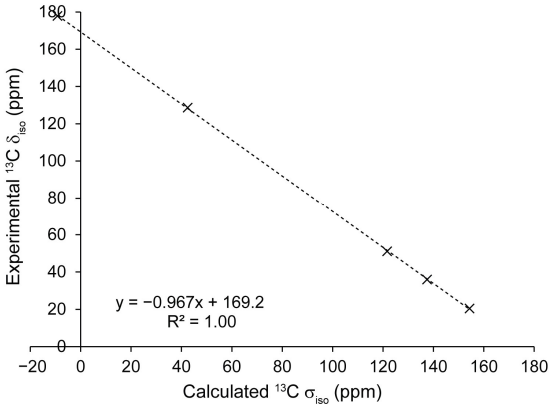

Figure 6.1. Calculated ^{13}C isotropic shielding against experimental ^{13}C chemical shifts referenced to tetramethylsilane (TMS).

The linear fit is of the form $\delta_{exp} = -0.967\sigma_{calc} + 169.2$ ppm (**Figure 6.1**), with calculated chemical shifts, δ_{calc}, being determined following $\delta_{calc} = \sigma_{ref} - 0.967\sigma_{calc}$, where $\sigma_{ref} = 169.2$

ppm. As discussed in previous studies, benzene is a well-suited choice of reference compound for the study of graphene as both structures comprise sp^2-hybdridised aromatic carbons.[106,346] The shielding reference obtained is in good agreement with other studies.[34,106,337,339]

6.3.2 Convergence of shielding parameters in GIPAW calculations on graphene

Initially, graphene was modelled using a 3 × 3 × 1 supercell, with the *z*-axis perpendicular to the ring-plane and an interlayer spacing, *d*, of 10 Å. Following geometry optimisation, where the total energy and forces were converged using an energy cut-off of 600 eV and a 4 × 4 × 1 Monkhorst-Pack *k*-grid, a C-C bond length of 1.42 Å was obtained, giving good agreement with the literature for monolayer graphene.[347–350] This configuration serves as a simplified model of a slit-pore formed by AA-stacked graphene sheets with a 10 Å interlayer separation (**Figure 6.2a**). Although energy and force convergence can be achieved, for the calculation of magnetic properties when sampling the Dirac cones, regions of *k*-space where the band gap is zero and the density of states is unoccupied (**Figures 6.2b,c**), pose a significant challenge when using perturbation theory due to the vanishing band gap at **K**.[339] A particular issue for this system is that, during conventional convergence methods, the use of increasingly fine Monkhorst-Pack *k*-grids for sampling reciprocal space will result in the periodic sampling of the Dirac point, preventing convergence.[339]

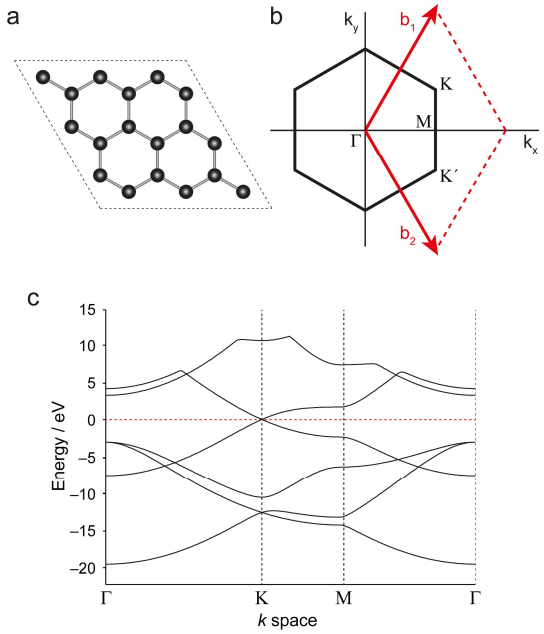

Figure 6.2. (a) Relaxed geometry of the 3 × 3 × 1 graphene supercell. (b) Real-space unit cell (red) and Brillouin zone (black) for a primitive graphene unit cell. Points of interest within reciprocal space are denoted. (c) Electronic band structure for the primitive unit cell of graphene. Energy is normalized by so that the Fermi Energy is at 0 eV. The Dirac cone with zero band gap is shown at the point **K**.

To gain further understanding of the shielding contributions, a single helium atom was inserted at the centre of the graphene slit-pore (5 Å above the plane and aligned above a carbon atom) to probe magnetic shielding at the centre of the void space (**Figure 6.3a**). Helium was selected as the probe as it is a simple closed-shell atom, with its response unaffected by geometry or orientation. Additionally, helium is tightly bound, minimising polarisation or atom-sheet interaction effects at this distance from the graphene surface.

For **Γ**-centred *k*-grids where *m* is odd, the calculated isotropic magnetic shielding, σ_{iso}, for both ^{13}C and ^{3}He, was substantially overestimated (by several orders of magnitude) compared to experimental values and did not converge with respect to *m*. This overestimation is due to the use of a 3 × 3 × 1 supercell as the *k*-point that samples the Dirac point, **K**, is folded back upon **Γ** within the first Brillouin zone. For **Γ**-centred *k*-grids with even-*m* values, direct sampling of **Γ** (and hence **K**) is avoided, giving more reasonable σ_{iso} values for both ^{3}He and ^{13}C. However, convergence is still not achieved; instead, σ_{iso} values for both nuclei decrease approximately linearly as *m* is increased (**Figure 6.3b**). This is attributed to *k*-points sampling increasingly close to **K** as the grid density increases.

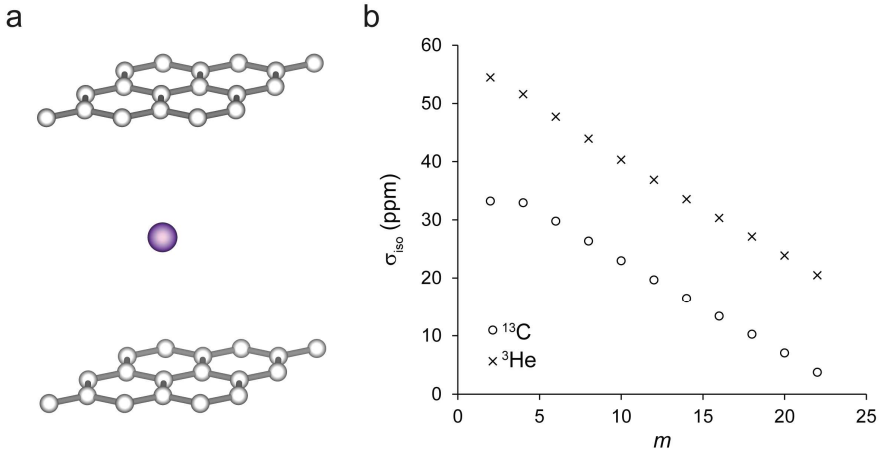

Figure 6.3. (a) Schematic representation of the helium probe within the graphene supercell slit-pore. (b) Isotropic shielding tensor values, σ_{iso}, for ^{13}C nuclei within graphene sheet and ^{3}He probe molecule calculated using a **Γ**-centred Monkhorst-Pack as a function of even integers of *m*.

To a first approximation, the relative changes in σ_{iso} with respect to increasing *m*, $\Delta\sigma_{iso}/\Delta m$, appears to be equivalent for both nuclei (**Figure 6.4a**); however, upon closer inspection, small differences are observed (*i.e.*, $\Delta\sigma_{iso}^{^{13}C}/\Delta m - \Delta\sigma_{iso}^{^{3}He}/\Delta m \neq 0$ ppm). Additionally, $\Delta\sigma_{iso}/\Delta m$ does not converge to a constant value for either nucleus, instead exhibiting oscillatory behaviour. To explore the convergence behaviour further, **Γ**-centred *k*-grids offset by half a *k*-grid-step along

the reciprocal lattice vectors parallel to the sheet plane, in one dimension, φk_x or φk_y, and two dimensions, φk_{xy}, were also investigated. φk_x offset grids with odd values of m (odd-m) avoid the direct sampling of $\mathbf{K}$, returning ^{13}C σ_{iso} values consistent with those for even-m grids with no offset. Notably, for φk_x shifted odd-m k-grids, $\Delta\sigma_{iso}^{^{13}C}/\Delta m - \Delta\sigma_{iso}^{^{3}He}/\Delta m$ converges to 0 ppm as $m \geq 29$ (**Figures 6.4b,c**), indicating that both ^{13}C and ^{3}He experience the same oscillatory convergence behaviour with respect to m. It is therefore inferred that, for φk_x shifted odd-m k-grids, the non-converging shielding contribution is uniform across the unit cell, being independent of nucleus and position.

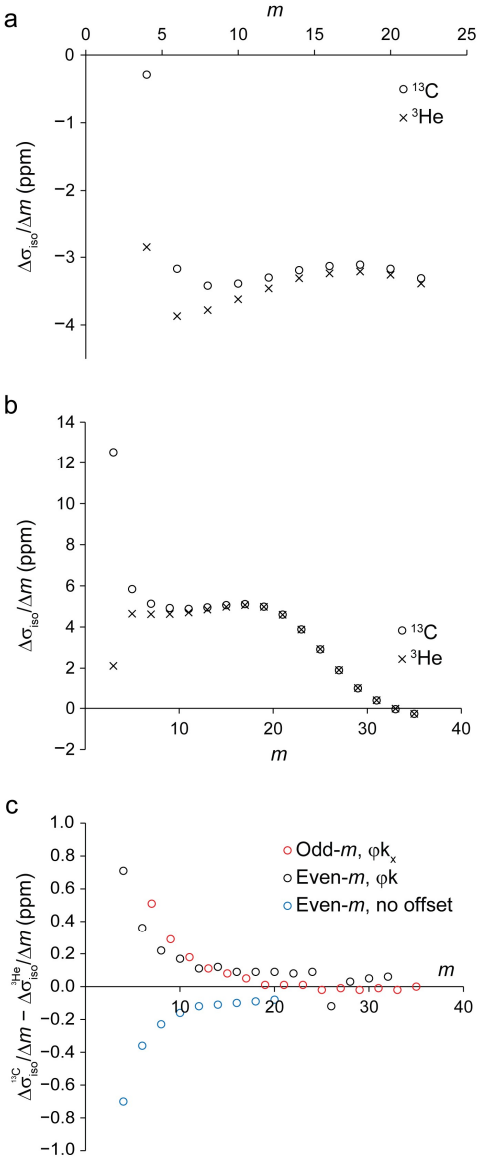

Figure 6.4. The change in σ_{iso} between even integers of m, $\Delta\sigma_{iso}/\Delta m$, for ^{13}C and ^{3}He with respect to increasing values of m calculated using a Γ-centred Monkhorst-Pack k-grid for (a) unshifted, even-m values and (b) odd-m values shifted by a half a grid-step in the x-dimension, φk_x. (c) ^{13}C and ^{3}He $\Delta\sigma_{iso}/\Delta m$ values for different offsets of Γ-centred Monkhorst-Pack k-grids against m.

To investigate the observed convergence behaviour, the contributions to the total shielding tensor were considered independently. Following Pickard and Mauri,[277] σ_{iso} can be separated into four isotropic shielding components:[351,352]

$$\sigma_{iso} = \sigma_{core}^{loc} + \sigma_{dia}^{loc} + \sigma_{para}^{loc} + \sigma_{bare}^{lr} \quad (6.1)$$

where σ_{core}^{loc} is the contribution from the core electrons to the shielding computed in a free-atom calculation that does not depend on the chemical environment.[352] The remaining terms are separated into short-range and long-range contributions, corresponding to currents arising within and outside the spherical region centred about the atom used for the PAW augmentation, respectively. The local components are separated into short-range diamagnetic contributions, σ_{dia}^{loc}, and short-range paramagnetic contributions, σ_{para}^{loc}. Long-range contributions to the magnetic shielding arising from the bare induced field are defined by σ_{bare}^{lr}.[339] This long-range shielding term is then separated into further contributions from ring current-induced diamagnetic fields, σ_{RC}^{lr}, magnetic susceptibility, σ_{BMS}^{lr}, and a term comprising remaining long-range contributions (*e.g.,* valence GIPAW contributions), σ_{α}^{lr}:[277]

$$\sigma_{bare}^{lr} = \sigma_{RC}^{lr} + \sigma_{BMS}^{lr} + \sigma_{\alpha}^{lr} \quad (6.2)$$

In GIPAW, the macroscopic magnetic susceptibility, χ, is determined as the volume-normalised second derivative of the total energy with respect to the magnetic field. σ_{BMS}^{lr} is then calculated assuming a spherical shape via $\sigma_{BMS}^{lr} = -(8\pi/3)\chi$ and added as a uniform contribution across the unit cell.[277,353,354] For φk_x shifted odd-m k-grids, $\sigma_{para.}^{loc}$ and $\sigma_{dia.}^{loc}$ converged at $m > 29$ for both ^{3}He and ^{13}C. As σ_{core}^{loc} is a constant contribution, the oscillatory behaviour of ^{3}He σ_{iso} and ^{13}C σ_{iso} with respect to m must therefore arise from σ_{bare}^{lr}. Indeed, σ_{BMS}^{lr} exhibits an oscillatory behaviour with respect to m that is identical to those observed for ^{3}He σ_{iso} and ^{13}C σ_{iso} (**Figure 6.5a**). Subtracting σ_{BMS}^{lr} from σ_{iso} removes the oscillatory behaviour and provides converged magnetic shielding values for ^{13}C (**Figure 6.5b**). Thus, the non-convergence of σ_{iso} is attributed to the failed convergence of the BMS and its contribution to the total magnetic shielding. This is ascribed to the approach used when determining of the BMS, wherein surface currents, and thus the σ_{BMS}^{lr} contribution, are inaccurately described for a sphere comprising periodic 2D materials that exhibit a vanishing band. Interestingly, if the BMS contribution is neglected, and the resulting ^{13}C shielding parameter ($\sigma_{iso} - \sigma_{BMS}^{lr}$, **Figure 6.5b**) is converted to a shift δ_{iso} by

subtracting it from the reference shielding, the calculation returns a converged value of 129.8 ppm for carbons within a d = 10 Å graphene slit-pore. This value gives good agreement with experimental values for graphitic and porous carbons.[106,355–358] This shows that the BMS contribution can be omitted for this system to give calculated magnetic shielding parameters that give relatively good agreement with experimental data.

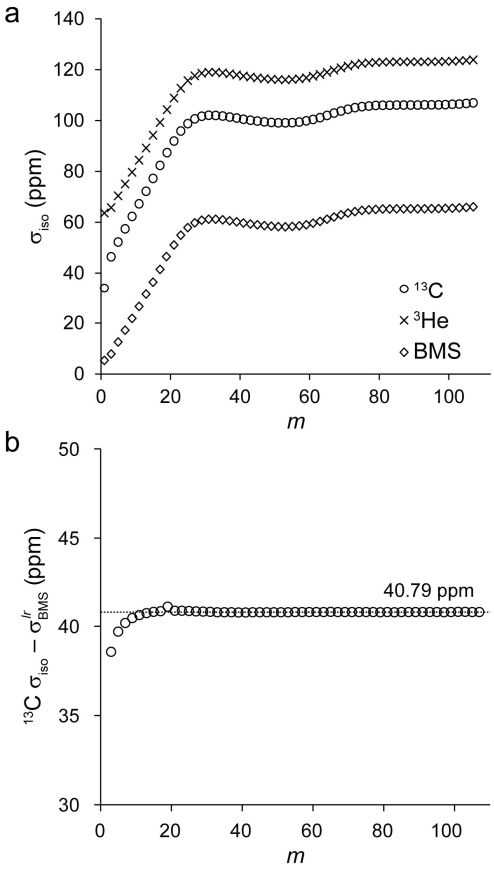

Figure 6.5. (a) Non-converging ^{13}C σ_{iso} and ^{3}He σ_{iso} values calculated using a Γ-centred φk_x offset odd-m k-grid plot against m on a d = 10 Å graphene slit-pore. The same oscillatory behaviour was observed for ^{13}C σ_{iso}, ^{3}He σ_{iso}, and the long-range bulk magnetic susceptibility (BMS) shielding contribution, σ^{lr}_{BMS}. (b) ^{13}C σ_{iso} − σ^{lr}_{BMS} against m. A converged value of 40.79±0.02 ppm was reached by m = 33.

6.3.3 Periodic NICS calculations for extended and molecular aromatic systems

Having established an approach for determining converged magnetic shielding parameters, we can now investigate the NICS above a graphene plane. This was investigated using the NICS package of CASTEP, in which the total current is integrated to give the induced magnetic field projected onto defined locations in space within the unit cell.[352] The magnetic shielding tensor at each position is given by:[22,359]

$$\sigma_{NICS} = -\left(\sigma^{lr}_{bare} - \sigma^{lr}_{BMS}\right) - \sigma_{ref} \qquad (6.3)$$

where σ_{ref} is zero in this instance. NICS values were calculated across different interlayer separations, with graphene layers positioned at $z = 0$ Å and $z = d$ Å. Odd-m φk_x shifted k-grids were used to converge the magnetic shielding parameters apart from the σ^{lr}_{BMS} contribution, which was neglected. **Figures 6.6a** shows that the NICS is approximately uniform at distances > 3 Å above the graphene surface. Uniformity of the NICS between graphene layers was observed across all values of d investigated (up to 75 Å). **Figure 6.6b** shows the NICS(d) values at the centre of the slit-pore across different values of d using φk_x shifted odd-m k-grids, where ^{13}C $\sigma_{iso} - \sigma^{lr}_{BMS}$ converged by $m = 33$ for all values of d. Despite the uniformity of the NICS between graphene layers, the magnitude of the NICS reduces as the interlayer spacing increases.

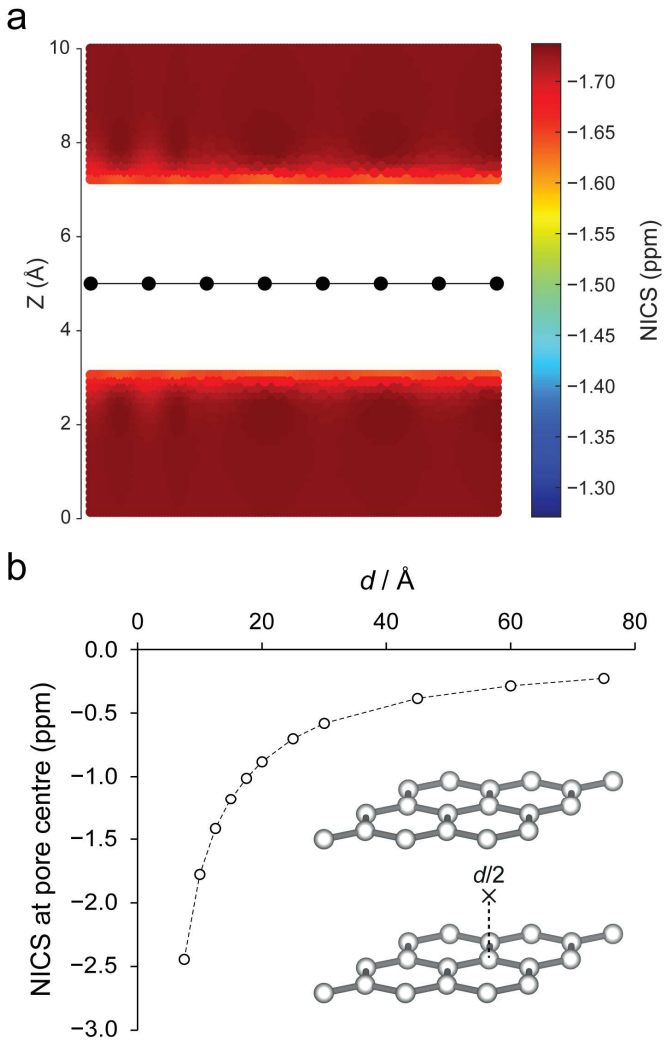

Figure 6.6. (a) Map of nucleus-independent chemical shift (NICS) above the graphene d=10 Å slit-pore with points < 2 Å from atomic coordinates removed to show gradient of the NICS through space. The plane is taken along the edge of the unit cell. (b) NICS values measured at the centre of the slit-pore against slit-pore width, d.

To gain a better understanding, periodic calculations were also performed on unit cells containing benzene or pyrene as model aromatic molecules comprising 4n+2 delocalised π-electrons (**Figure 6.7a**).[331,332,360] In contrast to graphene, these molecular systems have wide band gaps, enabling the straightforward convergence of magnetic shielding parameters. For these calculations, an intermolecular separation of 10 Å perpendicular to the molecular plane was employed, together with a large vacuum region (40 Å × 40 Å) parallel to the molecular plane. **Figure 6.7b** shows the NICS values calculated at different distances, *z*, between the surfaces of benzene and pyrene molecules. Expectedly, σ_{BMS}^{lr} was found to be a minor contributor for both systems, with values of +0.06 ppm and +0.16 ppm for benzene and pyrene, respectively; as such, the NICS for these systems is determined almost entirely by the ring current-induced shielding contribution, σ_{RC}^{lr}.

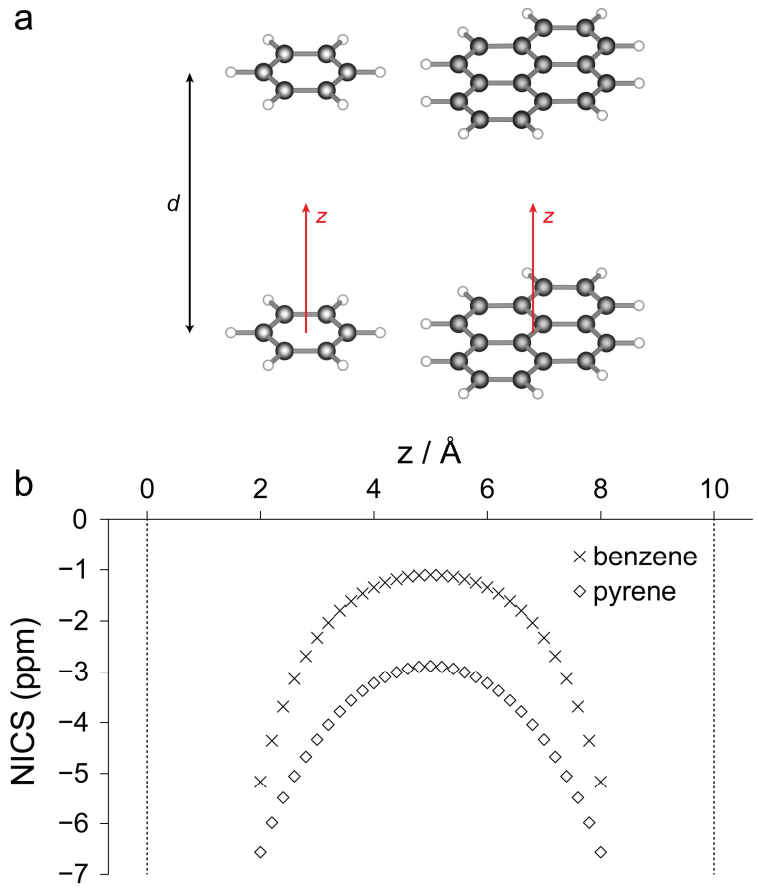

Figure 6.7. (a) Schematic of the aromatic molecule geometry for a 10 Å slit-pore within the unit cell with the path along which the nucleus-independent chemical shifts (NICS) were calculated indicated in red. (b) Calculated NICS values between parallel molecules along the *z*-axis which passes through the centre of mass of the molecules, with pore surfaces situated at 0 Å and 10 Å.

Both systems show a negative (diamagnetic) NICS that increases as the distance to the molecule surface is decreased. This is in good agreement with values determined in fragment-

based calculations of finite polyaromatic systems, in which the NICS field is predicted to reduce with increasing distance from the molecule and is additive between two parallel molecules.[22,34] **Figure 6.8** shows that, as the molecular separation is reduced, the NICS between the benzene molecules becomes increasingly uniform as the difference between the maximum NICS and minimum NICS decreases. Similar behaviour was observed in previous work by Forse *et al*.[22]

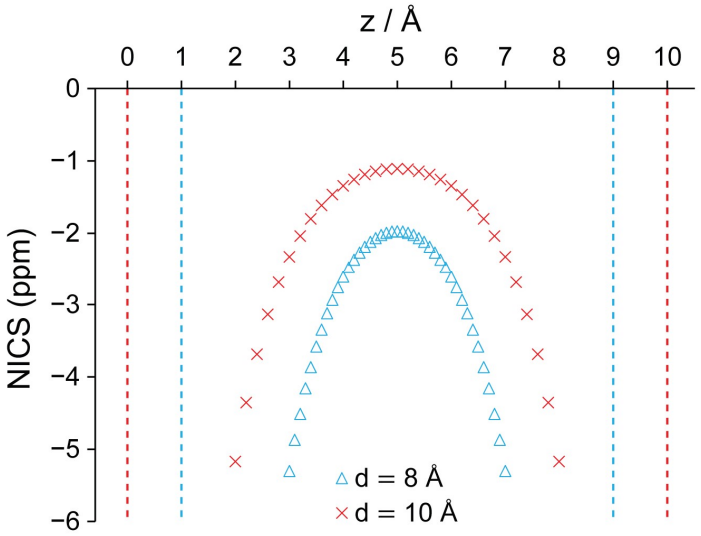

Figure 6.8. Calculated NICS values between parallel benzene molecules with interlayer separations of 8 Å and 10 Å. The *z*-axis is perpendicular to the surface and passes through the centre of mass of the benzene molecules. Surface positions are denoted using dashed lines.

As the size of the aromatic molecule is increased, the decay of the NICS with respect to increasing distance above the surface reduces. This has also been observed in other studies on large polyaromatic molecules such as coronene and dicircumcoronene, wherein the distance dependence of the NICS reduces as graphitic domain size is increased.[22,34] This is inferred to be a result of the increased number of aromatic rings below the position where the NICS was measured, and the increasing distance from the ring current circulating the edge of the molecule. However, this behaviour is different to the graphene case presented above, wherein a uniform NICS is observed. Instead, the constant NICS value between the graphene layers for a defined value of *d* is inferred to be due to the small interlayer separation with respect to the sheet size and the absence of an edge-current; and the reduction in the NICS with increasing interlayer separation is due to reducing cumulative NICS contributions from both the adjacent sheets and periodic replicas of the sheets.

Notably, despite the larger domain size and extended aromaticity, the NICS values for graphene were found to be of similar magnitude to those determined for a benzene slit-pore of the same

dimensions (**Figure 6.6b** and **Figure 6.7b**). Examination of the current flow reveals that the ring current 2 Å above the graphene surface (**Figure 6.9a**) is significantly reduced compared to that at the same distance above a benzene molecule (**Figure 6.9b**), with maximum current vector magnitudes of 0.40 nA T^{-1} and 18.22 nA T^{-1}, respectively. The reduced diatropic current flow in graphene is attributed to the equal likelihood of each ring within the plane being the centre of a ring current, with neighbouring diatropic ring currents opposing each other, subsequently localising the ring current to the 6-membered aromatic rings. Conversely, the ring arrangements in pyrene and benzene allows for the ring currents to organise themselves to avoid frustration with adjacent rings, facilitating an increased current flow, particularly around the molecular edge.[267]

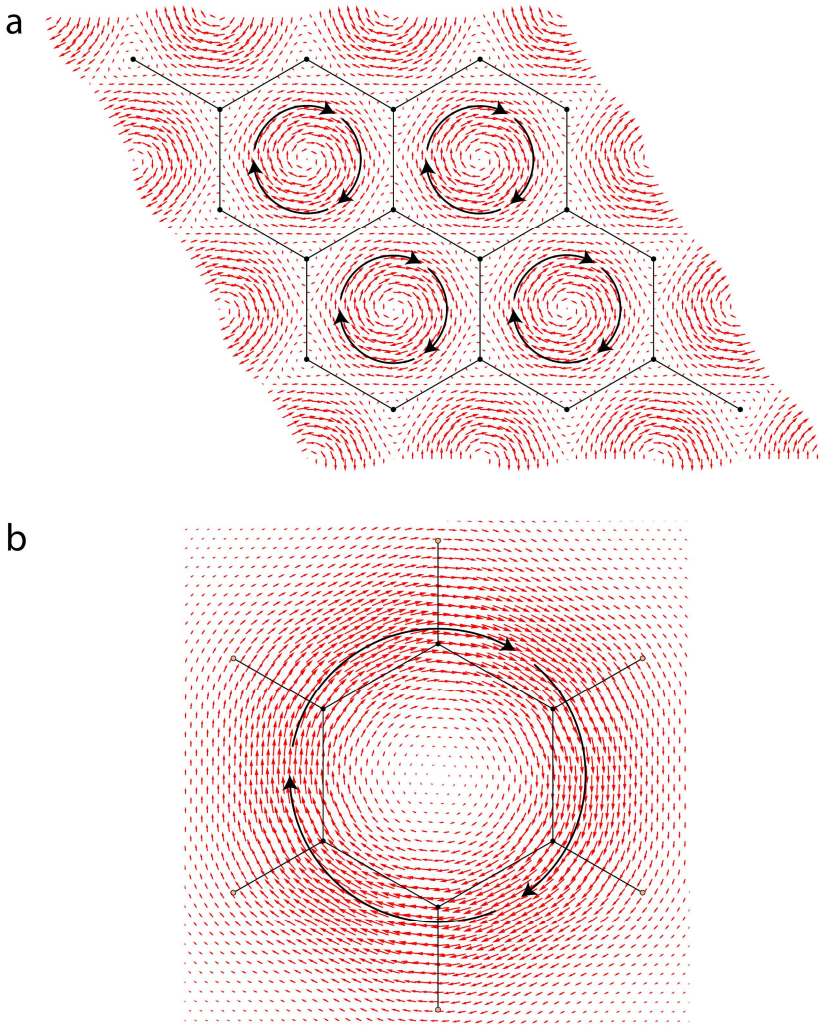

Figure 6.9. Current flow vector field plots at 2 Å above the surface for 10 Å wide slit-pores comprising (a) graphene sheets and (b) benzene molecules. Black arrows have been added to show the general direction of the current flow at the region exhibiting the largest current vector magnitudes. Current flow vectors are denoted using red arrows and are scaled to reflect their vector magnitudes. The maximum vector magnitudes of the graphene and benzene systems are 0.40 nA T^{-1} and 18.22 nA T^{-1}, respectively.

The NICS for graphene was shown to be significantly less negative than values calculated across the pyrene slit-pore (**Figure 6.6b** and **Figure 6.7b**) and reported values for extended polyaromatic hydrocarbons such as coronene, circumcoronene, and dicircumcoronene.[22] It may be reasonable to expect that the NICS for graphene should be very large due to its infinite size. However, for the infinite graphene plane, the absence of an edge removes contributions from edge-currents, causing the sole contribution towards the NICS to be that of the frustrated surface topology, potentially rationalising its relatively small NICS.

6.3.4 Periodic NICS calculations for defected graphene

NMR parameters, including the problematic BMS contribution, for periodic aromatic structures can be determined more straightforwardly provided the electronic structure does not demonstrate a vanishing band gap. In graphene, this can be achieved by the introduction of defects which remove the Dirac cones while maintaining a predominantly sp^2-hybridised 2D structure. Following a similar approach to that of Zurek *et al*.,[337] 6 × 6 × 1 supercells of graphene containing the low formation energy (~5 eV) Stone-Wales (SW) defect, or 5/7/7/5 defect formed from a 90° rotation of a C-C bond connecting two hexagons, were constructed.[337,361,362] Slit-pores comprising SW-defective graphene layers with an interlayer separation of 10 Å were relaxed, with the atomic coordinates and lattice vectors fixed in the *z*-dimension during optimisation to maintain layer planarity and a defined interlayer separation. **Figure 6.10a** shows the electronic structure of the optimised geometry (**Figure 6.10b**), where a bandgap of 0.21 eV is observed at **Γ**. All shielding parameters converged at $m \geq 14$ using an $m \times m \times 1$ **Γ**-centred Monkhorst-Pack *k*-grid with no offset.

Figure 6.10b shows a simulated ^{13}C NMR spectrum based on the calculated ^{13}C σ_{iso} values minus the σ_{BMS} contributions for the $d = 10$ Å SW-defected graphitic slit-pore. Chemical shifts between 122.6 ppm and 159.3 ppm are predicted for carbon atoms in the main sheet, together with a shift of 159.3 ppm for the two carbons in the bond connecting the two heptagonal rings. These values are in good agreement with shielding parameters calculated for SW-defected single-walled carbon nanotubes[337] and with experimental results obtained for sp^2-hybridised carbons.[338,363] Markedly, despite the convergence of all shielding parameters, experimental ^{13}C δ values are most accurately reproduced with the omission of the σ^{lr}_{BMS} contribution (σ^{lr}_{BMS}= +51.13 ppm). These results further indicate that, for 2D materials with narrow band gaps, the BMS contribution should be neglected when determining the isotropic magnetic shielding.

In addition to converged ^{13}C shielding parameters, the NICS across the 10 Å slit-pore was calculated and mapped.

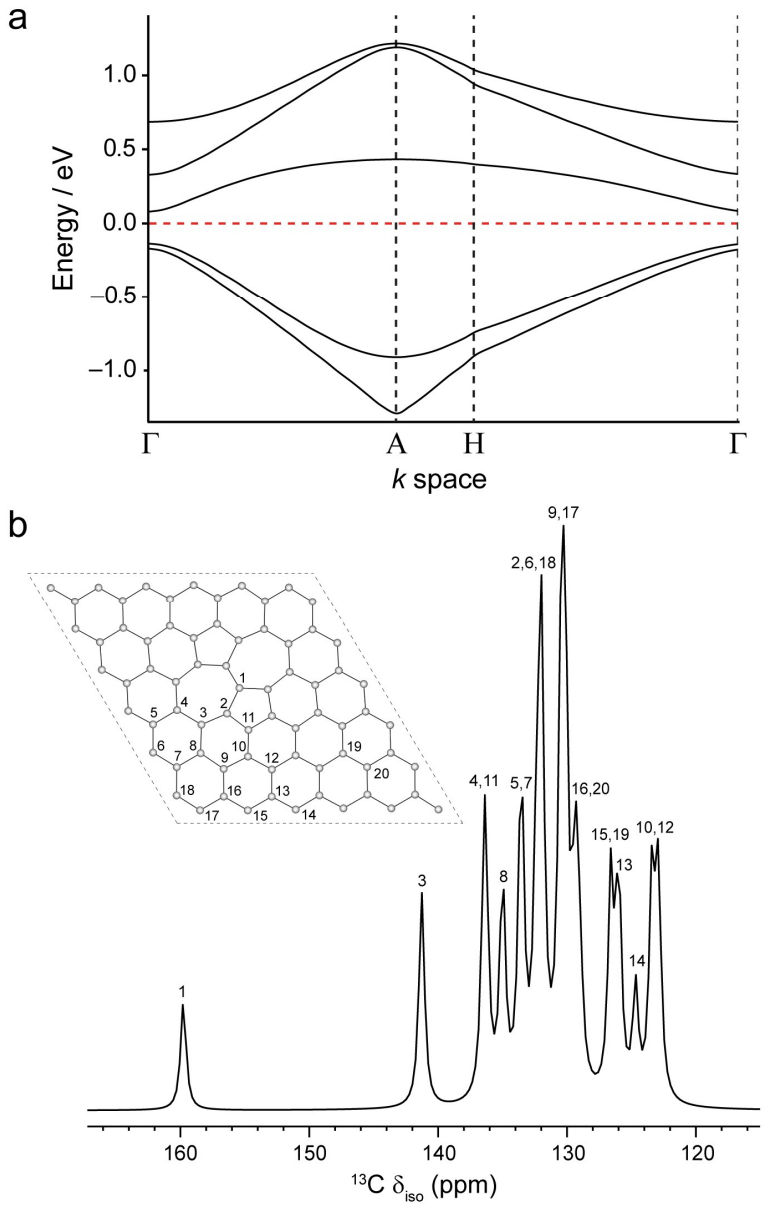

Figure 6.10. (a) Electronic band structure of SW-defected graphene layer slit-pore (d = 10 Å) and (b) simulated ^{13}C NMR spectra generated using calculated chemical shifts. The relaxed structure is shown in the inset of the figure with labelled sites that correlate with simulated peaks in the NMR spectrum.

Figure 6.11a-c shows maps of the NICS at planes across the unit cell, with layers situated at z = 0 Å and z = 10 Å. Notably, the induced field is no longer uniform, exhibiting spatial variation in the NICS, particularly centred about the defect site within the layer. Moreover, the magnitude of the NICS is larger than that of graphene and is positive which indicates paramagnetic character. This further suggests that the uniform field observed for defect-free graphene is a consequence of the absence of sheet edges.

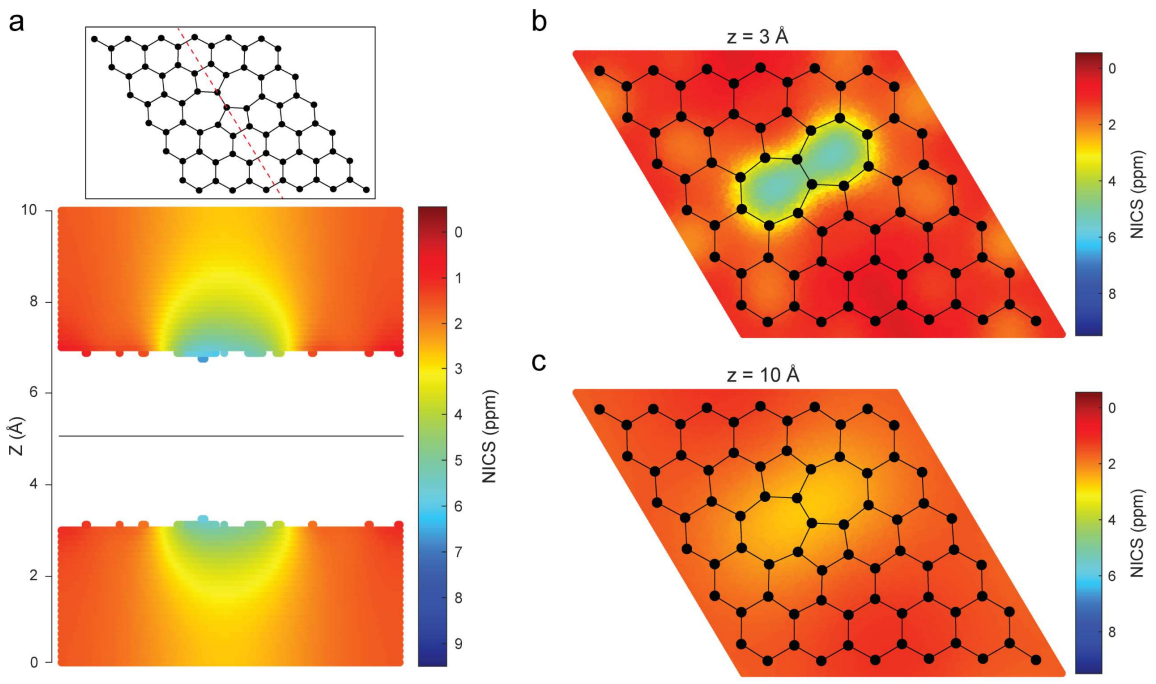

Figure 6.11. Nucleus-independent chemical shift (NICS) maps for a Stone-Wales defected 6 × 6 × 1 graphene supercell forming a *d* = 10 Å slit-pore taken along: (a) the *yz*-plane of the NICS along the centre the C-C bond between the two heptagonal rings; (b) the *xy*-plane at a height of *z* = 3 Å, or 2 Å above the surface; and (c) the *xy*-plane at z = 10 Å, or the centre of the slit-pore. NICS values calculated at positions < 2 Å from the defected layer atom positions are removed to better show the gradient in NICS across the pore.

Figure 6.12a shows the NICS with respect to *z* at two positions above the layer: (A) at the centre of the defect site and (B) at the centre of a six-membered aromatic ring away from the defect. The magnitude of the NICS induced above site A is similar to that induced by a pyrene slit-pore of the same dimensions, although opposite in sign. The NICS at sites A and B (or NICS-A and NICS-B, respectively) are shown to be different, with the largest paramagnetic NICS being induced directly above the defect site. As *z* is increased, the NICS measured at the two sites begin to converge. This is in good agreement with observations by Moran *et al*. for polyaromatic hydrocarbons.[132] **Figure 6.12b** shows a map of the ring current-flow tensors for the SW-defected layer. The previously frustrated ring currents of the pristine graphene layer are observed to circulate in a paratropic fashion around the SW defect, inducing a paramagnetic NICS across the slit-pore. The ring current is observed to travel around the edges of the two heptagonal rings and does not flow across the outer edges of the 5-membered carbon rings. The SW-defect exhibits a 12-electron paratropic current with a maximum current flow vector magnitude of 16.18 nA T^{-1}. This shows that the previously frustrated ring currents of the periodic graphene layer are freed by the introduction of a defect within the graphene surface.

As seen in **Figure 6.12a**, NICS-A and NICS-B do not reach a single value at the centre of the 10 Å slit-pore, showcasing translational variance in the magnetic environment across the entirety of the pore volume.

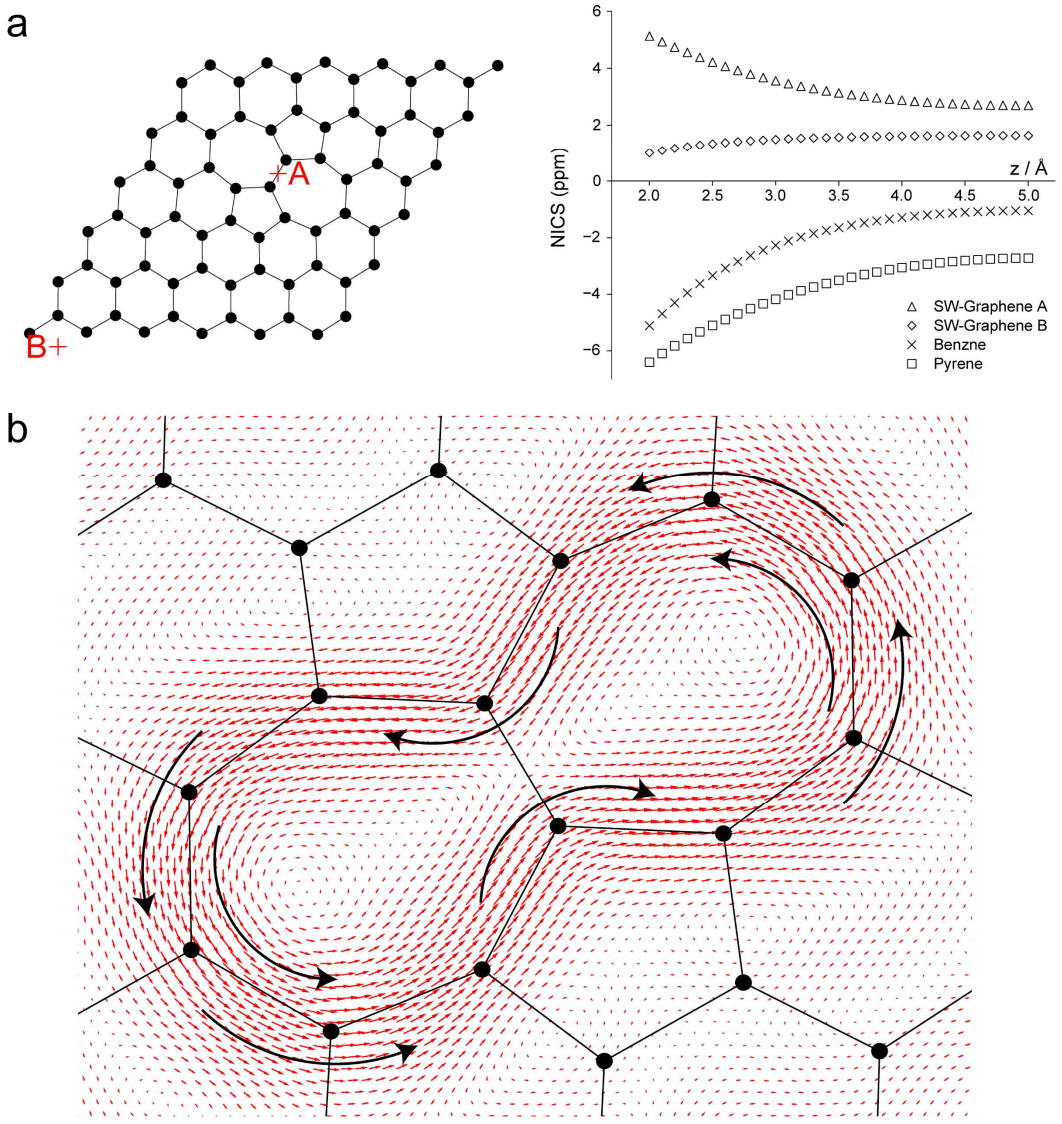

Figure 6.12. (a) Sites on the SW-defected graphene sheet where the NICS was mapped above and the corresponding values plot at various points between d = 10 Å slit-pores comprising benzene, pyrene, and SW-defected graphene layers. (b) Mapped current flow vectors across the SW-defected graphene surface. Black arrows are added for clarity and red arrows show the current-flow-vectors scaled by magnitude. The maximum current magnitude was 16.18 nA T^{-1}.

Figure 6.13 shows that by increasing d to 20 Å, the magnitude of both NICS-A and NICS-B converges to within 0.1 ppm across the xy-plane at the pore centre (z = 10 Å). The NICS along the z-axis at each position is shown to be more uniform (*i.e.,* a smaller difference between the maximum and minimum NICS values) for the narrower pore, following trends observed for systems comprising finite aromatic molecules.

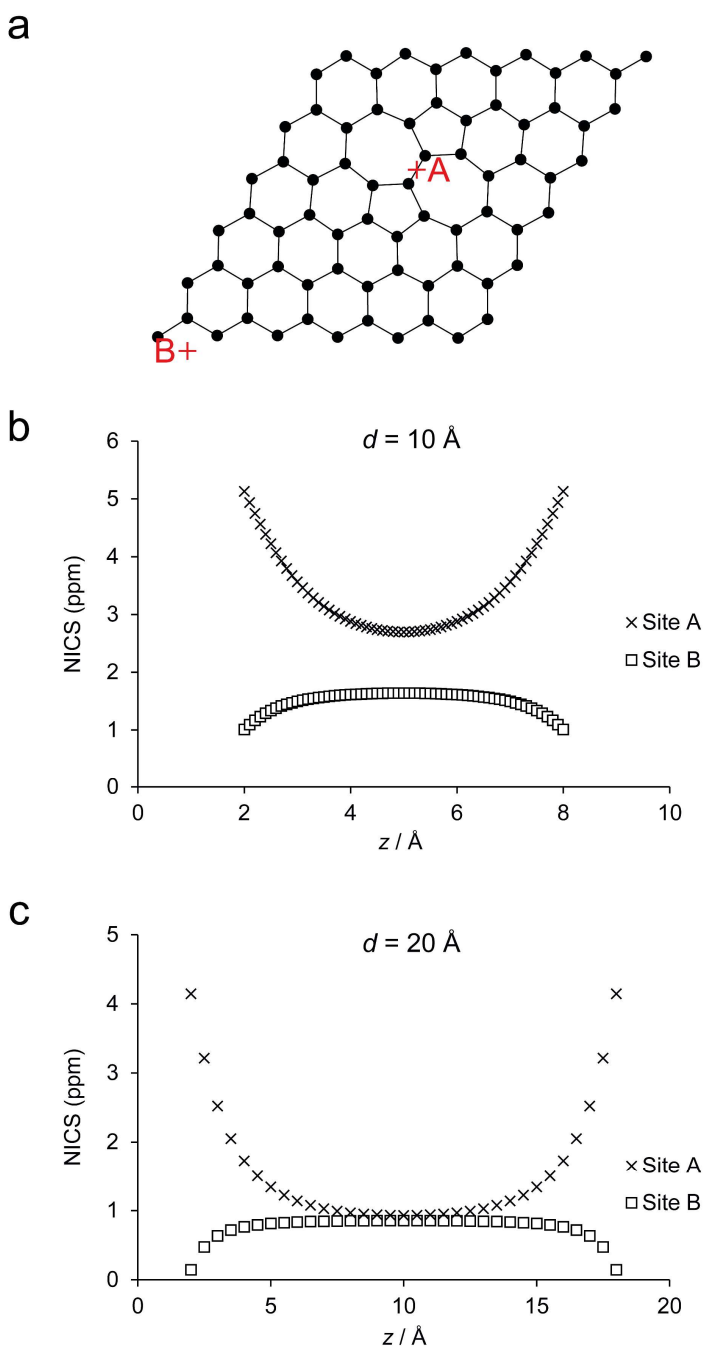

Figure 6.13. (a) Geometry optimised structure of the 6 × 6 × 1 Stone-Wales defected graphene supercell with the positions of sites A and B in the *xy*-plane marked. The calculated ring current-induced shifts at positions across the slit-pore (where the carbon surfaces are situated at z = 0 Å and z = d Å and are perpendicular to the z dimension) are mapped for sites A and B for slit-pores of (a) d = 10 Å and (b) d = 20 Å. For the d = 20 Å pore, the NICS values at sites A and B are shown to converge to within 0.1 ppm at the pore centre (z = 10 Å), exhibiting a more uniform magnetic environment at the centre of the pore when compared to the narrower d = 10 Å pore.

6.4 Summary and outlook

The determination of the bulk magnetic susceptibility and its correlated magnetic shielding contribution has been shown to pose significant challenges for periodic 2D materials with narrow band gaps. However, comparison between experimental and calculated chemical shifts suggests that the magnetic susceptibility contribution should in fact be omitted from the total shielding term to give the best agreement between experimental and calculated data.

The frustrated ring currents across the surface of a periodically repeating graphene surface have been shown to induce a minimal NICS above the ring-plane. This behaviour contrasts the domain-size dependency demonstrated in finite polyaromatic hydrocarbon molecules.[22,34,359] In the absence of an edge, the extended aromaticity of graphene has been shown to form a small ring current above its surface due to its frustrated topology. It is therefore inferred that the increased magnitude of the NICS with respect to domain size in finite polyaromatic molecules is determined by the presence of an edge, with the major contribution to the NICS being the current circulating the molecule edge.[331] Therefore, to accurately model the diamagnetic pore environment that is observed experimentally for microporous carbons, a carbon-edge should be included.

The insertion of defect sites into the graphene surface has been shown to alleviate the frustration of the ring currents across the graphene surface. The introduction of the SW defect results in a sizeable paratropic ring current, giving rise to a paramagnetic NICS of similar magnitude to the diamagnetic NICS observed in fragment-based DFT calculations upon polyaromatic hydrocarbons. Further work is required to probe the effects of other defects and surface-guest interactions upon the surface ring currents of graphene and the correlated NICS values induced above the sheet.

Chapter 7

Conclusions and outlook

NMR spectroscopy has been shown to be a powerful technique for studying the behaviour of aqueous electrolytes within porous carbon electrode materials. Through the quantitative analysis of NMR spectra from a wide range of aqueous electrolytes, valuable insights into the complex dynamics of the electrode-electrolyte system have been gained. This thesis advances the understanding of key factors influencing ion adsorption and electrosorption behaviour within aqueous supercapacitors. Additionally, this thesis presents the challenges of determining magnetic parameters for extended aromatic systems using the GIPAW approach, while also outlining strategies to overcome these obstacles.

Solid-state NMR spectroscopy has been employed to explore how ion properties influence the spontaneous partitioning of ions across microporous carbons. The intrinsic solvation properties of the ions are shown to affect the ionophilicity or ionophobicity of the pore environments. Weakly hydrated ions exhibit increased cation uptake within the pores, whereas strongly hydrated species show reduced cation insertion. Moreover, ionophilic and ionophobic systems demonstrate fundamentally different behaviours in relation to loading volume, particularly in terms of the stability of the ion population distribution as a function of loaded electrolyte volume. The measurement of $\Delta\delta$ across myriad systems has helped to rationalise ion and solvation behaviour, with results suggesting that pore confinement induces changes in ion solvation during pore insertion. Furthermore, pH has been shown to be intrinsically related to the ionophilicity of the system. Thus, for aqueous electrolytes, complex pH effects must be considered when investigating spontaneous adsorption behaviour. Further experiments are required to better understand the role of ion-solvent interactions on spontaneous partitioning within supercapacitor electrodes. Specifically, similar studies using electrolytes made using the same salts and organic solvents should be conducted to deconvolute contributions from pH effects and to investigate a broader range of solvation strengths for a given ion.

In situ NMR spectroscopy experiments were conducted to investigate the charge storage mechanisms in supercapacitor devices comprising aqueous electrolytes with contrasting solvation properties. The challenges of identifying electrochemically stable combinations of aqueous electrolytes and low-susceptibility current collectors are discussed, and suitable pairings for *in situ* studies of aqueous supercapacitors are presented. The findings reveal that the ionophilicity or ionophobicity of the electrolyte, under spontaneous adsorption conditions, affects the preference towards specific charge-balancing mechanisms. Thus, the solvation properties of electrolyte ions are shown to play a crucial role, with strongly solvated ions (*e.g.*, SO_4^{2-}) favouring co-ion expulsion, while weakly solvated ions (*e.g.*, $TFSI^-$) favour counter-ion insertion under an applied voltage. Across all electrolytes studied, a diamagnetic shift is observed for the in-pore species of the negatively polarised electrode. Further research is needed to fully understand the mechanisms determining this behaviour. Future studies should aim to comprehensively characterise the electrochemical performance of devices that exhibit different charge-balancing mechanisms.

Periodic models of extended aromatic systems are a valuable tool in developing our understanding of adsorbate behaviour in porous carbon materials. Periodic DFT calculations on periodic graphene layers show the challenges associated with obtaining converged magnetic parameters, due to graphene's unique electronic properties. The shielding contribution from magnetic susceptibility related to sample shape is identified as the primary cause of convergence issues. By omitting this contribution from the total isotropic shielding, a converged value is achieved that is in good agreement with experimental data. Periodic graphene is shown to exhibit a reduced NICS relative to finite aromatic molecules (*e.g.*, benzene and pyrene), a behaviour attributed to its frustrated ring current topology and lack of an edge current. Surface defects are shown to disrupt these frustrated ring currents, leading to an increase in the induced NICS above the periodic surface. Future research should explore how guest-surface interactions influence the frustrated ring currents on graphene surfaces and their associated NICS. Further studies on surface defects, particularly those that induce diatropic ring currents, are of significant interest. When selecting defects to model, inspiration should be drawn from experimental data to better understand features observed in experimental spectra.

In summary, this thesis provides new insights into guest-surface interactions within aqueous supercapacitor devices and related technologies (*e.g.*, capacitive deionisation and electrocatalysis). The findings demonstrate that ion solvation properties significantly influence

adsorption behaviour in the absence of an applied potential, with weakly solvated ions readily entering pores leading to increased in-pore ion concentrations. Furthermore, the spontaneous distribution of ions within uncharged carbon micropores has been shown to strongly affect the preferred charging mechanism. These results suggest that careful selection of ions based on their ion-solvent interactions could enable the design of devices with tailored spontaneous adsorption and electrosorption behaviours. Finally, planewave-based DFT has been shown to accurately calculate chemical shifts for previously non-converging periodic graphene-like sheets, achieving good agreement with experimental data by either omitting the bulk magnetic susceptibility component or by introducing an electronic band gap.

Bibliography

1 H. Marsh and F. Rodríguez Reinoso, *Carbon*, 1998, **36**, 159–175.

2 M. E. Suss, S. Porada, X. Sun, P. M. Biesheuvel, J. Yoon and V. Presser, *Energy Environ. Sci.*, 2015, **8**, 2296–2319.

3 P. Simon and Y. Gogotsi, *Philos. Trans. R. Soc. A Math. Phys. Eng. Sci.*, 2010, **368**, 3457–3467.

4 P. Simon and Y. Gogotsi, *Acc. Chem. Res.*, 2013, **46**, 1094–1103.

5 M. Oschatz, L. Borchardt, I. Senkovska, N. Klein, M. Leistner and S. Kaskel, *Carbon*, 2013, **56**, 139–145.

6 H. Marsh and F. Rodríguez Reinoso, *Activated Carbon*, Elsevier Science & Technology Books, 2006.

7 N. Fulik, F. Hippauf, D. Leistenschneider, S. Paasch, S. Kaskel, E. Brunner and L. Borchardt, *Energy Storage Mater.*, 2018, **12**, 183–190.

8 V. Presser, M. Heon and Y. Gogotsi, *Adv. Funct. Mater.*, 2011, **21**, 810–833.

9 L. Borchardt, M. Oschatz and S. Kaskel, *Mater. Horizons*, 2014, **1**, 157–168.

10 L. Cervini, O. D. Lynes, G. R. Akien, A. Kerridge, N. S. Barrow and J. M. Griffin, *Energy Storage Mater.*, 2019, **21**, 335–346.

11 J. S. Noh and J. A. Schwarz, *Carbon*, 1990, **28**, 675–682.

12 Y. Zhang, H. Feng, X. Wu, L. Wang, A. Zhang, T. Xia, H. Dong, X. Li and L. Zhang, *Int. J. Hydrogen Energy*, 2009, **34**, 4889–4899.

13 A. C. Forse, C. Merlet, C. P. Grey and J. M. Griffin, *Prog. Nucl. Magn. Reson. Spectrosc.*, 2021, **124**–**125**, 57–84.

14 N. M. Phuoc, E. Jung, N. A. T. Tran, Y. W. Lee, C. Y. Yoo, B. G. Kang and Y. Cho, *Nanomaterials*, 2020, **10**, 1–14.

15 M. E. Suss and V. Presser, *Joule*, 2018, **2**, 10–15.

16 J. M. Griffin, A. C. Forse, H. Wang, N. M. Trease, P. L. Taberna, P. Simon and C. P. Grey, *Faraday Discuss.*, 2014, **176**, 49–68.

17 K. Fic, G. Lota, M. Meller and E. Frackowiak, *Energy Environ. Sci.*, 2012, **5**, 5842–5850.

18 A. Sasikumar, J. M. Griffin and C. Merlet, *J. Phys. Chem. Lett.*, 2022, **13**, 8953–8962.

19 C. Merlet, C. Péan, B. Rotenberg, P. A. Madden, B. Daffos, P. L. Taberna, P. Simon and M. Salanne, *Nat. Commun.*, 2013, **4**, 2701–2706.

20 C. Merlet, B. Rotenberg, P. A. Madden, P. L. Taberna, P. Simon, Y. Gogotsi and M. Salanne, *Nat. Mater.*, 2012, **11**, 306–310.

21 C. A. Leon y Leon, J. M. Solar, V. Calemma and L. R. Radovic, *Carbon*, 1992, **30**, 797–811.

22 A. C. Forse, J. M. Griffin, V. Presser, Y. Gogotsi and C. P. Grey, *J. Phys. Chem. C*, 2014, **118**, 7508–7514.

23 J. Chmiola, G. Yushin, Y. Gogotsi, C. Portet, P. Simon and P. L. Taberna, *Science*, 2006, **313**, 1760–1763.

24 Z. X. Luo, Y. Z. Xing, Y. C. Ling, A. Kleinhammes and Y. Wu, *Nat. Commun.*, 2015, **6**, 1–8.

25 S. Kondrat, P. Wu, R. Qiao and A. A. Kornyshev, *Nat. Mater.*, 2014, **13**, 387–393.

26 S. Kondrat, G. Feng, F. Bresme, M. Urbakh and A. A. Kornyshev, *Chem. Rev.*, 2023, **123**, 6668–6715.

27 M. V. Fedorov and A. A. Kornyshev, *Chem. Rev.*, 2014, **114**, 2978–3036.

28 L. Cervini, N. Barrow and J. Griffin, *Johnson Matthey Technol. Rev.*, 2020, **64**, 152–164.

29 J. M. Griffin, A. C. Forse, W. Y. Tsai, P. L. Taberna, P. Simon and C. P. Grey, *Nat. Mater.*, 2015, **14**, 812–819.

30 R. K. Harris, T. V. Thompson, P. Forshaw, N. Foley, K. M. Thomas, P. R. Norman and C. Pottage, *Carbon*, 1996, **34**, 1275–1279.

31 H. Wang, A. C. Forse, J. M. Griffin, N. M. Trease, L. Trognko, P. L. Taberna, P. Simon and C. P. Grey, *J. Am. Chem. Soc.*, 2013, **135**, 18968–18980.

32 Y. Z. Xing, Z. X. Luo, A. Kleinhammes and Y. Wu, *Carbon*, 2014, **77**, 1132–1139.

33 L. Borchardt, M. Oschatz, S. Paasch, S. Kaskel and E. Brunner, *Phys. Chem. Chem. Phys.*, 2013, **15**, 15177–15184.

34 D. Kilymis, A. P. Bartók, C. J. Pickard, A. C. Forse and C. Merlet, *Phys. Chem. Chem. Phys.*, 2020, **22**, 13746–13755.

35 A. C. Forse, J. M. Griffin, H. Wang, N. M. Trease, V. Presser, Y. Gogotsi, P. Simon and C. P. Grey, *Phys. Chem. Chem. Phys.*, 2013, **15**, 7722–7730.

36 A. C. Forse, C. Merlet, P. K. Allan, E. K. Humphreys, J. M. Griffin, M. Aslan, M. Zeiger, V. Presser, Y. Gogotsi and C. P. Grey, *Chem. Mater.*, 2015, **27**, 6848–6857.

37 Z. X. Luo, Y. Z. Xing, S. Liu, Y. C. Ling, A. Kleinhammes and Y. Wu, *J. Phys. Chem. Lett.*, 2015, **6**, 5022–5026.

38 R. A. W. Dryfe and J. M. Griffin, *Curr. Opin. Electrochem.*, 2022, **35**, 101084–101090.

39 W. Shi, H. Li, X. Cao, Z. Y. Leong, J. Zhang, T. Chen, H. Zhang and H. Y. Yang, *Sci. Rep.*, 2016, **6**, 1–9.

40 J. M. Griffin, A. C. Forse and C. P. Grey, *Solid State Nucl. Magn. Reson.*, 2016, **74–75**, 16–35.

41 B. E. Conway, *Electrochemical Supercapacitors : Scientific Fundamentals and Technological Applications*, Plenum Press, New York, 1999.

42 H. Helmholtz, *Ann. Phys.*, 1853, **89**, 211–233.

43 J. W. Gittins, Y. Chen, S. Arnold, V. Augustyn, A. Balducci, T. Brousse, E. Frackowiak, P. Gómez-Romero, A. Kanwade, L. Köps, P. K. Jha, D. Lyu, M. Meo, D. Pandey, L. Pang, V. Presser, M. Rapisarda, D. Rueda-García, S. Saeed, P. M. Shirage, A. Ślesiński, F. Soavi, J. Thomas, M. M. Titirici, H. Wang, Z. Xu, A. Yu, M. Zhang and A. C. Forse, *J. Power Sources*, 2023, **585**, 233637.

44 E. Redondo, L. W. L. Fevre, R. Fields, R. Todd, A. J. Forsyth and R. A. W. Dryfe,

Electrochim. Acta, 2020, **360**, 136957–136967.

45 F. Béguin, V. Presser, A. Balducci and E. Frackowiak, *Adv. Mater.*, 2014, **26**, 2219–2251.

46 A. Carmona-Orbezo, L. W. Le Fevre and R. A. W. Dryfe, *Electrochim. Acta*, 2019, **325**, 134898.

47 M. D. Stoller and R. S. Ruoff, *Energy Environ. Sci.*, 2010, **3**, 1294–1301.

48 R. Kötz and M. Carlen, *Electrochim. Acta*, 2000, **45**, 2483–2498.

49 A. J. Bard and L. J. Faulkner, *Electrochemical Methods: Fundamentals and Applications*, Wiley, Chichester, 2nd edn., 2001.

50 L. Miao, Z. Song, D. Zhu, L. Li, L. Gan and M. Liu, *Mater. Adv.*, 2020, **1**, 945–966.

51 L. Zhang and X. S. Zhao, *Chem. Soc. Rev.*, 2009, **38**, 2520–2531.

52 S. Kondrat, N. Georgi, M. V. Fedorov and A. A. Kornyshev, *Phys. Chem. Chem. Phys.*, 2011, **13**, 11359–11366.

53 S. Zhang and N. Pan, *Adv. Energy Mater.*, 2015, **5**, 1–19.

54 R. Vicentini, L. M. Da Silva, E. P. Cecilio, T. A. Alves, W. G. Nunes and H. Zanin, *Molecules*, 2019, **24**, 1452–1461.

55 L. Köps, P. Zaccagnini, C. F. Pirri and A. Balducci, *J. Power Sources Adv.*, 2022, **16**, 100098–100104.

56 A. Mendhe and H. S. Panda, *Discov. Mater.*, 2023, **3**, 29.

57 Y. Jia, D. Yang, L. Zhang, Y. Shi, J. Xie, F. Lei and L. Fan, *ChemElectroChem*, 2022, **9**, 1–9.

58 A. Burke, *Electrochim. Acta*, 2007, **53**, 1083–1091.

59 A. Lewandowksi, A. Olejniczak, G. Maciej and I. Stepniak, *J. Power Sources*, 2010, **195**, 5814–5819.

60 P. Simon and Y. Gogotsi, *Nat. Mater.*, 2008, **7**, 845–854.

61 A. Burke, *Int. J. Energy Res.*, 2010, **34**, 133–151.

62 R. Burt, K. Breitsprecher, B. Daffos, P. L. Taberna, P. Simon, G. Birkett, X. S. Zhao, C. Holm and M. Salanne, *J. Phys. Chem. Lett.*, 2016, **7**, 4015–4021.

63 L. Miao, Z. Song, D. Zhu, L. Li, L. Gan and M. Liu, *Energy and Fuels*, 2021, **35**, 8443–8455.

64 A. C. Forse, J. M. Griffin, C. Merlet, P. M. Bayley, H. Wang, P. Simon and C. P. Grey, *J. Am. Chem. Soc.*, 2015, **137**, 7231–7242.

65 F. Lai, J. Feng, T. Heil, G. C. Wang, P. Adler, M. Antonietti and M. Oschatz, *Energy Storage Mater.*, 2019, **20**, 188–195.

66 J. Xu, N. Yuan, J. M. Razal, Y. Zheng, X. Zhou, J. Ding, K. Cho, S. Ge, R. Zhang, Y. Gogotsi and R. H. Baughman, *Energy Storage Mater.*, 2019, **22**, 323–329.

67 W. L. Yuan, X. Yang, L. He, Y. Xue, S. Qin and G. H. Tao, *Front. Chem.*, 2018, **6**, 1–12.

68 N. C. Osti, X. Lin, W. Zhao, X. Wang, C. Chen, Y. Gao, T. Torita, A. I. Kolesnikov, P. T. Cummings, Y. Gogotsi and E. Mamontov, *2D Mater.*, 2023, **10**, 14014–14023.

69 V. V. Chaban, I. V. Voroshylova, O. N. Kalugin and O. V. Prezhdo, *J. Phys. Chem. B*, 2012, **116**, 7719–7727.

70 I. Hwang, M. Leketas, K. Griffiths, R. Bragg, J. M. Griffin and R. A. W. Dryfe, *ChemElectroChem*, 2024, **11**, 1–8.

71 Y. Wang, Y. Song and Y. Xia, *Chem. Soc. Rev.*, 2016, **45**, 5925–5950.

72 P. Sharma and T. S. Bhatti, *Energy Convers. Manag.*, 2010, **51**, 2901–2912.

73 W. G. Pell and B. E. Conway, *J. Power Sources*, 2004, **136**, 334–345.

74 J. W. Long, D. Bélanger, T. Brousse, W. Sugimoto, M. B. Sassin and O. Crosnier, *MRS Bull.*, 2011, **36**, 513–522.

75 J. Feng, N. A. Chernova, F. Omenya, L. Tong, A. C. Rastogi and M. Stanley Whittingham, *J. Solid State Electrochem.*, 2018, **22**, 1063–1078.

76 T. H. Wu, C. T. Hsu, C. C. Hu and L. J. Hardwick, *J. Power Sources*, 2013, **242**, 289–298.

77 X. Zang, C. Shen, M. Sanghadasa and L. Lin, *ChemElectroChem*, 2019, **6**, 976–988.

78 S. Vaquero, J. Palma, M. Anderson and R. Marcilla, *Int. J. Electrochem. Sci.*, 2013, **8**, 10293–10307.

79 N. Chang, T. Li, R. Li, S. Wang, Y. Yin, H. Zhang and X. Li, *Energy Environ. Sci.*, 2020, **13**, 3527–3535.

80 J. Xie, Z. Liang and Y. C. Lu, *Nat. Mater.*, 2020, **19**, 1006–1011.

81 Q. Nian, J. Wang, S. Liu, T. Sun, S. Zheng, Y. Zhang, Z. Tao and J. Chen, *Angew. Chemie - Int. Ed.*, 2019, **58**, 16994–16999.

82 J. Han, A. Mariani, S. Passerini and A. Varzi, *Energy Environ. Sci.*, 2023, **16**, 1480–1501.

83 L. Suo, O. Borodin, T. Gao, M. Olguin, J. Ho, X. Fan, C. Luo, C. Wang and K. Xu, *Science*, 2015, **350**, 938–943.

84 Y. Yamada, K. Furukawa, K. Sodeyama, K. Kikuchi, M. Yaegashi, Y. Tateyama and A. Yamada, *J. Am. Chem. Soc.*, 2014, **136**, 5039–5046.

85 N. Dubouis, P. Lemaire, B. Mirvaux, E. Salager, M. Deschamps and A. Grimaud, *Energy Environ. Sci.*, 2018, **11**, 3491–3499.

86 Y. Yamada, K. Usui, C. H. Chiang, K. Kikuchi, K. Furukawa and A. Yamada, *ACS Appl. Mater. Interfaces*, 2014, **6**, 10892–10899.

87 K. Yoshida, M. Nakamura, Y. Kazue, N. Tachikawa, S. Tsuzuki, S. Seki, K. Dokko and M. Watanabe, *J. Am. Chem. Soc.*, 2011, **133**, 13121–13129.

88 K. S. W. Sing, D. W. Everett, R. A. W. Haul, L. Moscou, R. A. Pierotti, J. Rouquérol and T. Siemieniewska, *Pure Appl. Chem.*, 1984, **57**, 603–619.

89 M. Oschatz and R. Walczak, *C*, 2018, **4**, 56.

90 M. Endo, T. Takeda, Y. J. Kim, K. Koshiba and K. Ishii, *Carbon Sci.*, 2001, **1**, 117–128.

91 Q. Ke and J. Wang, *J. Mater.*, 2016, **2**, 37–54.

92 G. Wang, L. Zhang and J. Zhang, *Chem. Soc. Rev.*, 2012, **41**, 797–828.

93 S. M. Rezaei Niya and J. Andrews, *Electrochim. Acta*, 2022, **402**, 139534–139546.

94 C. Kim, P. Srimuk, J. Lee, S. Fleischmann, M. Aslan and V. Presser, *Carbon*, 2017, **122**, 329–335.

95 T. P. McNicholas, A. Wang, K. O'Neill, R. J. Anderson, N. P. Stadie, A. Kleinhammes, P. Parilla, L. Simpson, C. C. Ahn, Y. Wang, Y. Wu and J. Liu, *J. Phys. Chem. C*, 2010, **114**, 13902–13908.

96 R. J. Anderson, T. P. McNicholas, A. Kleinhammes, A. Wang, J. Liu and Y. Wu, *J. Am. Chem. Soc.*, 2010, **132**, 8618–8626.

97 I. P. P. Cansado, F. A. M. M. Gonçalves, P. J. M. Carrott and M. M. L. Ribeiro Carrott, *Carbon*, 2007, **45**, 2454–2455.

98 R. E. Franklin, *Acta Crystallogr.*, 1951, **4**, 253–261.

99 X. Liu, D. Lyu, C. Merlet, M. Leesmith, X. Hua, Z. Xu, C. P. Grey and A. C. Forse, *Science*, 2024, **384**, 321–325.

100 L. HaweŁek, J. KoŁoczek, A. Bródka, J. C. Dore, V. Honkimäki and A. Burian, *Philos. Mag.*, 2007, **87**, 4973–4986.

101 V. Petkov, R. G. Difrancesco, S. J. L. Billinge, M. Acharya and H. C. Foley, *Philos. Mag. B Phys. Condens. Matter; Stat. Mech. Electron. Opt. Magn. Prop.*, 1999, **79**, 1519–1530.

102 J. C. Palmer, S. J. Jain, K. E. Gubbins, N. Cohaut, J. E. Fischer, R. K. Dash and Y. Gogotsi, *Characterisation of Porous Solids VIII: Proceedings of the 8th International Symposium on the Characterisation of Porous Solids*, The Royal Society of Chemistry, 2009.

103 P. J. F. Harris, *J. Mater. Sci.*, 2013, **48**, 565–577.

104 P. J. F. Harris, *Crit. Rev. Solid State Mater. Sci.*, 2005, **30**, 235–253.

105 P. J. F. Harris, Z. Liu and K. Suenaga, *J. Phys. Conf. Ser.*, 2010, **241**, 1–4.

106 F. A. L. de Souza, A. R. Ambrozio, E. S. Souza, D. F. Cipriano, W. L. Scopel and J. C. C. Freitas, *J. Phys. Chem. C*, 2016, **120**, 27707–27716.

107 J. C. C. Freitas, F. G. Emmerich, G. R. C. Cernicchiaro, L. C. Sampaio and T. J. Bonagamba, *Solid State Nucl. Magn. Reson.*, 2001, **20**, 61–73.

108 D. L. Vanderhart, W. L. Earl and A. N. Garroway, *J. Magn. Reson.*, 1981, **44**, 361–401.

109 J. Zhang, T. Tian, Y. Chen, Y. Niu, J. Tang and L. C. Qin, *Chem. Phys. Lett.*, 2014, **591**, 78–81.

110 A. C. Ferrari, *Solid State Commun.*, 2007, **143**, 47–57.

111 F. Tuinstra and J. L. Koenig, *J. Chem. Phys.*, 1970, **53**, 1126–1130.

112 R. Dash, J. Chmiola, G. Yushin, Y. Gogotsi, G. Laudisio, J. Singer, J. Fischer and S. Kucheyev, *Carbon*, 2006, **44**, 2489–2497.

113 J. C. Palmer, A. Llobet, S. H. Yeon, J. E. Fischer, Y. Shi, Y. Gogotsi and K. E. Gubbins, *Carbon*, 2010, **48**, 1116–1123.

114 M. Ishida and T. Ohba, *Sci. Rep.*, 2020, **10**, 1–8.

115 P. Zetterström, S. Urbonaite, F. Lindberg, R. G. Delaplane, J. Leis and G. Svensson, *J. Phys. Condens. Matter*, 2005, **17**, 3509–3524.

116 S. K. Jain, R. J. M. Pellenq, J. P. Pikunic and K. E. Gubbins, *Langmuir*, 2006, **22**, 9942–9948.

117 T. X. Nguyen, S. K. Bhatia, S. K. Jain and K. E. Gubbins, *Mol. Simul.*, 2006, **32**, 567–577.

118 T. X. Nguyen, N. Cohaut, J. S. Bae and S. K. Bhatia, *Langmuir*, 2008, **24**, 7912–7922.

119 Y. Shi, *J. Chem. Phys.*, 2008, **128**, 234707–234718.

120 M. Thompson, B. Dyatkin, H.-W. Wang, C. Turner, X. Sang, R. Unocic, C. Iacovella, Y. Gogotsi, A. van Duin and P. Cummings, *C*, 2017, **3**, 32.

121 K. S. W. Sing, *J. Porous Mater.*, 1995, **2**, 5–8.

122 S. Brunauer, P. H. Emmett and E. Teller, *J. Am. Chem. Soc.*, 1938, **60**, 309–319.

123 M. Thommes, K. Kaneko, A. V. Neimark, J. P. Olivier, F. Rodriguez-Reinoso, J. Rouquerol and K. S. W. Sing, *Pure Appl. Chem.*, 2015, **87**, 1051–1069.

124 A. V. Neimark, Y. Lin, P. I. Ravikovitch and M. Thommes, *Carbon*, 2009, **47**, 1617–1628.

125 C. Lastoskie, K. E. Gubbins and N. Quirke, *J. Phys. Chem.*, 1993, **97**, 4786–4796.

126 A. V. Neimark, P. I. Ravikovitch and A. Vishnyakov, *J. Phys. Condens. Matter*, 2003, **15**, 347–365.

127 E. P. Barrett, L. G. Joyner and P. P. Halenda, *J. Am. Chem. Soc.*, 1951, **73**, 378–380.

128 J. P. Olivier, *Carbon*, 1998, **36**, 1469–1472.

129 A. M. Puziy, O. I. Poddubnaya, B. Gawdzik and M. Sobiesiak, *Adsorption*, 2016, **22**, 459–464.

130 R. J. Dombrowski, D. R. Hyduke and C. M. Lastoskie, *Langmuir*, 2000, **16**, 5041–5050.

131 A. Nandy, A. C. Forse, V. J. Witherspoon and J. A. Reimer, *J. Phys. Chem. C*, 2018, **122**, 8295–8305.

132 D. Moran, F. Stahl, H. F. Bettinger, H. F. Schaefer and P. v. R. Schleyer, *J. Am. Chem. Soc.*, 2003, **125**, 6746–6752.

133 D. Lyu, K. Märker, Y. Zhou, E. W. Zhao, A. Gunnarsdóttir, S. Niblett, A. C. Forse and C. P. Grey, *J. Am. Chem. Soc.*, 2024, **146**, 9897–9910.

134 T. M. Alam and T. M. Osborn Popp, *Chem. Phys. Lett.*, 2016, **658**, 51–57.

135 A. Striolo, A. A. Chialvo, P. T. Cummings and K. E. Gubbins, *Langmuir*, 2003, **19**, 8583–8591.

136 A. González, E. Goikolea, J. A. Barrena and R. Mysyk, *Renew. Sustain. Energy Rev.*, 2016, **58**, 1189–1206.

137 J. Chmiola, C. Largeot, P. L. Taberna, P. Simon and Y. Gogotsi, *Angew. Chemie - Int. Ed.*, 2008, **47**, 3392–3395.

138 C. Largeot, C. Portet, J. Chmiola, P. L. Taberna, Y. Gogotsi and P. Simon, *J. Am. Chem. Soc.*, 2008, **130**, 2730–2731.

139 E. Raymundo-Piñero, K. Kierzek, J. Machnikowski and F. Béguin, *Carbon*, 2006, **44**, 2498–2507.

140 T. A. Centeno, O. Sereda and F. Stoeckli, *Phys. Chem. Chem. Phys.*, 2011, **13**, 12403–

12406.

141 Z. Jin, X. Yan, Y. Yu and G. Zhao, *J. Mater. Chem. A*, 2014, **2**, 11706–11715.

142 L. Suárez, V. Barranco and T. A. Centeno, *J. Colloid Interface Sci.*, 2021, **588**, 705–712.

143 F. Stoeckli and T. A. Centeno, *J. Mater. Chem. A*, 2013, **1**, 6865–6873.

144 D. E. Jiang, Z. Jin, D. Henderson and J. Wu, *J. Phys. Chem. Lett.*, 2012, **3**, 1727–1731.

145 Y. M. Liu, C. Merlet and B. Smit, *ACS Cent. Sci.*, 2019, **5**, 1813–1823.

146 J. Chen, Y. Han, X. Kong, X. Deng, H. J. Park, Y. Guo, S. Jin, Z. Qi, Z. Lee, Z. Qiao, R. S. Ruoff and H. Ji, *Angew. Chemie - Int. Ed.*, 2016, **55**, 13822–13827.

147 C. D. Williams and P. Carbone, *Environ. Sci. Technol.*, 2016, **50**, 3875–3881.

148 Y. Zhang, C. Prehal, H. Jiang, Y. Liu, G. Feng and V. Presser, *Cell Reports Phys. Sci.*, 2022, **3**, 100689.

149 L. A. Richards, A. I. Schäfer, B. S. Richards and B. Corry, *Small*, 2012, **8**, 1701–1709.

150 O. Beckstein, K. Tai and M. S. P. Sansom, *J. Am. Chem. Soc.*, 2004, **126**, 14694–14695.

151 H. Liu, C. J. Jameson and S. Murad, *Mol. Simul.*, 2008, **34**, 169–175.

152 S. Kondrat and A. A. Kornyshev, *Nanoscale Horizons*, 2016, **1**, 45–52.

153 Y. Shim and H. J. Kim, *ACS Nano*, 2010, **4**, 2345–2355.

154 S. Kondrat and A. Kornyshev, *J. Phys. Chem. C*, 2013, **117**, 12399–12406.

155 A. A. Lee, D. Vella, A. Goriely and S. Kondrat, *Phys. Rev. X*, 2016, **6**, 1–11.

156 O. Stern, *Elektrochem.*, 1924, **30**, 508–516.

157 D. C. Grahame, *Chem. Rev.*, 1947, **41**, 441–501.

158 J. M. Bockris, M. A. V Devanthan and K. Müller, *Proc. R. Soc. Lond. A. Math. Phys. Sci.*, 1962, **274**, 55–79.

159 P. M. Biesheuvel, Y. Fu and M. Z. Bazant, *Phys. Rev. E - Stat. Nonlinear, Soft Matter Phys.*, 2011, **83**, 61507–61524.

160 P. M. Biesheuvel, S. Porada, M. Levi and M. Z. Bazant, *J. Solid State Electrochem.*, 2014, **18**, 1365–1376.

161 P. M. Biesheuvel, R. Zhao, S. Porada and A. van der Wal, *J. Colloid Interface Sci.*, 2011, **360**, 239–248.

162 H. A. Arafat, M. Franz and N. G. Pinto, *Langmuir*, 1999, **15**, 5997–6003.

163 T. Kim, J. E. Dykstra, S. Porada, A. van der Wal, J. Yoon and P. M. Biesheuvel, *J. Colloid Interface Sci.*, 2015, **446**, 317–326.

164 M. Simoncelli, N. Ganfoud, A. Sene, M. Haefele, B. Daffos, P. L. Taberna, M. Salanne, P. Simon and B. Rotenberg, *Phys. Rev. X*, 2018, **8**, 21024.

165 G. Jeanmairet, B. Rotenberg and M. Salanne, *Chem. Rev.*, 2022, **122**, 10860–10898.

166 D. E. Jiang, Z. Jin and J. Wu, *Nano Lett.*, 2011, **11**, 5373–5377.

167 G. Feng and P. T. Cummings, *J. Phys. Chem. Lett.*, 2011, **2**, 2859–2864.

168 C. Lian, D. E. Jiang, H. Liu and J. Wu, *J. Phys. Chem. C*, 2016, **120**, 8704–8710.

169 C. Merlet, M. Salanne, B. Rotenberg and P. A. Madden, *Electrochim. Acta*, 2013, **101**, 262–271.

170 M. Z. Bazant, B. D. Storey and A. A. Kornyshev, *Phys. Rev. Lett.*, 2011, **106**, 6–9.

171 S. Perkin, T. Albrecht and J. Klein, *Phys. Chem. Chem. Phys.*, 2010, **12**, 1243–1247.

172 S. Perkin, L. Crowhurst, H. Niedermeyer, T. Welton, A. M. Smith and N. N. Gosvami, *Chem. Commun.*, 2011, **47**, 6572–6574.

173 R. Atkin and G. G. Warr, *J. Phys. Chem. C*, 2007, **111**, 5162–5168.

174 H. Li, R. J. Wood, F. Endres and R. Atkin, *J. Phys. Condens. Matter*, 2014, **26**, 284115–284123.

175 M. M. Hantel, V. Presser, R. Kötz and Y. Gogotsi, *Electrochem. commun.*, 2011, **13**, 1221–1224.

176 M. D. Levi, N. Levy, S. Sigalov, G. Salitra, D. Aurbach and J. Maier, *J. Am. Chem. Soc.*, 2010, **132**, 13220–13222.

177 M. D. Levi, S. Sigalov, G. Salitra, R. Elazari and D. Aurbach, *J. Phys. Chem. Lett.*, 2011, **2**, 120–124.

178 G. Sauerbrey, *Zeitschrift für Phys.*, 1959, **155**, 206–222.

179 L. Niu, L. Yang, J. Yang, M. Chen, L. Zeng, P. Duan, T. Wu, E. Pameté, V. Presser and G. Feng, *Ind. Chem. Mater.*, 2023, **1**, 175–187.

180 W. Y. Tsai, P. L. Taberna and P. Simon, *J. Am. Chem. Soc.*, 2014, **136**, 8722–8728.

181 H. Shao, Y. C. Wu, Z. Lin, P. L. Taberna and P. Simon, *Chem. Soc. Rev.*, 2020, **49**, 3005–3039.

182 T. Lé, G. Bidan, F. Billon, M. Delaunay, J. M. Gérard, H. Perrot, O. Sel and D. Aradilla, *Nanomaterials*, 2020, **10**, 1–17.

183 F. W. Richey and Y. A. Elabd, *J. Phys. Chem. Lett.*, 2012, **3**, 3297–3301.

184 F. W. Richey, B. Dyatkin, Y. Gogotsi and Y. A. Elabd, *J. Am. Chem. Soc.*, 2013, **135**, 12818–12826.

185 F. W. Richey, C. Tran, V. Kalra and Y. A. Elabd, *J. Phys. Chem. C*, 2014, **118**, 21846–21855.

186 P. W. Ruch, M. Hahn, D. Cericola, A. Menzel, R. Kötz and A. Wokaun, *Carbon*, 2010, **48**, 1880–1888.

187 D. A. Stevens and J. R. Dahn, *J. Electrochem. Soc.*, 2000, **147**, 4428.

188 C. Prehal, C. Koczwara, N. Jäckel, A. Schreiber, M. Burian, H. Amenitsch, M. A. Hartmann, V. Presser and O. Paris, *Nat. Energy*, 2017, **2**, 16215–16223.

189 J. L. Bañuelos, G. Feng, P. F. Fulvio, S. Li, G. Rother, S. Dai, P. T. Cummings and D. J. Wesolowski, *Chem. Mater.*, 2014, **26**, 1144–1153.

190 C. Prehal, D. Weingarth, E. Perre, R. T. Lechner, H. Amenitsch, O. Paris and V. Presser, *Energy Environ. Sci.*, 2015, **8**, 1725–1735.

191 S. Boukhalfa, L. He, Y. B. Melnichenko and G. Yushin, *Angew. Chemie - Int. Ed.*, 2013, **52**, 4618–4622.

192 S. Boukhalfa, D. Gordon, L. He, Y. B. Melnichenko, N. Nitta, A. Magasinski and G.

Yushin, *ACS Nano*, 2014, **8**, 2495–2503.

193 C. P. Grey and N. Dupré, *Chem. Rev.*, 2004, **104**, 4493–4512.

194 L. E. Marbella, S. Zekoll, J. Kasemchainan, S. P. Emge, P. G. Bruce and C. P. Grey, *Chem. Mater.*, 2019, **31**, 2762–2769.

195 R. Bhattacharyya, B. Key, H. Chen, A. S. Best, A. F. Hollenkamp and C. P. Grey, *Nat. Mater.*, 2010, **9**, 504–510.

196 S. Chandrashekar, N. M. Trease, H. J. Chang, L. S. Du, C. P. Grey and A. Jerschow, *Nat. Mater.*, 2012, **11**, 311–315.

197 F. Chevallier, M. Letellier, M. Morcrette, J. M. Tarascon, E. Frackowiak, J. N. Rouzaud and F. Béguin, *Electrochem. Solid-State Lett.*, 2003, **6**, 225–228.

198 M. A. Hope, B. L. D. Rinkel, A. B. Gunnarsdóttir, K. Märker, S. Menkin, S. Paul, I. V. Sergeyev and C. P. Grey, *Nat. Commun.*, 2020, **11**, 2224–2232.

199 S. Menkin, C. A. Okeefe, A. B. Gunnarsdóttir, S. Dey, F. M. Pesci, Z. Shen, A. Aguadero and C. P. Grey, *J. Phys. Chem. C*, 2021, **125**, 16719–16732.

200 M. Deschamps, E. Gilbert, P. Azais, E. Raymundo-Piñero, M. R. Ammar, P. Simon, D. Massiot and F. Béguin, *Nat. Mater.*, 2013, **12**, 351–358.

201 H. Wang, T. K. J. Köster, N. M. Trease, J. Ségalini, P. L. Taberna, P. Simon, Y. Gogotsi and C. P. Grey, *J. Am. Chem. Soc.*, 2011, **133**, 19270–19273.

202 O. Pecher, J. Carretero-Gonzalez, K. J. Griffith and C. P. Grey, *Chem. Mater.*, 2017, **29**, 213–242.

203 M. J. Duer, *Introduction to Solid-State NMR Spectroscopy*, Blackwell, Oxford, UK, 2004.

204 D. C. Apperley, R. K. Harris and P. Hodgkinson, *Solid-State NMR Basic Principles & Practice*, Momentum Press, New York, 2012.

205 T. D. W. Claridge, *High-Resolution NMR Techniques in Organic Chemistry*, Elsevier, Oxford, 2nd edn., 2009.

206 J. Keeler, *Understanding NMR Spectroscopy*, John Wiley and Sons, Chichester, 2nd edn., 2010.

207 P. J. Hore, *Nuclear Magnetic Resonance*, Oxford University Press, Oxford, 2nd edn., 2015.

208 M. H. Levitt, *Spin Dynamics: Basics of Nuclear Magnetic Resonance*, Wiley, Chichester, 2nd Editio., 2008.

209 R. K. Harris, E. D. Becker, S. M. Cabral De Menezes, P. Granger, R. E. Hoffman and K. W. Zilm, *Pure Appl. Chem.*, 2008, **80**, 59–84.

210 U. Haeberlen, *Advances in Magnetic Resonance*, Academic Press, New York, 1976.

211 M. Munowitz and A. Pines, *Science*, 1986, **233**, 525–531.

212 G. E. Pake, *J. Chem. Phys.*, 1948, **16**, 327–336.

213 D. Massiot, F. Fayon, M. Deschamps, S. Cadars, P. Florian, V. Montouillout, N. Pellerin, J. Hiet, A. Rakhmatullin and C. Bessada, *Comptes Rendus Chim.*, 2010, **13**, 117–129.

214 S. E. Ashbrook and S. Wimperis, 2004, **45**, 53–108.

215 S. E. Ashbrook, *Phys. Chem. Chem. Phys.*, 2009, **11**, 6875–6875.

216 A. J. Pell, G. Pintacuda and C. P. Grey, *Prog. Nucl. Magn. Reson. Spectrosc.*, 2019, **111**, 1–271.

217 A. Kubo, T. P. Spaniol and T. Terao, *J. Magn. Reson.*, 1998, **133**, 330–340.

218 R. Ulrich, R. W. Glaser and A. S. Ulrich, *J. Magn. Reson.*, 2003, **164**, 115–127.

219 L. Zhou, M. Leskes, A. J. Ilott, N. M. Trease and C. P. Grey, *J. Magn. Reson.*, 2013, **234**, 44–57.

220 H. A. Lorentz, *The Theory of Electrons*, Dover, New York, 2nd edn., 1952.

221 D. L. VanderHart, *eMagRes*, 2007, 1–9.

222 D. Doskočilová, D. D. Tao and B. Schneider, *Czech J. Phys. B.*, 1975, **25**, 202–209.

223 L. E. Drain, *Proc. Phys. Soc.*, 1962, **80**, 1380–1382.

224 J. D. Jackson, *Classical Electrodynamics*, Wiley, New York, 2nd edn., 1975.

225 M. H. Levitt, *Concepts Magn. Reson.*, 1996, **8**, 77–103.

226 W. C. Dickinson, *Phys. Rev.*, 1951, **81**, 717–731.

227 J. R. Zimmerman and M. R. Foster, **61**, 282–289.

228 P. M. Vora, P. Gopu, M. Rosario-Canales, C. R. Pérez, Y. Gogotsi, J. J. Santiago-Avilés and J. M. Kikkawa, *Phys. Rev. B - Condens. Matter Mater. Phys.*, 2011, **84**, 1–8.

229 M. Ernst, A. Samosan and B. H. Meier, *Phys. Chem. Chem. Phys.*, 2001, **348**, 1–10.

230 M. Ernst, A. Samoson and B. H. Meier, *J. Chem. Phys.*, 2005, **123**, 64102–64112.

231 D. Marion, M. Ikura, R. Tschudin and A. Bax, *J. Magn. Reson.*, 1989, **85**, 393–399.

232 I. Scholz, P. Hodgkinson, B. H. Meier and M. Ernst, *J. Chem. Phys.*, 2009, **130**, 114510–114527.

233 M. Mehring, A. Pines, W. K. Rhim and J. S. Waugh, *J. Chem. Phys.*, 1971, **54**, 3240–3241.

234 M. Ernst, H. Zimmermann and B. H. Meier, *Chem. Phys. Lett.*, 2000, **317**, 581–588.

235 A. Pines, M. G. Gibby and J. S. Waugh, *J. Chem. Phys.*, 1972, **56**, 1776–1777.

236 S. R. Hartmann and E. L. Hahn, *Phys. Rev.*, 1962, **128**, 2042–2053.

237 S. E. Ashbrook, S. E. Dawson and J. M. Griffin, *Solid-State Nuclear Magnetic Resonance Spectroscopy*, Wiley, Chichester, 2013.

238 E. O. Stejskal, J. Schaefer and J. S. Waugh, *J. Magn. Reson.*, 1977, **28**, 105–112.

239 G. Metz, X. Wu and S. O. Smith, *J. Magn. Reson.*, 1994, **110**, 219–227.

240 E. L. Hahn, *Phys. Rev.*, 1950, **80**, 580–594.

241 D. G. Cory and W. M. Ritchey, *J. Magn. Reson.*, 1988, **80**, 128–132.

242 R. M. Bendall and R. E. Gordon, *J. Magn. Reson.*, 1983, **53**, 365–385.

243 E. L. Hahn, *Phys. Rev.*, 1949, **76**, 145–146.

244 L. E. Drain, *Proc. Phys. Soc. Sect. A*, 1949, **62**, 301–306.

245 D. C. Look and D. R. Locker, *Rev. Sci. Instrum.*, 1970, **41**, 250–251.

246 R. Wei, C. L. Dickson, D. Uhrín and G. C. Lloyd-Jones, *J. Org. Chem.*, 2021, **86**, 9023–9029.

247 A. G. Redfield, *Phys. Rev.*, 1955, **98**, 1787–1809.

248 F. Bloch, *Phys. Rev.*, 1946, **70**, 460–474.

249 J. R. Hendrickson and P. J. Bray, *A Phenomenological Equation for NMR Motional Narrowing in Solids*, 1973, vol. 9.

250 H. M. McConnell, *J. Chem. Phys.*, 1958, **28**, 430–431.

251 D. F. Hansen and J. J. Led, *J. Magn. Reson.*, 2003, **163**, 215–227.

252 C. L. Perrin and T. J. Dwyer, *Chem. Rev.*, 1990, **90**, 935–967.

253 J. Jeener, B. H. Meier, P. Bachmann and R. R. Ernst, *J. Chem. Phys.*, 1979, **71**, 4546–4553.

254 A. D. Bain, *Prog. Nucl. Magn. Reson. Spectrosc.*, 2003, **43**, 63–103.

255 I. R. Kleckner and M. P. Foster, *Biochim. Biophys. Acta - Proteins Proteomics*, 2011, **1814**, 942–968.

256 D. S. Scholl and J. A. Steckel, *Density Functional Theory: A Practical Introduction*, Wiley, New York, 2009.

257 K. A. Baseden and J. W. Tye, *J. Chem. Educ.*, 2014, **91**, 2116–2123.

258 M. Born and R. J. Oppenheimer, *Ann. Phys.*, 1927, **389**, 457–484.

259 D. R. Hartree, *The Calculation of Atomic Structures*, John Wiley and Sons, New York, 1957.

260 P. Hohenberg and W. Kohn, *Phys. Rev.*, 1964, **136**, 864–871.

261 P. Atkins and R. Friedman, *Molecular Quantum Mechanics*, Oxford University Press, Oxford, 4th edn., 2005.

262 W. Kohn and L. J. Sham, *Phys. Rev.*, 1965, **140**, 1133–1138.

263 J. P. Perdew, K. Burke and M. Ernzerhof, *Phys. Rev. Lett.*, 1996, **77**, 3865–3868.

264 S. F. Boys, *Proc. R. Soc. Lond. A. Math. Phys. Sci.*, 1950, **200**, 542–554.

265 M. C. Payne, M. P. Teter, D. C. Allan, T. A. Arias and J. D. Joannopoulos, *Rev. Mod. Phys.*, 1992, **64**, 1045–1097.

266 F. Bloch, *Zeitschrift für Phys.*, 1929, **52**, 555–600.

267 J. R. Yates and C. J. Pickard, in *eMagRes*, eds. R. Harris and R. Wasylishen, 2008, pp. 1–9.

268 J. R. Hook and H. E. Hall, *Solid State Physics*, Wiley, Chichester, 1991.

269 P. Kratzer and J. Neugebauer, *Front. Chem.*, 2019, **7**, 1–18.

270 H. J. Monkhorst and J. D. Pack, *Phys. Rev. B*, 1976, **13**, 5188–5192.

271 N. Marzari, University of Cambridge, 1996.

272 J. Jorgenson and G. L. W. Hart, *Model. Simul. Mater. Sci. Eng.*, 2021, **29**, 1–15.

273 F. J. Dos Santos and N. Marzari, *Phys. Rev. B*, 2023, **107**, 1–10.

274 C. L. Fu and K. M. Ho, *Phys. Rev. B*, 1983, **28**, 5480–5486.

275 U. von Barth and C. D. Gelatt, *Phys. Rev. B*, 1980, **21**, 2222–2228.

276 D. Vanderbilt, *Phys. Rev. B*, 1990, **41**, 7892–7895.

277 C. J. Pickard and F. Mauri, *Phys. Rev. B - Condens. Matter Mater. Phys.*, 2001, **63**, 2451011–2451013.

278 P. E. Blöchl, *Phys. Rev. B*, 1994, **50**, 17953–17979.

279 B. G. Pfrommer, M. Côté, S. G. Louie and M. L. Cohen, *J. Comput. Phys.*, 1997, **131**, 233–240.

280 J. Antony and S. Grimme, *Phys. Chem. Chem. Phys.*, 2006, **8**, 5287–5293.

281 S. Grimme, *J. Comput. Chem.*, 2004, **25**, 1463–1473.

282 S. Tsuzuki, K. Honda, T. Uchimaru and M. Mikami, *J. Chem. Phys.*, 2004, **120**, 647–659.

283 S. Grimme, S. Ehrlich and L. Goerigk, *J. Comput. Chem.*, 2011, **32**, 1456–1465.

284 N. Fairley, CasaXPS, www.casaxps.com.

285 M. J. Frisch, G. W. Trucks, H. B. Schlegel, G. E. Scuseria, M. A. Robb, J. R. Cheeseman, G. Scalmani, V. Barone, G. A. Petersson, H. Nakatsuji, X. Li, M. Caricato, A. V. Marenich, J. Bloino, B. G. Janesko, R. Gomperts, B. Mennucci, H. P. Hratchian, J. V. Oritz, A. F. Izmaylov, J. L. Sonnenberg, D. Williams-Young, F. Ding, F. Lipparini, F. Egidi, J. Goings, B. Peng, A. Petrone, T. Henderson, D. Ranasinghe, V. G. Zakrzewski, J. Gao, N. Rega, G. Zheng, W. Liang, M. Hada, M. Ehara, K. Toyota, R. Fukuda, J. Hasegawa, M. Ishida, T. Nakajima, Y. Honda, O. Kitao, H. Nakai, T. Vreven, K. Throssell, J. A. Montgomery, J. J. E. Peralta, F. Ogliaro, M. J. Bearpark, J. J. Heyd, E. N. Brothers, K. N. Kudin, V. N. Staroverov, T. A. Keith, R. Kobayashi, J. Normand, K. Raghavachari, A. P. Rendell, J. C. Burant, S. S. Iyengar, J. Tomasi, M. Cossi, J. M. Millam, M. Klene, C. Adamo, R. Cammi, J. W. Ochterski, R. L. Martin, K. Morokuma, O. Farkas, J. B. Foresman and D. J. Fox, Gaussian 16, Revision C.01.

286 S. Grimme, J. Antony, S. Ehrlich and H. Krieg, *J. Chem. Phys.*, 2010, **132**, 154104.

287 S. Bi, Y. Zhang, L. Cervini, T. Mo, J. M. Griffin, V. Presser and G. Feng, *Sustain. Energy Fuels*, 2020, **4**, 1285–1295.

288 P. Westreich, S. Selig, H. Fortier and J. R. Dahn, *Carbon*, 2006, **44**, 3145–3148.

289 F. Hofmeister, *Arch. für Exp. Pathol. und Pharmakologie*, 1888, **25**, 1–30.

290 K. P. Gregory, G. R. Elliott, H. Robertson, A. Kumar, E. J. Wanless, G. B. Webber, V. S. J. Craig, G. G. Andersson and A. J. Page, *Phys. Chem. Chem. Phys.*, 2022, **24**, 12682–12718.

291 K. D. Collins and M. W. Washabaugh, *Q. Rev. Biophys.*, 1985, **18**, 323–422.

292 K. Kiyohara, Y. Yamamoto and Y. Kawai, *Phys. Chem. Chem. Phys.*, 2020, **22**, 25184–25194.

293 L. A. Richards, B. S. Richards, B. Corry and A. I. Schäfer, *Environ. Sci. Technol.*, 2013, **47**, 8987–8988.

294 M. H. Abraham and Y. Marcus, *J. Chem. Soc., Faraday Trans.*, 1987, **83**, 339–349.

295 A. A. Merdaw, A. O. Sharif and G. A. W. Derwish, *Chem. Eng. J.*, 2011, **168**, 229–240.

296 Y. Marcus, *J. Chem. Soc., Faraday Trans.*, 1991, **87**, 2995–2999.

297 T. Osakai and K. Ebina, *J. Phys. Chem. B*, 1998, **102**, 5691–5698.

298 H. D. B. Jenkins and Y. Marcus, *Chem. Rev.*, 1995, **95**, 2695–2724.

299 C. D. Williams, J. Dix, A. Troisi and P. Carbone, *J. Phys. Chem. Lett.*, 2017, **8**, 703–708.

300 A. A. Papaderakis, J. S. Roh, K. Polus, J. Yang, M. A. Bissett, A. Walton, A. Juel and R. A. W. Dryfe, *Faraday Discuss.*, 2023, **246**, 307–321.

301 K. Ounnunkad, H. V. Patten, M. Velický, A. K. Farquhar, P. A. Brooksby, A. J. Downard and R. A. W. Dryfe, *Faraday Discuss.*, 2017, **199**, 49–61.

302 D. Liu, Z. Xiong, P. Wang, Q. Liang, H. Zhu, J. Z. Liu, M. Forsyth and D. Li, *Nano Lett.*, 2023, **23**, 5555–5561.

303 H. H. Loeffler and B. M. Rode, *J. Chem. Phys.*, 2002, **117**, 110–117.

304 C. N. Rowley and B. Roux, *J. Chem. Theory Comput.*, 2012, **8**, 3526–3535.

305 J. Mähler and I. Persson, *Inorg. Chem.*, 2012, **51**, 425–438.

306 K. Hayamizu, Y. Chiba and T. Haishi, *RSC Adv.*, 2021, **11**, 20252–20257.

307 N. Shpigel, M. D. Levi, S. Sigalov, T. S. Mathis, Y. Gogotsi and D. Aurbach, *J. Am. Chem. Soc.*, 2018, **140**, 8910–8917.

308 Y. Marcus, *Pure Appl. Chem.*, 2010, **82**, 1889–1899.

309 D. Russo, *Chem. Phys.*, 2008, **345**, 200–211.

310 S. Moelbert, B. Normand and P. De Los Rios, *Biophys. Chem.*, 2004, **112**, 45–57.

311 M. F. Chaplin, in *Water and Life: The Unique Properties of H2O*, CRC Press, 1st edn., 2010, pp. 69–86.

312 T. Morita, P. Westh, K. Nishikawa and Y. Koga, *J. Phys. Chem. B*, 2014, **118**, 8744–8749.

313 H. Ohtaki and T. Radnai, *Chem. Rev.*, 1993, **93**, 1157–1204.

314 R. W. Gurney, *Ionic Processes in Solution*, McGraw-Hill Book Company, Inc, New York, Toronto, London, 1953.

315 H. S. Frank and M. W. Evans, *J. Chem. Phys.*, 1945, **13**, 507–532.

316 Y. Marcus, *J. Solution Chem.*, 1986, **15**, 291–306.

317 M. Kibalchenko, M. C. Payne and J. R. Yates, *ACS Nano*, 2011, **5**, 537–545.

318 J. D. Halliday, R. E. Richards, F. R. S. Sharp and R. R. Sharp, *Proc. R. Soc. London. A. Math. Phys. Sci.*, 1969, **313**, 45–69.

319 D. Massiot, F. Fayon, M. Capron, I. King, S. Le Calvé, B. Alonso, J. O. Durand, B. Bujoli, Z. Gan and G. Hoatson, *Magn. Reson. Chem.*, 2002, **40**, 70–76.

320 M. Lundström, J. Aromaa and O. Forsén, *Hydrometallurgy*, 2009, **95**, 285–289.

321 R. J. Bragg, K. Griffiths, I. Hwang, M. Leketas, K. Polus, V. Presser, R. A. W. Dryfe and J. M. Griffin, *Carbon*, 2024, **229**, 119531.

322 J. F. M. Oth, E. P. Woo and F. Sondheimer, *J. Am. Chem. Soc.*, 1973, **6259**, 7337–7345.

323 S. Sharma and P. Chand, *Results Chem.*, 2023, **5**, 100885.

324 P. Srimuk, X. Su, J. Yoon, D. Aurbach and V. Presser, *Nat. Rev. Mater.*, 2020, **5**, 517–538.

325 W. Chen, Z. Fan, X. Pan and X. Bao, *J. Am. Chem. Soc.*, 2008, **130**, 9414–9419.

326 H. Gao, Y. Kong, D. Cui and C. S. Ozkan, *Nano Lett.*, 2003, **3**, 471–473.

327 M. Bühl, *Chem. - A Eur. J.*, 1998, **4**, 734–739.

328 N. A. Besley and A. Noble, *J. Chem. Phys.*, 2008, **128**, 101102–101106.

329 X. Liu, X. Pan, W. Shen, P. Ren, X. Han and X. Bao, *J. Phys. Chem. C*, 2012, **116**, 7803–7809.

330 Q. Chen, J. L. Herberg, G. Mogilevsky, H. J. Wang, M. Stadermann, J. K. Holt and Y. Wu, *Nano Lett.*, 2008, **8**, 1902–1905.

331 D. Sundholm, R. J. F. Berger and H. Fliegl, *Phys. Chem. Chem. Phys.*, 2016, **18**, 15934–15942.

332 P. W. Fowler, W. Myrvold, C. Gibson, J. Clarke and W. H. Bird, *J. Phys. Chem. A*, 2020, **124**, 4517–4533.

333 J. R. Yates, C. J. Pickard and F. Mauri, *Phys. Rev. B - Condens. Matter Mater. Phys.*, 2007, **76**, 1–11.

334 J. R. Yates, C. J. Pickard, M. C. Payne and F. Mauri, *J. Chem. Phys.*, 2003, **118**, 5746–5753.

335 L. Lai, J. Lu, W. Song, M. Ni, L. Wang, G. Luo, J. Zhou, W. N. Mei, Z. Gao and D. Yu, *J. Phys. Chem. C*, 2008, **112**, 16417–16421.

336 E. Zurek and J. Autschbach, *J. Am. Chem. Soc.*, 2004, **126**, 13079–13088.

337 E. Zurek, C. J. Pickard and J. Autschbach, *J. Phys. Chem. C*, 2008, **112**, 11744–11750.

338 E. Zurek, C. J. Pickard, B. Walczak and J. Autschbach, *J. Phys. Chem. A*, 2006, **110**, 11995–12004.

339 J. Vähäkangas, S. Ikäläinen, P. Lantto and J. Vaara, *Phys. Chem. Chem. Phys.*, 2013, **15**, 4634–4641.

340 T. Thonhauser, D. Ceresoli and N. Marzari, *Int. J. Quantum Chem.*, 2009, **109**, 3336–3342.

341 A. R. Ambrozio, J. M. Leyssale, R. J. M. Pellenq, F. A. L. De Souza, G. L. Vignoles, W. L. Scopel and J. C. C. Freitas, *J. Phys. Chem. C*, 2020, **124**, 12784–12793.

342 J. P. Perdew, M. Ernzerhof and K. Burke, *J. Chem. Phys.*, 1996, **105**, 9982–9985.

343 B. L. Dale, N. R. Halcovitch, M. J. G. Peach and J. M. Griffin, *Magn. Reson. Chem.*, 2019, **57**, 230–242.

344 C. M. Rice, Z. H. Davis, D. McKay, G. P. M. Bignami, R. G. Chitac, D. M. Dawson, R. E. Morris and S. E. Ashbrook, *Phys. Chem. Chem. Phys.*, 2020, **22**, 14514–14526.

345 J. B. Stothers, *Carbon-13 NMR Spectroscopy*, Academic Press, New York, 1st edn., 1972.

346 M. A. L. Marques, M. D'Avezac and F. Mauri, *Phys. Rev. B - Condens. Matter Mater. Phys.*, 2006, **73**, 1–6.

347 N. T. Thuy Tran, S. Y. Lin, Y. T. Lin and M. F. Lin, *Phys. Chem. Chem. Phys.*, 2016, **18**, 4000–4007.

348 Y. Zhang, C. H. Hu, Y. H. Wen, S. Q. Wu and Z. Z. Zhu, *New J. Phys.*, 2011, **13**, 63047–63056.

349 C. Berger, X. Wu, N. Brown, C. Naud, X. Li, Z. Song, D. Mayou, T. Li, J. Hass, a. Marchenkov, E. H. Conrad, P. N. First and W. a. De Heer, *Science*, 2006, **312**, 1191–1196.

350 J. Zhou, Q. Wang, Q. Sun, X. S. Chen, Y. Kawazoe and P. Jena, *Nano Lett.*, 2009, **9**, 3867–3870.

351 T. Charpentier, *Solid State Nucl. Magn. Reson.*, 2011, **40**, 1–20.

352 M. Zilka, S. Sturniolo, S. P. Brown and J. R. Yates, *J. Chem. Phys.*, 2017, **147**, 144203–144211.

353 F. Mauri, B. G. Pfrommer and S. G. Louie, *Phys. Rev. Lett.*, 1996, **77**, 5300–5303.

354 T. Gregor, F. Mauri and R. Car, *J. Chem. Phys.*, 1999, **111**, 1815–1822.

355 C. Goze-Bac, S. Latil, P. Lauginie, V. Jourdain, J. Conard, L. Duclaux, A. Rubio and P. Bernier, *Carbon*, 2002, **40**, 1825–1842.

356 M. A. Worsley, S. O. Kucheyev, H. E. Mason, M. D. Merrill, B. P. Mayer, J. Lewicki, C. A. Valdez, M. E. Suss, M. Stadermann, P. J. Pauzauskie, J. H. Satcher, J. Biener and T. F. Baumann, *Chem. Commun.*, 2012, **48**, 8428–8430.

357 T. K. Das, S. Banerjee, M. Pandey, B. Vishwanadh, R. J. Kshirsagar and V. Sudarsan, *Int. J. Hydrogen Energy*, 2017, **42**, 8032–8041.

358 A. M. Panich, A. I. Shames, A. E. Aleksenskii and A. Dideikin, *Solid State Commun.*, 2012, **152**, 466–468.

359 D. Sebastiani, *ChemPhysChem*, 2006, **7**, 164–175.

360 R. Gershoni-Poranne and A. Stanger, *Chem. Soc. Rev.*, 2015, **44**, 6597–6615.

361 J. C. Meyer, C. Kisielowski, R. Erni, M. D. Rossell, M. F. Crommie and A. Zettl, *Nano Lett.*, 2008, **8**, 3582–3586.

362 A. J. Stone and D. J. Wales, *Chem. Phys. Lett.*, 1986, **128**, 501–503.

363 L. B. Alemany, L. Zhang, L. Zeng, C. L. Edwards and A. R. Barron, *Chem. Mater.*, 2007, **19**, 735–744.